The Development of a Semi-deterministic Wear Model for a Fully Formulated Hydraulic Oil: Experimental and Numerical Study

Yajing Gong

Submitted in accordance with the requirements for the degree of

Doctor of Philosophy

The University of Leeds
School of Mechanical Engineering
Institute of Functional Surfaces
Leeds, UK

November, 2021

The candidate confirms that the work submitted is her own and that appropriate credit has been given where reference has been made to the work of others.

Acknowledgements

First of all, I would like to show a sincere appreciation to my supervisors Prof. Anne Neville, Prof. Ardian Morina and Dr Ali Ghanbarzadeh for their technical guidance and research support for the project, as well as their encouragement to me during the whole project. In addition, I would like to thank Komatsu Ltd. (Japan), the sponsor of the project, for providing the funding to my study and supporting the requirements in the project such as samples and equipment, as well as two staff Mr Yukio Tamura and Mr Akihito Ishihara from the company for their cooperation and communication.

Then, I would like to thank IFS member Dr Yuechang Wang for kindly sharing his knowledge and enlightening my research. Special thanks to Dr Chun Wang and her family for their support and help in the experiment and my life in the UK. Thanks also to the other members or staff in the University of Leeds, especially Aaron Thornley, Abdel Dorgham, Abdullah Azam, Bingyu Sun, Cailin Wang, Cayetano Espejo-Conesa, Dongming Yang, Fiona Slade, Gerda Vaitkunaite, Kabir Raheem, Jialin Wang, Jordan Thomas, Liuquan Yang, Nan Xu, Paul Byron, Qingyang Liu, Robbie Brittain, Shusheng Xu, Thawhid A. Khan, Wassim Taleb, Wenlong Ma, Yong Hua, etc.

Finally, I would like to thank my parents, Shuguang Gong and Guilan Xie, for their financial support for my life and their assistance in my studies. I would like to thank my friends in the UK and China for their companions and spiritual supports during the study.

Abstract

Wear is an important factor that affects the working efficiency of machines and even leads to catastrophic failures, so reducing wear has always been one of the topics of the industry. Lubricant additives with different functions and characteristics have been developed such as anti-wear additives, detergents, dispersants and antioxidants to improve the efficiency of machines and reduce wear. Although there have been enormous studies on the wear of single or multi-component additives, the wear process for fully formulated oils is still unknown, making it difficult to understand and predict wear for industrial users. This project is aimed to study the wear mechanism of a fully formulated oil (FFO) containing commonly used additives and develop a wear model involving tribochemistry that can be used for general FFO with similar formulations or properties.

In the experimental study of FFO, the in-situ growth process of tribofilm and the corresponding wear evolution were tested by Mini Traction Machine (MTM) and White Light Interferometry, respectively. The experiments involved three factors such as the effects of temperature, additive and λ ratio to investigate the wear mechanism of FFO (tribofilm). The temperature dependence of the wear mechanism of the FFO under boundary lubrication condition was found, that is, in the low-temperature range of 60~80℃, wear increases with the increase in temperature, while in the high-temperature range of 80~120 ℃, when the temperature increases, wear decreases. The wear trend did not change with λ ratios in boundary lubrication. However, at the high λ ratio, tribofilm thickness increases with increasing temperature when it reaches the stable phase, but the balanced thickness changed very little with the temperature at the low λ ratio. The hypothesis is that the FFO wear mechanism is mainly caused by the formation process and chemical compositions of tribofilm rather than tribofilm thickness.

Chemical analysis of tribofilm was carried out by Raman Spectroscopy and X-ray Photoelectron Spectroscopy (XPS). The main compositions in the FFO tribofilm were found to be phosphates and sulphides, with less calcium carbonate and sulphates on the top surface. For both λ ratios, with the increase of temperature, the peak intensity of phosphates increases while that of sulphides decreases. In addition, XPS analysis found that there was no evidence of the dispersant participating in the composition of the tribofilm. Although none of the components or additives conforms to the wear trend, the

composition of tribofilm and additives in FFO suggests that the two-phase wear mechanism of FFO may be caused by the reaction priority or antagonism between ZDDP and detergents at different temperatures.

Based on the layered contact model of rough surfaces, a tribochemical wear model framework of FFO was developed. Since the material properties of tribofilm are different from those of steel substrate, tribofilm is considered as a layer and the influence of its properties on elastoplastic deformation is considered. The mass of iron in tribofilm of any thickness has been calculated by using the curve of Fe% in XPS with tribofilm thickness in the tribochemical wear model, and according to the concept of mass conservation of iron, wear in the substrate is obtained. The tribofilm growth curve and wear process in the simulation results showed good agreement with the experimental results. Meanwhile, the contact stress at the top surface and shear stress of the subsurface layer considering the effects of friction coefficient under different temperatures are calculated, which provides a three-dimensional wear and stress approach involving tribochemistry for FFO.

Contents

List of Figures

List of Tables

Nomenclature

Letter Symbols

a_0, a	Contact radius
a, b	Length and width of Hertzian contact area in x and y direction, respectively
a_1	Maximum area of the contact point
A	- Contact area (CH2) - A coefficient related to the molar volume and effective frequency of the growth product (CH3) - Surface area (CH7)
A_m	Etching area
A_r	The effective area of the reactant
A_s	Scaling constant
AL	Constant to control aliasing phenomenon
$\bar{A}$, $\bar{B}$, $\bar{C}$	Complex conjugate of A, B, C, respectively
B	Degradation coefficient
C, D	Constants relevant to the two reaction rates
$C(h)$	Concentration of the substrate material
C_1	Constant
C_3, C_4	Removal constants
$C_p^{u_z}$	Influence coefficient matrix of displacement
C_p^{σ}	Influence coefficient matrix of stress
C_r	A parameter of surface characteristics
$C(0)$	Concentration of the diffusion compounds
$CoW_{\min}$	Minimum wear coefficient
CoW_{tr}	Wear coefficient of tribofilm
CoW_{steel}, K_{steel}	Wear coefficient of steel
D_f	Fractal dimension
D_d	Diffusion coefficient
e_n	Difference between the prescribed load and the calculated load
E	Elastic modulus
E_0	Nominal activation energy when no contact pressure P is applied
ΔE, Q	Activation energy
E_f^*, E^*	Reduced Young's modulus
E_{f0}^*	Reduced Young's modulus of the tribofilm when $H \le H_0$
F	Force
F_a	Adhesion force
F_d	Force related to deformation energy

F_f	Friction force
F_k	Dynamic friction force
F_n	Normal load
F_s	Static friction force
F_{total}	Total frictional force
g	Rough surface geometry
G	Shear modulus
G^*	Material dimensionless parameter
h	Film thickness
h'	Larger thickness between the ball and the disc
h_a, h_b	Maximum thickness that the two-step tribochemical reactions can reach, respectively
$h_{balance}$	Balanced thickness
h_c	- Centre film thickness (CH2) - Threshold thickness when tribochemical wear occurs (CH7)
$h_{\min}$	Minimum film thickness
$h_{\max}$	Maximum tribofilm thickness
h_{mx}	Thickness on the covered area
h_{net}	Net tribofilm growth
h_P	Plank's constant
h_r	Removed thickness
H	Hardness
H_0	Threshold hardness
H_c	Dimensionless centre film thickness
H_{film}	Hardness of the tribofilm
$H_{\min}$	Dimensionless minimum film thickness
H_s	Hardness of the substrate
i, j	Index of the point in x and y direction, respectively
I_e, I_p and I_0	Index of the elastic zone, plastic zone and the rest of the contact region, respectively
I_{plane}	Height error of the elastic deformation
$\sqrt{J_2}$	Von Mises stress
k, l	Index of the point in x and y direction, respectively
k_1, k_5	Rate constant
k_A	Apparent kinetic constant of the tribofilm
k_B	Boltzmann's constant
K_c	Constant related to concentrations and kinds of ZDDP
$k_{tribo\text{-}thermo}$	Influence constant of mechanical and temperature on the rate of inducing tribochemical reaction
k_{thermo}	Rate constant of temperature activation
K	Wear coefficient

K_0	Overall parameter in diffusion model
K_c	Constant related to concentrations and kinds of ZDDP
K_d	Constant in the diffusion model
K_{film}	Tribochemical wear coefficient
K_p, K_i, K_d	Constants in PID controller
K_{wear}	Dimensionless wear loss coefficient
l_c	Characteristic wear length
L	Load
m	Mass (CH3)
m, n	Corresponding frequency variables of of x and y in the frequency domain, $\alpha = \sqrt{m^2 + n^2}$ (CH7)
$m_{Fe\text{-}comp}$	Mass of iron removed in the surface layer of tribofilm
$m_{Fe\text{-}wear}$	Mass of iron lost in the substrate
M, N	Total discrete grid points
$M_{\exp}$, $N_{\exp}$	Refinement of the initial discrete grid points M and N, respectively
N_A	Avogadro's number
p, P	Normal pressure or force
p_h, $p_{\max}$	Maximum Hertzian contact pressure
q_x, q	Traction force, shear stress
r_{cA}	Consumption rate of lubricant precursors
r_{cF}	Generation rate of deposited mass due to chemical reaction
r_{mB}	Production rate of waste product
r_{mF}	Consumption rate of deposited mass by mechanical removal
r_{qA}, r_{qB}	Conversion rate
R	Gas constant
R^2	The coefficient of determination on goodness-of-fit
R_x	Composite radius of curvature in x direction
S	Sliding distance
S_{ku}	Kurtosis
S_{sk}	Skewness
s_z	Height of roughness surface
S_z	Surface topography
t	Time
t_c	Characteristic time
t_0	Delayed time of the latter reactions
T	Temperature
T_b	Bulk temperature
T_f	Flash temperature
u	Deformation
u, v, w	Velocity in x, y, and z direction, respectively in Equ. (2-3)

$\bar{u}$	Average velocity
u_e	Elastic deformation
u_p, U_p	Plastic deformation
u_{zi}	Calculated *z*-direction displacement components
u_{zi}^*	Prescribed *z*-direction displacement components
u_z	Sum of calculated deformations of two contacting solids in the z-direction $u_z = u_{z0} + u_{z1}$
ΔU_{act}	Internal activation energy
U_1, U_2	Velocities of two contact surfaces, respectively
U^*	Speed dimensionless parameter
U_e	Entrainment speed
U_E	Elastic strain energy
U_E^*	Complementary energy
U_s, v, V	Sliding speed
ΔV_{act}	Activated volume
V^*	Minimum internal complementary potential energy
V_f	Tribofilm volume
$V_{Fe\text{-}comp}$	The volume of iron contained in the removal part of tribofilm
$V_{Fe\text{-}wear}$	Wear volume lost in the substrate
V_m	Molecular volume
V_r	Removed volume of tribofilm
V_{wear}	Wear volume
W	Load
W^*	Load dimensionless parameter
W_m	Mass fraction of the diffusion compounds formed with the metal
W_{perc}	Wear rate
W_{wear}	Wear in the sliding direction
w	Wear depth
w_v	Wear volume
Δx	Activation length (CH3)
Δx, Δy	Spacing of each element area in *x* and *y* direction, respectively. (CH7)
x_{thermo}	Influence constant of temperature activation
x_{tribo}	Influence constant of mechanical activation
X	- The coordinate system of the reaction film thickness (Section 3.6.1.1 Diffusion Model) - The fraction that has been covered by tribofilm (Section 3.6.1.2 The Model Based on Morphology)
X_o	Existing fracture of tribofilm
Y	Shape function
z	Surface profile or depth

Greek symbols

α	Pressure-viscosity coefficient
γ	Refinement multiple
$\dot{\gamma}$	Shear rate
γ^n	Frequency spectrum of surface roughness
δ	Plastic penetration depth
δ_{ij}	Kronecker delta
ε_{plane}	Convergence error of the plane
ε^l_{plzz}	Plastic strain
ε_W	Convergence error of the load
η_0	Viscosity under atmospheric pressure
η , η_P	Dynamic viscosity
η_{Fe-Vol}	The volume fraction of iron in the removed volume of tribofilm
η_r	Ratio of removed thickness over current thickness
λ	Lambda ratio
μ	Friction coefficient
μ_a	Friction coefficient related to adhesion
μ_d	Friction coefficient related to deformation
ν	- Kinematic viscosity (CH2) - Poisson's ratio (CH7)
$\nu(\chi)$	Coverage fraction of tribofilm on the surface
ξ_I , ξ_T	Curvatures of the initial state and the transition state along with the reaction coordinate.
ρ	Density
$\rho_{FeO/S}$	Density of iron compounds(sulphides or oxides)
ρ_{steel}	Density of iron
ρ_f	Density of the deposited tribofilm
σ	Stress
σ^*	Equivalent RMS roughness
σ_1, σ_2	RMS roughness of the two contact surfaces
τ	Shear stress
ϕ_0, $\vec{\phi}$	*P-N* elastic potentials, $\vec{\phi}=(\phi_1,\phi_2,\phi_3)$
Φ_0, $\vec{\Phi}$	Fourier Transform of P-N elastic potentials
χ	Thickness
Ω	Real contact area

Acronyms / Abbreviations

ACF	AutoCorrelation Function
AFM	Atomic Force Microscopy
ALUS	Approaching Larger and Using Smaller
AW	Anti-Wear
BEM	Boundary Element Method
BL	Boundary Lubrication
BO	Bridging Oxygen
BSE	BackScattered Electrons
CGM	Conjugate Gradient Method
DC	Discrete Convolution
DDP	DialkylDithioPhosphate
DFT	Density Functional Theory
DLC	Diamond-Like Carbon
EDTA	EthyleneDiamineTetraAcetic
EDX	Energy-Dispersive X-ray spectroscopy
EHL	ElastoHydrodynamic Lubrication
EP	Extreme Pressure
FDM	Finite Difference Method
FEM	Finite Element Method
FFO	Fully Formulated Oil
FFT	Fast Fourier Transform
FGM	Functionally Graded Material
FRF	Frequency Response Function
FWHM	Full Width at Half Maximum
G-W	Greenwood and Williamson model
HL	Hydrodynamic Lubrication
HSAB	Hard and Soft Acids and Bases
IC	Influence Coefficient
IL	Ionic Liquid
M-B	Majumdar and Bhushan fractal model
MD	Molecular Dynamics
MIM	Matrix Inversion Method
ML	Mixed Lubrication
MLMS	Multi-Level Multi-Summation
MoDTC	Molybdenum DiThioCarbamate
MTM	Mini-Traction Machine
NBO	Non-Bridging Oxygen
OBCaSu	Over-Based Calcium Sulphonate

PAO	Poly-α-Olefin
PFPE	PerFluoroPolyEther
P-N	Papkovich-Neuber potentials
RMS	Root-Mean Square
SEM	Scanning Electron Microscopy
SLIM	Spacer Layer Imaging Method
SRR	Slide-to-Roll Ratio
TBN	Total Base Number
TCP	Tri-Cresyl Phosphate
W-M	Weierstrass-Mandelbrot fractal function
XPS	X-ray Photoelectron Spectroscopy
ZDDP	Zinc DialkylDithioPhosphate

Chapter 1 Introduction

1.1 *Background*

The term ‘tribology’ comes from the Greek words ‘tribos’ that means rubbing or sliding. The definition was formally proposed by a committee of the Organisation for Economic Cooperation and Development in 1967 [1]. It is a science and technology that studies the interaction of surfaces in relative motion and related practices, with friction, wear and lubrication as the main research contents. It is also an interdisciplinary subject involving mathematics, physics, chemistry, biology, materials, fluid mechanics and solid mechanics.

It was estimated that 23% of the world’s energy is consumed by frictional contact, of which 20% comes from the consumption of overcoming friction, and 3% is related to the wear of parts and equipment and wear-related failures [1]. Since wear can cause catastrophic failures and adversely affect production, reducing wear has always been one of the main concerns of the industry. Especially in the mining industry, the cost of replacement of parts due to wear accounts for about half of the total maintenance cost [2, 3]. Therefore, a better understanding of the wear mechanism and monitoring the dynamic process of wear could provide a solution for improving the machine's longevity and reducing the economic costs and energy consumption.

Lubrication is one of the effective approaches for wear control and friction reduction [1]. Since the oiliness additive was first discovered and used in 1918 [4], a variety of additives for improving the performance of lubricants have appeared successively, which have made great contributions to reducing friction and wear, as shown in Fig. 1-1 [5]. For example, zinc dialkyldithiophosphates (ZDDP), one of the most widely used anti-wear additives, became a lubricant additive in the late 1930s ~ early 1940s [5-8]. Although it contains P and S that will cause environmental pollution, its excellent anti-wear performance has made it difficult to find comparable substitutes. The use of detergents and dispersants can respectively clean the acidic substances and disperse/reduce the deposition of particles in the lubricants, which can greatly improve the stability of lubricant performance. Therefore, in practical applications, different types of additives will be added to the base oil to work together to achieve the best performance of lubricants.

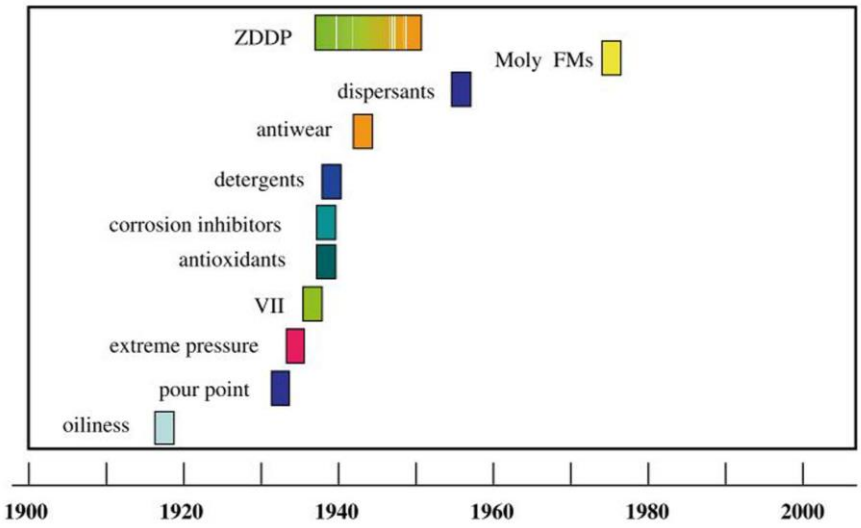

Fig. 1-1 Chronology of the development of main classes of lubricant additive [5].

1.2 *Motivations*

There is a commonly used hydraulic pump in the transmission system of heavy industry, called a swash-plate type axial piston pump. As shown in Fig. 1-2 [9], there is an inclination angle between the swash-plate and the cylinder block in the main structure so the metal contact occurs during the relative motion of the piston and the cylinder block, causing wear on the interface. Mild wear at these locations can cause oil leakage, leading to bad performances on pressure transmission while severe wear will cause the failure of the hydraulic pump and high cost of replacement. Thus, both understanding the wear mechanism at the failure location and further simulating the dynamic process of wear are of importance.

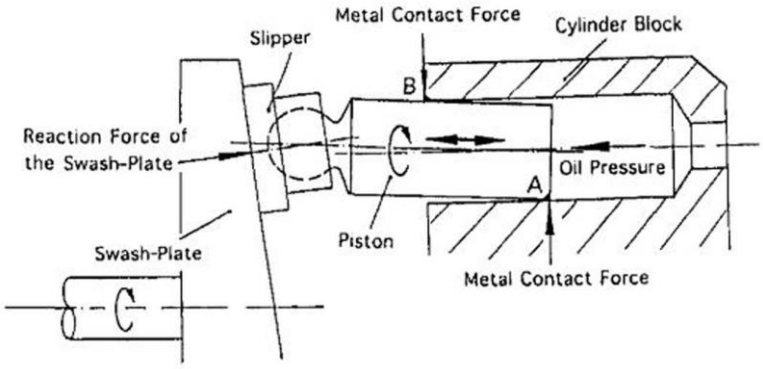

Fig. 1-2 Schematic description of the swash-plate type axial piston pump [9].

The lubricant used in the piston pump is a fully formulated oil (FFO) mainly containing ZDDP, detergent, dispersant, etc. to meet the multiple functions of pressure, lubrication and wear-reduction required by the hydraulic system. However, many of these additives will have different tribochemical reactions with the steel surface during the rubbing process, thereby changing the surface chemical compositions and surface topography, and affecting the wear mechanism. Researchers have carried out experimental studies on the antiwear mechanism of ZDDP on steel surfaces for many years [5, 10-20], in which the research has been extended on the combination of ZDDP and other additives such as detergents [21-27] and dispersants [28-40], or the surface of other materials such as diamond-like carbon(DLC) [41-43] and aluminium alloy [44-47]. But in fact, as long as there are any conditions such as additive types of concentration ratios, operation conditions (such as temperature, load, speed, etc.) change, the tribofilm produced by the tribochemical reactions and its wear mechanism may be different, especially for FFOs with a complex special formula of additives. Using the additives contained in it as a lubrication system to study its wear mechanism not only can it be compared and verified with the experimental results of additive combination with clear proportions and working conditions in the literature, but it can also be explored whether there will be different wear trends if it regarded as a whole system.

In order to systematically study the wear mechanism of the FFO, it is necessary to conduct a large number of experiments and chemical analysis to summarise the trend, but this takes a lot of time and money. Therefore, more and more experimental research has begun to be combined with theoretical research and simulation to achieve the prediction of key parameters such as the amount of wear, the location of failure and fatigue.

On the one hand, this is an interdisciplinary comprehensive problem. In addition to lubrication and wear-related theories, it also involves knowledge of contact mechanics, physical chemistry, mathematics, etc. On the other hand, this is also a multi-scale and multi-dimensional problem that needs to be considered. So far, there have been many models based on ZDDP experiments to establish the model of the growth reaction kinetics of tribofilm and the changes of wear on rough surface topography [48-53]. Analogous to its research method, based on the tribofilm generated by FFO and the corresponding wear results, a similar model can also be developed. However, considering that the material property of tribofilm is different from that of steel surface when the tribofilm is formed

and covered on the steel surface, it may affect the deformation and subsurface stress. It is related to the occurrence of plastic deformation and fatigue cracks that is also one of the issues which are worthy of attention. Therefore, considering the three-dimensional multi-layered structure in modelling is a possible solution, and it can also extend the existing model framework.

In short, the theme of this project is based on the application background of the hydraulic pump, from the perspective of lubricant to study the wear process and wear mechanism on the steel surfaces, and through the combination of modelling and experimental parameters to achieve the reasonable prediction of wear process involving tribochemistry.

1.3 *Aims and Objectives*

The aims of the project are to systematically study the characteristics of the tribochemical reaction and the wear mechanism of a fully formulated hydraulic oil in the rubbing process based on the application background of the wear failure of piston and cylinder in hydraulic pump and to develop a three-dimensional multi-layered model to simulate the wear process and stress distribution involving the influence of tribofilm growth.

In addition, it is necessary to summarise the wear trends based on the experimental results and use parameters to input in the model for calculation and prediction. Thus, the objectives are proposed as follows.

1) To study the basic trends of the tribofilm formation of FFO and the influence of different additives used in the FFO on the tribofilm and wear;

2) To study the influence of temperature and λ ratio on the tribofilm and wear and to investigate the correlation of wear mechanisms of FFO with tribochemistry or working conditions;

3) To develop a wear model for FFO involving tribochemistry based on the experimental results of FFO; and

4) To improve the modelling framework based on the asperity-asperity contact and a three-dimensional layered contact model that can predict the tribofilm growth and wear

process in the experiments of FFO and further calculate the subsurface stress distribution during the rubbing.

1.4 *Thesis Structures*

The contents of the thesis first introduce the tribological background, motivations based on hydraulic applications, aims and objectives of the project in Chapter 1.

Then, Chapters 2 and 3 are the literature reviews in the fundamental of tribology and modelling, respectively, in which Chapter 2 focuses on the definition of friction, wear and lubrication, as well as the physical properties related to this study; Chapter 3 concentrates on two parts. The first part is experimental research of lubricant additives such as ZDDP, detergents and dispersants and their interactions on tribological properties, especially wear behaviours. The second part mainly introduces the modelling framework in boundary lubrication and the modelling studies related to contact mechanics, tribochemistry and wear.

Chapter 4 is the methodology of the project which mainly describes the materials, experimental equipment including tribometers and chemical analysis equipment and the correlation between the modelling work and the experiment.

The experimental results are shown in Chapters 5~6. Chapter 5 focuses on the general trend of tribofilm growth of FFO and the effects of additives on the tribofilm and wear. Chapter 6 discusses the joint effects of temperature and λ ratio (lubrication regime) on tribofilm and the wear mechanism of FFO.

Chapter 7 is about the theoretical introduction of the modelling work and simulation results of FFO including tribofilm formation, wear evolution and stress distribution.

Chapter 8 is the overall discussion of the project.

Finally, Chapter 9 is the conclusion of the project and proposals for future work.

Chapter 2 Fundamentals of Tribology

Tribology is an art of operation analysis, which has great significance to the reliability, maintenance and wear of equipment from aerospace to household appliances. For example, there are many parts in the machine with relative movement that faces the problems of wear failure, such as gears, bearings, seals and clutches. The use of human joints also has the problem of wear and lubrication.

Friction, wear and lubrication are the three core topics of tribology, so this chapter briefly introduces the basic terms and related theories involved in these three fields. In addition, the terms related to physical properties are explained.

2.1 *Friction*

Friction is a kind of resistance in the relative movement of two objects, such as sliding or rolling. This resistance may be good or bad. If friction occurs during the operation of the machine's transmission parts, it may cause energy loss or wear. But the car brakes and conveyor belts require high friction to work properly.

Generally, it is mainly divided into two types: dry friction and fluid friction. When relative motion occurs or tends to occur between two dry surfaces the tangential component of the contact force is dry friction. When there is a fluid moving at different speeds relative to each other between two surfaces, the tangential component of the contact force between the fluid and the adjacent interface is the fluid friction. If a tangential force is applied to two contacting solids, the force used to start motion is the static friction force F_s , while the force used to maintain the motion after the motion occurs is the dynamic friction force F_k.

The early sliding friction theory was developed by Leonardo da Vinci (1452-1519), Amontons (1633-1705), Euler (1707) and Coulomb (1736-1806) who based on the interlocking effect between asperities on the contact surface [54]. It can be summarised that the friction force F_f and normal load F_n have the rules as follows [55].

$$F_f = \mu F_n \tag{2-1}$$

where μ is the sliding friction coefficient. If the value is originated from the experiment of pulling weight F_n on an inclined plane with an angle θ to generate friction, then $\mu = \tan\theta$.

In the three laws of friction by Amontons, it is considered that the friction coefficient is independent of normal load, contact area and sliding rate [56]. But in fact, this is only applicable under very limited working conditions. For example, the friction coefficient for the tribo-pairs of brass and copper decreases with the increase of the normal load [57] and the friction coefficient of a car tire increases as the tire width (contact area) increases [55]. This shows that its essence is still related to the friction mechanism of the material of the friction pair under specific working conditions.

Friction is a process of energy dissipation, so it is not enough to describe friction with the theory of mechanical interaction. For example, in the friction theory of metals and ceramics, in addition to the need to overcome the friction generated by adhesion, the micro-scale deformation during the movement also requires energy.

Therefore, for the contact surface with adhesion occurring, the total frictional force F_{total} can be expressed as the sum of the adhesion force (F_a) that needs to be overcome during the relative movement and the force (F_d) that needs to provide deformation energy [58].

$$F_{total} = F_a + F_d \quad \textbf{(2-2)}$$

Or it can be expressed as $\mu = \mu_a + \mu_d$ by the form of friction coefficient.

2.2 *Wear*

Wear is the major reason for the failures of tribological systems. Understanding wear mechanisms can help designers to prevent failures and to improve the lifetime of the systems. Wear is the destruction or removal of materials on the surface of the contact body during the relative movement of two solids. Wear can occur mechanically or chemically, and frictional heat or thermal process can generally accelerate the occurrence of wear [55].

2.2.1 *Classifications of Wear*

Researchers have different opinions on the classifications of independent wear phenomena because one or more wear phenomena usually occur at the same time in the study of wear and failure analysis. Here we mainly introduce five types of independent wear phenomena in hydraulic systems: 1) adhesive; 2) abrasive; 3) fatigue; 4) corrosive; and 5) erosive wear and a combination of multiple wear phenomena, but a widespread problem in engineering, called fretting.

2.2.1.1 *Adhesive Wear*

Adhesive wear happens due to high local friction that causes asperities junctions [59]. Then, the material of one surface is detached by shear tearing and fragmentation and attached to the other surface [54], whether it is dry or lubricated. This is one of the most common and serious phenomena of wear. It normally has the characteristics of a high wear rate, and the friction coefficient is large and unstable [1].

Adhesive wear is prone to occur between metals, especially when the lubrication fails. Under vacuum conditions, the results of measuring the adhesion between a variety of metals and the iron surface show that the adhesion can be significantly greater than the contact force, and the strongest adhesion occurs in the pair of iron-to-iron (ie, the same metal) [60]. Moreover, a large number of experiments have shown that when there is strong adhesion, the adhesion mechanism tends to transfer weak metal materials to strong metal materials, as shown in Figure 2-1 [1]. This could be explained by the electron transfer mechanism, based on the 'Jellium model' [61]. When the distance between the two metal surfaces is very small, the metal surface with a higher electron density tends to provide electrons to the other side, thus transferring the electron [1, 62]. The adhesion between metal contacts is related to the crystal structure, hardness, elastic modulus and surface energy [60, 63].

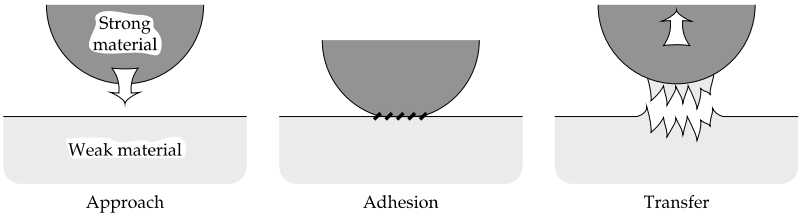

Fig. 2-1 The process of the adhesive wear in the contact between strong material and weak material [1].

In an atmosphere containing oxygen, the metal surface is usually covered with an oxide film with nanoscale thickness, which can reduce direct contact between metals and severe high wear [1, 64].

2.2.1.2 *Abrasive Wear*

Abrasive wear is the loss of surface materials (such as plastic deformation or fracture of the material) caused by hard particles or hard asperities on the surface sliding against the soft surface. It can also be divided into two types: two-body abrasive wear and three-body abrasive wear, as shown in Fig. 2-2. The former wear is caused by the asperity on the harder surfaces of the two rubbing bodies, or the harder abrasive particles mounted on one surface (that is, the abrasive particles cannot move) acting on the other softer surface. In the three-body abrasive wear, the harder object is the wear debris that can slide or roll freely between two surfaces, resulting in the wear on one or two of the surfaces during the relative movement [55].

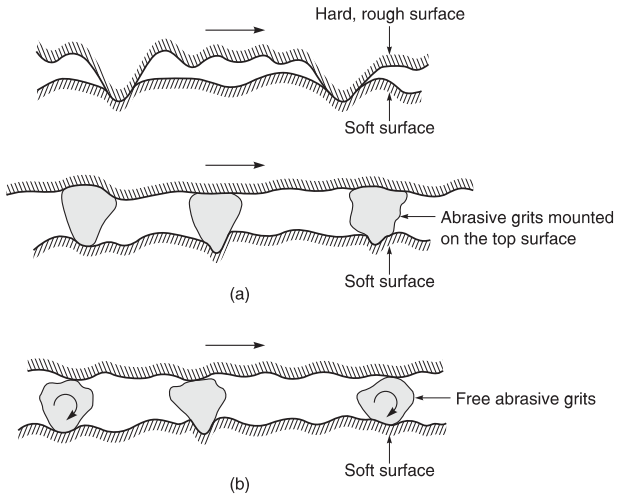

Fig. 2-2 The two situations of abrasive wear: a) two-body abrasion and b) three-body abrasion [55].

Sometimes, the transferred hard particles trap into the soft surface and then abrade the original surface, which is easy to confuse with adhesive wear. However, the wear debris generated by abrasion is larger than that produced by adhesion and the abrasive wear rate also much higher than the rate of adhesion, usually exceeding 2 to 3 orders of magnitude [55].

One important parameter to estimate the resistance to abrasive wear is the hardness of the material [55, 65]. Besides, the geometry of the abrasive particles and the presence or absence of lubricants also affect the mechanism of abrasive wear [1].

2.2.1.3 *Fatigue Wear*

Fatigue occurs in the process of repeated sliding or rolling. When the surface is suffered from cyclic loading force, the cracks will initiate in the subsurface. After a great number of cycles, when the crack spreads to the surface, it breaks to produce large abrasive particles and to leave large pits, which is also called pitting. Since fatigue wear occurs at the beginning of equipment operation, it is usually estimated by fatigue life rather than wear amount [55]. The surface subject to fatigue wear usually has a very high plastic strain [1].

Rolling fatigue wear often occurs on the surface of rolling bearings, which may be caused by surface defects, so it is also called ‘contact fatigue’ or ‘surface fatigue’ [1, 55]. Lubricants can affect contact fatigue by avoiding direct contact between the two rolling bodies. Under lubricated conditions, adhesive wear and abrasive wear are usually limited and can be ignored. However, because the contact stress on asperity is very high, even if there is no direct contact, the lubricant film can transmit stress in a large number of repeated loads, finally causing wear. The lubrication regime at this time is mostly elastohydrodynamic lubrication (EHL) [1], it will be introduced in Section 2.3.2.1.

2.2.1.4 *Corrosive wear*

Corrosive wear describes the results of chemical or electrochemical interactions of surfaces with the corrosive environment (gas, liquid or solid), in which reaction products can be formed on one or both surfaces. The corrosion media can be chemicals, reactive lubricants or even air [1].

Chemical corrosion mainly has characteristics of high temperature, strong corrosiveness and high humidity in the environment. Electrochemical corrosion is similar to a short-connected battery in that the chemical reaction takes place in two regions with a potential difference and is accompanied by the generation of electric current [66].

Oxygen in the air is the most common corrosive medium, which can accelerate corrosion, especially for ferrous alloys [67]. Because most metals and alloys are unstable in the presence of oxygen, a natural oxide layer is formed on their surface thermodynamically to prevent the metal oxidation loss to some extent. In the rubbing process, the oxide layer on the surface is removed by wear, so the exposure of the new metal or alloy surface leads to the loss of new oxidation wear [68]. Oxidative wear is usually accompanied by mechanical wear [69].

2.2.1.5 *Erosive wear*

Erosion wear is a kind of wear phenomenon in which the surface of materials is damaged by the impact of small and loose flowing particles, which is the result of a repetitive stress impact. Its mechanism is related to the size of the particles, the angle and the speed of the impact [1, 55].

2.2.1.6 *Fretting Wear*

Fretting wear is a high-frequency, small-amplitude repeated cyclic rubbing that occurs between two contact surfaces. These surfaces are nominally static. Because the sliding amplitude is small, usually from a very small micrometre to a few hundred micrometres, the generated abrasive particles will stay in the contact area, further resulting in oxidation corrosion or abrasive wear. After a large number of reciprocating cycles, it can also cause the initiation and development of fatigue cracks [54, 55]. Therefore, fretting is a phenomenon that combines adhesive, abrasive and corrosive wear, in which the main factors causing fretting are minimal vibration and oxidation [69].

2.2.2 *Running-in Process*

As shown in Fig. 2-3, a complete wear process mainly includes one stage: running-in, stable and accelerated phase [70]. Usually, the wear rate and the friction coefficient are defined in the stable phase after rubbing contact for a period of time. The transient

fluctuations that existed at the beginning of wear are sometimes ignored. This stage is defined as the ‘running-in’ stage and is sometimes also called ‘break-in’. The running-in stage may result in substantial material loss or the surface roughness change due to plastic deformation [71], which will further affect the subsequent stable operating conditions. After long-term engineering practice, it is found that the use of a certain approach to ensure the high-quality running-in of the machine can significantly increase the service life [72].

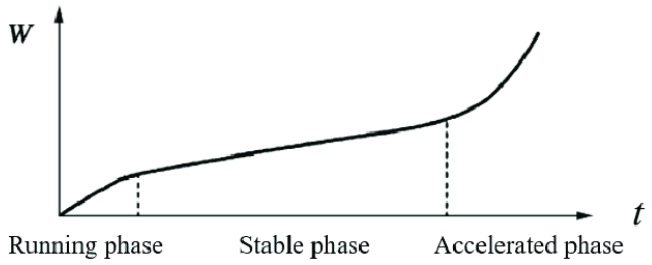

Fig. 2-3 The diagram of a typical wear process [70].

When sliding without lubrication, the original appearance of the contact surface is changed during the running-in process. Both the friction coefficient and the wear rate are changed compared to those during the long-term stable phase. Therefore, when a new machine starts to use, the low load will be applied for a period of time in the running-in phase for the subsequent long-term operation under high-load conditions [1]

Lubricants play an important role in surface protection during the running-in phase [71]. Under lubricated conditions, lubricants can smooth the surface roughness in the running-in phase to a certain extent, and at the same time additives in the lubricant oil and the surface can interact with surface or abrasive particles to form a protective film on it, which usually has the characteristics of reducing friction and/or wear, depending on its chemical compositions [1].

In addition, the duration and the wear condition during the running-in phase are not only determined by the surface roughness and relative hardness of the tribo-pairs [73], it is also related to the surface composition, microstructure and third-body distribution [72].

2.2.3 *Tribochemical Wear*

Tribochemistry is the study of the chemical reactions occurring between the additive/environment and surfaces under boundary lubrication regime, which are affected by friction force or mechanical energy [55, 74]. The interacting reactions and wear processes are the main concerned problems [75]. The wear phenomenon that occurs under this reaction is called tribochemical wear [76, 77].

Tribochemical wear is a complex type of wear [75]. The nature of its chemical reactions has not been well understood [74]. The common examples of tribochemical wear caused by the tribochemical reactions are the metal's oxidative wear and friction polymer films formed on the sliding surfaces [55]. The latter one related to this study is described in detail.

On the sliding surface, due to the increase in surface temperature during the contact process or the exposure of some new surfaces which are certain catalytic, organic matters (which can be solid, liquid or gas) undergo re-polymerisation or reactions, thereby producing friction polymer films, so-called tribopolymer films [78-81]. These films have the properties of reducing friction and wear under boundary lubrication or hydrodynamic lubrication conditions, and their chemical structure is related to their organic origin. For example, ZDDP can interact with the steel substrate to form the tribofilm under the influence of temperature and stress [10]. Although it is well known that the formation of the tribofilm can reduce the wear of steel-steel contact, the formation still cause iron consumption in the substrate, occurring tribochemical wear.

2.3 *Lubrication*

Lubrication is the application of a material to reduce the resistance of movement between two surfaces and the material is called lubricant. The objective of lubrication is to generate the lubrication film between the rubbing surfaces with low tangential strength and large normal load capacity. The films can be fluid film or solid film.

2.3.1 *Lubrication Theories*

Reynolds first derived the differential equation of incompressible fluid that controls the pressure distribution of fluid film lubrication, which describes the relationship between

sliding speed, surface geometry, lubricant characteristics and normal load, and further, the equation for compressible fluid has been derived. In order to explain the physical phenomenon in fluid lubrication and the Reynolds equation is derived through element analysis, as described in Fig. 2-4.

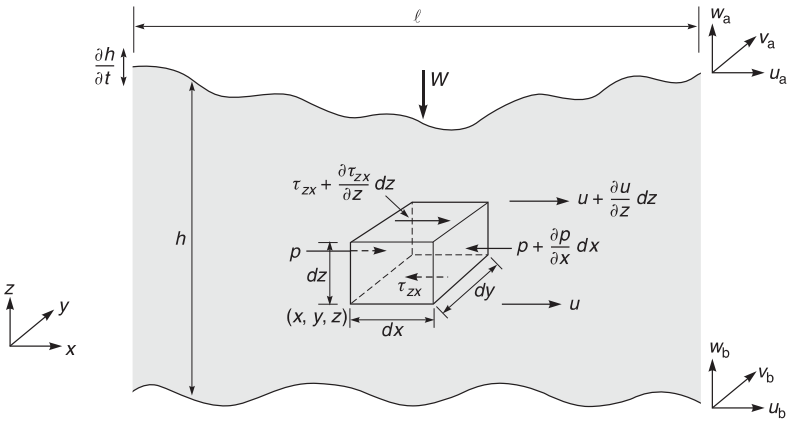

Fig. 2-4 A schematic diagram of stress and velocities in the *x*-*z* plane applied to a fluid element between two surfaces [55].

In deriving the Reynolds equation, there are many assumptions such as ignoring volume force, no sliding on the fluid interface, ignoring pressure change along the direction of the fluid film thickness, ignoring oil film curvature, Newtonian fluid, laminar flow, ignoring inertial force and constant viscosity in the thickness direction of the fluid film. The generalised Reynolds equation is expressed in Equ. (2-3) [82].

$$\underbrace{\frac{\partial}{\partial x}\left(\frac{\rho h^3}{12\eta}\frac{\partial p}{\partial x}\right)+\frac{\partial}{\partial y}\left(\frac{\rho h^3}{12\eta}\frac{\partial p}{\partial y}\right)}_{\text{Poiseuille flow}}=\underbrace{\frac{\partial}{\partial x}\left[\frac{\rho h\left(u_a+u_b\right)}{2}\right]+\frac{\partial}{\partial y}\left[\frac{\rho h\left(u_a+u_b\right)}{2}\right]}_{\text{Couette flow}}+\underbrace{\rho\left[\left(w_a-w_b\right)-u_a\frac{\partial h}{\partial x}-v_a\frac{\partial h}{\partial y}\right]}_{\text{squeeze flow}}+\underbrace{h\frac{\partial \rho}{\partial t}}_{\text{local expansion flow}} \quad \textbf{(2-3)}$$

According to the numerical method of the solution and the specific boundary conditions, it can be further simplified. For example, for the one-dimensional unidirectional flow of an incompressible fluid, as shown in Fig. 2-5, the Reynolds equation can be simplified in Equ. (2-4).

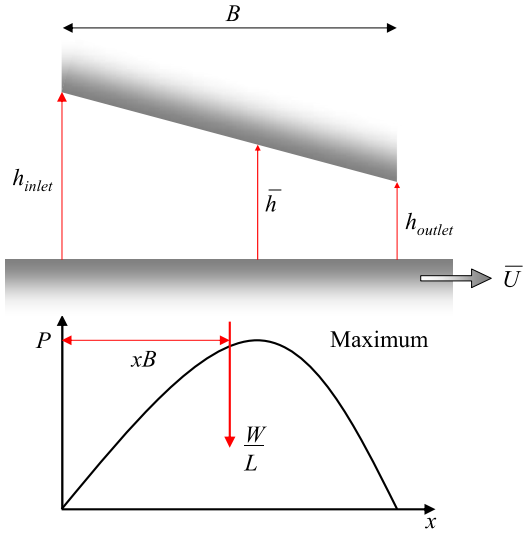

Fig. 2-5 A schematic diagram shows that the viscous fluid is entrained by relative motion into two surfaces with convergent geometric shapes, generating a pressure that can separate the two surfaces and balance with the normal load [83].

$$\frac{\partial p}{\partial x} = 12\bar{u}\eta\left(\frac{h-h_m}{h^3}\right) \tag{2-4}$$

However, the solution of the Reynolds equation did not take into account the problem of thickening of the oil film at the contact region due to the local high pressure and the partly increase in the lubricant viscosity under high contact loads. The solution by Grubin [84] first took into account the influence of not only elastic deformation but also viscosity, which is a breakthrough in understanding the EHL mechanism. He assumed that the elastic deformation in the lubrication with a heavy load is the same as that in the dry contact and that the hydrodynamic pressure tends to be infinite at the entrance of the Hertzian boundary. Then, the expression for predicting lubricant film thickness is obtained.

$$H_c = \frac{h_c}{R_x} = 1.95\left(G^* U^*\right)^{8/11}\left(W^*\right)^{-1/11} \tag{2-5}$$

The contour of the fluid film h described by this equation is more complicated than the one based on Fig. 2-5 in which the ratio of pressure to distance is positive. If there is high pressure at the entrance, it will increase further at the exit as the high pressure will remain in the Hertzian contact region. However, it is ambient pressure at the exit, which is contrary to the assumption. Therefore, in order to maintain the continuity of the fluid flow,

the oil film thickness near the outlet will reduce. There is a minimum film thickness $H_{\min}$ appearing at this position, accompanied by a pressure peak exceeding the maximum Hertzian contact pressure, as shown in Fig. 2-6a [1]. In the point contact, as illustrated in Fig. 2-6b, the oil film shrinks and the pressure peak extends to the outlet, forming a horseshoe-shaped constraint, which was observed in many experiments [85].

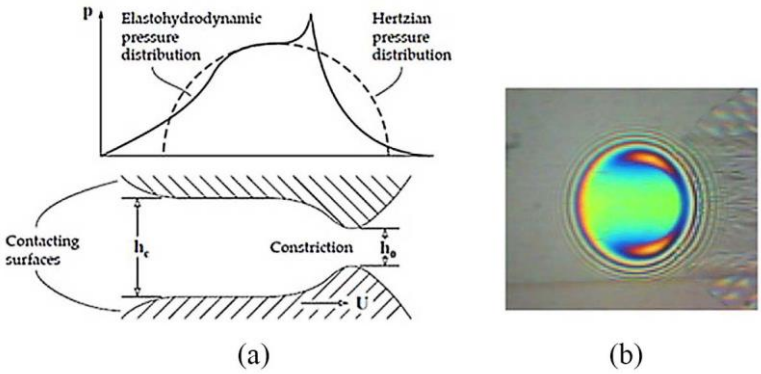

Fig. 2-6 (a) The diagram of the typical pressure distribution and elastic deformation in the EHL regime [1] and (b) the interference image of oil film by EHD [85].

The dimensionless parameters G^*, U^*, W^* in Equ. (2-5) represent the effects of material, speed and load parameters on the film thickness, respectively, but the equation did not consider the effect of the local oil film shrinkage and did not give the physical meaning to the contact.

The next landmark study on the establishment of the EHL theory is the publication of numerical solutions for elastohydrodynamic problems by Dowson and Higgison in 1959 [86]. In 1961, they proposed a fitting equation [87] for predicting the minimum film thickness of the EHL curve, which was further modified by Dowson in 1965 [88], as shown in Equ. (2-6). Later in 1978, Dowson and Toyoda [89] gave the expression of the centre film thickness as expressed in Equ. (2-7).

Line contact:

$$H_{\min} = \frac{h_{\min}}{R_x} = 2.65 G^{*0.54} U^{*0.7} W^{*(-0.13)} \quad \textbf{(2-6)}$$

$$H_c = \frac{h_c}{R_x} = 3.06 G^{*0.56} U^{*0.69} W^{*(-0.10)} \quad \textbf{(2-7)}$$

In the point contact problem [58], Hamrock and Dowson [90-93] comprehensively discussed the effects of speed, load, material properties, contact ellipticity and starvation lubrication conditions, and gave the fitting equations for the minimum film thickness and the centre film thickness in Equ. (2-8) and Equ. (2-9), respectively [92]:

Point contact:

$$H_{\min} = 2.69G^{*0.53}U^{*0.67}W^{*(-0.067)}\left(1-0.61e^{-0.73k}\right) \quad \textbf{(2-8)}$$

$$H_{c} = 3.63G^{*0.49}U^{*0.68}W^{*(-0.073)}\left(1-e^{-0.68k}\right) \quad \textbf{(2-9)}$$

2.3.2 *Lubrication Regimes and Stribeck Curve*

2.3.2.1 *Lubrication Regimes*

According to the fluid film thickness between the two surfaces and the solid contact, there are four basic lubrication regimes including hydrodynamic lubrication (HL), elastohydrodynamic lubrication (EHL), mixed lubrication (ML) and boundary lubrication (BL) [58, 94]. The contact behaviours between interfaces in different lubrication regimes are shown in Fig. 2-7.

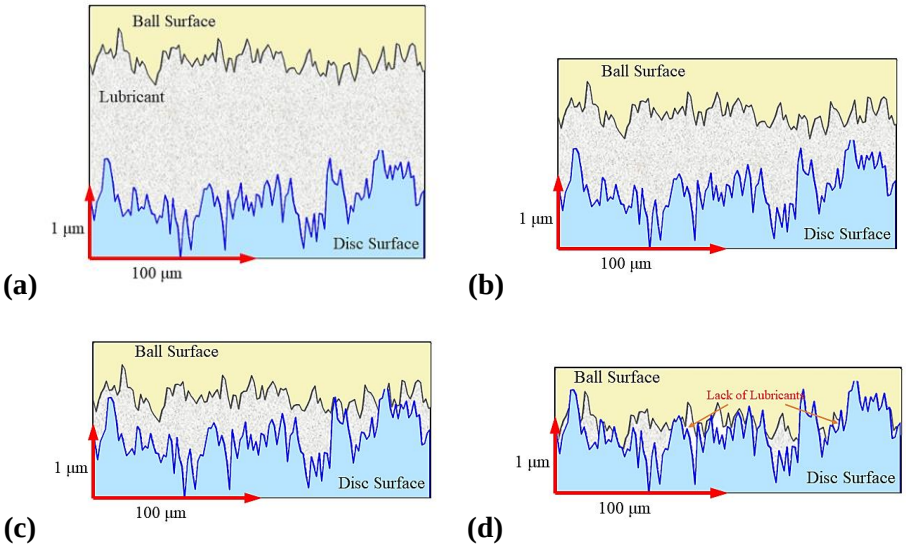

Fig. 2-7 Schematic diagrams of four types of lubrication regimes (a) hydrodynamic lubrication (b) elastohydrodynamic lubrication (c) mixed lubrication and (d) boundary lubrication [83].

- ***Hydrodynamic Lubrication***

As shown in Fig. 2-7a, hydrodynamic lubrication is generally considered to be an ideal lubrication condition. At this phase, the fluid film is thick enough to fully withstand the pressure, so there is no direct contact between the two surfaces. The friction coefficient at this stage is very small and can be as low as 0.001. Its contact behaviour is determined by the characteristics of the lubricant such as viscosity, which can be solved by the Reynolds equation.

- ***Elastohydrodynamic Lubrication***

As shown in Fig. 2-7b, elastohydrodynamic lubrication is a subset of hydrodynamic lubrication. In contrast, the EHL fluid film has a lower thickness. But more importantly, EHL mainly occurs in non-conformal contacts [58]. Elastic deformation and pressure distribution of contact solids play a significant role in lubrication. The surface shapes will usually be modified because of local elastic deformation and the increase of viscosity caused by high pressure. Thus, the modelling of EHL contact needs to solve not only the Reynolds equation but also the equations related to elastic deformation, viscosity, and pressure, and even consider the effects of heat and shear rate.

- ***Mixed Lubrication***

Mixed lubrication is a transition zone between hydrodynamic/elastohydrodynamic lubrication (HL/EHL) and boundary lubrication (BL). When the fluid film thickness continues to decrease, there are two lubricating mechanisms. A part of the surface begins to have solid contact, which causes the transfer of surface material and detachment to form abrasive particles, so the friction coefficient begins to increase. The rest of the part is still supported by the hydrodynamic film.

- ***Boundary Lubrication***

In the boundary lubrication regime, direct contact occurs between surfaces, so the friction coefficient can rise to a very large value. Meanwhile, the single or multiple molecules in the lubricant interact with the surface. Thus, the friction and wear behaviours are determined by the surface materials, physical/chemical properties of lubricants and the interaction between surfaces and lubricants [58].

2.3.2.2 *Lambda Ratio (λ)*

Theoretically, in ideally smooth surface contact, the film thickness may decrease indefinitely as the load increases. But in fact, the presence of surface roughness will locally cause the lubrication regime to enter boundary lubrication in advance, and even cause wear due to solid contact. Therefore, a method for determining the lubrication regime that includes the effect of surface roughness is described in Equ. (2-10), which defines a ratio of the minimum film thickness *h* to the equivalent root mean square σ^* of the roughness of the two contact surfaces (σ_1, σ_2), is called the specific film thickness or lambda ratio (λ).

$$\lambda = \frac{h}{\sigma^*} = \frac{h}{\sqrt{(\sigma_1^2 + \sigma_2^2)}} \tag{2-10}$$

in which

- Hydrodynamic lubrication: λ > 10
- Elastohydrodynamic lubrication: λ > 4 or 5
- Mixed lubrication: 1 < λ < 5
- Boundary lubrication: λ < 1

2.3.2.3 *Stribeck Curves*

Stribeck diagram is a common tool to recognise the lubrication regime by friction coefficient against the lubrication parameter $\eta V / P$ (Hersey number) related to load P on the interface per unit width, fluid viscosity η and sliding speed *V*, shown in Fig. 2-8.

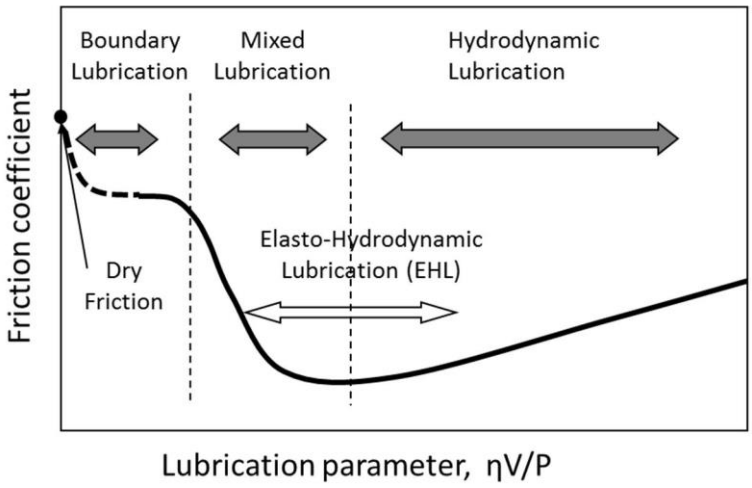

Fig. 2-8 Schematic of the Stribeck curve [95].

2.3.3 *Hydraulic Fluids and Additives*

The main function of hydraulic fluids is to serve as a medium to transfer energy and to provide sufficient lubrication on the surface of the hydraulic system to protect the components in the system from damage. In addition, there is a lot of heat generated during the friction process, so the hydraulic oil can also absorb the heat to cool the system. The typical hydraulic fluid contains about 95% base oil with 5% additives [96]. The presence of additives can enhance the performance of the base oil, such as adjusting viscosity, reducing friction, anti-wear, anti-extreme pressure, anti-oxidation, cleaning and dispersing by-products during the rubbing, etc. The types and functions of additives commonly used in hydraulic fluids are shown in Table 2-1 [97].

Table 2-1 The types and functions of the typical additives in hydraulic fluids and their functions [97].

Additive	Function	Typical Compounds
Anti-oxidant	Prevent oxidation by forming inactive compounds or removing radicals.	Compounds containing S, P or N such as ZDDP.
Viscosity Index Improver	Reduce the rate of viscosity change with temperature.	Polymerised or iso-olefins
Pour Point Depressant	Prevent solidification at low temperature and lower the pour point temperature.	Alkylated naphthylene or phenols
Anti-wear Additive	Form a tribofilm to reduce wear.	ZDDP, organic phosphates and phosphites
Extreme Pressure Additive	Form a film with low shear to prevent scoring, galling, and seizure	Material containing S, Cl and P
Detergent	Neutralise the acidic precursors in the oil to keep the surface clean.	Metallo-organic compounds of Ba, Ca and Mg, phenolates, and sulphonates
Dispersant	Disperse insoluble, macromolecular pollutants to prevent agglomeration.	Polymeric alkylsuccinamides and alkylthiophosphonates
Rust Inhibitor	Reduce or prevent rust.	Sulphonates, amines, fatty oils
Oiliness Agent/ Friction Modifier	Reduce friction under boundary lubrication conditions.	High-molecular-weight compounds: fatty oils, waxes, MoDTC
Antifoamant	Prevent air from getting in the oil or the formation of foam to reduce compression.	Silicone polymers
Corrosion Inhibitor	Avoid the formation of acidic substances and corrosion on metal or alloy surfaces.	Organic compounds containing S, P or N

2.3.3.1 *Base oil*

It is the main component of hydraulic fluid, providing the main functions of pressure transfer, lubrication, and heat dissipation. Conventional base oils are divided into three categories: mineral oils, synthetic oils, and biological oils. With the development of lubricants, new types of lubricants, ionic liquid lubricant and mesogenic lubricant, have also been extensively studied.

- **Mineral Oils**

Mineral oil is the most commonly used lubricant. It comes from crude oil and is widely used because of its economic cost. The main component of mineral oil is hydrocarbons, and there are three basic chemical forms such as paraffinic, naphthenic and aromatic [96]. By adding a small amount of sulphur, the performance of lubrication and oxidation resistance can be improved and it can also reduce wear. The excessive addition of S may accelerate corrosion. This standard is different according to the producing area of crude oil and the oil refining process [96].

- **Synthetic Oils**

Synthetic oil is developed as an alternative for countries without the supplement of mineral oil at the beginning, and the price is relatively expensive. However, since mineral oil is easy to oxidise or even burn at high temperature, and it is easy to solidify at low temperature, it is not suitable for the conditions of the high-temperature lubrication such as gas turbine engines, and the low-temperature and low-pressure lubrication such as vacuum pumps. Thus, synthetic oil will be a better choice. Nowadays, synthetic oil is mainly used due to its superior functions over wider temperature ranges, even extreme temperatures.

Commonly used synthetic oil types are synthetic hydrocarbons, such as polyalphaolefins (PAO), Ethers and polyglycol; Silicon analogues of hydrocabons, such as silicones; and organohalogens, such as perfluoropolyethers and chlorofluorocarbons. Some structures of the molecular chain are shown in Fig. 2-9 [96].

a) Poly-α-olefins(PAO):

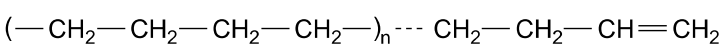

b) Silicones:

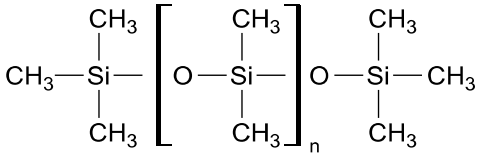

c) Perfluoropolyethers (PFPE):

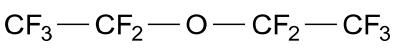

Fig. 2-9 The chemical structures of typical synthetic oils: a) poly-α-olefins(PAO), b) silicones and perfluoropolyethers (PFPE) [96].

- **New Development of Fluids**

In recent years, there are many new developments in synthetic lubricants, such as ionic liquid and mesogenic lubricant.

Ionic liquid (IL) [98] is a molten salt with a melting point < 100 ℃. A subset of it, room temperature ionic liquids are ILs whose communication temperature is lower than room temperature, mainly composed of organic cations containing N or P and weak coordination anions such as BF_4^- and PF_6^-. ILs have the advantages of good thermal stability, volatility and low melting point, and are considered as potential lubricants for extreme conditions. It can be used alone or as an additive.

Mesogenic phase [96] substances can flow like liquids, but the molecules are arranged in a crystalline form. It is found to provide an extremely low coefficient of friction when used as a lubricant. It can be used alone or added to mineral oil or synthetic oil.

2.3.3.2 *Anti-wear and Extreme Pressure (AW/EP) Additives*

The AW/EP additive has a polar structure that can be physically or chemically adsorbed to the metal surface. When the hydrodynamic fluid film cannot be maintained and surface contact occurs, the AW/EP additives may interact with the surface physically or chemically to form a film on the surface to avoid wear caused by direct surface contact. AW additive is mainly used to reduce the wear and tear of the machine running under

moderate stress while EP additive is more active than AW additive, which mainly acts on resisting the impact under heavy-load conditions and avoiding welding and severe wear.

- **Phosphorus Compounds**

Organo-phosphorus compounds have good AW properties under moderate stress. Most of them are neutral or acidic phosphate derivatives, and their reactivity decreases with decreasing acidity. Tricresylphosphates (TCP) is a typical neutral phosphate AW additive.

- **Sulphur - Phosphorus Compounds**

The most widely used AW/EP additive containing S and P compounds is ZDDP (zinc dialkyldithiophosphate). In addition to its excellent AW and EP properties, it is also a good antioxidant and metal passivator. The wear resistance properties and related research progress of ZDDP will be introduced in detail in Chapter 3. In addition, the dialkyldithiophosphates (DDPs) combined with other cations such as ammonium, antimony, molybdenum and lead have also been studied, but the latter is no longer considered due to environmental pollution [99].

- **Sulphur - Nitrogen-Containing Compounds**

The EP additives containing S and N are mainly zinc-bis (diamyl-dithiocarbamate) and ashless methylene-bis (di-n-butyl-dithiocarbamate), which are also excellent antioxidants. They are commonly used in lubricating grease and some gear oils [99].

- **Sulphur Compounds**

The element sulphur was added to mineral oil to improve EP performance in the early stages of lubrication development. Generally, organic sulphides are used to increase and improve the solubility and reactivity of S.

According to the number of sulphur atoms, it can be divided into inactive and active sulphur carriers. Disulphide belongs to the inactive type due to the relative stable C-S bond only reacting at elevated temperatures. The sulphur atoms with a number between 3 and 5 are more reactive. The basic mechanism of sulphur carriers as EP additives are shown in Fig. 2-10. The final product is to form an iron sulphide film on the metal surface. The active temperature of sulphur-containing EP additive is from 600 ℃ to 1000 ℃ [68].

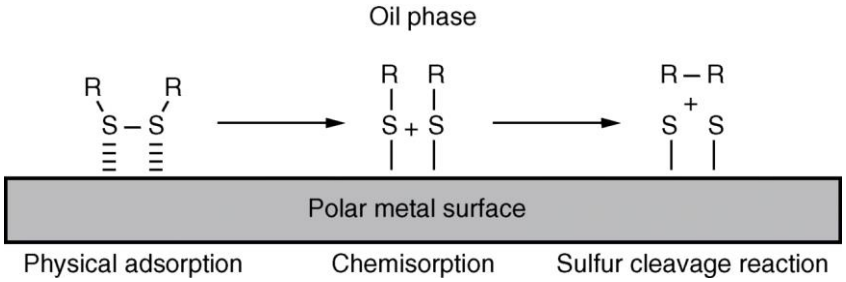

Fig. 2-10 The diagram of the basic mechanism of sulphur carriers interacting with metal surfaces [99].

Other sulphur-containing EP additives are sulphurised fatty oils and fatty acid esters.

2.3.3.3 *Detergents*

The detergent is a polar molecule, the functions of which are to neutralise the acid compositions in oils and to make the contacting surfaces clean. Detergents can be neutral or alkaline. The degree of alkaline is usually TBN (Total Base Number) to evaluate. A neutral detergent will form a film on the metal surface to prevent surface corrosion and rust, while an over-based detergent is a micellar structure with the core of alkaline mineral salt such as $CaCO_3$, which can thicken or gel acidic substances or water in the oil [68]. In addition, the over-based sulphonate can react with the iron surface to form a boundary film to prevent direct surface contact and welding [100].

Over-based calcium sulphonate is one of the commonly used detergents, and a "concentric shell" model was established to describe its chemical structure, as shown in Fig. 2-11 [83, 101-104]. The spherical core of $CaCO_3$ in the centre has a diameter of about 1-10 nm and is surrounded by a surfactant layer of about 1-5 nm, in which its polar group faces the mineral core and the hydrocarbon-based tail faces the lubricant. This micellar structure allows alkaline mineral salts that are insoluble in organic solvents but have excellent tribochemical properties to be added to the lubricant. The mineral core can be a mineral salt containing metals such as Ba, Ca, Li, K or Na [105].

The types of several commonly used surfactants are sulphonate, phenate and salicylate and their molecular formula are shown in Fig. 2-11 (a-c), respectively.

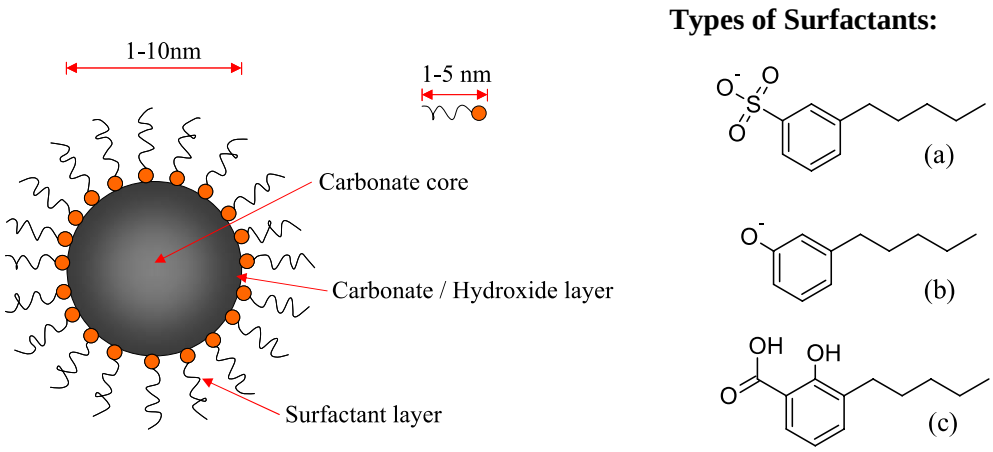

Fig. 2-11 The concentric shell model of over-based calcium detergent and the types of surfactants: a) sulphonate, b) phenate and c) salicylate [83, 101].

In contrast, the detergency of sulphonate is better, but its TBN is usually higher [105]. Phenate has both detergency and antioxidant properties, but the effect is weaker than that of sulphonate. Salicylate also has detergency and antioxidant properties at the same time, and its TBN is relatively low.

2.3.3.4 *Dispersants*

The function of dispersant is to maintain the insoluble compositions suspended in the oil and to prevent deposits on the surface. The dispersant is metal-free and consists of polar end groups and non-polar hydrocarbon tail groups. Its polar end groups can combine with degradation products, combustion by-products or soot in crude oil to prevent the oil from thickening due to agglomeration, and help maintain the viscosity of crude oil.

The types of commonly used dispersants are polyamine succinimides and imidazolines, and their chemical structures are shown in Fig. 2-12 [68].

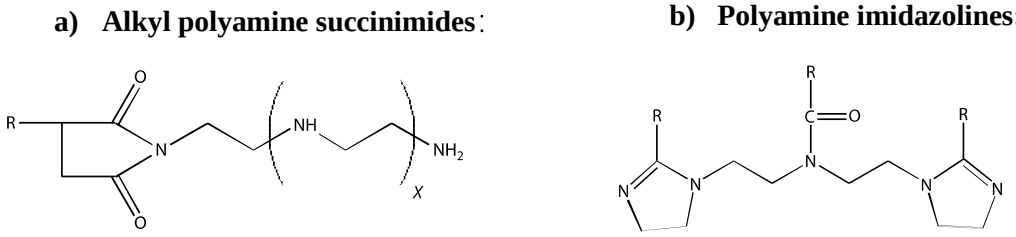

Fig. 2-12 The chemical structures of typical dispersants: a) alkyl polyamine succinimides and b) polyamine imidazolines [68].

2.3.3.5 *Antioxidants*

Since lubricants are mainly hydrocarbons, whether they are natural or synthetic, they will inevitably oxidise during use. The service life of many lubricants is limited by oxidative ageing [99]. For hydrocarbon lubricants, the oxidation process generally involves the reaction of free radicals of oxygen or nitrogen oxides with C-H bonds, resulting in the degradation of the lubricant, as shown in Fig. 2-13 [106]. Another oxidation process is thermal degradation under high-temperature conditions. Since most of the oxidation products are acidic, which increases the risk of metal corrosion, the dissolved metal salt may also be deposited to form sludge or soot due to high temperature [99]. The use of antioxidants, also known as oxidation inhibitors, can improve these phenomena.

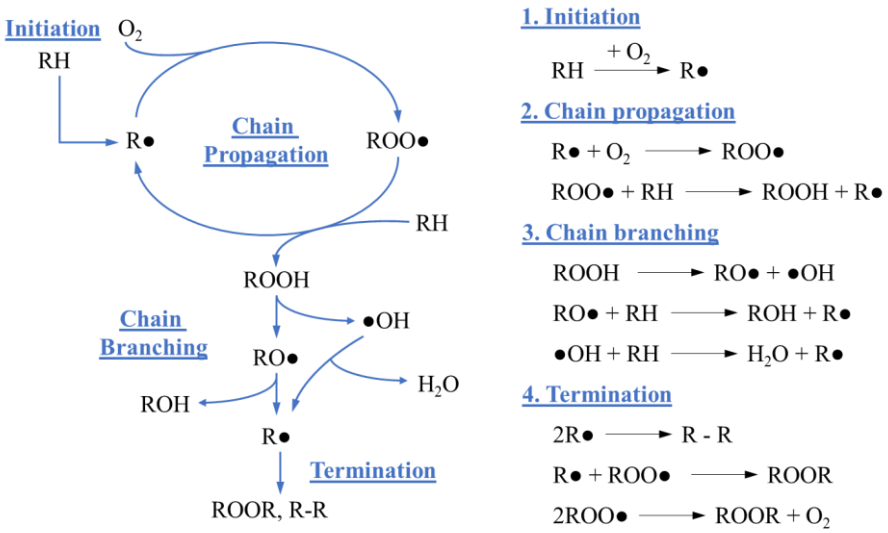

Fig. 2-13 Mechanism of autoxidation process (R● - alkyl radicals, ROO● - peroxide radicals, ROOR - non-radical products) [106].

Antioxidants mainly include phenolic antioxidants, aromatic amines, organic-sulphur compounds, organic-phosphorous compounds and transition metal peroxide decomposers. Its main mechanism is to compete with lubricant molecules and preferentially react with free radicals or peroxides to generate inactive free radicals, thereby stopping the process of auto-oxidation [99].

2.4 *Physical Properties*

2.4.1 *Viscosity*

One of the most basic and important physical properties of hydraulic oil is viscosity, which can be divided into dynamic viscosity and kinetic viscosity. The definition is shown in Fig. 2-14. The upper surface is subjected to a force *F* and moves relative to the lower stationary surface at a speed *V*. The contact area is *A* and the distance between the surfaces is *h*.

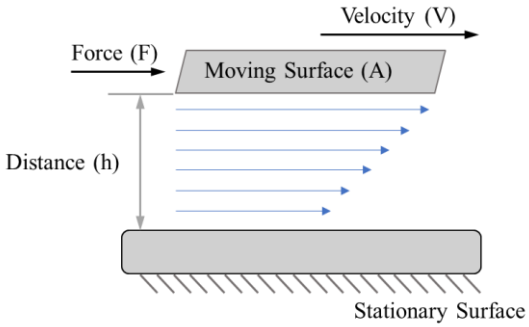

Fig. 2-14 The schematic diagram of one surface moving relative to the other stationary surface at the velocity (*V*) acted by a force (*F*), and the distance between the two surfaces is (*h*).

The shear stress τ and shear rate $\dot{\gamma}$ are calculated by Equ. (2-11) and (2-12), respectively.

$$\tau = F/A \quad \textbf{(2-11)}$$

$$\dot{\gamma} = V/h \quad \textbf{(2-12)}$$

When the fluid is a Newtonian fluid, the dynamic viscosity η is a ratio of shear stress divided by shear rate, as expressed in Equ. (2-13). The dynamic viscosity is affected by temperature and pressure, which in turn affects the working state of the hydraulic oil.

$$\eta = \tau/\dot{\gamma} \quad \textbf{(2-13)}$$

Kinematic viscosity ν is expressed as the ratio of the dynamic viscosity to the fluid density at the same temperature (2-14).

$$\nu = \eta/\rho \quad \textbf{(2-14)}$$

2.4.1.1 *Viscosity-Temperature*

The relationship between viscosity and temperature can be expressed by the Eyring and Ewell equation (2-15) [107].

$$\eta = \frac{h_P N_A}{V_m} e^{\Delta E / RT} \tag{2-15}$$

in which ΔE is the activation energy of viscous flow; N_A is the Avogadro's number; V_m is the molecular volume; h_P is the Plank's constant; R is the gas constant; T is the absolute temperature with the unit of K.

Now the more widely used is an empirical formula, called McCoull-Walther-Wright equation (2-16) [108], which is often used to predict the viscosity-temperature relationship of mineral oil.

$$\log\log\left(\eta / \rho + c\right) = a - b\log T \tag{2-16}$$

where constants a and b are related to special fluids, and the constant c changes with viscosity, which can be obtained from the standard ASTM D341 [109].

2.4.1.2 *Viscosity-Pressure*

Viscosity and pressure have an exponential relationship, which can be described by the Barus equation (2-17) [110].

$$\eta_p = \eta_0 e^{\alpha P} \tag{2-17}$$

in which η_0 is the viscosity under atmospheric pressure; α is the pressure-viscosity coefficient under pressure P, which is related to temperature, pressure and the chemical composition of the fluid.

2.4.2 *Thermal Effect*

Temperature not only affects the viscosity characteristics of the fluid, but the increase in temperature also affects the strength of the surface film and the deformation of the material in the near-surface area. The total temperature T can be expressed as the sum of

the bulk temperature T_b of the material and the flash temperature T_f related to the instantaneous temperature rise caused by rubbing in the lubricated contact. The expression is as follows.

$$T = T_b + T_f \tag{2-18}$$

Flash temperature rises greatly at high sliding speed but its influence is generally small when the sliding speed is less than 0.1 m/s [20]. For ZDDP antiwear tribofilm generated at a lower speed, it is proposed that flash temperature is not the driving force of tribofilm so it can be ignored [111].

2.4.3 *Slide-to-Roll Ratio (SRR)*

The entrainment motion of the surface is directly related to the fluid film thickness, which affects the degree of engagement between the two asperities [97]. The entrainment speed is defined as follows.

$$U_e = \frac{1}{2}\left(U_1 + U_2\right) \tag{2-19}$$

where U_1 and U_2 are the velocities of two contact surfaces, respectively.

The sliding speed U_s represents the relative shear motion between two contact surfaces defined as

$$U_s = U_1 - U_2 \tag{2-20}$$

When sliding and rolling motions exist at the same time, a parameter representing the sliding or shearing state, namely the sliding-to-roll ratio (*SRR*) is commonly used. It is the ratio of the sliding speed divided by the entrainment speed.

$$SRR = \frac{U_s}{U_e} = \frac{2\left|U_1 - U_2\right|}{U_1 + U_2} \tag{2-21}$$

in which $SRR = 2$ for the pure sliding condition while $SRR = 0$ for the pure rolling condition. The sliding speed and entrainment speed can be considered as an engineering link to the strain degree when the two asperities are in contact [97].

2.5 *Summary*

This chapter mainly introduces the basic principles and related tribological theories of friction, wear and lubrication, as well as explanations of terms related to physical properties such as viscosity, temperature and slide-to-roll ratio, so as to facilitate the subsequent analysis and discussion. The literature review for this study, including experimental and model aspects, will be described in detail in the next chapter.

Chapter 3 Literature Reviews

3.1 *Introduction*

This chapter is a literature review of this research, which is mainly divided into two parts. The first part introduces the research progress on lubricant additives of ZDDP, detergents, dispersants and their interactions from the experimental point of view. The second part introduces the development of boundary lubrication modelling, mainly including the theory and numerical methods of contact mechanics for homogeneous surfaces and layered surfaces, tribochemical kinetics and wear models.

3.2 *ZDDP as an Anti-wear Additive*

Zinc dialkyldithiophosphate (ZDDP) has been studied for about 80 years. There is enormous research on ZDDP in the view of different aspects, in which one of the most widely discussed is its excellent anti-wear property. In addition, it also has superior performances on EP (extreme pressure) conditions, antioxidation and corrosion inhibition [5]. It contains sulphur and phosphorus, which are harmful to the ecological environment, so there has been a lot of research in recent years to reduce the content of S and P in it, or to find its substitute directly. At present, there is still a long way to go in the development of additives with excellent performance and economic advantages equivalent to ZDDP.

3.2.1 *Structure and Tribofilm Formation*

ZDDP, as a lubricant additive, first appeared in some patents from the end of the 1930s to the early 1940s as a corrosion inhibitor and antioxidant [5-8]. It was found to have the characteristics of reducing wear at the end of the 1950s and was rapidly applied in the automotive industry of the United States [112-114]. Next, ZDDPs with different structures and different chemical formulas are optimised for different applications, such as secondary alkyl ZDDP in gasoline due to its better reactivity [5].

The basic chemical structural formula is shown in Fig. 3-1. Different *R* groups distinguish the types of ZDDP such as primary alkyl, secondary alkyl and aryl type, which also influence the anti-wear performances, with the ranking as secondary alkyl > primary alkyl > aryl [115].

Fig. 3-1 Chemical structural formula of ZDDP and the R-groups can be alkyl or aryl types [116].

Film formation is a significant characterisation for ZDDP including thermal film and tribofilm. Fig. 3-2 illustrates the chemical compositions of ZDDP antiwear tribofilm [5]. It is a pad-like structure. The main compositions from the inner layer (next to the substrate) to the outer layer are iron/zinc sulphides, glassy phosphates, polyphosphates and alkyl phosphate precipitates. The chain length is shorter and the content of iron is higher with closer to the substrate.

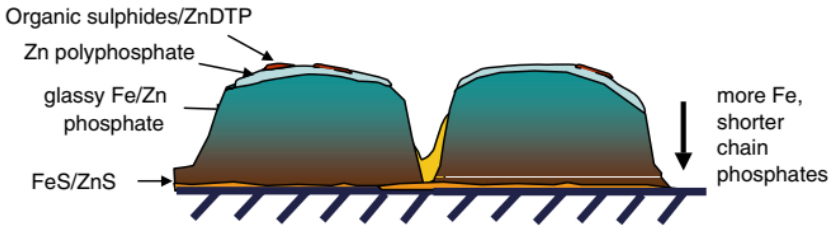

Fig. 3-2 The schematic diagram of ZDDP tribofilm and compositions [5].

The formation temperature of tribofilm is lower than that of thermal film, even at room temperature [111]. Many studies showed that tribofilm only formed within the rubbing tracks [111, 117], and the tribofilm thickness tends to stabilise over 50~150 nm on steel surfaces [48, 111, 118]. The formation rate of tribofilm increases with the rise of temperature and concentration of ZDDP, and the secondary alkyl ZDDP has a faster growth rate than the primary alkyl ZDDP [48].

The formation rate of the thermal film also increases with the increase of temperature, and the thickness can reach at least 200 nm on the steel surface [118, 119]. The chemical compositions of the thermal film are similar to those of tribofilm [119-121], but the difference is that the cations of the thermal film are mainly zinc and almost no iron [122] The thermal film has also been found to show the antiwear property [120]. Fujita and Spikes stated that the thermal film can be neglected when the temperature is lower than 110℃ [111].

3.2.2 *Wear Mechanisms*

The main compositions of tribofilm produced are phosphates and sulphides. Studies have shown that under mild wear conditions, the main component of tribofilm is phosphate, while under high load conditions, tribofilm is thinner and contains a high content of sulphur [123]. It is found that the antiwear effect of ZDDP is mainly derived from the formation of phosphates, while the EP property mainly comes from iron sulphides [10], which is consistent with many studies. For example, the non-sulphur additive has antiwear properties but no EP effect. For non-phosphorous additives such as organic sulphides, which is normally considered as an EP additive but it can also reduce wear [1, 124]. Therefore, the discussion of the wear mechanism of ZDDP is mainly based on the conditions of mild wear to distinguish the severe wear for EP additives.

There are three main explanations for the antiwear mechanisms of ZDDP [5].

1) The formation of the mechanically protective film can reduce the direct metal-metal contact and adhesion [10].

   It is one of the most widely accepted views. In addition, the antiwear tribofilm is softer than the metal, so it can also provide a cushioning effect when subjected to stress. Besides, ZDDP tribofilm is also considered to be very durable. In the mild wear condition, even if the base oil is used to replace the lubricant after the tribofilm thickness is stable, the wear amount is very small [48, 118, 120].

2) It reacts with peroxide and peroxy-radicals to prevent corrosion [11, 12].

   In addition to being an antiwear additive, ZDDP is also used as a corrosion inhibitor and antioxidant. This mechanism has been studied more maturely. However, when it is used as a peroxide decomposer, the product will no longer be a phosphate tribofilm of antiwear nature, but dithiophosphate sulphides, ZnO or $ZnSO_4$ [125].

3) ZDDP can react with hard and iron oxide particles to prevent three-body abrasion [13-15].

   Martin *et al.* explain the wear mechanism of ZDDP from the perspective of the 'Hard Acid Soft Base (HASB)' principle, that is, when iron oxide abrasive debris is embedded in the antiwear tribofilm, an acid-base neutralisation reaction occurs to

produce softer iron phosphate, thereby reducing abrasion [15]. However, it is still controversial due to the lack of evidence of direct digestion of iron [5].

In addition, In recent years, the formation of ZDDP tribofilm may promote the occurrence of micropitting wear has been concerned [126-131]. When the tribofilm grows faster and thicker, it hinders the adequate running-in of asperity, resulting in an increase in the contact stress in asperity. As the stress cycle increases, it eventually leads to the occurrence of micropitting wear [126, 127].

3.2.3 *Mechanical Properties*

Experimental research on nanoindentation and AFM has advanced the understanding of the mechanical properties of ZDDP tribofilm. Bec *et al.* [132] measured both the hardness and reduced modulus of ZDDP tribofilm layer by layer, indicating that the mechanical properties are affected by the chemical compositions or the measurement area of tribofilm. As shown in Fig. 3-3, they found that the hardness of tribofilm is about 1~2 GPa for (poly)phosphate in the bulk of tribofilm and 4.7 GPa for the sulphide-oxide layer between the phosphate and substrate or at the edge of tribofilm. The reduce modulus of tribofilm are 15~90 GPa. They also provided a stiffness model (3-1) that when pressure increase to a threshold value H_0, the reduced Young's modulus E_f^* and hardness H have a linear relationship.

$$E_f^* = E_{f0}^* \frac{H}{H_0} \quad \textbf{(3-1)}$$

where E_{f0}^* is the reduced Young's modulus of the tribofilm when $H \leq H_0$.

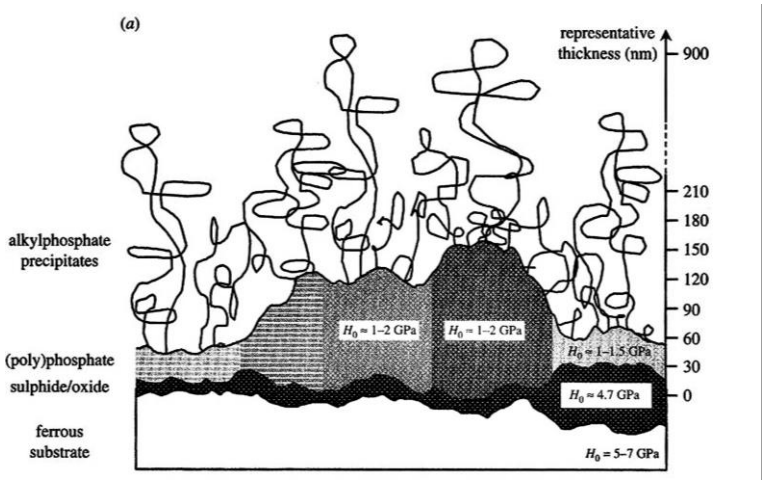

Fig. 3-3 The structure of ZDDP antiwear tribofilm, showing the composition and dimension of the various components of ZDDP tribofilm [132].

Demmou *et al.* [133] studied the mechanical properties from 24 ℃ to 80 ℃. They found that the experimental results in all tested temperatures were similar to the trend in Fig. 3-4 and the consistent results were obtained by using Equ. (3-1) to fit the relationship between the modulus and hardness of tribofilm. Furthermore, Pereira *et al.* [134] expanded the test temperature range to 25~200 ℃ to study the elastic modulus of tribofilm and summarised that the value is relatively stable at ~100 GPa when the temperature is lower than 150 ℃.

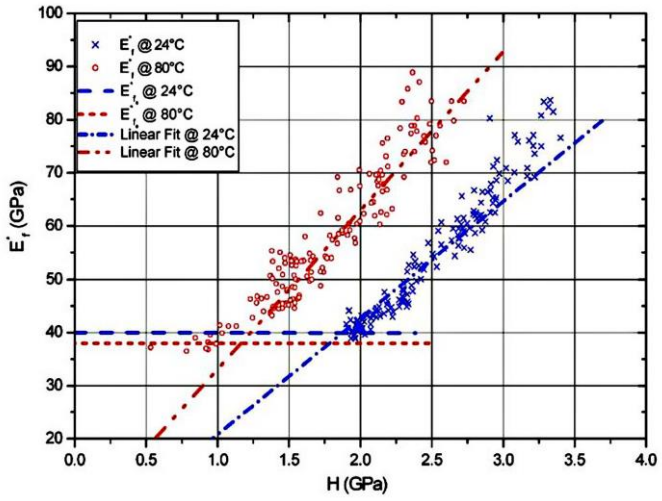

Fig. 3-4 The relationship between the reduced Young's modulus and the hardness at 24 ℃ and 80 ℃, linearly fitted by Equ. (3-1) [133].

In contrast, although the thermal film has chemical compositions similar to that of tribofilm, its mechanical strength is weaker than that of tribofilm. The elastic modulus of the thermal film is about 35 GPa and the hardness is about 1.5 GPa [18].

3.2.4 *Friction Property*

Many studies showed that the formation of ZDDP tribofilm will increase the friction coefficient. At first, it was thought that this might be due to the increase of roughness after tribofilm formation. For example, Talyor *et al.* reported that the roughness reached 50-75 nm at 100 ℃, and the orientation was along the sliding direction [117]. However, it was later found that in mixed lubrication, the smooth ZDDP tribofilm can also cause high friction [135, 136]. It is considered that the smooth tribofilm may inhibit the entrainment of the fluid film. When the fluid slides on the smooth phosphate surface, it will not be entrained into the frictional contact [137].

The apparent effect is that the generation of ZDDP antiwear tribofilm will cause elastohydrodynamic lubrication or mixed lubrication regimes moving towards boundary lubrication regime [5, 117], as shown by the Stribeck curves in Fig. 3-5.

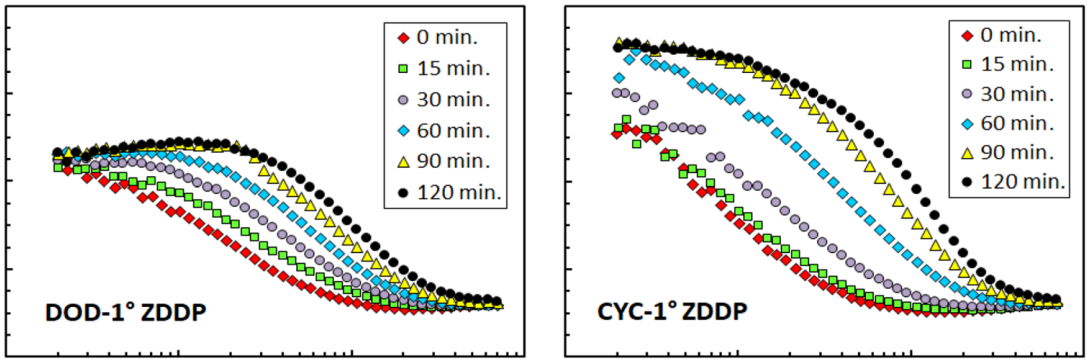

Fig. 3-5 The Stribeck curve of primary ZDDPs [138].

In most cases, the increase of friction is detrimental to machines. For example, it will affect fuel economy in the engines [139]. For passenger cars, it can be improved by adding a friction modifier and using low-viscosity oil [140]. However, there are also some situations requiring high friction such as continuously variable ratio transmissions (CVT) where ZDDP can play a good role in both wear reduction and friction maintenance [141].

3.2.5 *Rheology Property*

Studying the rheological properties of ZDDP tribofilm can further understand its formation and wear mechanism. Many studies have shown that the outer layer of ZDDP tribofilm has certain viscous and flowable properties [132, 142, 143], which is different from the sulphide layer near the substrate and the phosphate in the bulk tribofilm. Bec *et al.* used solvent removal to confirm the presence of alkyl phosphate precipitates on the surface of polyphosphate [132].

Alliston-Greiner *et al.* studied the rheology of ZDDP tribofilm and concluded that ZDDP tribofilm is considered a solid, which exhibits elasticity under normal pressure while it shows a plastic-like, strain and strain rate-independent, ductile nature under shearing. Its shear properties are similar to many organic polymers such as PTFE (Polytetrafluoroethylene) [144]. Aktary *et al.* proposed that the formation mechanism of ZDDP has three stages: 1) nucleation, 2) coalescence and 3) disintegration. They also showed that tribofilm has high plasticity and sacrificial properties, and tribofilm is continuous formatted and removed at the interface [18]. As the temperature rises, the elastic modulus of tribofilm decreases, which indicates that it is easy to deform at high temperatures [134]. In contrast, other studies showed that ridges of tribofilm have a high elastic deformation ability, that is, resistance to plastic deformation [145-147].

Dorgham *et al.* [148, 149] proposed a mechanism of 'local occupancy of tribofilm pads' to explain the antiwear behaviour of tribofilm, in which tribofilm will deform and flow under high shear and contact stress, resulting in a decrease in pressure between asperities, thereby reducing wear. They used AFM as a tribometer to form the tribofilm by reciprocating sliding at different scanning line intervals (an example of 8 lines is shown in Fig. 3-6) and found that when the line interval was larger than the nominal diameter of the tip, the tribofilm grew along the scanning line at first, then beginning to flow gradually around and filling the nearby spaced area. It proved the fluidity of ZDDP tribofilm.

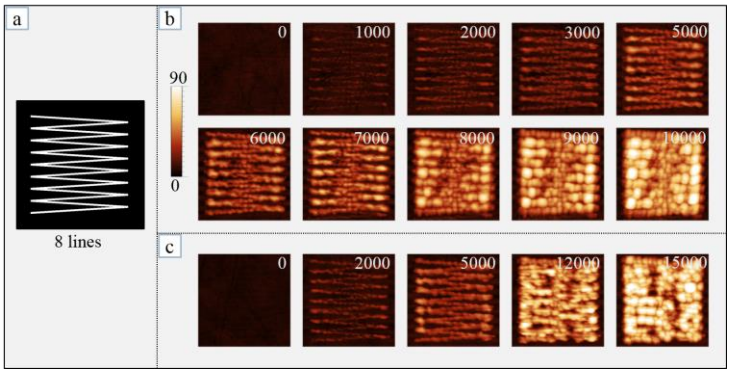

Fig. 3-6 The evolution of ZDDP tribofilm formation using AFM rubbing at 8 scanning lines under different cycles [148].

In addition, they used different pressure rubbing on the mature tribofilm in the base oil without ZDDP to further verify that the deformation comes from the high contact pressure. The experimental results show that as the normal pressure increases, the tribofilm thickness decreases and the contact area increases, see Fig. 3-7, which can be explained as a phenomenon of squeezing flow [148].

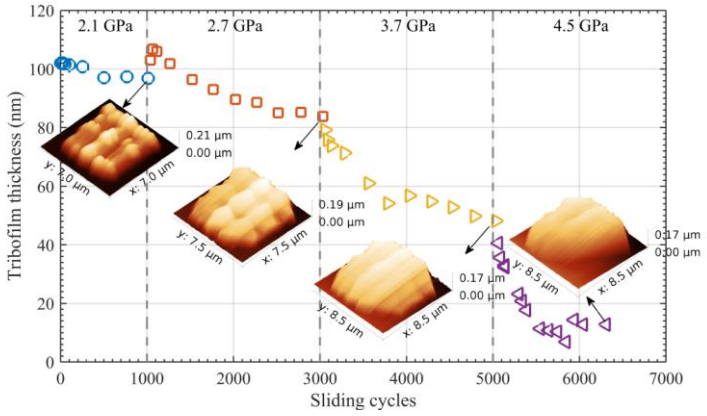

Fig. 3-7 The tribofilm thickness after rubbing in the base oil under different normal pressure [148].

Thus, the shape and formation of the tribofilm are affected by the fluidity of the tribofilm and the local occupation of the pads, as well as the interactions between pads, which will also influence the durability and wear of the tribofilm [149].

3.3 *Interactions between Additives on Steel Surfaces*

3.3.1 *Detergents and ZDDP*

3.3.1.1 *Film-formation and Antiwear Performance of Detergents*

Among the different detergents, sulphonates and salicylates have film-forming properties, which can prevent metals from rusting, but phenates have no such effect [98]. Calcium sulphonate is the most widely used detergent, so it has become one of the key research objects of detergents.

Topolovec-Miklozic *et al.* [150] studied the film formation of over-based calcium sulphonate detergent, the thickness of which can grow to 80 nm in 5 minutes and 160 nm in 2 hours on the surface. [151]. Under a certain condition, the film thickness of detergent can even reach 240 nm [152].

Some studies have shown that calcite crystallised by $CaCO_3$ is found in the boundary film of the contact area, and the sulphonate is removed from the film due to rubbing [153-155]. Mansot *et al.* [153] proposed that after the detergent colloidal particles are adsorbed to the metal surface in the boundary film mechanism, part of its organic shell layer is fractured and oxidised due to rubbing. It is discharged from the rubbing area and the $CaCO_3$ core is crystallised. In particular, Giasson *et al.* [155] found that after the sulphonate is discharged from the contact area due to high pressure and shear, $CaCO_3$ crystallises into calcite. Cizaire *et al.* [154] also proposed a similar film-forming mechanism and pointed out that when the pressure and the shear increase, the long-chain hydrocarbon surfactant will shorten. The disappearance of sulphonate from the contact area is because the ionic Ca-S bond is not resistant to high contact pressure and long sliding. They also found that the crystallisation of $CaCO_3$ to calcite is because of the presence of carbon-rich joints.

Further studies have shown that $CaCO_3$ may be decomposed into CaO and CO_2 [154], and even the structure of the detergent film is considered to be mainly composed of the top layer of $CaCO_3$ and the bulk film of CaO (decomposed by $CaCO_3$) [22, 156, 157], whether it is crystallised or amorphous detergents [157]. Kubo *et al.* [152] found that the formation of CaO is not only promoted by the pyrolysis of $CaCO_3$ but more importantly

by the rubbing process. In addition, there is adsorption of sulphonate found on the surface of the film, see in Fig. 3-8.

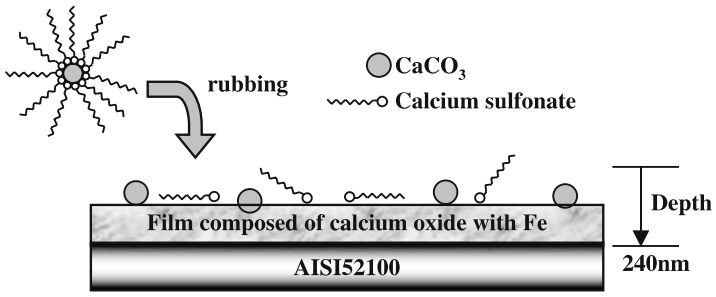

Fig. 3-8 Schematic diagram of the film formation process of calcium sulphonate detergent on AISI52100 steel surfaces [152].

Overbased calcium sulphonate detergents have been found to reduce the wear properties of metal surfaces [104, 153, 158-163], but there are different opinions on its antiwear mechanism. The first possibility mainly comes from surfactants. The reaction film will produce delamination during the rubbing process, that is, preferential shearing instead of the abrasion of the metal surface. But this reaction is different from that of ZDDP. The boundary film does not come from a chemical reaction with the metal surface, because the film formation process does not require much iron to participate [153]. However, some studies have reported that changing the surfactants has little effect on the effectiveness of antiwear performance while changing the diameter of the colloidal core has a greater effect [104]. The second possibility is due to $CaCO_3$ colloidal particle or CaO from boundary film [158-161]. The third possibility of the antiwear mechanism depends on the colloidal structure and overbased character [162, 163].

Although the molecular structure of the colloidal particles of different detergents is similar, its physical properties and performance are related to mineral salt cores, surfactants, molecular weight, ion size, crystallinity, acidity and alkalinity, etc. This requires separate analysis for specific structural combinations [98]. For example, in the aspect of antiwear performance, over-based detergent is better than neutral type [152]. Crystalline detergent has better wear performance than amorphous type, and the surface film produced by crystalline detergent is found to contain more $CaCO_3$ [157, 159].

3.3.1.2 *Interactions between Calcium-based Detergents and ZDDP*

Although calcium-based detergents have been reported to have good antiwear and anti-scuffing properties [27, 160], when they are mixed with ZDDP in the lubricant, they may have an antagonistic effect on the antiwear performance.

When no detergents are involved, the cations in the bulk of ZDDP tribofilm are mainly zinc, and close to the substrate is mainly iron [164]. When calcium detergents participate, they will compete with ZDDP. Calcium ions replace zinc ions and become the main cations in tribofilm [27], which will lead to the formation of thermally unstable products, thereby deteriorating the anti-wear properties of ZDDP [21]. When the concentration of detergents is too high, it will not only change the structure of tribofilm but also form a separate carbonate region [23].

Secondly, overbased calcium sulphonate detergent can significantly shorten the chain length of phosphate, thereby reducing the effectiveness of antiwear [22-27]. Costello *et al.* [22] found that crystalline detergents are easier to deposit on the metal surface and prevent the formation of long polyphosphate chains, instead of forming calcium phosphate. Since there is more calcium carbonate in the crystalline film than in the amorphous film, it is presumed that the crystalline carbonate is more easily adsorbed, and there is also competition between carbonate and phosphate.

However, some studies show that neutral calcium sulphonate detergent has little effect on the polymerisation of phosphates while the addition of basic calcium phenate leads to the shorter chain length of polyphosphate [24]. Therefore, it shows that the influence of detergent on ZDDP tribofilm is related to its acidity and alkalinity and the type of surfactants.

3.3.2 *Dispersants and ZDDP*

Some of the dispersants may have a certain degree of wear-reducing properties. For example, the borated succinimide dispersant can provide some antiwear performance without ZDDP, possibly because of the mixed iron-boron oxides formed [165]. However, in general, it has little benefit to friction and wear [83]. The dispersant normally has a high molecular weight so it can increase the oil viscosity and may further increase friction.

Moreover, it may compete with antiwear additives or friction modifiers and interfere with their surface activity.

Some studies have shown that the dispersant has a certain synergistic effect on improving the dispersion performance with ZDDP [166, 167]. However, more studies have shown that it has an antagonistic effect in the blended oil of dispersant and ZDDP, which is mainly manifested in the following three aspects.

Firstly, Complexation is considered to be the main mechanism of antagonism between ZDDP and dispersant [28-31]. The complexes may be produced by the decomposition products of ZDDP through P-N bonding [30, 32] or Zn-N bonding [31, 33-35, 165], which may occur on the oil solution or the metal surface. The formed complex is affected by the structure of amine groups [31]. For example, the interaction between ZDDP and mono-succinimide is stronger than that bis-succinimide [36], and the high molecular weight, the high nitrogen content of dispersants will promote the complexation interaction with ZDDP [35]. The stronger the complexation reaction, the more adversely affected wear, which may be due to the ZDDP being suspended away from the surface [165].

Secondly, the dispersant can adsorb or react with the metal surface, so the effectiveness of ZDDP will be reduced [38-40]. The reaction products are different from the types of dispersants and the presence of ZDDP [39]. When no ZDDP is participating, nitrogen atoms in the dispersant may form nitrogen chemisorbs on the steel surface through nitrogen lone-pair electrons. When ZDDP is present, interactions between the two additives will happen. Yamaguchi *et al.* [168] found by N K-edge XANES that the nitrogen atoms in the film may come from ammonium phosphates or primary amine. In addition, dispersant was reported to promote the decomposition of ZDDP in oil and steel surfaces [39] and increase the decomposition temperature of ZDDP [160].

Thirdly, the dispersant can dissolve the existing ZDDP tribofilm [28]. Fujita *et al.* found another possible antagonistic mechanism, that is, the dispersant can promote the removal of the tribofilm [48]. This may be due to the substitution of amino groups with zinc ions in the tribofilm, or the acidic products produced by hydrolysis that dissolve on the surface of the tribofilm. This may also occur during the formation of tribofilm. Studies have shown that dispersants will reduce phosphate film formation, but does not change the structure of the film [169].

Especially for the impact of antiwear performance, some studies have shown that under mild wear conditions, dispersants have little or no effect on the antiwear performance of ZDDP [168, 170]. Yamaguchi *et al.* [168] showed that dispersants did not play the role of wear reduction, and under the given experimental conditions, dispersants have no effect on the antiwear performance of ZDDP. However, although dispersants will not affect the formation of polyphosphate, compared to dispersant-free ZDDP oil solution, it can reduce the chain length of polyphosphate, which is consistent with other research results [24]. In addition, Martin *et al.* also stated that under severe wear conditions, the antagonistic effect of dispersants on ZDDP is predictable [170].

The study by Ramakumar *et al.* showed that the influence of dispersants on the antiwear performance of ZDDP is related to the concentration of dispersants [32]. Lower dispersant concentration has little effect on wear, while high dispersant concentration harms the antiwear performance of ZDDP. Similar results are also shown by Zhang *et al.* [28]. Under given conditions, the wear coefficient increases approximately linearly with the dispersant concentration. In the mixed oil solution containing a low concentration of dispersant and medium concentration of ZDDP, the mechanism of mild wear is presumed to come from corrosive-abrasive wear. At a low concentration of dispersant, wear is dominated by the film formation rate of ZDDP, while at a high concentration of dispersant, wear is dominated by the film removal rate.

It should be noted that this does not mean that dispersant will prevent film formation in a fully formulated oil. In oils containing both dispersant and ZDDP, the film formation rate of ZDDP slows down from the beginning. The thickness decreases but is stable in the equilibrium, and it decreases with the increase of N:P [48]. It is also proposed that the influence of dispersant on ZDDP is the absolute concentration of dispersant rather than the content ratio of dispersant to ZDDP [28]. This may indicate that under the influence of dispersant, there is still a balance between tribofilm formation and removal.

Although synergistic or antagonistic effects between two-component additives have been widely studied for many decades, competitions and interactions among multiple additives in a specific formulation are still expected to have a different performance from that in a single or dual-additive lubrication system [171]. Commercial fully formulated oils contain many multi-functional additives, each of which may affect the friction and wear

behaviours of the lubricant interacting with the metal surface, so the contribution of each additive to the overall system is complex.

3.4 *Modelling in Tribological Phenomenon: Tribochemistry and Wear*

3.4.1 *Introduction of Modelling and Simulation in Tribology*

Since tribology problems are multiscale and interdisciplinary in nature, different theories and calculation methods need to be used for different applications in modelling problems. Vakis *et al.* [172] summarised the overview of tribological modelling on different time and spatial scales in 2018, as shown in Fig. 3-9 which includes commonly used computational methods at multiscale and examples of calculations.

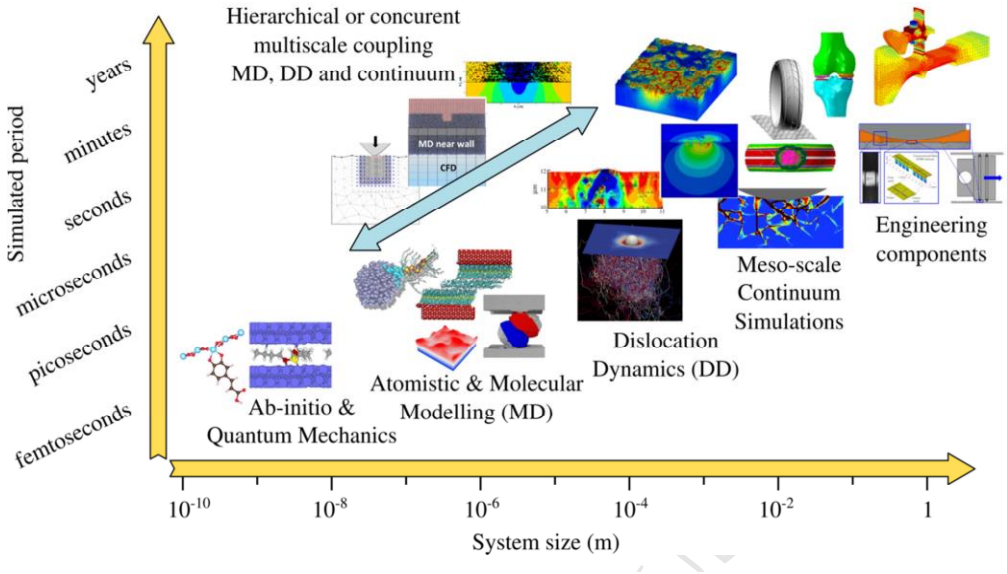

Fig. 3-9 Tribology modelling for engineering applications in the map of time and space scales [172].

For the calculation of tribological problems and interface chemical reactions in hydraulic systems, there are also different research objectives at different scales. In macroscopic applications, the finite element method (FEM) [173-175] can directly simulate the contact of relatively moving parts of the machine, such as gear pairs or the piston-cylinder liners, the stress distribution, the thermal effect and other multi-physics coupling problems. In the microscopic interface, the local contact between asperities of the friction pairs, and the tribochemical reactions between the lubricant affecting friction and wear can be calculated through analytical methods and numerical methods [50, 176-179]. At the atomic and molecular scale, the assumptions of continuum mechanics will no longer be

applicable, and will then be transferred to the field of quantum mechanics. The molecular dynamics (MD) method [19, 180-182] can be used to simulate the tendency of adsorption or reaction between the two surfaces and lubricant molecules or additive molecules to explain the causes of tribochemical reactions or the causes of friction and wear. In quantum mechanics calculations, the use of the density functional theory (DFT) and the ab-initio molecular dynamics [183-185] can supplement the information that cannot be captured in molecular science to study the movement of atoms in interface reactions.

Due to the difference in the theoretical basis of mechanics and numerical methods between macroscale and microscale, the method under a single scale may have limitations if both the tribochemical mechanism of the interface and macro phenomena such as machine wear should be considered. Therefore, multiscale coupling modelling methods have also begun to be studied, such as the coupling of MD and FEM [186, 187]. In addition, the experimental research also has certain limitations. For example, many physical parameters are not easy to measure by experiments, and the experimental results may also be affected by the errors of equipment, environment, personnel, etc. Therefore, for the modelling and simulation of specific applications, it is often necessary to develop some empirical formulas or use statistical methods to achieve the prediction of the target phenomenon through experimental results such as wear.

3.4.2 *Boundary Lubrication Modelling*

Vakis *et al.* [172] summarised the tribological phenomena that occur near the solid interfaces, including the aspects of mechanical, thermal, electric, environment, etc., as shown in Fig. 3-10. Under the condition of boundary lubrication, there is no more pressure-bearing effect of fluid between the two contact surfaces theoretically. The molecules of the base oil or additives interact with the contact interface to form a solid film that changes the morphology or material properties of the surface, which affects friction and wear phenomena. This brings certain difficulties to the selection of theoretical basis and numerical methods in boundary lubrication modelling.

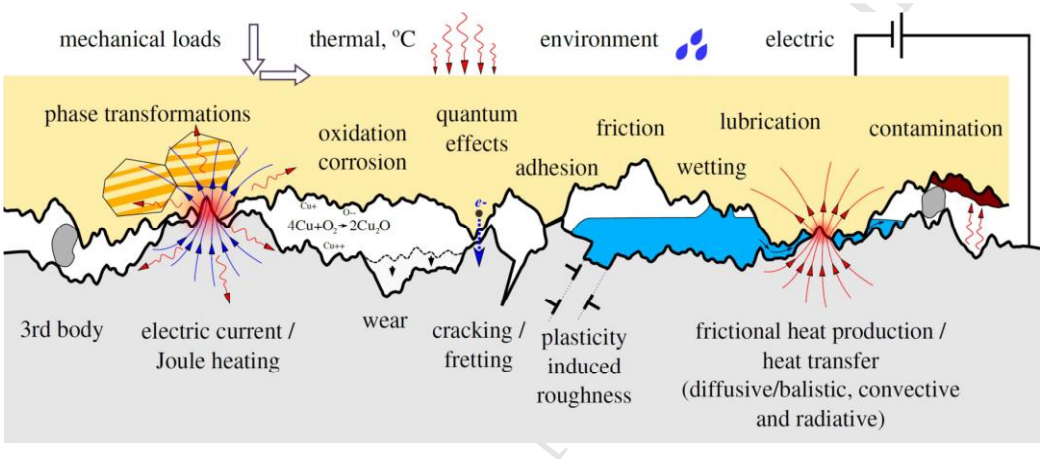

Fig. 3-10 Common tribological phenomena inside solids or between solid interfaces [172].

The modelling of boundary lubrication includes mechanical, physical, chemical and other aspects, and the discussions of their effects on friction and wear [19, 132, 173, 186, 188]. This is also a common multiscale simulation. The research theme can start from the contact mechanics of asperities on rough surfaces, increase the scale upwards to connect the deformation and wear between macroscopic elements or decrease the scale downwards to study nano-scale geometric features or adsorption or chemical reactions between lubricant additives molecules.

Contact mechanics of rough surfaces and tribochemical reaction mechanisms are two themes in boundary lubrication modelling. There are also many multi-scale computing methods emerging. For example, Anciaux *et al.* [189] used the Finite Element Method (FEM) and Molecular Dynamics (MD) coupling mechanism to calculate the contact mechanics of rough surfaces and realised the multiscale calculation combining continuum mechanics with atomic-scale simulation. Modelling in tribochemistry is often combined with experimental results, in addition to using MD to directly simulate interactions between molecules. For example, Akchurin and Bosman [50] applied the equation of tribofilm formation kinetics based on micro-tests to calculate the results from macro-tests.

According to the experimental background of this study and the framework of boundary lubrication modelling based on asperity contact, the theories and computational methods related to contact mechanics (including homogeneous and layered surfaces), tribofilm growth and wear are reviewed below.

3.5 *Contact Mechanics Model: Homogeneous and Layered Rough Surfaces*

Hertzian contact theory is one of the fundamental theories in contact mechanics and tribological modelling [172]. It is mainly based on nominally smooth surfaces to study pressure distribution and elastic/plastic deformation on non-conformal surfaces under frictionless conditions [190], but it also has certain limitations. Much progress has been made in theories and algorithms for other applications, such as layered materials like coatings or anisotropic functional gradient materials [191-202], sharp edges [203-206], the contact problem of conformal surfaces [207], etc.

3.5.1 *Homogeneous Rough Surfaces*

3.5.1.1 *Statistical Model*

In boundary lubrication, the generations of the interactions and the physical phenomena originate from the contact between two solid surfaces. In the microscopic view, it originates from the interaction between the asperities of the solid surfaces.

In 1957, Archard first assumed [208] that a rough surface is composed of a large spherical asperity with evenly distributed small asperities, and explained that the real contact area and load has a power relationship. Bowden and Tabor [209] pointed out that when two nominally flat surfaces come into contact, the contact area is the actual contact area calculated by surface asperities in the contact rather than the apparent contact area.

Rough surfaces are divided into regular rough surfaces and random rough surfaces [69]. The measured engineering rough surfaces are generally random, as shown in Fig. 3-11, which mainly contain information such as shape deviation, waviness and roughness. More statistical parameters have been formulated corresponding to international standards. The topography of the rough surfaces is usually considered a random process, so statistical methods can be used to describe its characteristics.

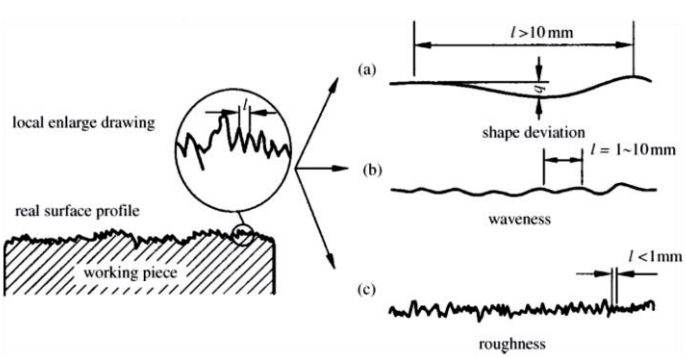

Fig. 3-11 The real surface profiles with shape deviation, waviness and roughness [69].

The classic statistical model combining rough surface and elastic-plastic contact was proposed by Greenwood and Williamson (GW model) [210], which describes the relationship between the pressure generated in a nominal flat but rough surface and the real contact area. In the GW model, for the contact between asperities satisfying Gaussian distribution, the real contact area has an approximately linear relationship with the normal load, which is consistent with the classic friction law.

Another classic model developed by Nayak [211] based on the statistical geometry theory established by Longuet-Higgins [212] on the ocean surface, proposed a new multi-asperities statistical model of elastic/plastic contact. It assumes that the height, slope, and peak curvature of the asperity obey the joint Gaussian distribution, and uses a two-dimensional normal process to simulate a random rough surface. It is very close to the analysis result of the GW model.

The complete statistical rough surface contact model (BGT model) was proposed by Bush *et al.* [213]. Compared with the GW model, it is more accurate in contact response, but the form is more complex. In subsequent research, Greenwood extended Nayak's analysis of isotropic random surfaces [214], reproduced the results of the BGT model, and greatly reduced the complexity of the model.

The development of experimental instruments, such as optical interferometer and scanning tunnelling microscope, reveals the different morphologies of roughness on the millimetre and nanometre scales and reflects the scale dependence of statistical parameters (such as root mean square, curvature and slope), which will lead to the solution predicted by the model to be not unique [215]. Panda *et al.* used the method of spectral analysis to show that when the resolution is from the nanometre scale increasing

to the micrometre scale, the average radius of asperity gradually increases [216]. Therefore, in general, it can be considered that most of the contact points are between nanometres and micrometres [217].

3.5.1.2 *Fractal Model*

The characterisation and contact calculation of rough surfaces can be simulated by fractal models in addition to statistical models. The roughness of the majority of surfaces was found to have the properties of statistical self-affinity, as well as continuous and non-differentiable, so the surface profile can be characterised by the Weierstrass-Mandelbrot (W-M) fractal function, as shown in Equ. (3-2) [218].

$$z(x) = A_s^{(D_f-1)} \sum_{n=n_1}^{\infty} \frac{\cos 2\pi\gamma^n x}{\gamma^{(2-D_f)_n}} \qquad 1 < D_f < 2,\ \ \gamma > 1 \tag{3-2}$$

in which D_f is the fractal dimension, A_s is scaling constant, and γ^n is the frequency spectrum of surface roughness.

Mandelbrot found the fractal characteristics of coastline and established the fractal geometry [219]. Majumdar and Bhushan [215] proposed a fractal model (M-B model) for calculating the elastic-plastic contact of rough surfaces based on the W-M fractal function. It is derived from the fractal roughness parameters that are independent of the scale, which can avoid the scaling problem of statistical parameters such as root mean square (RMS), slope and curvature. In subsequent research, Wang and Komvopoulos corrected the deficiencies of the M-B model [220].

The M-B model, based on the pioneering work of Mandelbrot, proposed an assumption that the area distribution probability of contact points are similar to that of islands distributed in the sea, and finally obtained the actual contact area under the nominal contact area. Yan and Komvopoulos [221] believed that when the nominal contact area exceeds a certain value, the relationship between the total number of asperities *N* and the area *a* of the contact point is $N(A_s > a) = ka^{-D_f/2}$, where *k* is the proportionality coefficient. Then, the final contact area is

$$A_c = \int_0^{a_1} n(a) a \mathrm{d}a = \frac{D_f}{2 - D_f} \cdot a_1^{(2-D_f)/2} \quad \textbf{(3-3)}$$

where a_1 is the maximum area of the contact point; $n(a)$ is the area distribution function of the contact point.

Because of its scale independence, the analysis result will not be affected by the resolution and sampling length of the measuring instrument. It has certainty and uniqueness [218], but the limitation is that the engineering surface must meet the features [222].

3.5.1.3 *Numerical Methods*

In recent models, rough surfaces are generally used as the initial profiles to be input into the contact model to calculate the distribution of contact pressure and displacement, based on the theory of elasticity. Especially for some complex surfaces, the number of different loads in the minimum set may be very large, which makes the solution of the analytical model difficult. At this condition, it is necessary to use numerical analysis to obtain an approximate solution as accurately as possible [222].

Numerical methods need to discretise complex surfaces into small units and obtain approximate numerical solutions by solving the governing differential equations [222]. Many complex discrete schemes and methods have been developed, such as the Finite Difference Method (FDM), Finite Element Method (FEM), and Boundary Element Method (BEM) [201].

- Finite Difference Method (FDM)

FDM is the most widely used numerical method. It is based on the expansion of the Taylor series and expresses the differential formula as the difference equation defined on the discrete grid points, iteratively calculating the values on the unknown boundary by the difference relation between the close grid points according to the given boundary conditions. But this is not feasible for rough surface contact calculation, because it is restricted by the regular domain.

- Finite Element Method (FEM)

FEM is a very stable method in continuum mechanics. At present, there is mature commercial software such as ANSYS, ABAQUS, etc. for computer-aided FEM calculations. However, the calculation of three-dimensional rough surfaces requires a large number of fine and irregular grids, causing an extremely long computing time, which is undesirable in commercial software. In addition, it also has obvious limitations in terms of material loss caused by wear, or changes in surface morphology or material chemical properties due to the formation of tribochemical films.

- Boundary Element Method (BEM)

BEM is widely used in three-dimensional contact problems. It only needs to directly discretise the rough surface into elements that are small enough to ignore the shape effect of the rough surface. There is no need to assume the isotropy of the surface roughness, the shape of the asperity, and some statistical parameters such as height and curvature. BEM has developed different calculation criteria, such as the direct formulation, the weight residual formation, and the minimum total potential energy formulation [222].

3.5.2 *Layered Surfaces with Roughness*

Due to the development of materials science and technology, coating technology and functional surfaces are used to improve the tribological properties of materials. Correspondingly, in the numerical analysis, the elastoplastic contact models of the multilayer rough surface have also made great progress. Its application objects include various surface topography, elastic or elastoplastic materials, normal or tangential load, dry and lubricated contact and other aspects [222]. In addition, the existence of the layer has been proved to have a significant effect on the stress field, so the extension of the stress field from two-dimensional to three-dimensional layered is also meaningful [223]. Different from the contact calculation of homogeneous materials, the exact solution for the contact of layered surfaces is very complicated mathematically. In order to balance the accuracy and the computation complexity, an approximate method is generally selected.

3.5.2.1 *Single-asperity Contact*

Single asperity contact is the basis for studying multiple asperity contact [224]. The contact algorithms of multiple asperities are usually verified by that of single asperity contact. According to the shape of asperity such as cylindrical or spherical, the contact regime can be two-dimensional or three-dimensional, as shown in Fig. 3-12a and b, respectively [222].

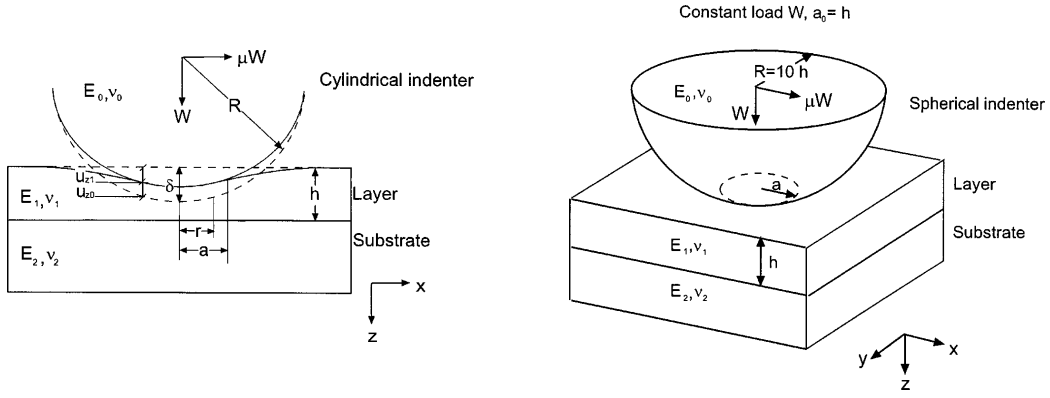

(a) **(b)**

Fig. 3-12 Schematic diagrams of the contact between a layered half-space with a) a smooth cylinder (2D) and b) a smooth sphere (3D) [222].

The displacement and pressure conditions of a single asperity contact problem in polar coordinates can be described in Equ. (3-4).

$$\begin{aligned} &u_{z0}(r,0)+u_{z1}(r,0)=u_{z0}^{*}(r,0)+u_{z1}^{*}(r,0),\ \ |r|\le a \\ &u_{z0}(r,0)+u_{z1}(r,0)>u_{z0}^{*}(r,0)+u_{z1}^{*}(r,0),\ \ |r|>a \\ &p(r)\ge 0,\ \ |r|\le a \\ &p(r)=0,\ \ |r|>a \end{aligned} \tag{3-4}$$

where p is the contact pressure; a is the contact radius; the subscripts 0 and 1 respectively represent the cylinder/sphere and the layered elastic half-space; u_{zi} and u_{zi}^{*} represent the calculated and prescribed z-direction displacement components in the actual contact domain between the cylinder/sphere and the layered elastic half-space, respectively. Since the prescribed $u_{z0}^{*}(r,0)+u_{z1}^{*}(r,0)$ is a function of the known R and a, the contact problem (3-4) is turned to find a suitable $p(r)$ satisfying the elastic governing equations at given displacements $u_{zi}(r,0)$.

To solve the contact problem of a single asperity with a layered surface, approximate methods are often used to achieve a balance between calculation amount and accuracy, such as semi-analytical methods [201, 223, 225-230], BEM [231, 232], FEM [194, 233-239] and equivalent inclusion methods [193, 195].

- **Semi-analytical methods**

The 'least-square error method' is an analytical method that uses a weighted residual formula. It is interpreted as that under the approximate pressure distribution, the square error ε^2 between the calculated and prescribed surface displacements on the actual contact area should be the smallest. It should be noted that the selection of the basis function of pressure will affect the accuracy of the approximate solution. The Hertzian solution of homogeneous materials is a good choice. There are a small number of models using other higher-order basis functions (usually no more than 5), in order to increase the accuracy of the pressure distribution [222].

The elastic theory for solving the stress state on the surface of a single-layer material was originally developed by Burmister [225] and based on a given axisymmetric normal pressure profile. Then, Chen [228] extended it to a non-axisymmetric pressure profile. Later on, Chen and Engel [229] used the least-square error method to solve the normal contact problem on the layered elastic half-space, as well as the pressure profiles and subsurface stresses under different geometric shapes of indentations.

For the layered contact problem under three-dimensional conditions, O'Sullivan and King [223] used the least-square error method to calculate the normal and quasi-static sliding contact stress fields of a smooth rigid sphere in a layered elastic half-space. This method is an important reference for the subsequent development of the layered contact model. Peng and Bhushan [201, 230] verified the work of O'Sullivan and King by the quasi-Newton method to find the minimum.

- **Boundary Elemental Method (BEM)**

The matrix inversion method is a BEM method based on the direct formulation method. Its solution idea is very intuitive, as shown below.

$$\mathbf{p} = \left[\mathbf{C}^{\mathbf{u}_z} \right]^{-1} \mathbf{u}_{\mathbf{z}}^{*} \tag{3-5}$$

where $\mathbf{p}^T = \{ p_1, p_2, ... p_k, ..., p_N \}$ is the pressure vector containing *N* discrete points in the computational domain; $\mathbf{C}^{\mathbf{u}_z}$ is the matrix of influence coefficient (IC); $\mathbf{u}_{\mathbf{z}}^{*\mathbf{T}} = \{ u_{z1}^{*}, u_{z2}^{*}, ... u_{zk}^{*}, ..., u_{zN}^{*} \}$ is the total prescribed displacement vector along the *z* direction.

Compared with analytical methods, the pressure distribution is composed of a set of discrete point loads, rather than pressure distributions represented by continuous basis functions. Similarly, it is necessary to calculate the error between the prescribed and calculated displacement to sort out the pressure distribution. However, this error is performed at discrete points, unlike the least-square error of the entire contact domain. The solution process between numerical methods and analytical methods are the same.

Gupta and Walowit [231] first used it to solve the elastic problem of 2D cylindrical indentation, as shown in Fig. 3-12a. Cole and Sayles [232] used the matrix inversion method to calculate the maximum contact pressure and contact radius changed with different layer thickness under different Young's modulus ratios between the layer and the substrate. In the single asperity contact, it seems to have no superiority of using the matrix inversion method compared to analytical methods. However, in the contact of multiple asperities, it is complicated and hard to obtain a closed-form of pressure expression and decompose it into some basis functions. At these conditions, the advantages of the matrix inversion method as flexible numerical methods can be exhibited.

- **Finite Element Method (FEM)**

Although the surface structure of a single asperity is simple, the contact may have various complicated conditions such as impact, cracks, and viscoelasticity. When simple pressure distribution and stress formulas cannot be derived, an effective tool for determining stress and strain field is finite element modelling. With the development of commercial FEM software, it provides a lot of convenience in meshing, multi-physics coupling simulation and calculation of various nonlinear materials.

For example, by using the commercial FEM software, Komvopoulos [233, 234] simulated 2D cylindrical indentation and Kral and Komvopoulos [239] simulated 3D spherical indentation under sliding contact. Kot *et al.* [194] used spherical indentation and FEM modelling to simulate the contact calculation of TiN coating and combined it with the nanoindentation experiment to analyse the load on the part that caused coating damage. However, one of the drawbacks of the FEM is the extreme long computing time for irregular and fine mesh required in the simulation of rough surfaces.

3.5.2.2 *Multi-asperities Contact with Roughness*

Most solid surfaces contain irregular geometric morphologies at different scales, and asperity is expressed as the high peak or summit on the surface. When two nominally flat surfaces come into contact, the contact and deformation actually happen between multiple asperities. Meanwhile, the stress occurring at all contact points carries the applied load together, and the real contact area is composed of the sum of the areas at all contact points.

Considering a contact problem of a 3-dimensional layered rough surface in the Cartesian coordinate system, it is described as follows [222].

$$\begin{aligned} &u_{z0}(x,y,0)+u_{z1}(x,y,0)=u_{z0}^{*}(x,y,0)+u_{z1}^{*}(x,y,0),\ \ (x,y)\in\Omega \\ &u_{z0}(x,y,0)+u_{z1}(x,y,0)>u_{z0}^{*}(x,y,0)+u_{z1}^{*}(x,y,0),\ \ (x,y)\notin\Omega \\ &p(x,y)\geq 0,\ \ (x,y)\in\Omega \\ &p(x,y)=0,\ \ (x,y)\notin\Omega \end{aligned} \qquad \textbf{(3-6)}$$

It is different from the description of the single asperity contact problem in (3-4) that Ω is the real contact area, but $p(x,y)$ and $u_{zi}(x,y,0)$ are also required to satisfy the elastic governing equations. In the multi-asperity contact problem, because of the complexity of the geometry, it cannot be solved directly by analytical methods, so numerical methods are needed to obtain approximate solutions.

FEM is one of the numerical methods that are often used to study the stress and deformation of multi-layered materials. One of its advantages is that it can involve the constitutive relationship of various materials. Theoretically, the problem of elasticity on rough surfaces can be solved as well. In the contact calculation of 2D rough surfaces, there have been attempts for homogeneous surfaces [240] and sliding contact [241, 242]

by FEM. However, for the contact problem of a three-dimensional layered surface, a large number of irregular and fine meshes need to be divided for the rough surface, which leads to an extremely long calculation time.

In comparison, BEM only needs to discretise the boundary surface into finite elements and convert the differential equations of the continuous area within the object into the integral equation sets of the corresponding boundary on the object surface. It has the advantages of reducing the dimensionality of the problem and computational quantity. When solving the contact problem of rough surfaces, the rough surface is usually discretised into small rectangular elements. The size of the element depends on the balance of computational time and accuracy. In the BEM method, direct formulation (such as matrix inversion method (MIM) or conjugate gradient method (CGM)) and minimum total potential energy formulation are often performed to calculate the contact problems of layered rough surfaces.

- **Matrix Inversion Methods (MIM)**

As introduced in the layered contact of a single asperity, MIM is mainly to solve equations $\mathbf{p} = \left[\mathbf{C}^{\mathbf{u}_z}\right]^{-1}\mathbf{u}_z^*$ converted from direct formula $\mathbf{u}_z^* = \mathbf{C}^{\mathbf{u}_z}\mathbf{p}$ [222]. Gupta and Walowit [231] first applied the MIM to calculate the elastic contact problem between a cylinder and a layered solid. Then, Cole and Sayles [232] used a similar method to calculate cylindrical contacts between different combinations of smooth or rough surfaces and verified the MIM by available theoretical analysis. This method was extended to frictional contact by Mao *et al.* [243]. Moreover, Tian and Bhushan [244] used a direct quadratic mathematical programming method to process the formula $\mathbf{p} = \left[\mathbf{C}^{\mathbf{u}_z}\right]^{-1}\mathbf{u}_z^*$. By triangular decomposition of the inverse influence coefficient matrix, it is guaranteed that it remains positive definite and non-singular after finite rounding.

- **Conjugate Gradient Method (CGM)**

For the three-dimensional rough surface contact problem, there are many contact points, resulting in a very large influence coefficient matrix. It is easy to cause the influence coefficient matrix to lose the positive definiteness under the rounding error, which makes the matrix inversion method have serious non-convergence problems. Therefore, the

introduction of the Conjugate Gradient Method can speed up the calculation and convergence speed on the one hand and avoid the problem of solving the inverse matrix on the other hand.

Nogi and Kato [245] used the CGM method to calculate the contact of a layered rough surface under normal pressure. They used the given rigid approach δ to calculate the initial prescribed surface displacement $\mathbf{u}_z^*$ based on geometric interference. In each CGM iteration step, Fast Fourier Transform (FFT) technique was used to improve calculation efficiency.

Polonsky and Keer [246] solved the pressure distribution of a layered rough surface by a single loop based on the CGM method [247]. They used the Multi-Level Multi-Summation (MLMS) method to provide a special correction term to compensate for the periodic error in the FFT algorithm and improve the accuracy of FFT based on the concentrated contacts.

- **Minimum Total Potential Energy Formulation**

CGM and MIM have a common disadvantage that since the initial prescribed displacement in the direct formulation is unstable, it may not converge when the influence coefficient matrix is large or ill-conditioned, and the uniqueness of the solution cannot be guaranteed. Another method, the minimum total potential energy formulation, is derived from the formula of physical principles. It can be used to solve the optimisation problem with the quadratic form and in principle guarantee the convergence and uniqueness of solutions [222].

There are two types of minimum energy formulations, namely the principle of the minimum total elastic energy and the principle of the minimum total complementary energy, which are suitable for elastic-perfectly plastic problems [201, 248, 249]. The latter is more suitable for conditions where the pressure is unknown, but it is only effective for small displacements. The principle of minimum total complementary energy points out that in all possible equilibrium stress fields, the real values of the prescribed load and boundary surface displacement of a solid are determined by the minimum value of the total complementary energy.

Tian and Bhushan [244] proposed the variational principle for solving the elastic-plastic contact problem of homogeneous rough surfaces. Peng and Bhushan extended the method to the layered rough surfaces under dry and wet conditions [201] or sliding conditions [230, 250]. The variational form [244] for finding the minimum value of the total complementary energy is expressed as

$$\min V^* = \frac{1}{2}\int_\Omega p u_z d\Omega - \int_\Omega p u_z^* d\Omega \tag{3-7}$$

BEM is used to discretise the contact interface into small rectangular boundary elements. As long as the elements are small enough, the pressure value on each boundary element can be assumed to be constant. Combining the displacement related to the pressure p_l and the influence coefficient matrix $C_{lk}^{u_z}$, Equ. (3-7) can be discretely expressed as

$$\begin{aligned} \min V^* &= \frac{1}{2}\sum_{k=1}^{M} p_k u_{zk} - \sum_{k=1}^{M} p_k u_{zk}^* \\ &= \frac{1}{2}\sum_{k=1}^{M} p_k \left(\sum_{l=1}^{M} C_{lk}^{u_z} p_l \right) - \sum_{k=1}^{M} p_k u_{zk}^* \end{aligned} \tag{3-8}$$

where *k* is the index of the contact point, *l* is the point acted by the pressure and *M* is the total number of the points.

The BEM method based on the minimum total complementary energy principle is also used in this project, so the detailed theory and related numerical method will be explained in Chapter 7.

3.5.2.3 *Fully-bonded and Imperfectly Bonding Interfaces*

As shown in Fig. 3-13, when two materials are bonded, an interface will be formed between them, and the displacement and traction on both sides may be continuous or discontinuous.

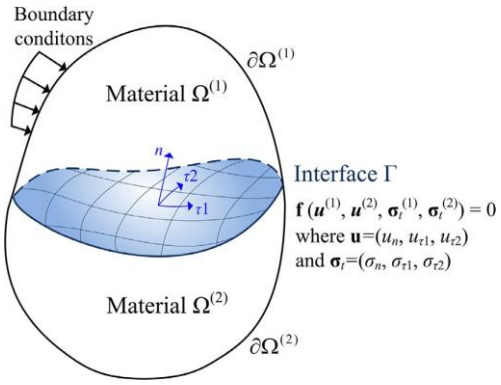

Fig. 3-13 The schematic diagram of the force and displacement at the interface of a composite material composed of material *1* and material *2* [251].

The transfer characteristics of displacement and stress at the interface can be described by the following general condition [251].

$$\mathbf{f}\left(\mathbf{u}^{(1)}, \mathbf{u}^{(2)}, \boldsymbol{\sigma}_{\mathbf{t}}^{(1)}, \boldsymbol{\sigma}_{\mathbf{t}}^{(2)}\right) = 0 \tag{3-9}$$

where superscripts *(1)* and *(2)* represents the layer and the substrate; $\mathbf{u} = \left(u_n, u_{\tau 1}, u_{\tau 2}\right)$ and $\boldsymbol{\sigma}_{\mathbf{t}} = \left(\sigma_n, \sigma_{\tau 1}, \sigma_{\tau 2}\right)$ are the displacements and the stress at the interface respectively; $\mathbf{f} = \left(f_1, f_2, ..., f_n\right)$ are a series of functions.

In the contact model containing the layer-substrate system introduced in the previous two sections, there is generally a perfectly bonded assumption of force and displacement at the layer-substrate interface. For example, under the conditions of normal and quasi-sliding contact, the fully bonded assumptions in the Cartesian coordinate system [201] can be described as:

$$\begin{aligned}
&\sigma_{xz}^{(1)}\left(x, y, h\right) = \sigma_{xz}^{(2)}\left(x, y, 0\right), \quad u_x^{(1)}\left(x, y, h\right) = u_x^{(2)}\left(x, y, 0\right) \\
&\sigma_{yz}^{(1)}\left(x, y, h\right) = \sigma_{yz}^{(2)}\left(x, y, 0\right), \quad u_y^{(1)}\left(x, y, h\right) = u_y^{(2)}\left(x, y, 0\right) \\
&\sigma_{zz}^{(1)}\left(x, y, h\right) = \sigma_{zz}^{(2)}\left(x, y, 0\right), \quad u_z^{(1)}\left(x, y, h\right) = u_z^{(2)}\left(x, y, 0\right)
\end{aligned} \tag{3-10}$$

where *h* is the thickness of the layer; and the superscripts (1) and (2) represents the layer and the substrate, respectively.

Yu *et al.* assumed that all the interfaces between the layers are fully bonded, extended the contact model to a surface with *N* layers [202], and explored the maximum von Mises

stress problem of the trilayered surface contact [252]. In these models, the elastic modulus of the material of each layer is constant.

But for real layered material systems such as coatings, which affect the transfer of interfacial force, displacement, heat and electromagnetic effects of the material, generally, the interface between layers may not be perfectly bonded [253]. Specifically, material defects may appear inside the material or in the manufacturing process, such as dislocation, micro-cracks, voids and de-bonding.

Therefore, in recent years, researchers have developed many elastic contact models with different imperfect bonding interfaces or layered surfaces with embedded inclusions. Assuming that Equ.(3-9) has a simple linear relationship, in addition to fully bonded interface [202, 252, 254, 255], there are also linear spring-like interface [256-261], dislocation-like interface [262-264], force-like interface [264, 265], frictionless contact interface [264, 266-268].

The linear spring-like interface can be considered as a thin layer that allows continuous traction across the interface with discontinuous displacements [251], but the displacement and the traction on both sides of the interface has a proportional relationship. However, when the thickness of the middle film layer disappears, the traction force cannot penetrate physically [269]. Dislocation-like interface can satisfy that when the traction force is continuous, the displacement on the interface can be discontinuous and has a proportional relationship between the displacements on both sides. Contrary to the dislocation-like interface, the force-like interface has continuous displacement on the interface, but the traction force can be discontinuous, or it can be defined as a proportional relationship. For frictionless contact interface, normal displacement as well as the normal traction are continuous only, but the tangential traction at the interface is zero.

The layered contact models with different force and displacement conditions at the interfaces and variable material properties of the layers provide the flexible theory and numerical methods for contact calculation under the condition of different coating materials or boundary films on the surface, which establishes a good mechanical foundation for subsequent friction and wear calculations.

3.5.3 *Fast Fourier Transform (FFT)*

In contact analysis, the analytic relationship between the elastic response of objects, such as displacement or stress, and the excitation, such as normal or traction force on the surface, is generally described in the form of convolution integral (3-11) [244]. If a complex spatial problem is mapped to the frequency domain, the solution can become much simpler, so the fast Fourier transform (FFT) method is applied to improve the computational efficiency.

$$\left(\bar{u}_z\right)_l = \frac{1}{\pi E^*} \iint_{\Omega} \frac{p\left(x', y'\right) dx' dy'}{\sqrt{\left(x' - x\right)^2 + \left(y' - y\right)^2}} \tag{3-11}$$

Ju and Farris first applied FFT to the solution of contact mechanics. They used spectrum analysis instead of continuous integral transformation, which greatly improved the computational efficiency [270]. In the simulation of the layered elastic contact model, O'Sullivan and King [223] directly used the Papkovich-Neuber (P-N) potentials in the frequency domain and the corresponding boundary conditions to solve the unknown constants in the linear equations of displacement and stress. Then, the displacement and stress were calculated by numerical inverse fast Fourier calculation because the closed equation was explicitly deduced. Nogi and Kato [245] used FFT and CGM algorithm to apply the solution of O'Sullivan and King's explicit frequency response functions to the contact of a single-layer surface with roughness. In the recurrence equations of CGM, the influence coefficient matrix is calculated by the explicit frequency response functions, and then it is transformed to the spatial domain by inverse FFT, thereby entering the iterative loop of CGM. Cai and Bhushan [249] and Yu *et al.* [252] used the same methods to calculate the contact problems of the trilayered or double-coated materials with rough surfaces.

Although the FFT method can speed up the computational efficiency, it is reported that there will be errors at the boundary of the computational domain, which is called periodic error. In order to control the error in a reasonable range, values close to the boundary need to be discarded [270]. And the size of the calculated physical domain may need to be expanded to 5 [270] or 8 [271] times the size of the target domain, which will increase the computing time. FFT requires the transformed object to have periodicity, but most of the rough surface is random.

Therefore, many researchers have investigated the sources of errors in the FFT method and provided reasonable solutions. Polonsky and Keer [247, 272] studied the periodic error related to FFT and proposed a hybrid algorithm that uses multi-level multi-summation (MLMS) technology for periodic correction. Liu *et al.* [272] proposed a discrete-convolution and fast Fourier transform (DC-FFT) algorithm, which completely avoided any additional errors other than the discretisation error, and proved to be an effective tool in solving the point contact problem without periodic errors. In the DC-FFT method, the linear convolution in the contact problem needs to be discretised into a cyclic convolution, in which the methods of zero-padding and wrap-around order [273] are needed, as shown in Fig. 3-14.

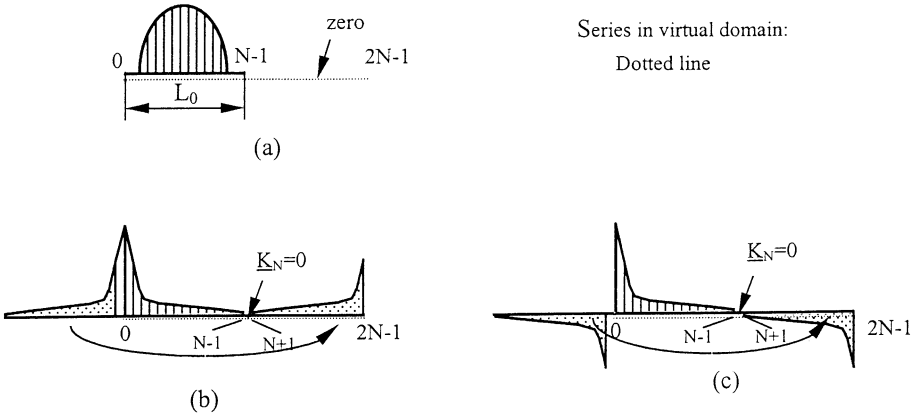

Fig. 3-14 Diagrams of zero-padding and wrap-around order: a) pressure distribution, b) and c) are the influence coefficients for normal and tangential pressure, respectively [272].

Liu and Wang [274] proposed two paths using DC-FFT. Since the relationship between the load and response of an elastic body can be correlated with Green's functions, frequency response functions (FRFs) or influence coefficients (ICs). When Green's function is known, the solution path is DC-FFT→ICs→Green's function, while when the FRF is known, the solution path is: FFT→ICs→conversion.

In the layered contact algorithm, explicit expressions of FRFs can be directly established for both the displacement field and the stress field, which reduces a lot of numerical calculations. Theoretically, FRFs with any number of layers can be solved by the following two steps [202]: 1) use *P-N* potentials and boundary conditions to establish a linear equation system, and 2) solve the unknown coefficients of the equation sets to obtain potential functions or FRFs, which corresponds to the influence coefficient matrix.

Then, the DC-FFT technology can be used to obtain the displacement or stress distribution in the spatial domain.

3.6 *Simulation in Interfacial Reactions and Wear*

Contact mechanics is the mechanical basis of the boundary lubrication model. By solving the contact model of the homogeneous or multilayered material, the surface pressure and elastic/plastic deformation, as well as the stress distribution of the elastic body can be obtained. However, in boundary lubrication modelling, in addition to the elastic/plastic contact between two surfaces, the main focus is on the tribological phenomena related to friction and wear, as well as the interactions between lubricant additives and the surfaces.

Simulations can explore some of the influence factors of tribological phenomena based on theory, such as surface roughness, mechanical properties, tribofilm thickness, formation and removal rate, and can also study the mechanisms of friction and wear from the perspective of atoms/molecules. The following mainly introduces several models for simulating the growth and removal of ZDDP tribofilm and wear models.

3.6.1 *Models for Tribofilm Growth and Removal*

ZDDP is recognised as an excellent antiwear additive. Through experimental research, it is found that its antiwear performance is mainly derived from the tribofilm formation [10], which is a balanced process of growth and removal [48-51]. In addition, many studies have shown that the physical and chemical process of tribofilm formation is related to both temperature and stress and it has been proved in recent years that it has the characteristics of stress-assisted thermal reaction, so many models of tribochemistry were developed based on it [20, 50, 52, 53, 179, 275].

In microscopic experiments, Atomic Force Microscope (AFM) can be used as an in-situ tribometer that when the tip contacts or slides on a steel substrate immersed in base oil containing ZDDP, tribofilm growth and the reaction kinetics based on single asperity can be analysed [52, 53]. In macroscopic experiments, by using the 3D Spacer Layer Imaging methods (SLIM), ZDDP tribofilm thickness can be measured in-situ under different conditions such as temperature, load, speed and the slide-to-roll ratio [20, 48, 111, 276]. It also provides important parameters for developing the tribofilm formation model,

which is closer to engineering applications. The following sections introduce several models of tribofilm growth and removal.

3.6.1.1 *Diffusion Model*

So and Lin [17] used the diffusion model to simulate the chemical reaction process of ZDDP. Because the chemical reaction of ZDDP tribofilm is very complicated, and the chemical composition is not easy to identify, the physical methods are used to identify the elements in tribofilm, and the atomic concentration is used to correlate with tribofilm thickness. It treated all diffusion substances containing P, S, O, Zn as a whole, and the diffusion of individual species was not considered. This model is based on a special solution to the moving boundary diffusion problem [277]. The coordinate system of the reaction film thickness X is shown in Fig. 3-15, and its expression is :

$$X = \left[\frac{2D_d C(0)t}{W_m \rho} \right]^{\frac{1}{2}} \qquad \textbf{(3-12)}$$

where D_d is diffusion coefficient; $C(0)$ is the concentration of the diffusion compounds at $x = 0$ and time t; W_m is the mass fraction of the diffusion compounds formed with the metal; ρ is the density of the compounds.

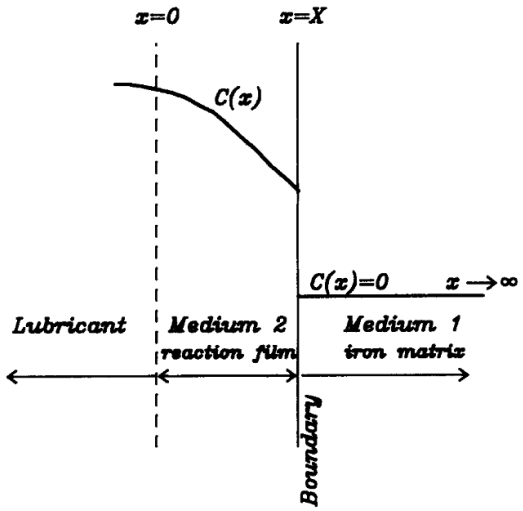

Fig. 3-15 Reaction coordinate system of the film thickness *X* [17].

It is indicated in the experiments that the chemical reactions of ZDDP on the iron substrate are affected by many parameters such as temperatures, kinds and concentrations of ZDDP, and the surface characteristics, so the Equ. (3-12) is modified by

$$X = K_c C_r \cdot e^{-\left(\frac{Q}{RT}\right)} K_d t^{\frac{1}{2}} \quad \textbf{(3-13)}$$

in which K_c is a constant related to concentrations and kinds of ZDDP; C_r is a parameter of surface characteristics include surface roughness, flow stress and hardness, etc.; Q represents the activation energy of ZDDP; R and T represent the gas constant and absolute temperature, respectively; $K_d = \left[\frac{2D_d C(0)}{W_m \rho}\right]^{\frac{1}{2}}$.

There are four unknown parameters in it, namely K_c, C_r, K_d and Q. In order to simplify the curve-fitting of the experimental results, an overall parameter K_0 is first used to represent the summary of all individual effects on tribofilm, so Equ. (3-13) can be transcribed as

$$X = K_0 t^{\frac{1}{2}} \quad \textbf{(3-14)}$$

The tribofilm thickness is experimentally obtained by the depth measurement of the Auger electron spectroscope. At a contact pressure of 22.22 MPa, the relationship between K_0 and temperature T is fitted as follows.

$$K_0 = -7.07\times10^{-12}T^2 + 6.95\times10^{-9}T - 1.31\times10^{-6} \quad \textbf{(3-15)}$$

Subsequently, methods to determine other parameters C_r, K_d and Q, and the growth rate of the tribofilm was also given separately.

The critical thickness calculated by this model or the elastic model was larger than the measured value by experiments, which may be because the gel-like layer and chemisorption on the tribofilm were not included.

3.6.1.2 *The Model Based on Morphology*

Fujita and Spikes [49] used SLIM to study the growth curves of primary and second ZDDP tribofilm at different temperatures. Then the oil was changed to contain only dispersant additives to study the removal process of ZDDP tribofilm. According to the

experimental results, two different tribofilm formation processes were proposed, as shown in Fig. 3-16.

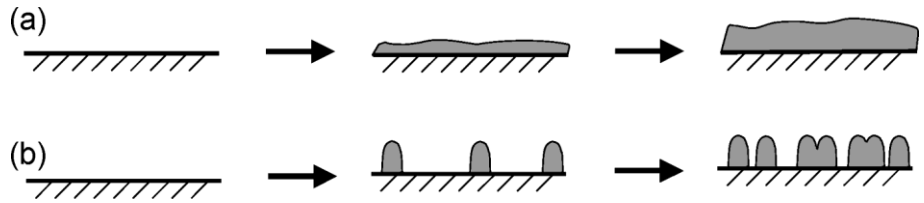

Fig. 3-16 Schematic Diagram of tribofilm growth: a) ascensive thickening of evenly distributed tribofilm and b) ascensive coverage of free surfaces [49].

According to the possible formation process, four theoretical coverage models were proposed to fit the growth curve of primary ZDDP tribofilm such as 1) proportional area model, 2) island enlargement model, 3) combined model of overall thin tribofilm and island, and 4) combined model of the proportional area and height growth of the island. Those models can also be combined to capture more growth schemes. However, one of those is sufficient to describe most of the characteristics of the tribofilm growth curve.

In the "Proportional Area Model", it is assumed that the formation rate of the ZDDP pad is proportional to the surface area covered by the unreacted island, and the formation rate is

$$\frac{dX}{dt} = k_1(1 - X) \qquad \textbf{(3-16)}$$

where X is the fraction that has been covered by tribofilm, and k_1 is the rate constant.

In the removal part of tribofilm, the removal rate is assumed to be proportional to the tribofilm coverage or the tribofilm thickness. When the existing fracture of X_o is not removed, a simple power relationship can be expressed as

$$\frac{dX}{dt} = -k_5(X - X_o)^n \qquad \textbf{(3-17)}$$

where k_5 is the rate constant.

Although secondary ZDDP grows to the maximum film thickness faster than primary ZDDP, the film thickness will decrease in the further rubbing process, so its kinetics of

formation should consider the combination of tribofilm formation and removal. For example, by combining the model of growth (3-16) and removal (3-17) and integration, the rate of net tribofilm formation can be expressed as

$$\left(\frac{dX}{dt}\right)_{net} = k_1(1-X) - k_5 X^4 \quad \textbf{(3-18)}$$

or

$$\left(\frac{dh_{mean}}{dt}\right)_{net} = h_{mx}\left(k_1(1-X) - k_5 X^4\right) \quad \textbf{(3-19)}$$

Where h_{mx} is the thickness on the covered area,

It can be obtained in tribofilm's net growth model (3-19) that the film thickness in a steady state mainly depends on the ratio between the growth rate constant k_1 and the removal rate constant k_5, namely k_1 / k_5. In addition, it can be obtained from the experimental results that there is an induction period during the initial growth of ZDDP [49, 278, 279]. During this period, a thin, uniform film was produced instead of the later island. Therefore, if this induction period is to be included in the model, the simple form is limited.

Since the growth rate constant k_1 has a weak dependence on temperature and ZDDP type, but the square root of the concentration of ZDDP increases approximately, which may indicate that the formation of the island depends on contact activation rather than thermal activation. This model provides a good reference for describing the growth and removal process of ZDDP tribofilm.

3.6.1.3 *The Model Based on Kinetics of Mechano-activation*

Ghanbarzadeh *et al.* [51] proposed a mechano-chemical model to describe tribofilm growth and removal and correlate it with wear, based on MTM-SLIM results. This model is developed based on the studies of Bulgarevich *et al.* [275], who use active collision theory and activated complex theory to express the general kinetic equations that can be used for mechanically activated tribochemical reactions under boundary lubrication conditions. The expression of the tribochemical reaction rate is as follows:

$$k_{tribo-thermo} = \frac{x_{tribo}}{x_{thermo}} k_{thermo} \quad \textbf{(3-20)}$$

in which x_{tribo} is the influence of mechanical activation and $x_{thermo} = e^{(\Delta E/RT)}$ is the influence of temperature activation, which respectively illustrate the influence of mechanical and temperature on the rate of inducing tribochemical reaction.

$$k_{thermo} = \frac{k_B T}{h_P} e^{(\Delta E/RT)} \quad \textbf{(3-21)}$$

where k_B and h_P represent Boltzmann and Plank constants, respectively; T is absolute temperature; ΔE is activation energy; R is gas constant.

Substituting the expressions of x_{thermo} and k_{thermo} into Equ. (3-20), the simplified tribochemical reaction rate is

$$k_{tribo-thermo} = \frac{k_B T}{h_P} x_{tribo} \quad \textbf{(3-22)}$$

Andersson *et al.* developed a tribofilm growth model based on the Arrhenius equation [280]. The assumption is that the formation process of tribofilm is assumed that substance *A* (lubricant additive) and substance *B* (steel) undergo a chemical reaction to produce substance *C* (tribofilm). Combined with the reaction rate $k_{tribo-thermo}$, the formation rate of substance *C* is:

$$\frac{\partial C}{\partial t} = k_{tribo-thermo} AB \quad \textbf{(3-23)}$$

where *A*, *B*, and *C* are the concentration of the two reactants and the product, respectively, in which *B* is sufficient to provide a chemical reaction, and only *A* limits the reaction rate. Therefore, the maximum film thickness depends on the concentration of substance *A*, expressed as

$$A = A_1(h_{\max} - h) \quad \textbf{(3-24)}$$

Assuming that the thickness of the tribofilm is related to the concentration of the substance *C*. After the equations (3-22) and (3-24) are substituted into the equation (3-23), the growth rate of the tribofilm is

$$\frac{\partial h}{\partial t} = C_2(h_{\max} - h)\frac{k_B T}{h_P} x_{tribo} \quad \textbf{(3-25)}$$

After integrating over time *t*,

$$h = h_{\max}(1 - e^{-\left(\frac{k_B T}{h_P} x_{tribo}\right)t}) \quad \textbf{(3-26)}$$

Assuming that the removal model of the tribofilm is an exponential form, the net tribofilm growth is

$$h_{net} = h_{\max}(1 - e^{-\left(\frac{k_B T}{h_P} x_{tribo}\right)t}) - C_3(1 - e^{-C_4 t}) \quad \textbf{(3-27)}$$

where C_3 and C_4 are the removal constants.

The Equ. (3-27) is used to fit the experimental results by SLIM to determine the unknowns x_{tribo}, C_3 and C_4 at different temperatures. After combining the calculation with the contact model and the wear model, the calculation results are consistent with the experiment results. The evolution of tribofilm thickness and surface roughness under different SRR conditions were simulated as well.

3.6.1.4 *Single Asperity Model*

Chemical reactions can be driven by mechanical stress, and the reaction products are affected by the magnitude and direction of the applied force. By using AFM equipment, it is possible to quantitatively measure the stress-driven reaction kinetics and to explore the reaction mechanism from the atomic scale. In principle, it can also be extended to any combination of different tip materials, substrate and chemical groups [281].

Gosvami *et al.* [52] used AFM to study the morphology and growth volume of tribofilm under different temperatures and pressures, and found that the growth process of the tribofilm is divided into two stages: 1) linear growth stage (zero-order reaction), and the growth stage at *n*-th order power-law function form (n = 0.22). The morphology and volume of the tribofilm are strongly affected by the contact pressure, and this growth rate fits well with the stress-activated Arrhenius model.

$$\Gamma_{growth\ rate} = Ae^{-\left(\frac{\Delta G_{act}}{k_B T}\right)} \tag{3-28}$$

where A is the coefficient related to the molar volume and effective frequency of the growth product; k_B is Boltzmann's constant; T is the absolute temperature; ΔG_{act} is the free activation energy assumed to be related to stress, expressed as

$$\Delta G_{act} = \Delta U_{act} - \sigma \Delta V_{act} \tag{3-29}$$

in which ΔU_{act} is the internal activation energy; σ is the contact pressure; ΔV_{act} is the activated volume [282].

The growth results of the tribofilm under different pressures are shown in Fig. 3-17. After curve-fitting by Equ. (3-28), $\Delta U_{act} = 0.8 \pm 0.2$ eV and $\Delta V_{act} = 3.8 \pm 1.2$ Å^3 are obtained respectively. This result is further consistent with the growth results of the tribofilm at different temperatures, which verifies that the formation kinetics of ZDDP tribofilm on silicon conforms to the stress-activated thermal model.

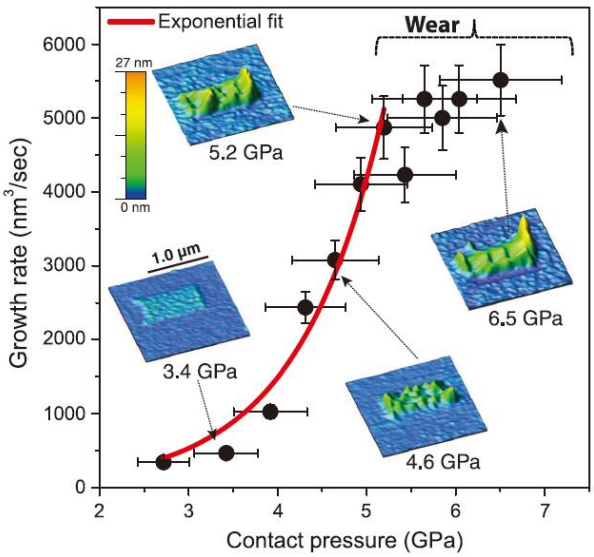

Fig. 3-17 The growth rate of tribofilm at different contact pressure by AFM [52].

Dorgham *et al.* [53] also used AFM to study the growth kinetics and reaction order of ZDDP and ashless DDP driven by different temperatures and pressures on the AISI52100 steel substrate. The model (3-28) is applied for analysis, but the coefficient A is assumed to be the frequency at which the reactant molecule across the energy barrier along the

reaction coordinate. The activation energy term ΔG_{act} is represented by $E_a(P)$, and different expansion formulas are used as follows.

$$E_a(P) = \left(E_0 - \mu P A_r \Delta x + \frac{\mu^2 P^2 A_r^2}{2}(\xi_I - \xi_T) \right)\left(1 + \sqrt{\frac{\Delta x}{v t_c}} \right) \quad \textbf{(3-30)}$$

where E_0 is the nominal activation energy when no contact pressure *P* is applied; A_r is the effective area of the reactant; Δx is the activation length from 0 to the transition state along the reaction coordinate, which is further calculated as 0.2 Å and 0.8 Å for ZDDP and DDP, respectively; ξ_I and ξ_T are the curvatures of the initial state and the transition state along with the reaction coordinate, respectively, and $\left(1 + \sqrt{\frac{\Delta x}{v t_c}} \right)$ represents the term of the applied external force.

It is suggested that the entire tribofilm growth data can be fitted with a single exponential rate, which is different from the two-stage fitting suggested in Gosvami *et al*.'s work. However, for comparison, the two-stage fitted reaction order was also analysed and found that at the beginning of the reaction, it is an approximate zero-order reaction of $n = 0.073 \pm 0.1$, while it can approximately satisfy the first-order reaction of $n = 0.71 \pm 0.14$ in the rapid growth period. Nevertheless, the entire data set can still be fitted with first-order reaction kinetics.

The single asperity model can well discuss the influence of various parameters on the chemical reaction mechanism of tribofilm growth. However, for macroscopic experiments and applications, due to differences in time and space scales, some parameters related to activation energy cannot be easily obtained through macroscopic experiments. Therefore, the application of the single asperity model on the macro-scale needs further exploration.

3.6.1.5 *Mass Balance Model*

Dominguez-Garcia *et al.* [283] proposed a tribofilm growth and removal model based on mass balance. The entire lubrication system is assumed to be a constant volume lubrication system with no inlet and outlet, in which the mass balance of the tribofilm only considers the accumulation, production and consumption of three parts. The whole

reaction process is that lubricant precursors *A* (additives) are deposited on the surface, and the substances *F* (tribofilm) is formed after the reaction, which is then converted into waste products *B* when it is removed. The mass of deposition is the mass of tribofilm.

First, consider the chemical conversion rate of substance *A* into substance *F*. The net deposited mass of substance *F* is equal to the generation rate r_{cF} of deposited mass due to chemical reaction plus the consumption rate r_{mF} of deposited mass by mechanical removal.

$$\frac{dm_F}{dt} = r_{cF} + r_{mF} \tag{3-31}$$

In addition, the mass balance of *A* and *B* need to be considered.

$$\frac{dm_A}{dt} = r_{qA} \tag{3-32}$$

$$\frac{dm_B}{dt} = r_{qB} \tag{3-33}$$

where r_{qA} and r_{qB} represent the conversion rates of A→F and F→B, respectively.

Based on the assumption that the chemical reaction of the lubrication system is pseudo-first-order kinetics [284], the constant variables of the reaction system under special conditions can be combined into the apparent kinetic constant [284-287]. Therefore, the apparent kinetic constant of the tribofilm is set as k_A, which includes the influence of temperature, the concentration of the lubricant additives, tribological contributions, and even catalytic effect.

Therefore, the growth rate r_{cF} of tribofilm *F* and the consumption rate r_{cA} of lubricant precursors *A* are respectively expressed as

$$r_{cF} = k_A m_A \tag{3-34}$$

$$r_{cA} = -k_A m_A \tag{3-35}$$

Next, consider the mechanical rate between the deposited film *F* and the removal of the product *B*. The mechanical removal rate r_{mF} of the deposited film *F* and the production rate r_{mB} of waste product *B* are respectively expressed as

$$r_{mF} = \left(\frac{d\chi}{dt}\right)_m \frac{dV_f}{d\chi}\rho_f \tag{3-36}$$

$$r_{mB} = -\left(\frac{d\chi}{dt}\right)_m \frac{dV_f}{d\chi}\rho_f \tag{3-37}$$

where $\left(\frac{d\chi}{dt}\right)_m$ is the removal of the tribofilm thickness over time *t* related to the mass; $\frac{dV_f}{d\chi}$ is the change of the tribofilm volume V_f with the thickness χ; ρ_f is the density of the deposited tribofilm.

Finally, the growth rate $\frac{d\chi}{dt}$ of the overall tribofilm is the sum of the thickness change $\left(\frac{d\chi}{dt}\right)_c$ related to the chemical deposition mass and the thickness change $\left(\frac{d\chi}{dt}\right)_m$ related to mechanical removal, that is

$$\frac{d\chi}{dt} = \left(\frac{d\chi}{dt}\right)_c + \left(\frac{d\chi}{dt}\right)_m \tag{3-38}$$

in which

$\left(\frac{d\chi}{dt}\right)_c = \frac{r_{cF}}{\rho_f}$, and r_{cF} is the chemical formation rate of tribofilm.

$\left(\frac{d\chi}{dt}\right)_m = \left(\frac{d\chi}{dt}\right)_X \nu(\chi)$, and $\left(\frac{d\chi}{dt}\right)_X$ is the removal rate constant of tribofilm, $\nu(\chi)$ is the coverage fraction of tribofilm on the surface, which is related to the roughness of the substrate.

The model can evaluate and predict the dynamics of the thickness profiles of the tribofilm through the mass balance of the tribofilm. In addition, this idea is also extended to calculate the dynamics of friction coefficient and wear.

3.6.2 *Wear Models*

The wear process is not a simple mechanical process, it is often accompanied by physical and chemical reactions between mechanical components. Meng and Ludema [288] investigated 182 wear models, summarised the contents and usability of most wear models, and gave certain suggestions.

The wear model is derived from solid mechanics, including material properties, thermodynamics, engineering parameters, etc. It can be divided into three categories: empirical equation [289, 290], model based on contact mechanics [291] and model based on material failure mechanism [292-295]. The empirical equation is directly established by the different conditions in the tests and is usually valid within the test range. Models based on contact mechanics generally assume a simple relationship between a system model and working conditions, usually including material properties. For local contact, it may also contain surface topography information. Archard's wear equation is the one based on contact mechanics. Wear modelling based on material failure mechanism is more inclined to consider material fracture, flow, strain and other phenomena.

Because boundary lubrication modelling in this study is based on the calculation of contact mechanics, the follow-up mainly focuses on the Archard wear equation and introduces the modelling mechanisms of other wear models.

3.6.2.1 *Archard's Wear Equation*

Archard's wear equation is one of the most widely used equations in wear calculation [68]. This equation has been developed by Holm [296] based on the sliding electrical contact, and then Archard has given the expression of general adhesive sliding wear. The equation shows that the wear is proportional to the load L and the sliding distance S, and has no relationship with the nominal contact area, which is consistent with Amonton's laws of friction.

Under the non-lubricated condition, one surface slides on another surface, and the wear volume is expressed as:

$$V_{\text{wear}} = K\frac{LS}{H} \tag{3-39}$$

where H is the hardness or shear strength of the softer material; K is the wear coefficient, which is a dimensionless scale coefficient that can be determined by different sliding conditions, usually including the influence of other factors such as surface topography, pollution, material microstructure, surface chemical substance formation and abrasive particle formation. For mild wear, the value of K is generally between $10^{-8} \sim 10^{-4}$. For severe wear, the K value is usually $10^{-4} \sim 10^{-2}$.

From a design point of view, the depth of wear has attracted more attention, which affects the durability and functionality of a frictional contact. For plastic-type contact, the rate of wear depth h_{wear} changing with time is

$$\frac{dh_{wear}}{dt} = \frac{kpv}{H} \tag{3-40}$$

in which p is a positive pressure and v is the sliding speed.

For abrasive wear, there are hard asperity or abrasive particles that cause surface plastic deformation or material fracture in the sliding process, so the wear rate is usually 2 to 3 orders of magnitude higher than that of adhesive wear. Many experiments have shown that the Archard wear equation (3-39) is also applicable to abrasive wear conditions, including two-body and three-body abrasive wear, and the general wear coefficient is between $10^{-6} \sim 10^{-1}$.

For the wear model with tribochemistry, the calculation of wear can also directly use Archard wear equation or related forms. But more importantly, it is necessary to link the wear coefficient with the parameters related to tribochemical reaction, such as tribofilm thickness and amount of iron.

3.6.2.2 *Correlation to Tribofilm Thickness*

Ghanbarzadeh *et al.* [179] proposed a linear relationship between the wear coefficient *K* in Archard's wear equation and the tribofilm thickness, as described in Fig. 3-18.

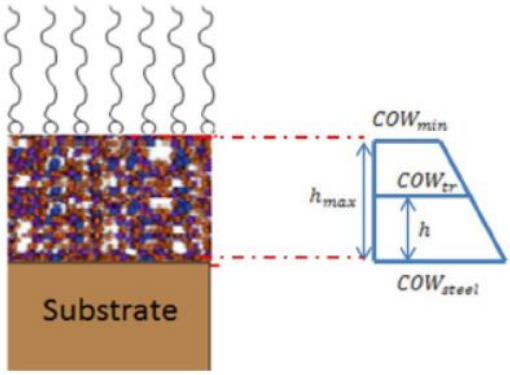

Fig. 3-18 Schematic diagram of the relationship between tribofilm thickness and wear coefficient [179].

When there is no tribofilm, the wear rate is the largest, which is the wear rate of the steel substrate CoW_{steel}. When the tribofilm reaches the maximum thickness, the wear rate is the smallest, namely $CoW_{\min}$. When the tribofilm grows to any thickness h $(0 < h < h_{\max})$, the wear rate can be expressed as

$$CoW_{tr} = CoW_{steel} - (CoW_{steel} - CoW_{\min})\frac{h}{h_{\max}} \quad \textbf{(3-41)}$$

Combining the Archard wear equation and the tribofilm formation model (3-27), the evolution of the wear depth for ZDDP tribofilm at different temperatures is simulated, as shown in Fig. 3-19, which is consistent with the wear results measured by the white light interferometry.

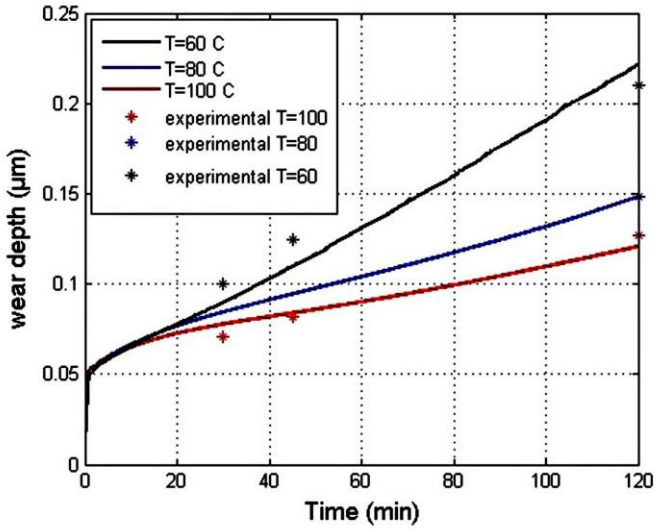

Fig. 3-19 The comparisons of simulation and experimental results of wear under different temperatures for ZDDP in the oil [179].

Akchurin and Bosman [50] used a concentration parameter related to the tribofilm thickness to calculate the wear of the substrate material. Although mechanical removal occurs on the surface of the tribofilm, due to the diffusion of Fe in the substrate, abrasion will also occur in the substrate. This amount of wear decreases as the thickness increases. The relationship between the concentration $C(h)$ of the substrate material and the tribofilm thickness *h* is expressed as:

$$C(h) = e^{-C_1 h} \tag{3-42}$$

where C_1 is a constant.

The wear depth of the substrate material is expressed as

$$h_w^m = \int_0^t C(h)\left(\frac{\partial h}{\partial t}\right)_w dt \tag{3-43}$$

where $\left(\frac{\partial h}{\partial t}\right)_w$ is the removal rate of the tribofilm, which is assumed to have a linear relationship with the tribofilm thickness *h*.

This model calculated and compared the modelling work of Ghanbarzadeh *et al.* (Fig. 3-19). It shows that the wear depth decreases as the temperature increases (and the

tribofilm increases). At the same time, the concentration of the substrate material decreases as the temperature increases, so the wear amount is maximum at 60 ℃.

3.6.2.3 *Correlation to the Amount of Iron*

Bosman and Schipper [178] related the wear coefficient to the amount of iron in tribofilm. The depth profile of the main elements (C, O, Fe, Ni, P, S, Ca, Zn, Mo and Co) in the tribofilm and substrate were analysed XPS, as shown in Fig. 3-20a. Then, the volumetric percentage of Fe atoms in the tribofilm was calculated using the relative atomic radius, see Fig. 3-20b.

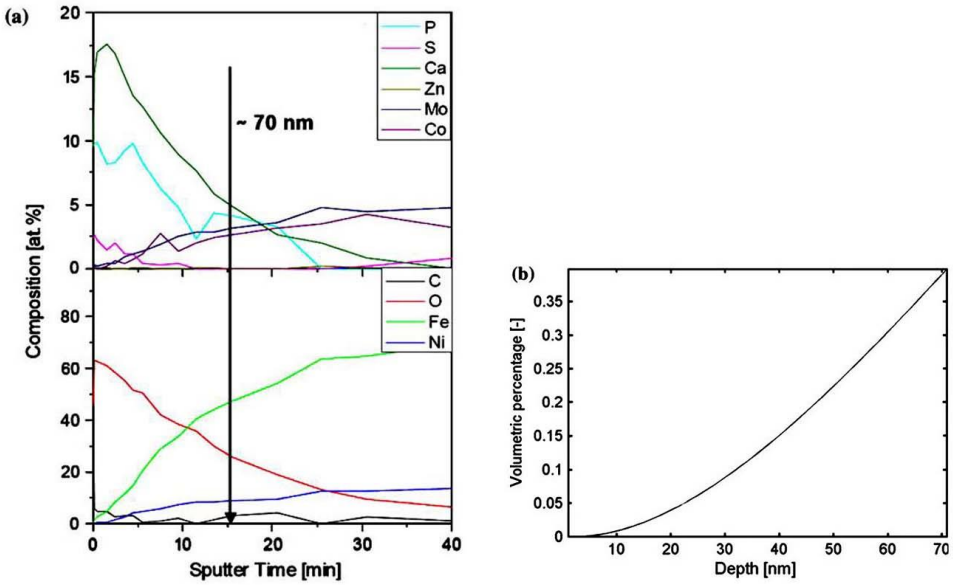

Fig. 3-20 (a) XPS depth profiles of atomic percentages of different elements in tribofilm and (b) the volumetric percentage of iron as the function of the depth [178].

When the depth is larger, it means closer to the substrate. The polynomial function is used to fit the curve in Fig. 3-20b, and then the formula of wear rate can be obtained.

$$W_{perc}(\delta) = \frac{4.5\times10^{19}\delta^4 - 2.83\times10^{13}\delta^3 + 1.75\times10^{-7}\delta^2 + 0.001\delta}{h_{balance}} \quad \textbf{(3-44)}$$

where $\delta = \varepsilon^l_{plzz} h_{balance}$ is the plastic penetration depth; $h_{balance}$ is the thickness when the tribofilm reaches equilibrium; and ε^l_{plzz} is the plastic strain.

In a wear cycle, a characteristic wear length l_c is defined, which can represent an average micro-contact length that produces wear W_{wear} in the sliding direction. The dimensionless wear loss coefficient K is

$$K_{wear}(x,y)=\frac{W_{wear}}{\Delta x\Delta y l_c}=\frac{W_{perc}(\varepsilon_{plzz}^{l}h_{balance})\varepsilon_{plzz}^{l}h_{balance}}{l_c} \tag{3-45}$$

In order to prove the numerical validity of the model, a specific wear rate is derived from Equ. (3-45), which is constant in each sliding cycle.

$$k(x,y)=\frac{K(x,y)}{p(x,y)} \tag{3-46}$$

Therefore, according to Archard wear law, for a sliding incremental step Δs, the increase in wear depth [297] is

$$\Delta h(x,y)=k(x,y)\,p(x,y)\Delta s=K_{wear}(x,y)\Delta s \tag{3-47}$$

The verification of the model was achieved through two groups of tests. The first is the contact between the smooth ball and the disc under boundary lubrication conditions, and the second is the contact between a barrel-shaped specimen and the plate for the elliptical contact. The simulation results are shown in Fig. 3-21.

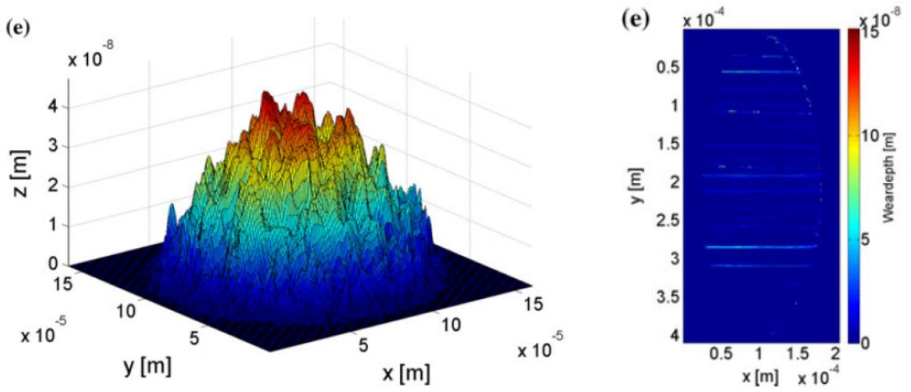

(a) **(b)**

Fig. 3-21 Mild wear simulation results: (a) ball-on-disc and (b) roller-on-disc [178].

Specific wear rate is used to verify the effectiveness of the model, and the result is consistent with the value obtained in the experiment. Therefore, it can be used to characterise the wear under mild wear.

3.6.2.4 *Degradation-Entropy Model*

Bryant *et al.* [298] developed a thermodynamic characterisation of degradation kinetics and a theorem linking entropy generation to irreversible degradation. Regarding sliding wear as a degradation process, the expression of sliding wear rate derived has the same form as the Archard wear equation.

In order to simplify the description, the specific theory and derivation process are not shown. According to the degradation analysis procedure provided in the paper, the change rate of the wear volume w_v with time t is expressed as

$$\frac{dw_v}{dt} = YJ = \frac{B\mu}{T} L \frac{dx}{dt} \quad \textbf{(3-48)}$$

where μ is the friction coefficient; L is the normal load; T is the contact temperature; dx/dt is the sliding speed; and B is a degradation coefficient, which can be measured.

Compared with Archard wear equation (3-39), the expression of wear coefficient K is

$$K = \frac{B\mu H}{T} \quad \textbf{(3-49)}$$

Doelling *et al.* [299] used a large number of wear experiments to plot the function relationship between normalised wear and normalised entropy, where the slope is the coefficient B. Then the wear rate is calculated according to Equ. (3-49) is 1.01×10^{-4}. This is consistent with the wear rate of 1×10^{-4} calculated by Rabinowicz [300] through the Archard wear equation. This also shows that wear, as a kind of material degradation, is closely related to entropy. Conversely, the known relationship between entropy and temperature can be used to predict material degradation - wear.

3.7 *Summary of Literature Reviews*

3.7.1 *Summary of Literature Review*

This chapter first reviews the relevant experimental research on lubricant additives, including several aspects: 1) The tribofilm formation mechanism, anti-wear mechanism, mechanical properties, wear properties and rheological properties of ZDDP as an anti-

wear additive; 2) Detergents have cleaning and anti-wear effects when used alone, but when ZDDP is used in combination, the interactions or competitions between the two can cause an antagonistic effect on the anti-wear performance; and 3) The mixed oil of dispersants and ZDDP may improve the dispersibility, but due to the formation of complexes between the two, the reaction between ZDDP and the iron substrate is hindered, so the anti-wear performance is negatively affected. Although the wear mechanism of FFO cannot be predicted by the combination of additives, understanding the interaction between various additives can guide the experimental study of the wear mechanism of FFO.

The second part of the chapter mainly reviews the theory and numerical methods related to the contact mechanics of homogeneous and layered surfaces, interface reaction and wear equations in the boundary lubrication model. In the existing multi-scale modelling system, the contact and stress state between the components can be directly simulated in the macroscopic view by FEM for instance, while the MD or DFT method can be used to directly calculate the motions between molecules or atoms to explain the mechanism of the tribological phenomenon in the nanoscopic view. For simulating the interface reactions and wear under boundary lubrication conditions, the commonly used calculation framework is to start from the rough surfaces, use different contact mechanics theories and numerical methods to calculate the elastic/plastic pressure distribution and displacement, and then combine the experimental results of interface reaction and wear equations, which can be used to predict the tribofilm growth and wear.

3.7.2 *Knowledge Gaps*

In general, the effect of the interaction between additives on wear is affected by the type of additive, its concentration, and external working conditions such as temperature and load. For commercial fully formulated oil, the additive formula has been designed and optimised according to specific application conditions. For the users of FFO, it is necessary to summarise its wear mechanism and prediction. Although there have been many experimental studies on FFO and its related additives, it is difficult to summarise its wear trends because of the diversity of its formulations. It is worthwhile for FFO to study the growth and wear processes of FFO tribofilm simultaneously because of the competition between the different additives and the potential reaction priority.

The formation of tribofilm will change the surface topography and mechanical properties, thus affecting the elastoplastic contact and stress state of the subsurface layer. Although the contact model of the rough surface is relatively mature, and many methods for calculating interface reaction and wear have been proposed, there are still many aspects to be improved.

In the contact calculation of rough surfaces, the influence of tribofilm is usually reflected in the surface topography and mechanical properties such as hardness of the contact interface, but the influence of tribofilm on the subsurface stress is less discussed. The problem of stress calculation can be solved by using layered contact models of rough surfaces, but in the author's limited knowledge, there are little research on the joint modelling of the layered contact model with the interface reaction and wear models.

In the calculation of interface reaction, because the growth of tribofilm is affected by the working conditions, theoretical and experimental methods are usually used to build models, such as the stress-activated Arrhenius model. At present, the research object is mainly a single additive such as ZDDP, and there is almost no discussion on the application of FFO. Among the wear models, the Archard wear model is one of the most widely used models. Its flexibility is mainly reflected in the change of wear coefficient K according to external factors such as working conditions or tribofilm thickness, and only a few of them reflect the influence of chemical compositions in tribofilm. Therefore, there is a lack of a wear calculation method that can be generalised to FFO.

Based on the gap in the existing research, the research objective of this project is to systematically study the wear mechanism of a commercial fully formulated oil containing commonly used additives by both experiments and modelling. In the experimental work, the FFO is considered as a lubrication system to investigate and summarise the general trends of the wear mechanism of FFO involving tribochemistry. In the modelling work, a universal wear calculation approach involving tribochemistry is developed for FFO with similar formulations and properties.

Chapter 4 Methodology for Experimental Procedure and Modelling Framework

This chapter introduces the methodology of the experimental works including materials, lubricants, test rigs for friction and wear tests and the equipment for chemical analysis. The experimental matrix and the parameters used are linked to the modelling work and described in detail.

4.1 *Materials and Lubricants*

4.1.1 *Materials*

The ball and disc samples are shown in Fig. 4-1. Both the ball and the disc are made of AISI52100 steel, in which the diameter of the ball is ¾ inch (~19.25mm) and the diameter of the disc is 46mm.

(a) ball sample **(b) disc sample**

Fig. 4-1 Images of ball and disc samples.

The roughness of both 5 balls and 5 discs have been analysed by Atomic Force Microscope (Bruker). The sampling results are listed in Table 4-1, where the average roughness of the ball and the disc are about 20 nm and 10 nm respectively.

Table 4-1 Roughness of MTM balls and discs, measured by AFM.

No. of Discs	**Disc - 1**	**Disc - 2**	**Disc - 3**	**Disc - 4**	**Disc - 5**	**Average**
Ra/ nm	8.9	7.6	6.6	7.0	8.6	7.7 ± 1
No. of Balls	**Ball - 1**	**Ball - 2**	**Ball - 3**	**Ball - 4**	**Ball - 5**	**Average**
Ra/ nm	22.1	10.5	21.3	30.0	6.7	18.1 ± 9.4

The hardness of discs is measured by Nanoindenter (Micro Materials). The four areas with 90-degree distribution have been measured, as shown in Fig. 4-2. Each area has 36 points with 30 μm intervals for both directions. The hardness for each disc is the average hardness of 36 x 4 points.

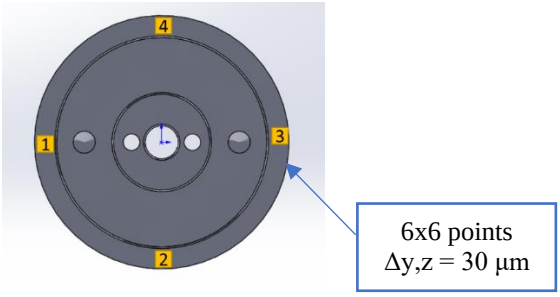

Fig. 4-2 Schematic diagram of sampling methods for hardness.

Both hardness and elastic modulus of five discs are 868 HV and 212 GPa, respectively, as listed in Table 4-2. The results of the samples are consistent well with the standard specifications of AISI52100 steel.

Table 4-2 Hardness results of five sampling discs.

No.	Disc - 1	Disc - 2	Disc - 3	Disc - 4	Disc - 5	Average
Hardness/HV	907	867	835	860	873	868
Elastic modulus/ GPa	215	211	204	212	218	212

4.1.2 *Lubricants*

A commercial Fully Formulated Oil (FFO) for hydraulic systems is the main lubricant used in the experiments and modelling work. Its main components are shown in Table 4-3, in which the base oil is mineral oil with kinetic viscosity of 36 mm/s at 40 ℃ and 5.9mm/s at 100 ℃; the main additives are the mixture of primary and secondary ZDDP with 0.08 wt.% P as the antiwear additive, the mixture of over-based calcium sulphonate and phenate with 0.38 wt.% Ca as the detergent and the succinimide as the dispersant. There are also antioxidants in the FFO, but their effects will not be discussed separately.

In addition, other lubricants used to test the influence of a single additive are summarised in Table 4-4. The concentration of each additive in the Base Oil (BO) is equivalent to the same concentration in the Fully Formulated Oil (FFO).

Table 4-3 Specification of the Fully Formulated Oil (FFO).

Base Oil	**Mineral Oil**	**Kinetic viscosity**	
		at 40 ℃	**at 100 ℃**
		36 mm/s	5.9 mm/s
Main Additives	**ZDDP**	Primary and Secondary (0.08 wt.% P)	
	Detergent	Over-based calcium sulphonate/phenate (0.38 wt.% Ca)	
	Dispersant	Succinimide	

Table 4-4 Other Lubricants.

Oil A (Base oil)	Mineral Oil
Oil B	BO + ZDDP
Oil C	BO + Detergent

*** The recipes of the additives are provided by the sponsor (Komatsu Ltd.).**

4.2 *Tribological Test Rigs*

4.2.1 *Mini Traction Machine (MTM)*

4.2.1.1 *Basic Principles*

Mini Traction Machine (PCS Instrument) is used in this project to test the friction coefficient and tribofilm thickness under different test conditions. The main reasons for choosing this instrument are as follows: (I) it can adjust the rotation speeds of the ball and the disc independently to achieve different sliding/rolling conditions, which can be adapted to the working conditions in industrial applications; and (II) the SLIM component can capture the formation process of tribofilm on the ball and provide the optical images for further thickness analysis, which has been widely used in many studies ZDDP [20, 111, 276, 301].

MTM is a ball-on-disc configuration, see in Fig. 4-3a. A 3/4 inch ball is loaded against the disc by a traction transducer, and then the traction force can be detected through the traction transducer and measured by the force sensor. An oil pot is used to create and replenish the lubricants in the contact during the tests, in which the heater is immersed in the lubricant and the temperatures can be detected from the pot or the lube. After setting up the test step through the built-in software, it can test the friction coefficient, Stribeck curve, etc.

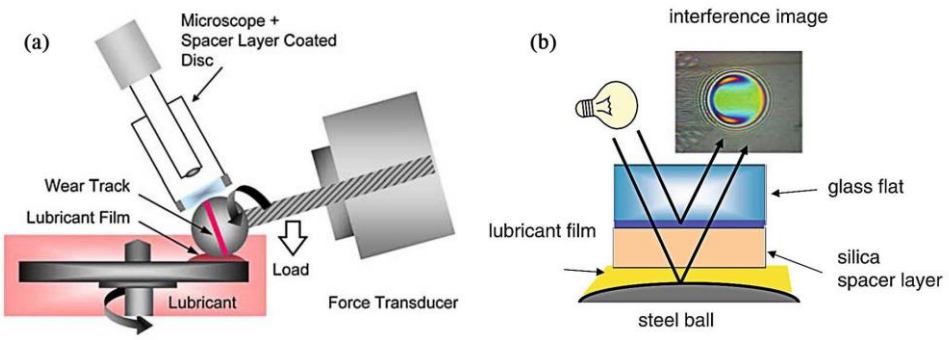

Fig. 4-3 a) Schematic diagram of MTM-SLIM; b) SLIM principle [150, 301].

4.2.1.2 *3D Spacer Layer Imaging methods (SLIM)*

SLIM is an external component of MTM, used to test the in-situ growth process of the tribofilm and analyse the thickness after the test. Its main principle is shown in Fig. 4-3b. A white light source illuminates the ball surface through the lens which is consisted of the bulk of glass, a thin semi-reflective chromium layer and coated silica spacer layer at the surface. The light reflected from the Cr layer interferes with the light reflected from the surface of the ball. Then, the interference image will be captured by a colour camera and microcomputer. Next, the image is analysed after the tests by an offline software to convert the RGB colour of each pixel in the image to the path difference between the steel surface and the Cr layer, that is the composite thickness of the silica layer and tribofilm [302]. Before the start of the experiment, the calibration of the silica layer thickness is required by adjusting the light intensity and the image is captured. Then, the first image will be analysed by the software and the data from the rest of the images will subtract the first value automatically to get the tribofilm thickness.

4.2.1.3 *Experimental Matrix*

In order to understand the tribochemistry and wear behaviours of FFO in many aspects, different groups of experiments are designed, which are introduced as follows.

- Group I - Effects of temperatures

  The main testing conditions are shown in Table 4-5. The relative motion of piston and cylinder is complicated which can include mainly sliding, rolling and jumping sometimes. The main running conditions can be treated as mainly sliding with the slightly rolling condition, so the slide-to-roll (SRR) ratio is set to 150%. According to the real working condition of the piston pump, the entrainment speed and load are

0.1 m/s and 60 N (about 1.2 GPa maximum Hertzian pressure), respectively to develop an approximate boundary lubrication condition. Considering the influence of temperatures on tribo-chemistry and wear properties, the different temperatures are 60, 75, 80, 100 and 120 ℃. At each temperature, testing durations are mainly 0.5, 1, 2, 3 and 6 hours for the wear measurement. Each kind of test is repeated twice at least.

Then, the Stribeck curves are tested to understand the lubrication regimes at different temperatures and tribofilm thickness. The difference of test parameters from the main tests is that the entrainment speeds drop from 2000 mm/s to 10 mm/s. All the tests in this part use steel samples and FFO as the lubricant.

Table 4-5 MTM testing conditions for temperature effects.

	Steady State	**Stribeck Curve**
Temperatures	60, 75, 80, 100 and 120 ℃	
Load	60 N	
Entrainment Speed	100 mm/s	2000 mm/s – 10 mm/s
SRR	150 %	
Durations	6 h with different time intervals (mainly 0.5h, 1h, 2h and 3h)	

- Group II - Effect of additives

Due to the variety of additives in FFO, two groups of experiments are designed for better understanding the impact of additives on tribofilm and wear: comparison test on BO and oil change test after tribofilm formation. The detailed testing conditions are listed in Table 4-6. The temperature is fixed to 100 ℃.

In the comparison test with BO, the only difference is the lubricant. In the oil change test, the FFO is used at first during a 4-hour test to generate tribofilm at a steady state. Then, the used FFO is drained out from the oil pot and replaced by other lubricants such as BO, BO+ZDDP, BO+detergent and FFO (as reference). In the process of changing oils, the newly added oil is reheated. In order to show that the tribofilm thickness is not consumed during the heating process, the thickness before and after the heating is measured before loading.

Table 4-6 MTM testing conditions for additive effects.

	Comparison test with BO	Oil Changes
Lubricants	BO	4h FFO + 2h BO
	FFO	4h FFO + 2h (BO+ZDDP)
	-	4h FFO + 2h (BO+Detergent)
	-	4h FFO + 2h FFO
Durations	6h, 3h and 1h	6h in total
Constant parameters	Temperature – 100 ℃; Load – 60 N Entrainment speed – 100 mm/s; SRR – 150 %	

- Group III - Effects of λ ratio

  In order to further verify the effectiveness of the 'temperature-tribofilm thickness-wear' trend in the first group of tests under boundary lubrication, according to the results in the Stribeck curve, the entrainment speed is reduced from 100 mm/s to 10mm/s to achieve a test condition of a lower λ ratio and to reduce the influence of viscosity of lubricant on wear. The specific test parameters are listed in Table 4-7.

Table 4-7 MTM testing conditions for λ ratio effects.

	Steady state
Temperatures	60, 80 100 and 120 ℃
Load	60 N
Entrainment Speed	10 mm/s
Slide-to-Roll (SRR) Ratio	150 %
Durations	3h and 1h, 0.5h

4.2.1.4 *Sample Cleaning Procedures*

Before the test, the ball and the disc are simply washed with heptane to remove the anti-rust oil and dust on the surface. Then, the samples are immersed in a beaker containing acetone and washed in an ultrasonic bath at 40 ℃ for 20-30 mins. Finally, the samples are taken out and dried naturally.

After the MTM tests, heptane is used to rinse off the remaining lubricant on the surface of samples and dry them naturally for further measurements.

To measure the wear, 0.05 mol/L Ethylenediaminetetraacetic (EDTA) solution is used to remove the tribofilm. The solution is normally used to remove the tribofilm formed by ZDDP [301, 303] and it has also been proved to work on the tribofilm formed by the detergent [150]. Thus, it is considered that this solution is also applicable to the tribofilm produced by FFO containing both film-forming additives.

A droplet of the solution is put on the wear track by a syringe for 1 minute and then the soft tissue paper is used to remove the droplet. In this case, the step will be repeated twice to make sure the removal of tribofilm.

4.2.2 *White Light Interferometry*

The white light interferometry (NPFLEX^{TM}, Bruker) is used to measure the surface roughness, 2D profile and 3D images of the wear track. The data analysis is executed by Vision64® software to visualise the results and calculate surface parameters.

The principle of white light interferometry is to utilise the interference generated by the phase difference between two optical waves. Any change of the difference will influence the motion of interferometric fringes which can reflect the tiny variation of the geometric length or refractive index. As is shown in Fig. 4-4, the broadband light source passes through the condenser lens to be parallel lights. Then, the light will be reflected by a beam splitter partly on the rough surface of samples and pass through it to the reference mirror. The phase difference between the reflected light from the rough surface and that from the reference mirror can be captured by the imaging system. Therefore, the surface morphology can be measured. The resolution of the measurement is determined by the resolution of the optical path length. The main characteristics of white light interferometry are non-contact, high-resolution, fast measurement and good stability.

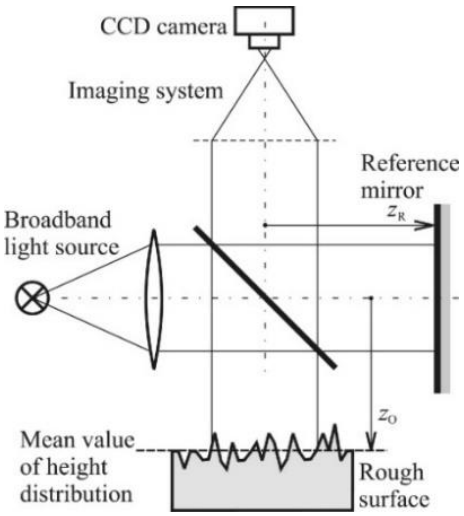

Fig. 4-4 Schematic layout of an interference microscope [304].

Since the thickness and transparency of the tribofilm will produce an optical path difference, which will affect the wear measurements by interferometry [303]. Thus, the wear was measured after the removal of tribofilm.

Due to the test being run under a high slide-to-roll ratio (SRR) of 150%, the disc speed is 7 times the ball speed (For example, when the entrainment speed is 0.1m/s, the ball speed and the disc speed are 0.025m/s and 0.175m/s, respectively), so the sliding distance of the disc is higher than that of the ball for the same test duration. The circumference of the wear track on the disc is about 3 times that on the ball, so the disc wears more than the ball.

The wear images on the ball and the disc, measured by NPFLEX, also confirm this. An example is the samples tested for 6 hours at 100 ℃, as shown in Fig. 4-5. The steel ball only has a small wear groove on the surface for such a long test time, as shown in Fig. 4-5a, so the wear on the ball can be ignored. In contrast, the steel disc has a smoother surface and clearer shape in the wear track (see Fig. 4-5b). The wear volume on the disc, therefore, is chosen as the parameter to represent the wear behaviour of the lubricants tested.

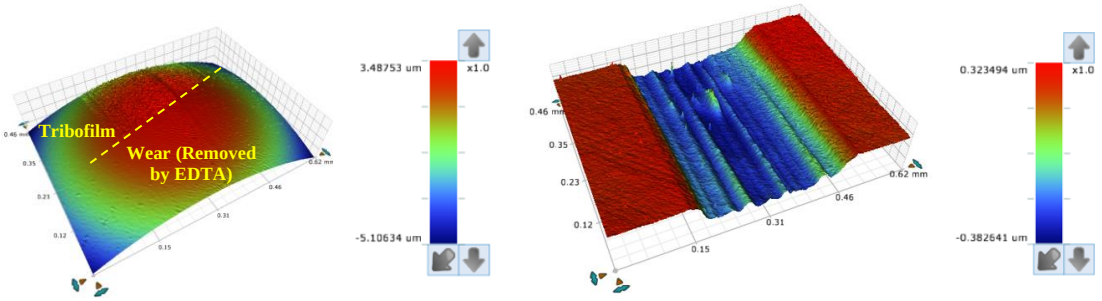

(a) steel ball **(b) steel disc**

Fig. 4-5 The 3D images of worn surfaces on the steel ball (a) and the steel disc (b) after 6-hour testing at 100 °C, captured by NPFLEX with 10x magnification.

The wear volume can be obtained with reference to the plane of the unworn area by the Vision64® software. Four areas on each disc sample will be randomly selected to measure and then calculate the average value of wear volume for further discussion.

4.3 *Chemical Analysis*

4.3.1 *Scanning Electron Microscope with Energy-dispersive X-ray Spectroscopy (SEM-EDX)*

The chemical elements of tribofilms are detected by SEM (Hitachi TM3030Plus Benchtop) equipped with an Oxford X-ray analysis system for elemental identification and mapping (EDX). The fundamental principle of SEM is that when the electron beam scanning on the samples, the interactions between the high-energy incident electrons and samples can generate different signals from secondary electrons, backscattered electrons, diffracted backscattered electrons, photons, visible light and heat [305]. The different signals will be received by the detector and have different utilisations. For example, the signals of secondary electrons and backscattered electrons can be used to produce the morphology and topography of samples. The simplified schematic diagram of SEM is illustrated in Fig. 4-6, the high-energy electron beam is emitted from an electron gun, passing through the acceleration of an anode and the focus of 2-3 magnetic lenses, finally focusing on the sample surface. Each scanning signal from the electron beam can be displayed on the output device after magnification. After the electron beam scans all the tested areas, the whole image will be obtained from all scanning points one by one.

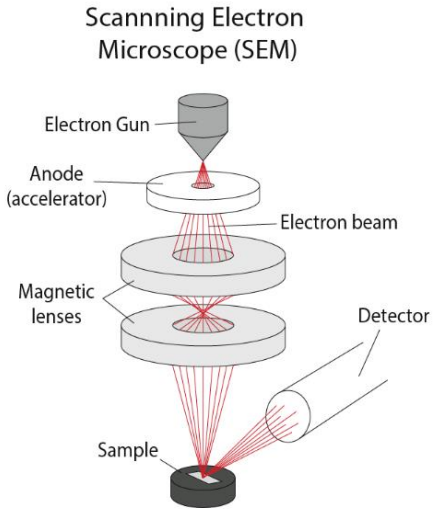

Fig. 4-6 The schematic diagram of SEM [306].

The EDX (AZtec) is assembled with the SEM to obtain characteristic X-ray from the surfaces of specimens. A built-in detector (Oxford Instrument, UK) can convert the X-ray into voltage signals. The voltage used in this study is 15 kV in the backscattered electrons (BSE) mode. Considering the chemical compositions of additives, the elements studied are mainly P, S, Ca and Zn are mainly concerned.

4.3.2 *Raman Spectroscopy*

Raman spectroscopy is a kind of molecular vibrational spectrum obtained by the principle of light scattering, which is one of the commonly used methods for analysing the types and chemical structure of materials. The schematic diagram of Raman spectroscopy is shown in Fig. 4-7. When the sample is irradiated with a monochromatic laser beam, the photons in the laser interact with the molecules in the sample, resulting in elastic collisions and inelastic collisions, and scattering occurs in all directions. Most of the scattered light has the same frequency as the incident light without energy loss (elastic collision), which constitutes Rayleigh scattering. The frequency of a small part of the scattered light is different from that of the incident light (when some molecules gain or lose energy and collide inelastically), it constitutes Raman scattering. When the incident light frequency is higher than the scattered light frequency, the Stoke spectrum appears in the Raman spectrum, and on the contrary, the anti-Stokes spectrum appears.

The Raman spectrometer used in the project is a Renishaw inVia spectrometer to analyse sulphide and phosphate in tribofilm. The laser with the wavelength of 488 nm is chosen and its maximum energy is 10 mW. The laser intensity used in the experiments is 50%. It should be noted that the laser intensity has been verified to not cause damage to the sample. The acquisition range is 150 cm^{-1}~1600 cm^{-1}, and the acquisition time is 30 seconds. The temperature of all tests is performed at room temperature.

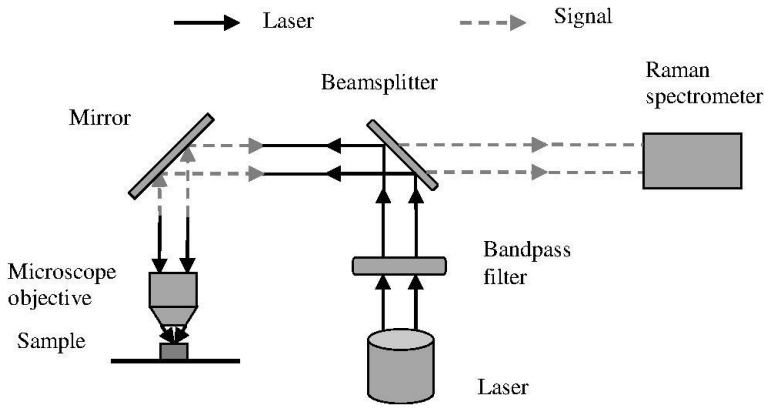

Fig. 4-7 A schematic diagram of Raman spectroscopy [307].

Before proceeding with the measurement, the Si wafer is used for calibration and the Si peak is checked to be located at about 520±1 cm^{-1}. Due to the uneven distribution of tribofilm, the mapping setting is used to automatically sample multiple points in the measurement area. The mapping settings are shown in Fig. 4-8 as an example.

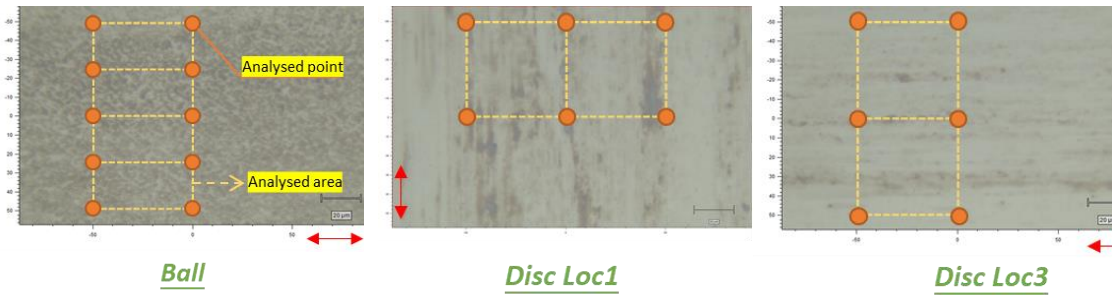

*Ball sample: 2x5 spectra in the area of (50 μm x 100 μm).

*Disc sample: 2x3 spectra in the area of (50 μm x 100 μm) and two areas will be analysed.

Fig. 4-8 Diagrams of mapping settings of Raman analysis on the tribofilm on the ball and the disc samples.

After obtaining the Raman spectrum, the baseline of the raw data is removed first. Then, a mixed Gaussian/Lorentzian method is used to fit the peaks to obtain the information of

frequency, intensity and full width at half maximum (FWHM). The raw spectra and filtered results can be seen in Appendix A.

4.3.3 *X-ray Photoelectron Spectroscopy (XPS)*

Raman analysis can generally determine the possible presence of sulphides and phosphates in tribofilm but is not easy to distinguish information about cations such as Fe, Zn and Ca. Therefore, XPS is used to further analyse the chemical compositions that may exist in the tribofilm and depth profiling is applied to analyse the distribution and changes of the chemical compositions in the depth direction.

The schematic diagram of the XPS principle is shown in Fig. 4-9a [308]. When the sample is radiated by the X-ray beam, the electrons from atoms or solids are emitted. Then, the kinetic energy of the emitted electrons is detected, which is discrete and a function of binding energy. The binding energy is related to the elements and environments. The basic types of XPS data are energy spectrum, spatial image and depth profile.

The XPS instrument used in this project is the PHI5000 Versa Probe II^{TM} (ULVAC-PHI, Inc.). An Al Kα monochromatic source is applied at 15 kV and 50 W with step energy of 1486.6 eV. The size of the analysed area is about 200 μm in the tribofilm, as shown in Fig. 4-9b. In the measurement of depth profiling, the Ar ion sputters the specimen surface and the etching rate is 18.175 nm/mins (relative to SiO_2 rate) with the energy of 4 kV and 20 mA. The tribofilm at different depths will be analysed through the etching process. Both the high-resolution spectrum and atomic concentration as the function of depth are obtained. The maximum depth is about 120 nm, estimated by the etching rate.

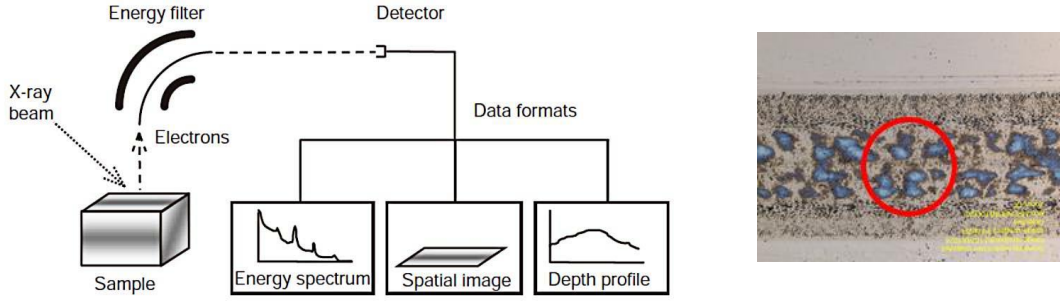

(a) **(b)**

Fig. 4-9 The diagrams of (a) XPS principle with the basic types of XPS data [308] and (b) an example of the analysed area in the tribofilm for XPS analysis.

The post-processing process of XPS data uses CasaXPS software, in which Shirley–Sherwood iterative method is used for background subtraction and Gaussian and Lorentzian functions are applied for curve-fitting the peaks. For 2p spectra of elements P, S, and Ca, due to the split of spin orbits, the doublet with an area ratio of 2:1 is set in the peak fitting.

4.4 *Correlations between Experiments and Modelling*

In addition to the experimental study of the tribochemistry and wear behaviour of the fully formulated oil, the predictions of the key results such as tribofilm growth and wear are also important objectives. The framework to explain the correlation between experiments and modelling is shown in Fig. 4-10, in which the interactions of critical parameters are marked by numbers.

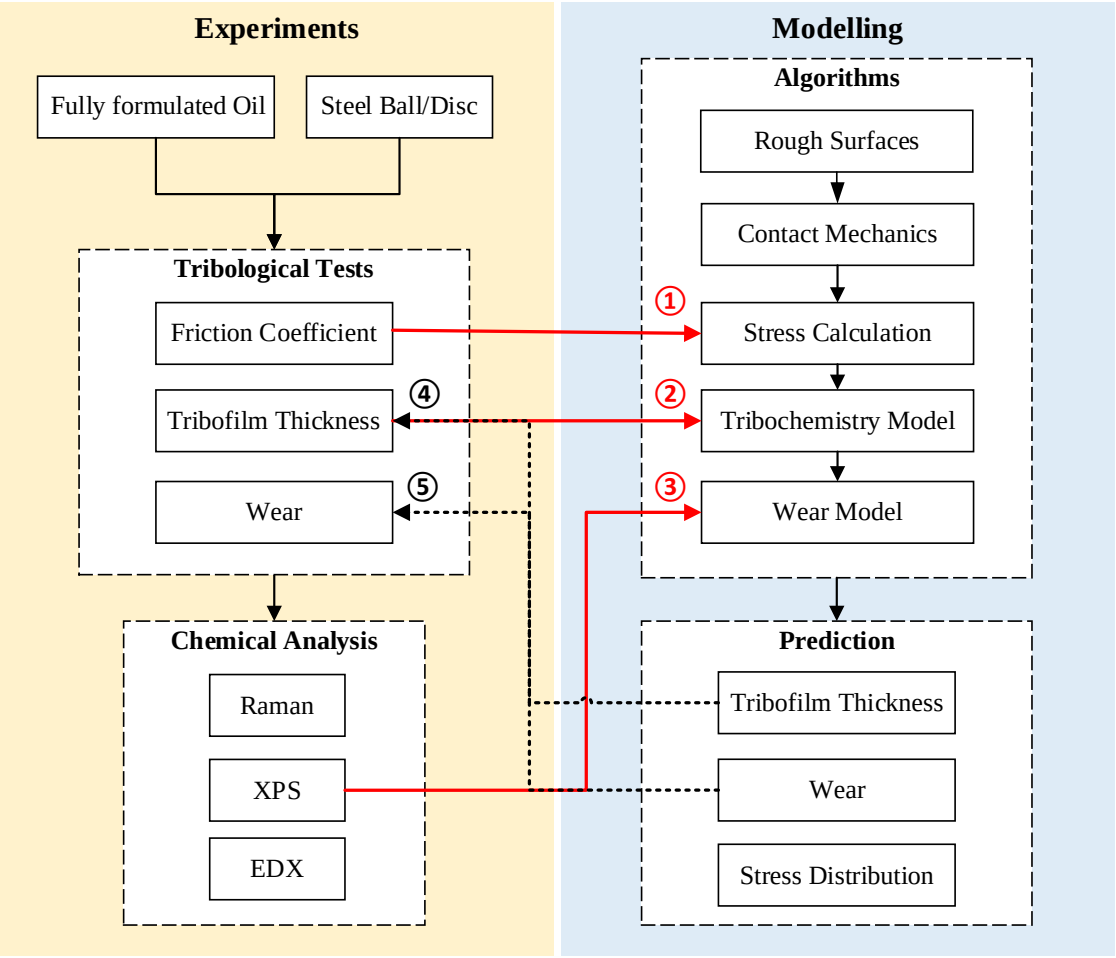

Fig. 4-10 The framework of coupling the experiments and modelling work. The key correlations are marked by numbers.

The modelling framework used in this study is mainly based on the asperity contact in the boundary lubrication modelling, which mainly includes rough surface generation, contact mechanics, tribofilm formation model and wear model. In order to simulate and predict the growth and wear of FFO tribofilm in the experiments, the experimental results are used to fit the parameters or as the inputs into the model.

Link One is to input the friction coefficient in the stress calculation step and to calculate the stress distribution with traction. Link Two is to obtain the parameters in the tribochemistry model by fitting the experimental data of tribofilm thickness as the function of time. Link Three is to calculate the wear coefficient in the wear model. The detailed theory and process of wear calculation will be explained in Chapter 7. In addition, other inputs such as surface roughness, material properties and working conditions in the model are as consistent as possible with those in the experiments.

The main parameters predicted from the model are tribofilm thickness, wear and stress distribution. The tribofilm thickness and wear in the simulation (Link 4 and 5 respectively) are compared with experimental results at the same working conditions to verify the effectiveness of the model.

4.5 *Summary*

This chapter mainly introduces the materials, lubricants, experimental equipment, and operating procedures used in tribological experiments and chemical analysis. Then, the correlations between the key parameters in the experimental results and the model are explained.

In the next chapters, the results in the experimental studies of FFO will be first discussed to obtain the tribochemistry and wear behaviours and followed by the discussions and predictions in the simulation work.

Chapter 5 Tribological Properties of the Fully Formulated Oil at Different Temperatures and Effects of Additives

The effects of temperatures and additives on tribofilm growth and wear of FFO are first studied in this chapter. The chapter is divided into two sections. Section One discusses the effects of temperatures on friction coefficient, tribofilm thickness and wear results. Then, the chemical composition of tribofilm at different temperatures was analysed by XPS to basically understand the relationship between the tribochemical reaction and the wear mechanism of FFO. Section Two studies the influence of additives in FFO on maintaining the tribofilm thickness by using different combinations of additives and base oil. Similarly, it follows the chemical analysis on the tribofilm to compare the composition changes under the influence of different additives and to further understand the performance of FFO.

5.1 *Effect of Temperature on Tribofilm Growth and Wear Behaviour*

5.1.1 *Tribological Results*

The growth curves of tribofilm within the testing time of 180 minutes at different temperatures (60, 75, 80, 100 and 120 ℃) are shown in Fig. 5-1a. It can be seen in the figure that the growth process of tribofilm can be roughly divided into two phases, namely the growth phase and the stable phase. The higher the temperature, the faster the tribofilm thickness reaches the stable phase. Specifically, at 120 ℃, it takes about 40 minutes for the tribofilm thickness to reach equilibrium, while from 60 ℃ to 80 ℃, tribofilm still has a light growth trend after 70 minutes.

The tribofilm thickness at the equilibrium stage is calculated by the average value of the thickness after testing for 2 hours. The relationship between thickness and temperature is shown in Fig. 5-1b. When the temperature rises, the tribofilm thickness at the stable phase increases, but the growth rate is not constant. From 60 ℃ to 80 ℃, the thickness at the steady phase increases more than twice with the increase of temperature, but when the temperature is higher than 80 ℃, the increase of balanced thickness becomes very slow.

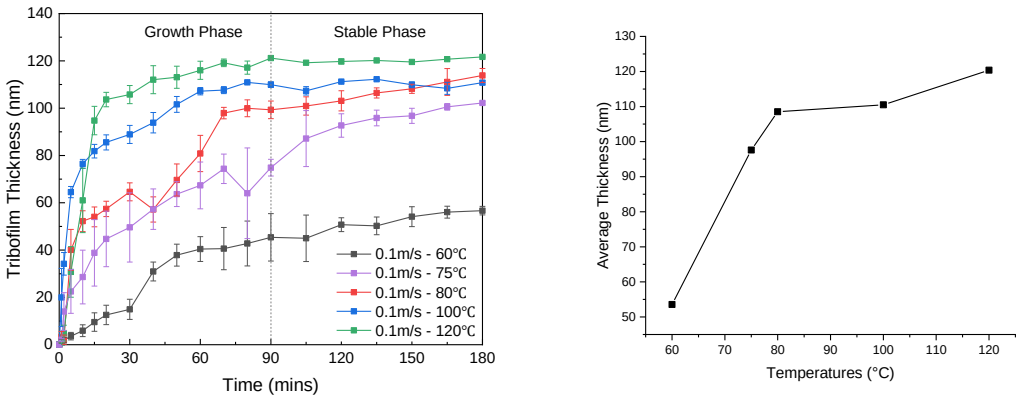

(a) **(b)**

Fig. 5-1 MTM-SLIM results of the steel/steel contact lubricated by FFO at different temperatures (60, 75, 80, 100 and 120 ℃): (a) Tribofilm thickness as a function of time. Error bars are the reproducibility of the test. (b) Average thickness at steady state.

In addition, the evolution of the tribofilm on the ball at different temperatures can be seen in Fig. 5-2. In general, as the temperature rises, the growth rate of the tribofilm and its uniformity of distribution increase. The uneven distribution of tribofilm during growth can be seen at 60 ℃ and 75 ℃, which may be related to the contact conditions of the ball-disc interface. Therefore, the effects of temperature on the tribofilm growth by FFO are not only reflected in the increase in the tribochemical reaction rate but may also be related to the viscosity of the lubricant, which in turn affects the contact state.

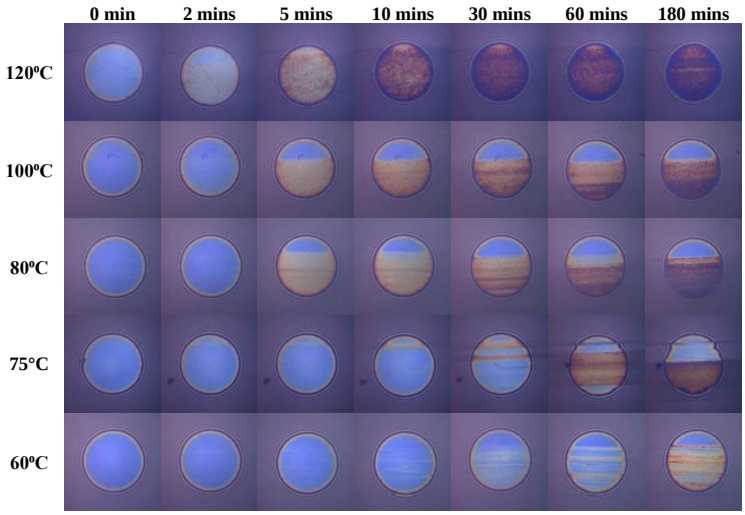

Fig. 5-2 Part of SLIM images of the In-situ tribofilm growth on the ball samples at different temperatures.

Fig. 5-3a is the friction coefficient curve measured at different temperatures in the MTM experiment. The increasing trend of the friction coefficient at each temperature is similar

to its corresponding tribofilm growth curve. The difference is that the friction coefficient at 75 ℃ fluctuates greatly, which may be attributed to the uneven distribution of tribofilm. In addition, the friction coefficient reaches the equilibrium earlier than the tribofilm thickness, as compared with Fig. 5-1a.

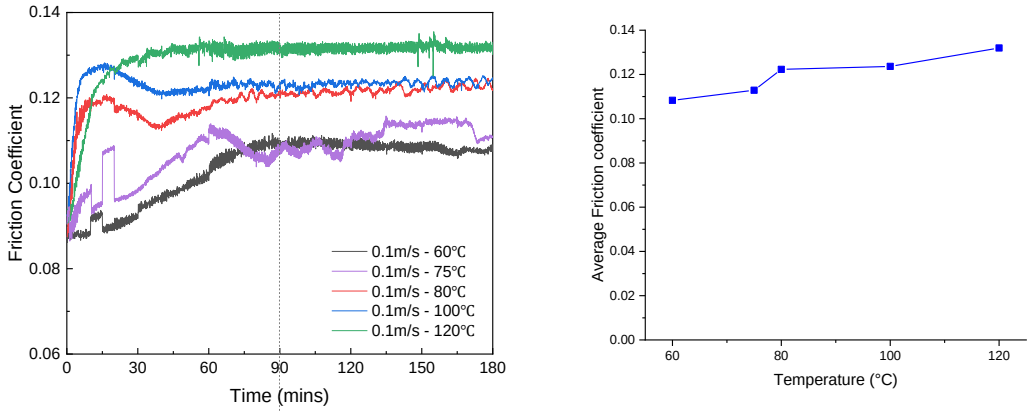

(a) **(b)**

Fig. 5-3 (a) Friction coefficients as the function of time on the steel/steel contact lubricated by FFO at different temperatures (60, 75, 80, 100 and 120 ℃). (b) Average friction coefficient at steady state.

The average friction coefficient at the stable stage as a function of temperature is calculated by the average value after 90 mins of testing, as shown in Fig. 5-3b. During this phase, the friction coefficient also increases with increasing temperature.

After removing the tribofilm by the EDTA solution, the wear volume at different temperatures as the function of test time was measured and is shown in Fig. 5-4a. The trend of wear volume changing with temperature can be divided into two phases: (I) from 60 to 80 ℃, wear increases with increasing temperature; and (II) from 80 to 120 ℃, wear decreases with increasing temperature. Specifically, the wear volume is the lowest among all test temperatures at 60 ℃, and the wear rate decreases with the test time. At 80 ℃ and 100 ℃, the wear curves are very similar, but the wear volume at 80 ℃ is slightly higher. At 120 ℃, after one hour of testing, the wear rate starts to decrease, which may be due to the tribofilm reaching a stable phase.

In particular, the wear is the largest at 75 ℃ after 360 mins of testing. Before that, the maximum value of wear occurs at 80 ℃. This can be seen more directly from Fig. 5-4b, which is obtained by extracting the data at 60mins and 360mins from Fig. 5-4a. It is

speculated that the change of the wear mechanism of FFO may happen around 75/80 ℃. As the difference between the two temperatures is small, in order to simplify the description, the subsequent description uses 80 ℃ as the threshold to divide the wear trend of FFO.

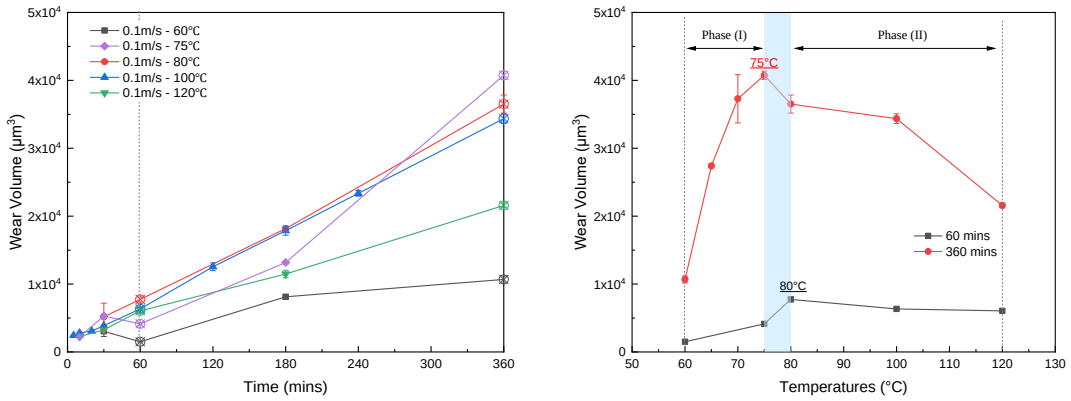

(a) **(b)**

Fig. 5-4 Wear measurements on steel discs by NPFLEX (The measured area is 400 μm x 600 μm): (a) wear volume as the function of time at different temperatures; (b) wear volume vs temperature at the end of 60 mins/360 mins, extracted from (a).

The studies of ZDDP tribofilm in the same range of temperatures [50, 179] has shown that when the temperature rises, the tribofilm thickness increases and the corresponding wear decreases. According to the results of tribological experiments using FFO, the tribofilm thickness still increases with the increase of temperature, which can be attributed to the increase in the tribochemical reaction rate. However, its corresponding wear behaviour is different to ZDDP. For FFO, this can be divided into two phases. In the first phase, at 60~80 ℃, as the temperature increases, both tribofilm thickness and wear increase. In the second phase of 80~120 ℃, the tribofilm thickness continues to increase, but wear decreases.

The rubbing tests and wear results show that the wear mechanism of FFO can be affected by temperature. In addition, it can be speculated that it is related to the formation process of tribofilm and the chemical compositions of tribofilm at different temperatures. In order to prove this, the next step is to select tribofilm that has reached a stable stage at 60, 75 and 120 ℃ respectively for surface analysis, so as to compare the difference in the chemical compositions of tribofilm and to discuss the factors to influence the wear mechanism of FFO.

5.1.2 *Surface Analysis by XPS*

XPS analysis is an effective method for detecting the chemical compositions of the tribofilm. It is expected that the chemical composition in tribofilm generated at different temperatures may be different, which is one of the reasons why the wear curve of FFO is different from ZDDP. According to the film-forming additives in FFO such as ZDDP and over-based calcium sulphonate detergent, it is speculated that the main composition of the tribofilm contains phosphates and sulphur-containing compounds, and the cations bonding to them can be Zn, Ca and Fe, which will be the focus of attention in the XPS analysis.

5.1.2.1 *Elemental Analysis*

By identifying and fitting the peaks of the XPS signals C1s, O1s, P2p, S2p, Ca2p and Zn2p related to the elements that may exist in tribofilm, the results are shown in the six sub-diagrams in Fig. 5-5, respectively. Each sub-diagram compares the spectral results of tribofilm generated at 60, 75, and 120 ℃, respectively. In addition, the binding energies of the peaks identified in Fig. 5-5 are listed in Table 5-1.

The C1s spectra have four peaks fitted and shown in Fig. 5-5a. The first peak presents at 284.8 eV, attributed to the organic carbon (C-C, C-H) [309-311]. The second peak has a higher binding energy of 288.9±0.1 eV, which is attributed to the O-C=O group in calcium carbonate [22, 309, 310]. This is produced by the detergent of over-based calcium sulphonate in the FFO during the rubbing process. It is also found in the tribofilm produced by this detergent, and it exists on the surface of the tribofilm [157]. The other two peaks are 283.5 eV and 286.2±0.3 eV, respectively, representing iron carbide [312, 313] and C-O bond in C-OH or C-O-C groups [309, 310]. When the temperature increases, the iron carbides in the substrate have a reduction, which indicates that the thickness or coverage of the tribofilm increases.

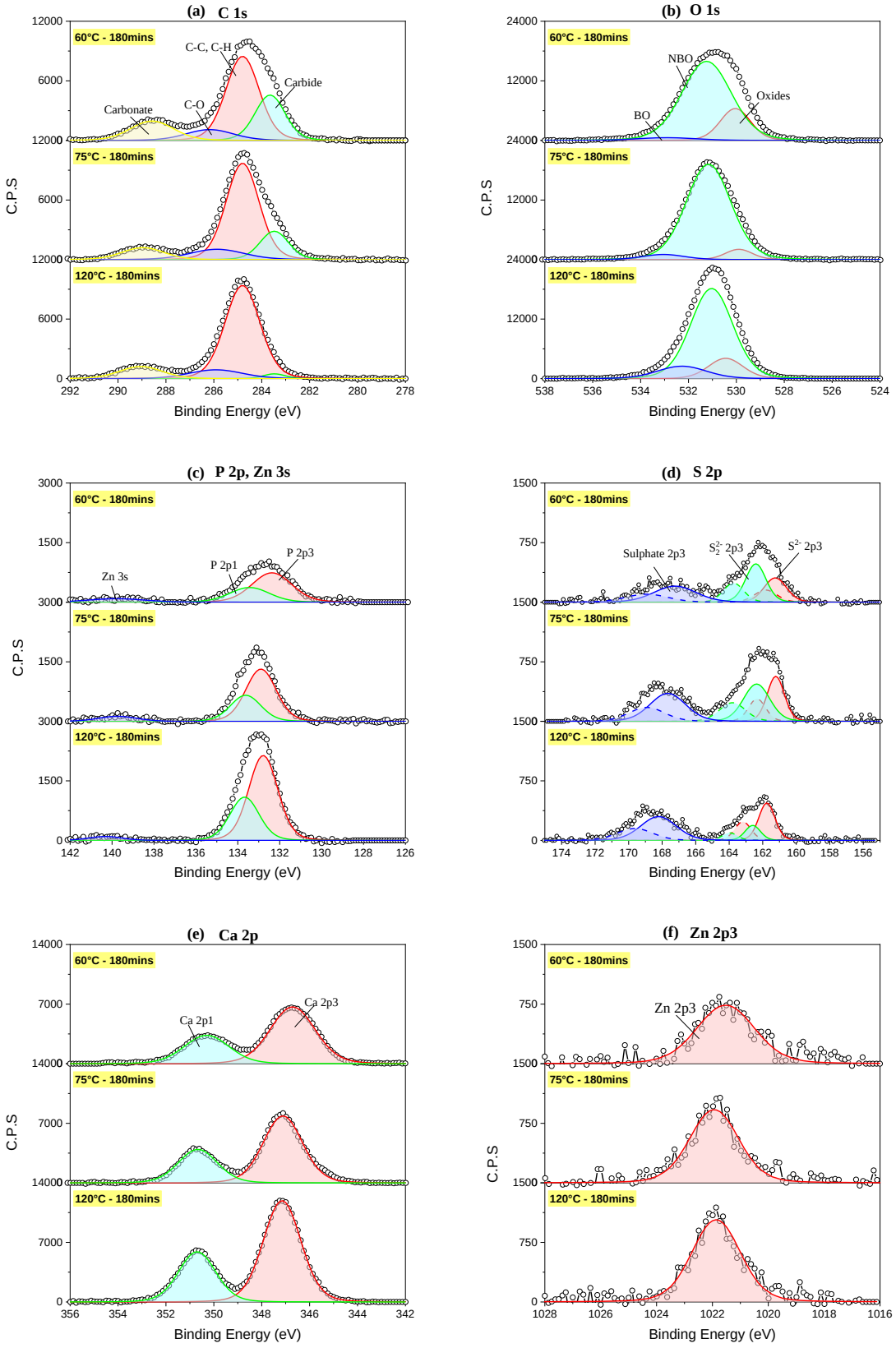

Fig. 5-5 Peaks identification in the XPS elemental analysis of a) C1s, b) O1s, c) P2p, d) S2p, e) Ca2p and f) Zn2p3 spectra in the tribofilms formed at 60, 75 and 120°C after 180 mins of rubbing.

Table 5-1 The binding energy of peaks fitted in XPS elemental analysis of C1s, O1s, P2p, S2p, Ca2p and Zn2p3 spectra.

Temperatures	60 ℃	75 ℃	120 ℃	
Components	**Binding Energy(eV)**			**Assigned to**
C 1s	288.9	288.9	289.0	Calcium carbonate
O 1s	531.3	531.1	531.2	NBO in phosphate and carbonate or hydroxide
	532.8	532.5	532.3	Phosphate groups or sulphate
	530.0	529.7	530.5	Iron oxides
P 2p3	132.4	132.8	132.9	Mainly calcium phosphate
Zn 3s	139.8	139.8	140.1	Zinc phosphate
S 2p3	161.2	161.2	161.6	ZnS/FeS
	162.4	162.2	162.5	FeS_2
	167.4	167.8	168.2	$CaSO_3$/$CaSO_4$
Ca 2p3	346.7	347.1	347.1	$CaCO_3$, calcium phosphate, $CaSO_3$/$CaSO_4$, or CaS
Zn 2p3	1021.6	1021.8	1021.9	ZnS, or possible zinc phosphate

There are three peaks in the O1s spectra illustrated in Fig. 5-5b. The first one with the largest peak area has the binding energy of 531.2±0.1 eV, assigned to the non-bridging oxygen (NBO) in the phosphate and carbonate or hydroxides [22, 309-311, 314]. The second peak with higher binding energy which is at 532.5±0.3 eV represents the phosphate groups or sulphate [309, 311, 315]. The third peak appears at 530.1±0.4 eV, attributed to iron oxides [157, 310].

The P2p spectra are shown in Fig. 5-5c, in which the peak of P2p3 at 60 ℃ appears at 132.4eV and the binding energy increases to 132.8eV at 75 ℃ and 132.9 at 120 ℃. This peak is attributed to the phosphate, but the cations may be one or more of the Ca, Zn and Fe ions. According to many XPS studies of zinc phosphate, calcium phosphate and iron phosphate, their corresponding binding energy for P2p3 peak present at 133.6±0.2 eV [310, 316], 133.3±0.3 eV [314] and 134.6±0.7 eV [317-319], respectively. Besides, the peak of Zn 3s can also be fitted at 140.0±0.2 eV, attributed to zinc phosphate [310]. Thus, at the surface of tribofilm, the main phosphate detected is calcium phosphate but there

may be less zinc phosphate existing. However, the peak intensity of Zn 3s is very weak, which also indicates that the content of zinc phosphate is very less in the tribofilm.

The identifications of S2p spectra are exhibited in Fig. 5-5d. Due to the split of the 2p orbit, there are three representative peaks identified by controlling the area ratio of S2p3 and S2p1 of 2:1. The first peak appears at 161.4±0.2 eV, attributed to sulphides such as ZnS [320], FeS [321] or CaS [321, 322]. The second peak has a binding energy of 162.4±0.2 eV, assigned to FeS_2 [323, 324]. The third peak has higher binding energy apparently, attributed to the SO_3 group in the calcium sulphonate absorbed on the surface of tribofilm or the SO_4 group in the calcium sulphate oxidised by the over-based calcium sulphonate detergent during the rubbing. Their corresponding binding energy of S2p3 are 167.1±0.3 eV and 168.9±0.2 eV [322, 325], respectively. In the tribofilm, the binding energy of this peak is 167.4±0.2 eV, 167.8±0.1 eV and 168.2±0.1 eV at 60, 75 and 120℃, respectively. It shows that as the increase of temperature, the process of decomposition and oxidation of detergent increases. In addition, the area ratio of sulphides and disulphides reach the maximum at 75 ℃, which is consistent with the trend of wear results.

The identification results of Ca2p spectra are shown in Fig. 5-5e, where the main Ca2p3 peak appears at 346.7±0.1 eV, 347.1±0.1 eV and 347.1±0.0 eV at 60, 75 and 120 ℃, respectively. According to the analysis of the additives in FFO, the calcium components in the tribofilm can be $CaCO_3$(CaO), calcium phosphate, $CaSO_4$($CaSO_3$), or CaS. According to the referred binding energy values of Ca 2p3 spectra listed in Fig. 5-2, the Ca2p3 peak at 60 ℃ can be assigned to $CaSO_3$**,** CaS or $CaCO_3$, while it is mainly attributed to $CaCO_3$ and calcium phosphate at 75 and 120 ℃.

Table 5-2 The reference binding energy values of Ca 2p3 spectra.

Species	B.E. (eV)	References
$CaSO_3$	345.6~346.5	[322, 325]
CaS	346.5~347.0	[309, 322]
$CaCO_3$	346.6~347.2	[309, 311, 325]
$Ca(PO_4)_x$	347.0~347.2	[314]
$CaSO_4$	347.6~348.0	[309, 321, 322, 325]

The signal of the Zn2p3 peak is shown in Fig. 5-5f. The peak appears at 1021.8±0.2 eV, attributed to ZnS [320] or possible zinc phosphate [310, 316].

5.1.2.2 *Correlation with Tribofilm and Wear*

There is apparent evidence that the elements Zn and P are only from ZDDP in the oil while the element Ca is derived from detergents only. Fig. 5-6a shows the correlation between the average tribofilm thickness in the stable phase and the area of P2p3, Zn2p3 and Ca2p3 peak. The growth trend of the P peak area is consistent with that of tribofilm thickness as the function of temperature, which is agreed with the fact that the bulk tribofilm is composed of phosphate and the thicker the tribofilm, the more phosphate. However, the content of Zn does not change with the increase of temperature, but that of Ca has a linear growth with temperature, indicating that the main composition of tribofilm is calcium phosphate instead of zinc phosphate. This is also in agreement with the results of tribofilm generated by the fully formulated oil containing both ZDDP and detergent [171, 326].

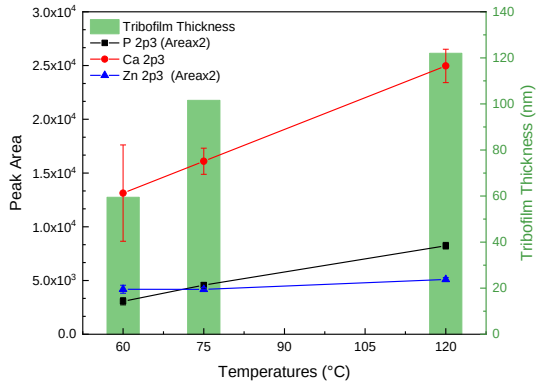

(a) Area of P2p3, Ca2p3 and Zn2p3 correlated to tribofilm thickness

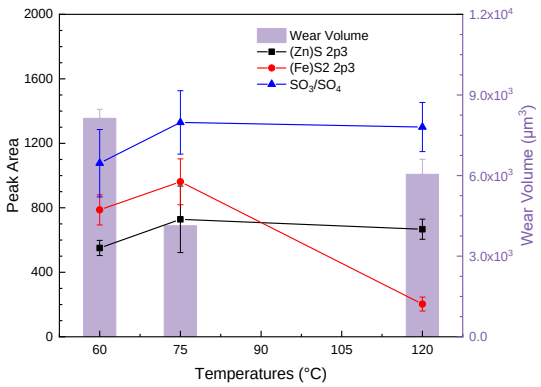

(b) Area of signals S2p3, $S_2$2p3 and SO_3/SO_4 correlated to wear volume

Fig. 5-6 Correlation of the tribofilm thickness or wear volume with the area of representative peaks as the function of temperature. All the samples are tested after 180 mins.

The S atom can come from ZDDP or over-based calcium sulphonate detergent. In Fig. 5-5d, the identification of the S2p spectra has divided the three types of S-components into mono-sulphides (Zn/Fe/CaS), disulphide(FeS_2) and sulphate. To analyse the effect of the sulphur content on the wear volume, the areas of those are obtained to correlate the corresponding wear results at different temperatures, as shown in Fig. 5-6b. In the lower temperature range of 60~75 ℃, the sulphur content increases but the wear decreases. It should be noted that the wear at 75 ℃ is not the highest at this time, unlike the wear at 6h. However, in the higher temperature range of 75~120 ℃, FeS_2 decreases sharply with

temperature, but the mono-sulphides and sulphate reduce slightly, indicating that the formation of FeS_2 and/or formation of sulphates may be the cause of the wear mechanism to a certain extent.

5.2 *Effect of Additives*

5.2.1 *Compared with Base Oil*

In order to study the effect of individual additives in FFO on wear as a lubricating system, the comparison tests between the base oil and FFO are conducted at 100 ℃. Fig. 5-7(a, b) respectively show the 3D images and wear profiles of the wear track after 1 hour and 6 hours of rubbing tests using base oil and FFO. There are apparent unevenness and severe plastic deformation in the wear track under the lubrication of base oil. In contrast, both the worn surface with FFO after rubbing 1 hour and 6 hours are flat and even, as illustrated in Fig. 5-7(c, d), respectively. In addition, by calculating the average wear depth from the wear profile, it can be seen that the wear of base oil is greater than that of FFO.

Since the wear morphology of using base oil is uneven, in order to reduce the error of choosing the cross-sectional position of wear profile, the wear volume of base oil is also calculated instead of wear depth and compared with the wear volume of FFO at the same temperature as the function of test duration, as shown in Fig. 5-8. Similarly, when using the base oil, both the wear volume and wear rate are more than three times larger than those when using FFO after 60 minutes of test time. It can also be seen that the wear rate of FFO is almost unchanged at 100 ℃, even in the running-in phase.

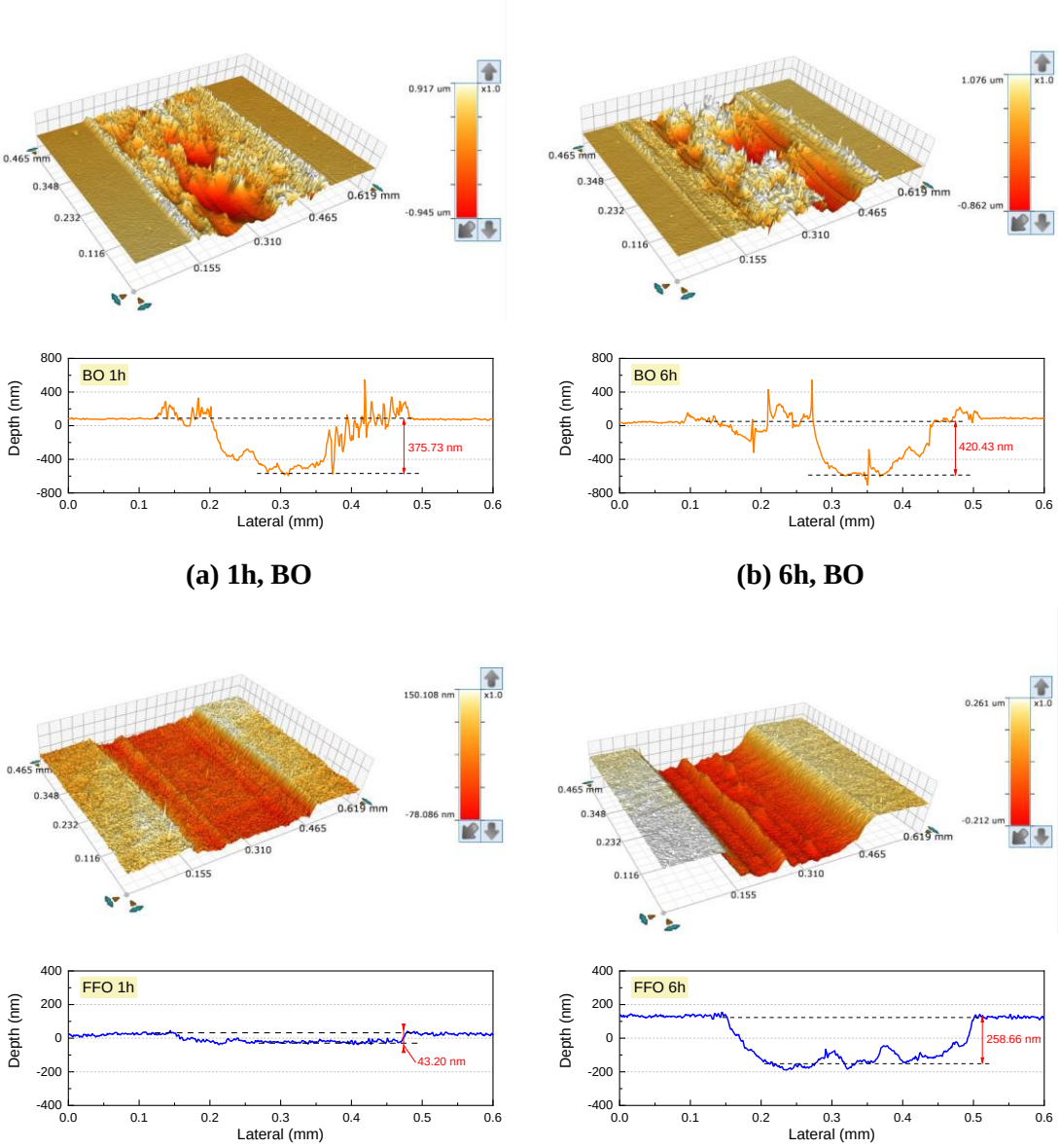

(a) 1h, BO **(b) 6h, BO**

(c) 1h, FFO **(d) 6h, FFO**

Fig. 5-7 The 3D images and depth profiles of worn surfaces on the steel discs at 100 ℃, lubricated by (a,b) base oil and (c,d) FFO after 1 hour or 6 hours of rubbing time. The magnification of the 3D images is 10x1, and the measurement area is 400x600 μm^2.

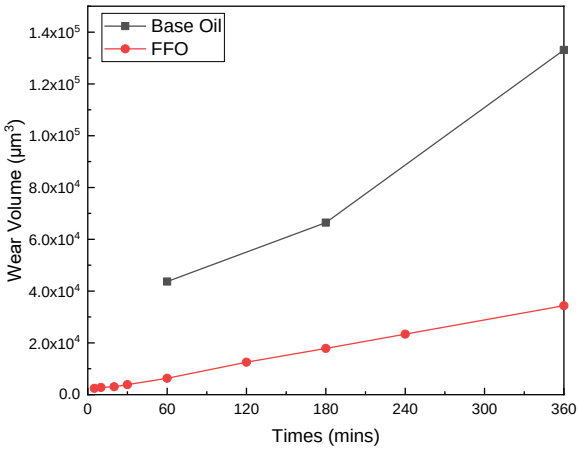

Fig. 5-8 Comparisons of wear volumes on the steel discs as the function of time when using base oil and FFO at 100 ℃.

Therefore, one of the mechanisms by which the combination of additives in FFO can effectively reduce wear is that the tribofilm produced by the tribochemical reaction between the additive and the surface can reduce the plastic deformation and adhesion effect of the surface. Another behaviour is that FFO can reduce the fluctuation of wear rate at the running-in phase, which is usually relatively higher than that at the steady-state. Even when the tribofilm is still in the growth stage, the wear rate could maintain stability to provide a smooth working condition.

5.2.2 *Tribofilm and Wear Properties after Changing Oils*

According to the study of tribofilm and wear of FFO, it can be obtained that the relationship of 'temperature-tribofilm thickness-wear' has a two-phase mechanism. It is different from the relationship of ZDDP mono-oil that when the temperature increases, the tribofilm thickness increases while the wear reduces. In addition, The XPS analysis suggests that ZDDP and detergents play an important role in the formation of FFO tribofilm and wear. Thus, in order to explore the effect of ZDDP and detergent on maintaining the durability of tribofilm and wear rate, after the growth of tribofilm formed by FFO reaches a stable stage, FFO is replaced with different lubricants such as base oil, base oil + ZDDP and base oil + detergent.

In these experiments, firstly, the fully formulated oil is used for 4-hour tests to form tribofilm, and the tribofilm thickness has reached the state of dynamic equilibrium. Then, the oil is taken out from the oil pot and replaced with a different oil: base oil, base oil

with ZDDP, base oil with detergent or FFO (as reference). The tribofilm thickness before and after the heating process of the new oil is compared to ensure that the heating process has no significant influence on the existing tribofilm thickness. Other test conditions have been listed in Section 4.2.1.

Fig. 5-9a shows the variation of tribofilm thickness after changing oils at 4 hours. It can be seen that in the first 5 mins after changing oils, the tribofilm thickness has different degrees of reduction, and the order of tribofilm removal is ZDDP>detergent>base oil. Then, the tests of these three different oils all have a rapid re-formation of tribofilm. After changing oil for another two-hour test, the tribofilm thickness for the base oil test is almost unchanged compared to that of the FFO test. In the tests replaced by the base oil with detergent or with ZDDP, the tribofilm thickness increases and decreases respectively compared with FFO. In the optical images in Fig. 5-9b, it can also be observed that the colour of the interference pattern changes from dark to light, then turns to dark again after changing to the base oil with ZDDP or with detergent, which also indicates the process of removal and re-formation of tribofilm.

After MTM tests, EDTA solution is used to remove the tribofilm as the preparation for wear measurement. The wear results by NPLEX after two hours of oil change test are shown in Fig. 5-10. Taking the four-hour test with FFO as a starting point, the next two-hour tests are carried out using base oil, base oil + ZDDP, base oil + detergent, and FFO respectively. The dashed line indicates the continuous six-hour experiment with FFO only. From the results, after the lubricant is replaced by ZDDP or base oil, the average wear depths remain almost unchanged, which means that the changes in tribofilms protect the contact surface, reducing wear. The wear volume increases the most when changing to the base oil with detergent, but this value is much smaller than using FFO directly.

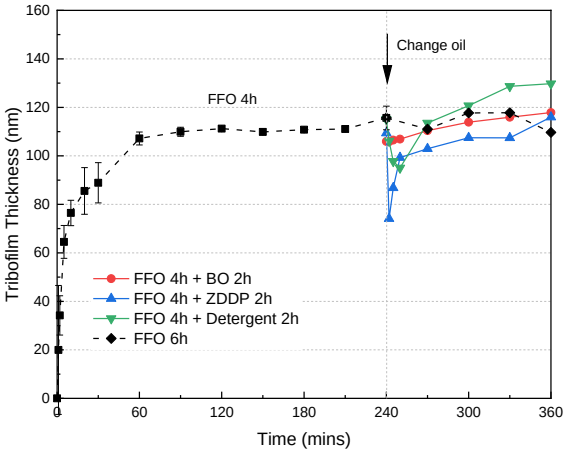

(a)

t	0 min	10 mins	30 mins	1 h	2 h	4 h	+2 mins	+5 mins	+30mins	+ 2 h
4h FFO + 2h BO										
4h FFO + 2h ZDDP										
4h FFO + 2h Detergent										
FFO 6h							-	-		

(b)

Fig. 5-9 MTM-SLIM results as the function of time: (a) tribofilm Growth and (b) In-situ images of tribofilm in the tests of changing oils from FFO after 4 hours of rubbing time to base oil, base oil + ZDDP and base oil + detergent for another 2-hour test, respectively. The 6-hour test with FFO is used for comparison.

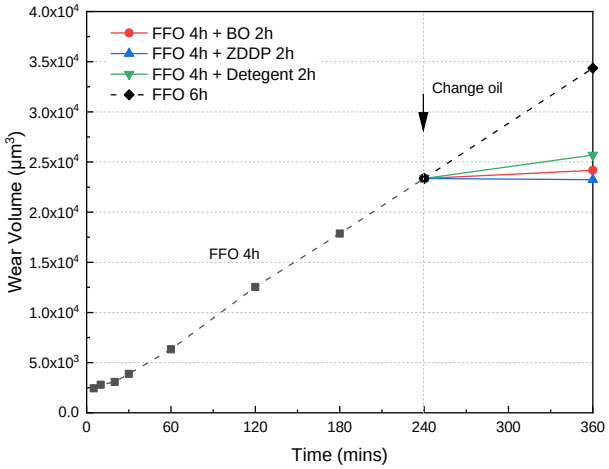

Fig. 5-10 Wear results by NPFLEX as the function of time in the tests of changing oils from FFO after 4 hours of rubbing time to base oil, base oil+ZDDP and base oil+detergent for another 2-hour test, respectively. The 6-hour test with FFO is used for comparison.

Correlating the results of tribofilm thickness and wear, when using the oil with detergent replacing the FFO, both tribofilm thickness and wear increase. It has been studied that when using over-based calcium sulphonate detergent and ZDDP in the lubricant, the Ca ion can replace Zn ion to generate calcium phosphate and shorten the chain length of polyphosphate [25], which will influence the effectivity of wear-reduction of ZDDP. Besides, the sulphonate groups may also generate sulphides or sulphates during the rubbing process [26]. However, the wear results in Fig. 5-10 show that detergents can reduce wear under certain conditions. Therefore, for FFO containing both ZDDP and detergents, synergistic or antagonistic effects may occur under different working conditions, resulting in a two-phase wear mechanism.

5.2.3 *Chemical Analysis of Tribofilms after Changing Oils by EDX*

In order to further understand the changes in the contents of chemical elements in the tribofilm before and after the oil change tests, EDX is used to detect the content and distribution of P, S, Ca and Zn elements contained in the tribofilm on the ball and the disc, as shown in Fig. 5-11. From the micrographs of the scanned area of tribofilm (grey images), the distribution of tribofilm on the ball is more even than that on the disc, in which the tribofilm is dot-like while the shape of tribofilm on the disc shows a band-like distribution.

The images in the first row show the results of the test with FFO for 4 hours, as a reference before the oil change test. It can be seen that the contents of S and Ca in the tribofilm on the ball and the disc are relatively high, and the tribofilm also contains a small amount of P. However, the Zn element is not detected. After continuing the test with FFO for another 2 hours, that is, the tests for 6 hours with FFO, the proportions of P and S on the ball increase by 0.1% and 0.2% respectively, and 0.5% of Zn is detected. The ratio of the four elements on the disc is unchanged compared with the results before the oil change. That is to say, Zn is present in the tribofilm produced by FFO, and the error comes from the difference of samples.

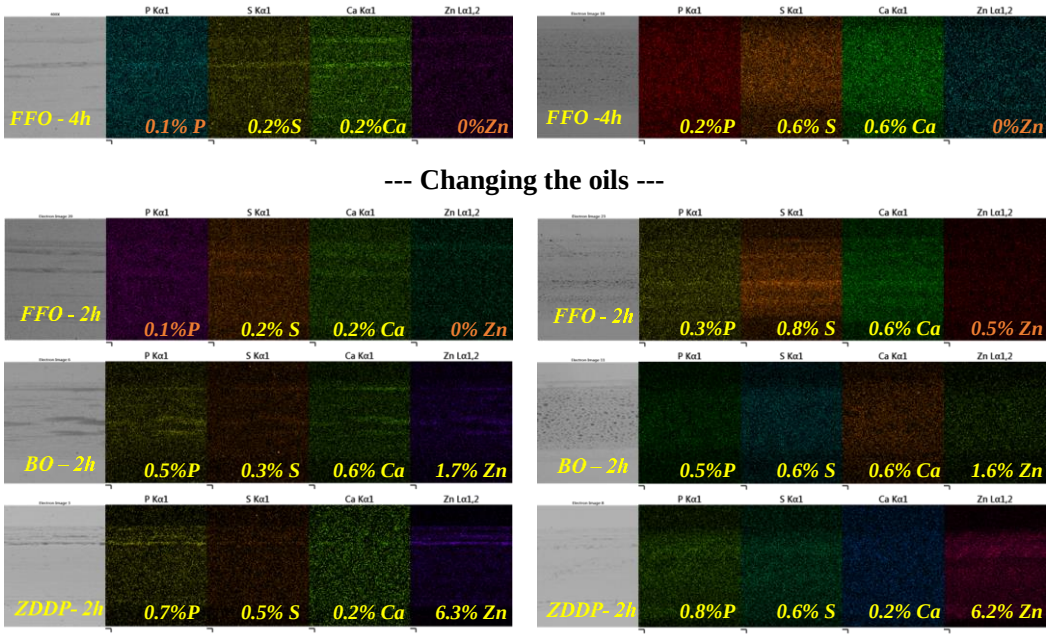

Fig. 5-11 Chemical elements of tribofilms and their relative contents on the steel balls and steel discs before and after changing the oils. (The orange colour means that the presence of the element is unstable.)

Ideally, after replacing to base oil, there is no additive supplying the contact zone, so the next two-hour test is the process of removal and re-formation of the components in the generated tribofilm itself. When the oil is changed to base oil, it can be seen from the results in the third row of Fig. 5-11 that the ratios of P and Zn in the tribofilm on the ball or the disc increase. In addition, although the content of S and Ca on the ball remains the same numerically compared to the one with FFO, the actual ratio of S and Ca has a reduction, which may be because a small amount of it enters the base oil during the rubbing process. From the results of EDX, the increase of P and Zn ratios suggests that the proportion of zinc phosphate in tribofilm increases slightly, which may be one of the reasons for the lower wear in this test with base oil.

When the oil is replaced by the base oil with ZDDP, it is clear that from the images in the last row the content of the Zn element increases significantly, as well as the ratio of P. The ratio of S has a little increase only on the disc while the ratio of Ca has a reduction only on the ball. In the absence of additional Ca ion supplementation, the new zinc phosphate produced by ZDDP gradually replaces the calcium phosphate and other Ca containing-components in the original tribofilm formed by FFO during the rubbing

process. This can explain why the tribofilm thickness decreases largely after the oil change. The wear volume changes the least after the oil change, which may also be attributed to the increase in zinc phosphate.

Thus, it can be seen that when the ratios of P and Zn increase, that is, when the content of zinc phosphate increases, wear will reduce. Then, in the tribofilm formed by FFO, the higher ratio of S and Ca is the key to the higher wear rate of FFO. It can be inferred from this that in the experiment of replacing FFO with detergent which can only provide the S and Ca, the ratios of S and Ca in the tribofilm increase, so the wear will increase. It is consistent with the results of wear in Fig. 5-10 that the test with detergent has higher wear than that with ZDDP and base oil.

5.3 *Summary*

This chapter first studies the tribofilm growth and wear behaviours and their correlations at different temperatures. Then, the effects of a single additive on maintaining the tribofilm thickness and on wear are studied by changing FFO to the base oil with different additives. The main results are summarised as follows.

1) In the tested temperature range of 60-120 ℃, when the temperature increases, the tribofilm thickness increases when it reaches the stable phase. However, the corresponding wear results are divided into two phases: (I) 60-80℃, wear increases with tribofilm thickness; and (II) 80-120℃, wear decreases when the tribofilm thickness increases. The two-phase wear mechanism is different from the wear trend of ZDDP mono-oil that when the temperature increases from 60 ℃ to 100 ℃, wear decreases as the tribofilm thickness increases [179]. In addition, the changing trend of wear amount in Phase (I) is not stable. For example, at 75 ℃, when the test time is less than 180 mins, the wear amount is lower than that at 80 ℃, while when the test time is 360 mins, the wear amount is higher.
2) It can be seen from XPS analysis of the chemical compositions of tribofilm at 60, 75 and 120℃ that the main component of bulk tribofilm is calcium phosphate rather than zinc phosphate. When the tribofilm thickness increases, calcium phosphate increases. At 75℃, where the wear amount is the least one, both intensities of the XPS signal representing sulphides and sulphates are the largest. In addition, wear at 60 ℃ is greater than that at 120 ℃, and the former has a larger

sum of sulphides' peak areas, while the latter contains more sulphates and phosphates. Therefore, it indicates that the wear mechanism is influenced by both sulphides and phosphates.

3) In the experiment of using different additives with base oil to replace FFO, it was found that the use of detergent can cause both tribofilm thickness and wear to increase, while the use of ZDDP has the least change in wear. In contrast, the amount of wear using FFO only is much higher than that of replacing different additives.
4) In the EDX analysis, S% and Ca% in the tribofilm produced by FFO are higher than that of P and Zn. The types of detergent in FFO are mainly over-based calcium sulphonate and calcium phenate, which mainly provides S and Ca elements for the components of tribofilm. According to the analysis results of EDX, compared with ZDDP alone, S% and Ca% increase in the tribofilm using FFO, resulting in higher wear.
5) After replacing FFO by base oil and ZDDP (with base oil), the relative ratio of P and Zn has increased significantly, especially ZDDP. Combined with the growth curve of tribofilm, it shows that after replacing by ZDDP, the main composition of tribofilm is changed to zinc phosphate, which may be one of the reasons for wear reduction.

The first chemical analysis indicates that the chemical reaction of the detergent during the formation of tribofilm plays an important role in the wear mechanism. The calcium phosphate is not as effective as zinc phosphate formed by ZDDP in reducing wear. However, compared with FFO, there is a clear decrease in wear after changing FFO with detergent mono-oil. Therefore, the wear mechanisms of FFO cannot be simply attributed to the effect of one additive. More tests are needed to investigate the correlation between the chemical compositions of tribofilm and wear under different working conditions.

In the two-phase wear mechanism, the relationship between the tribofilm thickness and wear of Phase (II) is more similar to the trend of ZDDP, especially when the temperature reaches 120 ℃, the reduction of sulphur-containing compounds and the formation of a large amount of phosphate can be detected. In this case, wear reduces due to the formation of tribofilm. In the lower temperature range of Phase (I), the increase of tribofilm thickness fails to reduce wear. It is speculated that one of the reasons may be that the

formation of tribofilm is dominated by the detergent, and the wear mechanism is mainly determined by the sulphur-containing compounds. In addition, since the tribofilm thickness is significantly lower in Phase (I), it cannot be ruled out that the test conditions enter the mixed lubrication regime due to the higher viscosity of lubricant at low temperature, thereby reducing surface contact, resulting in a decrease in tribofilm thickness and wear.

In the next chapter, the λ ratio is reduced by reducing the entrainment speed to make the experimental conditions closer to the boundary lubrication regime and to study the tribofilm and wear at different temperatures. The surface analysis of Raman and the depth profiling analysis of XPS are used to investigate sulphides and phosphates in tribofilm in more detail, and to obtain the change of chemical compositions in tribofilm along the depth direction.

Chapter 6 Joint Effects of λ ratio and Temperature on the Tribological Properties of the Fully Formulated Oil and Wear Mechanisms

In this chapter, the influence of the lubrication regime on the growth and wear behaviour of tribofilm is studied by changing the λ ratio. On the one hand, it is necessary to eliminate the influence of viscosity at lower temperatures, and on the other hand to confirm the universality of the two-phase wear mechanism under boundary lubrication conditions. The experiment is mainly divided into two parts. First, the Stribeck curves at different temperatures are obtained by the MTM test rig to understand the changes in the lubrication regime under the growth stage of the tribofilm. Secondly, by reducing the λ ratio to make the experimental conditions closer to boundary lubrication, the growth and wear behaviour changes of tribofilm at different temperatures are studied. Based on the MTM results, Raman analysis is used to study the presence of phosphates and sulphides in tribofilm at different λ ratios and temperatures. Then, through the depth profiling analysis of XPS, the distribution of the chemical compositions of tribofilm from surface to depth and its correlation with wear can be understood in more detail.

6.1 *Stribeck Curves at Different Temperatures*

The Stribeck curve illustrates the relationship between friction coefficient and the lubrication parameter Hersey number (dynamic viscosity x load/entrainment speed). Under the same temperature and working conditions, it is considered that the viscosity of the lubricant does not change much, and the load is constant, so the abscissa is simplified to the entrainment speed in the logarithmic representation. Fig. 6-1 shows the Stribeck curves at four temperatures 60, 80, 100 and 120 ℃ under the influence of the tribofilm formation. The position of the friction coefficient under the entrainment speeds of 0.1 m/s and 0.01 m/s in Stribeck curves are marked with dash lines, respectively.

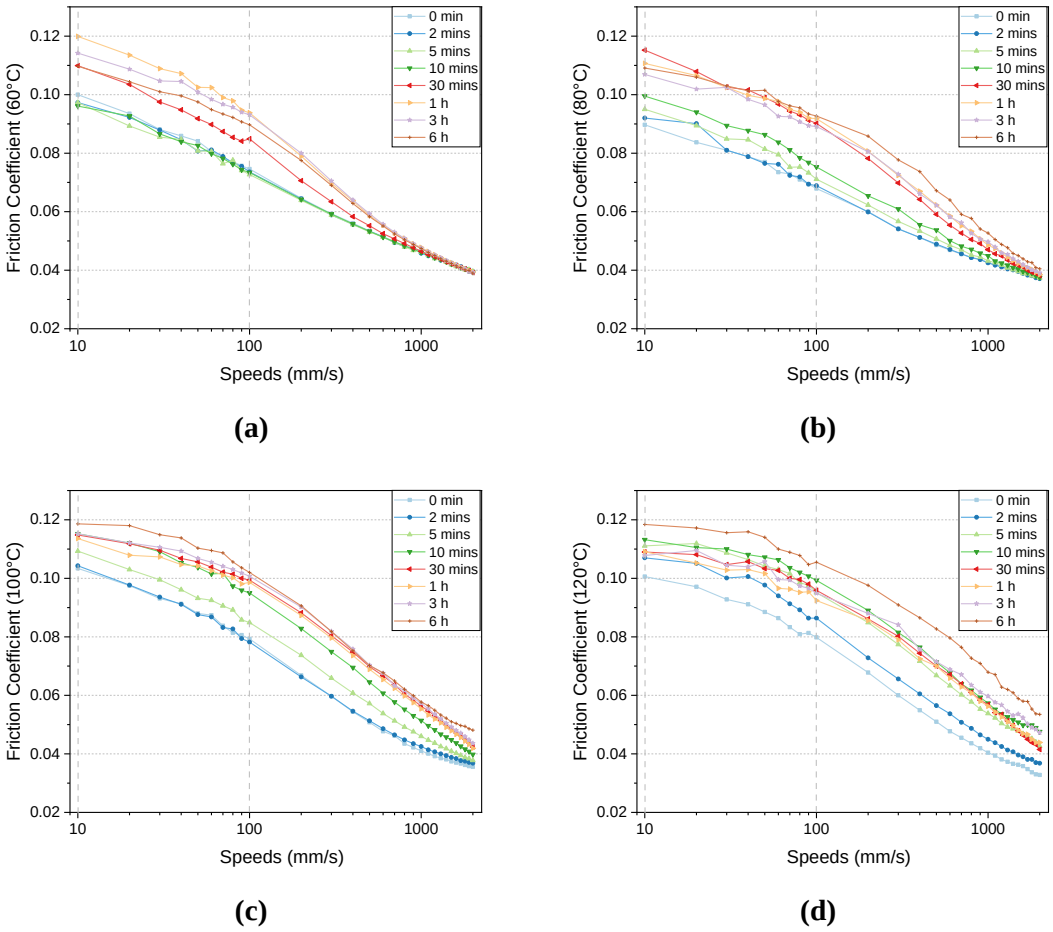

Fig. 6-1 Stribeck curves on steel/steel contact lubricated by FFO at different temperatures (a) 60 ℃, (b) 80 ℃, (c) 100 ℃ and (d) 120 ℃.

When the entrainment speed is 0.1 m/s, the position of friction coefficient in the Stribeck curves is in the transition zone from mixed lubrication regime to boundary lubrication regime at the four test temperatures. However, as the temperature increases, the lubrication regime moves towards the boundary lubrication regime. When the entrainment speed reduces to 0.01 m/s, it can be seen from Fig. 6-1a that the friction coefficient at 60 ℃ has not yet fully reached the plateau stage representing boundary lubrication. However, when the temperature rises to 120 ℃, the friction coefficient reaches the plateau stage at the beginning of the test.

In addition, with the increase of the test time, the increase in the tribofilm thickness not only increases the friction coefficient but also promotes shifting the testing conditions to boundary lubrication. It is most obvious in Fig. 6-1c that under the condition of the entrainment speed of 0.01m/s, when the experiment progressed to 6 hours, a plateau stage of friction coefficient appeared.

The Stribeck curves in Fig. 6-1 are tested by experiments, but the specific λ ratios can be estimated by the ratio of minimum film thickness $h_{\min}$ over the composite surface roughness σ^*, as described in Equ. (6-1).

$$\lambda = \frac{h_{\min}}{\sigma^*} = \frac{h_{\min}}{\sqrt{\sigma_1^2 + \sigma_2^2}} \quad \textbf{(6-1)}$$

where σ_1 and σ_2 are the root-mean-square roughness (RMS) of two contacting surfaces, respectively.

The minimum film thickness $h_{\min}$ is predicted by the Hamrock-Dowson equations [327] for the point contact, see Equ. (6-2).

$$h_{\min} = 3.63 R_x U^{*0.68} G^{*0.49} W^{*-0.073} \left[1 - e^{-0.68k}\right] \quad \textbf{(6-2)}$$

In the estimation of λ ratios, the pressure-viscosity coefficient α is 1.81×10^{-8} Pa^{-1} ; the viscosity at ambient pressure η_0 at different temperatures 60, 75, 80, 100, and 120℃ are estimated as 0.057, 0.036, 0.031, 0.017 and 0.009 kg/m·s (relative to SAE10W), respectively.

The values of λ ratio as the function of the temperature under the influence of different entrainment speeds are shown in Fig. 6-2. According to the classification of the lubrication regime, when λ<1, it can be considered that the experiment has reached the boundary lubrication condition. However, compared with the Stribeck curves in Fig. 6-1, when the entrainment speed is 0.1 m/s, although the estimated value of λ is less than 0.4 at the four test temperatures, the plateau stage of friction coefficient is not reached. When the entrainment speed is reduced to 0.01 m/s, λ is less than 0.1, but boundary lubrication is only achieved in the Stribeck curve at 100 ℃ and 120 ℃.

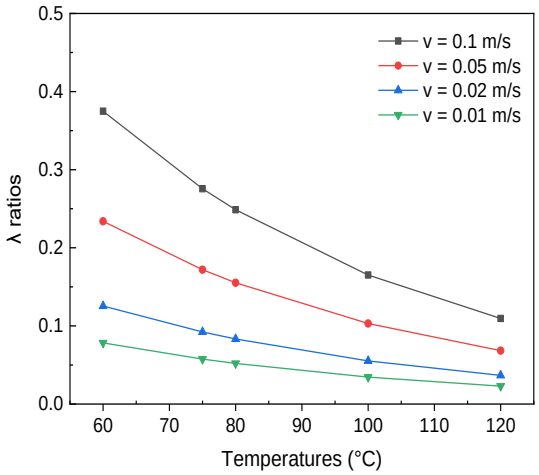

Fig. 6-2 The values of the λ ratio as the function of temperatures at different entrainment speeds, estimated by the Hamrock-Dowson equation.

Nevertheless, ignoring the error caused by the tribofilm growth and wear in the theoretical calculation of λ ratio, it is considered that when the entrainment speed is 0.01m/s, the λ ratios at the four test temperatures are all small enough to achieve boundary lubrication. In addition, the values of η_0 may be overestimated, so the actual λ ratio should be less than the calculated value. Thus, the influence of temperature on the viscosity of lubricating oil can be ignored.

6.2 *Tribofilm Growth and Wear Behaviour at Different λ Ratios*

6.2.1 *Tribological Results*

Fig. 6-3 shows the tribofilm growth results as the function of time at the lower λ ratio by reducing the entrainment speed to 0.01 m/s under different temperatures (solid lines). The dashed lines are the results at the higher λ ratio under different temperatures for comparison, which are also presented in Chapter 5. The rest of this section will use the low and the high λ ratio instead of entrainment speeds of 0.01 m/s and 0.1 m/s, respectively.

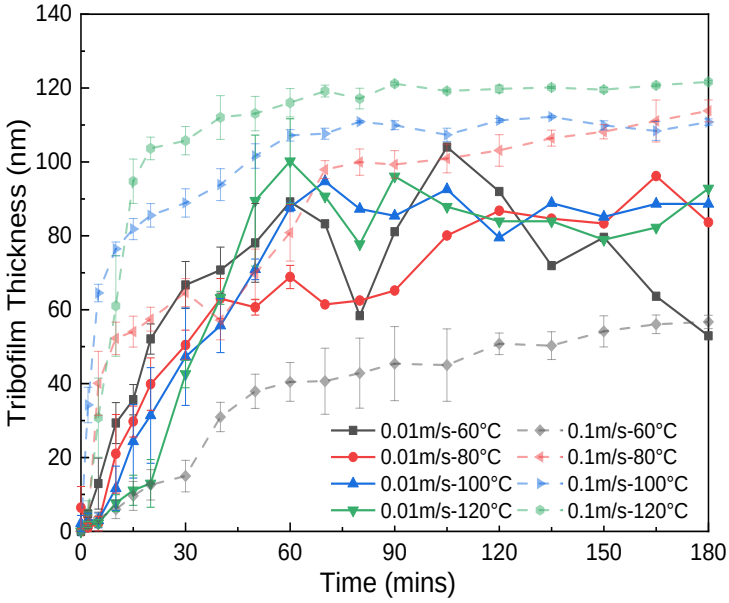

Fig. 6-3 MTM-SLIM results of tribofilm growth at different temperatures with a low entrainment speed of 0.01 m/s (solid lines). The dashed lines are the results at a speed of 0.1m/s at different temperatures for comparisons.

At the low λ ratio, the differences among the tribofilm thickness at different temperatures are small. When the tribofilm grows to the stable phase, the tribofilm thickness remains basically to 85 nm, but the thickness at 60 ℃ has a large fluctuation. In addition, at the first 30 minutes of testing, during the growth phase of tribofilm, the initial growth rate of tribofilm has a slight decrease with the increase in temperature, which means that temperature has a certain influence on the tribochemical reactions in the early growth stage of the tribofilm.

Fig. 6-4 exhibits the friction coefficient results corresponding to the tribofilm growth curves in Fig. 6-3 under different temperatures. The solid lines are the results at the low λ ratio and the dashed lines are those at the high λ ratio.

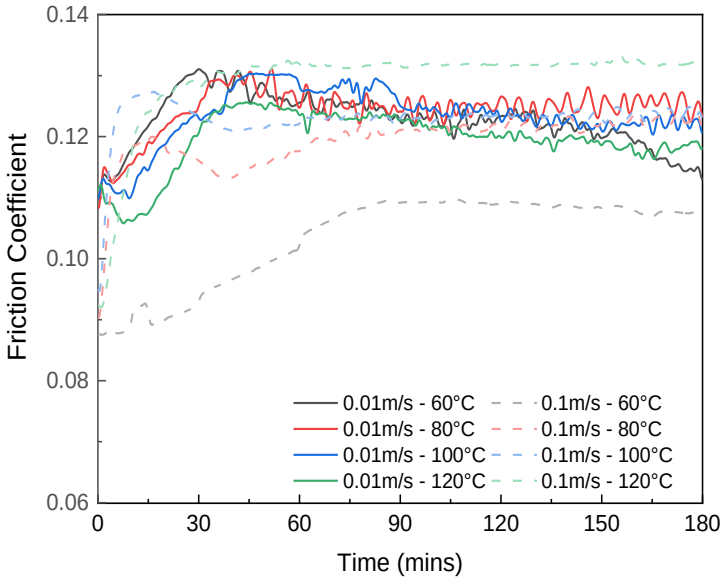

Fig. 6-4 MTM-SLIM results of friction coefficient at different temperatures with a low entrainment speed of 0.01 m/s (solid lines). The dashed lines are the results at a speed of 0.1m/s at different temperatures for comparisons.

When the λ ratio is low, the variation trends of friction coefficient with temperature and the corresponding growth curves of tribofilm have a certain similarity. That is, in the growth stage of tribofilm, the friction coefficient increases with the increase of tribofilm thickness. However, it is different from the results under the high λ ratio that the friction coefficient at higher temperature has a lower value at the beginning 30 minutes of tests. Then, the friction coefficient at all four temperatures begins to stabilise after about 40 minutes of testing, and the differences of the values at this stage are very small. Especially a slight decrease and then increase of friction coefficient can be observed in the first 10 minutes of the test at both 100 ℃ and 120 ℃.

In comparison with the results at the high λ ratio, as shown in Fig. 6-5, only under the condition of 60 ℃, the reduction of λ ratio increases the tribofilm thickness in the stable stage, so the friction coefficient increases. However, in the condition of 80~100 ℃, the tribofilm thickness in the stable stage decreases, but the difference in the friction coefficient between the two λ ratios is small. At 120 ℃, both the tribofilm thickness and the friction coefficient decrease as the reduction of λ ratio. This also indicates that the variation of friction coefficient of FFO cannot be estimated only by the tribofilm thickness, and it may also be related to roughness and other factors like ZDDP tribofilm. Under

boundary lubrication conditions, different trends may indicate that the chemical compositions of FFO tribofilm at different temperatures are also different.

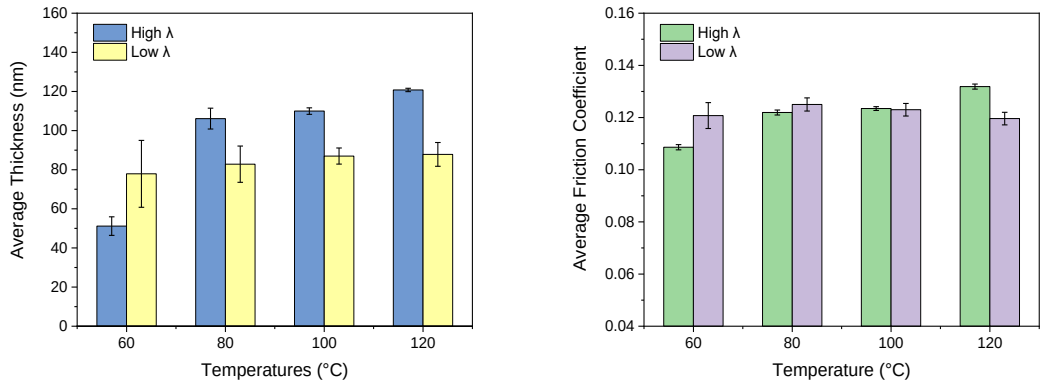

(a) **(b)**

Fig. 6-5 Comparisons of (a) tribofilm thickness and (b) friction coefficient in the stable phase at high and low λ ratio, respectively.

Fig. 6-6 shows the wear volume after rubbing for 30 mins and 180 mins at the low λ ratio and after testing for 180 mins at the high λ ratio under four temperatures 60, 80, 100 and 120 ℃. At the low λ ratio, the maximum wear volume still appears at 80 ℃ which is consistent with the result at the high λ ratio, which is confirmed that the wear mechanism of FFO has the characteristics of two phases at both λ ratios, that is, in boundary lubrication regime.

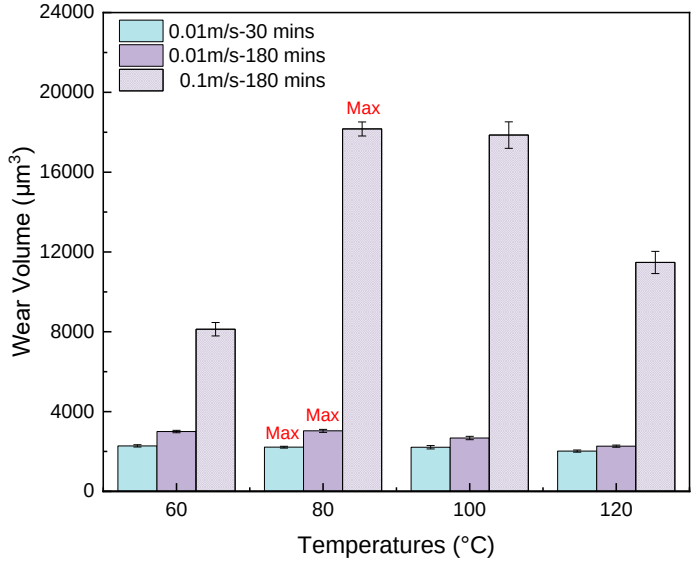

Fig. 6-6 Wear results after testing for 3 hours as a function of temperatures at different entrainment speeds by NPFLEX.

Although the effect of temperature on the tribofilm thickness and friction coefficient reduces when the λ ratio decreases, the temperature with the highest wear volume is almost unchanged. Furthermore, it can be reasonably speculated that the two-phase wear mechanism of FFO is more likely to be caused by the different reaction process of tribofilm generation and/or the different chemical compositions of tribofilm in the stable phase under different temperatures. Therefore, the chemical analysis of the tribofilm is required and the focus will still be on the phosphates and sulphur-containing compounds.

In the next sections of chemical analysis, the differences of both phosphates and sulphur-containing compounds in the tribofilm generated at different temperatures and λ ratios will be discussed. The presence of phosphates and sulphides under different conditions were preliminarily detected by Raman spectroscopy. Then, the depth profiling analysis of XPS was used to study the distribution of chemical components in the tribofilm and the atomic percentage of key elements along with the depth direction.

6.2.2 *Raman Analysis*

The chemical compositions in the tribofilm on the ball and disc can be detected directly by using Raman spectroscopy. The specific measurement methods are described in Section 4.3.2 of the Methodology. In several spectra detected on the same part of ball and disc samples, the spectrum with the strongest signal peak is chosen to represent the maximum content or final structural state of the substances that can be measured under this working condition. Thus, the spectra with the highest intensity under different test conditions will be the focus of comparison and discussion in the next sections.

It is known from Chapter 5 that the FFO tribofilm generated at the high λ ratio mainly contains sulphides and phosphates. Therefore, sulphides and phosphates are also the focus in the Raman analysis for both λ ratios. The evolution of their contents or structures with test time will be discussed as well as the changes under different temperatures or λ ratios.

6.2.2.1 *Sulphides*

The possible types of sulphides in tribofilm may be FeS/FeS_2, ZnS and CaS. According to the reference spectra of these sulphides [328-331] in the literature, the representative peaks are shown in Fig. 6-7, so the range of Raman shift is selected to be 200~500 cm^{-1} for the analysis of sulphides under different working conditions.

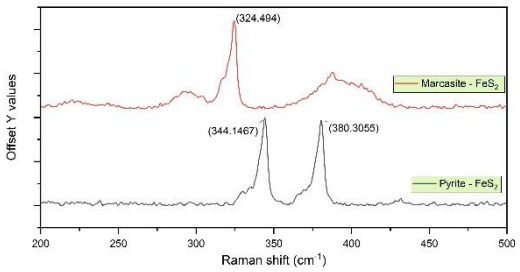

(a) FeS_2 – Marcasite and Pyrite crystal [328]

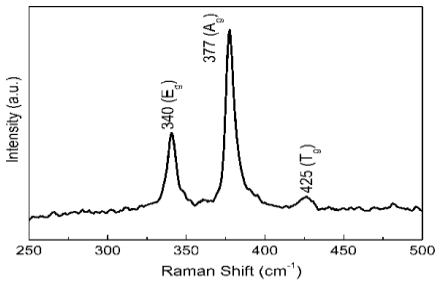

(b) FeS_2 – Pyrite [329]

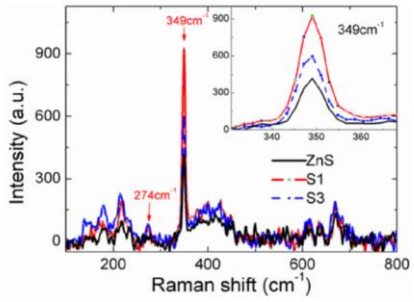

(c) ZnS [330]

Fig. 6-7 The reference Raman spectra of sulphides in different microstructures and types.

At different temperatures and λ ratios, the sections representing sulphides in Raman analysis are shown in Fig. 6-8. In addition, Fig. 6-8 (a-d) also includes the evolution process of the types and contents of sulphides in tribofilm with the test time at different temperatures under the condition of low λ ratio.

It can be clearly seen that at the low λ ratio, as the test progress to 3 hours (blue lines), the Raman spectra are mainly composed of a strong peak at 375 cm^{-1} accompanied by a small peak at 339 cm^{-1} and a weak peak at 419 cm^{-1} at all tested temperatures, which is consistent with the reference spectrum of pyrite-FeS_2 in Fig. 6-7b. This indicates that when the tribofilm growth reaches a stable stage, although the change of thickness is small at four temperatures, the pyrite-FeS_2 in tribofilm decreases with the temperature rise in the range of 60~100 ℃, then it increases slightly at 120 ℃.

In addition to the pyrite peaks, there is a peak located at 312~318 cm^{-1} appearing with the first hour of the test, which may show another FeS_2 microstructure in tribofilm, that is marcasite exhibited in Fig. 6-7a. This peak is especially apparent in spectra after testing for 30 mins at 80 ℃ and 100 ℃, and its intensity decreases with the increase of the test time, but the intensity of pyrite-FeS_2 increases at the same time.

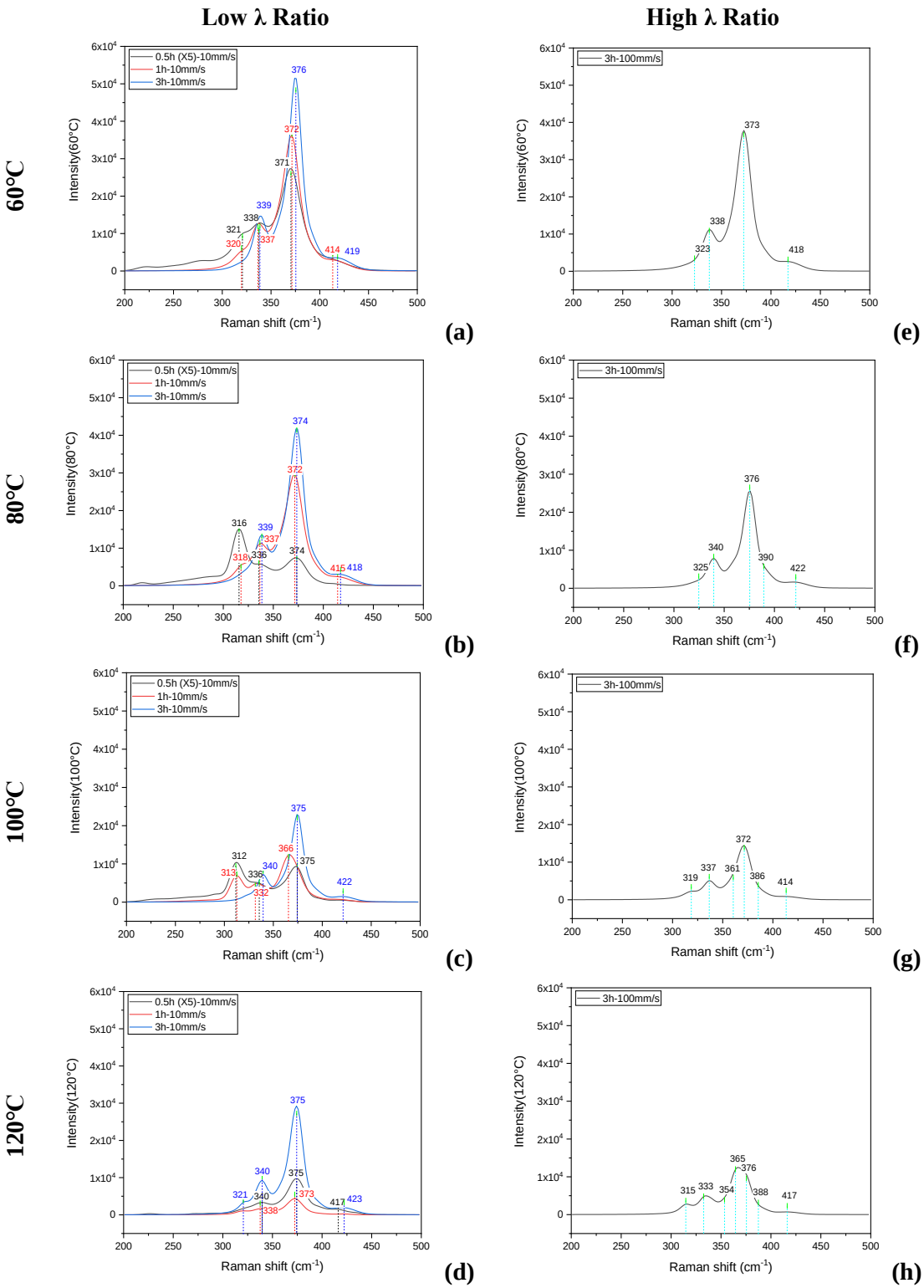

Fig. 6-8 The sections of sulphides in the Raman spectra from 200 cm^{-1} to 500 cm^{-1} at different temperatures and λ ratios. (a-d) are the spectra of the sulphides in the tribofilm after testing for 0.5h, 1h and 3h under different temperatures at the low λ ratio. (In order to show more clearly, all the results at 0.5h are enlarged by 5 times). (e-h) are the results only at 3h under different temperatures at the high λ ratio for comparisons.

Fig. 6-8 (e-h) shows the Raman spectra of the sulphides in the tribofilm at the high λ ratio after testing for 3 hours under four temperatures. Similar to the results of low λ ratio tests, it is the most apparent that there are also three peaks assigned to the reference spectrum of FeS_2-pyrite (see Fig. 6-7b) at all temperatures, although there is a slight deviation in the peak positions. Especially the peak at 365 cm^{-1} in the spectrum for 120 ℃, which may be caused by errors of calibration or other kinds of sulphides. In addition, the weak peaks at 319 cm^{-1} and 315 cm^{-1} appear at 100 ℃ and 120 ℃, respectively, which may also be attributed to the marcasite structure of FeS_2.

In contrast, when the tribofilm thickness reaches the stable phase, more sulphides are produced at the condition of the low λ ratio after three hours of testing. In both results of high and low λ ratios, the main type of sulphides obtained by Raman analysis is FeS_2 of the pyrite structure. However, under some working conditions, especially when the spectral signal is weak, FeS_2 of the marcasite structure appears. Moreover, except for the spectra 120 ℃ under the condition of the low λ ratio, the peak area of FeS_2 decreases with the increase of temperature at both λ ratios.

In particular, it can be seen from the reference spectrum of Fig. 6-7 that the symbolic peak of ZnS is located at 349 cm^{-1} [330, 331], which is not shown clearly in the Raman results. In addition, the main Raman frequencies of Ca-S are 285 cm^{-1}, 215 cm^{-1}, 185 cm^{-1} and 160 cm^{-1} [332], which are not found in the measurement range of the Raman analysis.

Compared to Raman results of ZDDP tribofilm in the reference, the peaks of sulphides detected may be Fe-S at 386 cm^{-1} and Zn-S at 351 cm^{-1} [333]. However, for the engine oil containing ZDDP and calcium S-based detergent, the peak of FeS_2 was detected [334]. Thus, the iron sulphides detected in FFO tribofilm are mainly from the product of interaction between ZDDP and detergent.

6.2.2.2 *Phosphates*

Due to the different structures and chain lengths of phosphates, there should be different vibration modes, resulting in a variety of Raman peaks. Taking zinc phosphate and calcium phosphate as examples, Raman frequencies corresponding to vibration modes of different phosphate groups are listed in Table 6-1, respectively [335, 336]. Although the Raman peak of phosphate has a wide frequency range, the Raman analysis results of FFO

samples show that the main range of the peaks appears at 800-1200 cm^{-1} of the Raman shift. The phosphate peaks located at other Raman shifts do not exist obviously in the results. Therefore, the follow-up comparison and discussion will focus on this range.

Table 6-1 Reference Raman bands of zinc phosphate and calcium phosphate [335, 336].

Zinc phosphate		Calcium phosphate	
Shift (cm^{-1})	**Assignment**	**Shift (cm^{-1})**	**Assignment**
970	$(PO_4)_{sym}$ stretch(NBO), Q^0 species	951~960	$(\nu_1PO_4)_{sym}$ stretch
1010	P-O stretch, Q^1 chain terminator	1011~1022	$(HPO_4)_{sym}$ stretch
1048	$(PO_3)_{sym}$ stretch(NBO), Q^1 species	1038~1058	$(\nu_3PO_4)_{sym}$ stretch
1138	P-O stretch, Q^2 chain terminator	573~594	$(\nu_4PO_4)_{asym}$ bend
1206	$(PO_2)_{sym}$ stretch(NBO), Q^2 species	428~433	$(\nu_2PO_4)_{sym}$ bend
1252	$(PO_2)_{asym}$ stretch(NBO), Q^2 species	1071~1084	$(\nu_1CO_3)_{sym}$ stretch
758	POP_{sym} stretch(BO), Q^1 species		
702	POP_{sym} stretch(BO), Q^2 species		
571	Bend mode		

Fig. 6-9 shows Raman spectra of tribofilm representing the peaks of phosphates between 800 cm^{-1} and 1200 cm^{-1} at different temperatures and λ ratios, in which the Fig. 6-9 (a-d) shows the results of tribofilm under the condition of low λ ratio at four test temperatures after testing for 0.5 h, 1 h and 3 h, respectively, while Fig. 6-9 (e-h) only shows the results of tribofilm at different temperatures after testing for 3 hours at the high λ ratio.

As shown in Fig. 6-9, there are mainly two obvious strong peaks and one weak peak. The first peak is located at 951±1 cm^{-1}, which can be assigned to ν_1-PO_4 with the symmetrical stretching mode [336]. In addition, it is more likely to be calcium phosphate at both λ ratios due to its lower Raman shift, as listed in Table 6-1. For most results of the two λ ratios, when the temperature increases, the intensity of this peak increases. In contrast, however, in the results from 60 ℃ to 80 ℃, there is little difference in the intensity of the ν_1-PO_4 peak under two λ ratios. When the temperature rises to 100 ℃, the signal intensity of the ν_1-PO_4 peak at the low λ ratio is slightly stronger. Then, at 120 ℃, the signal intensity at the high λ ratio suddenly increases more than that at a lower λ ratio.

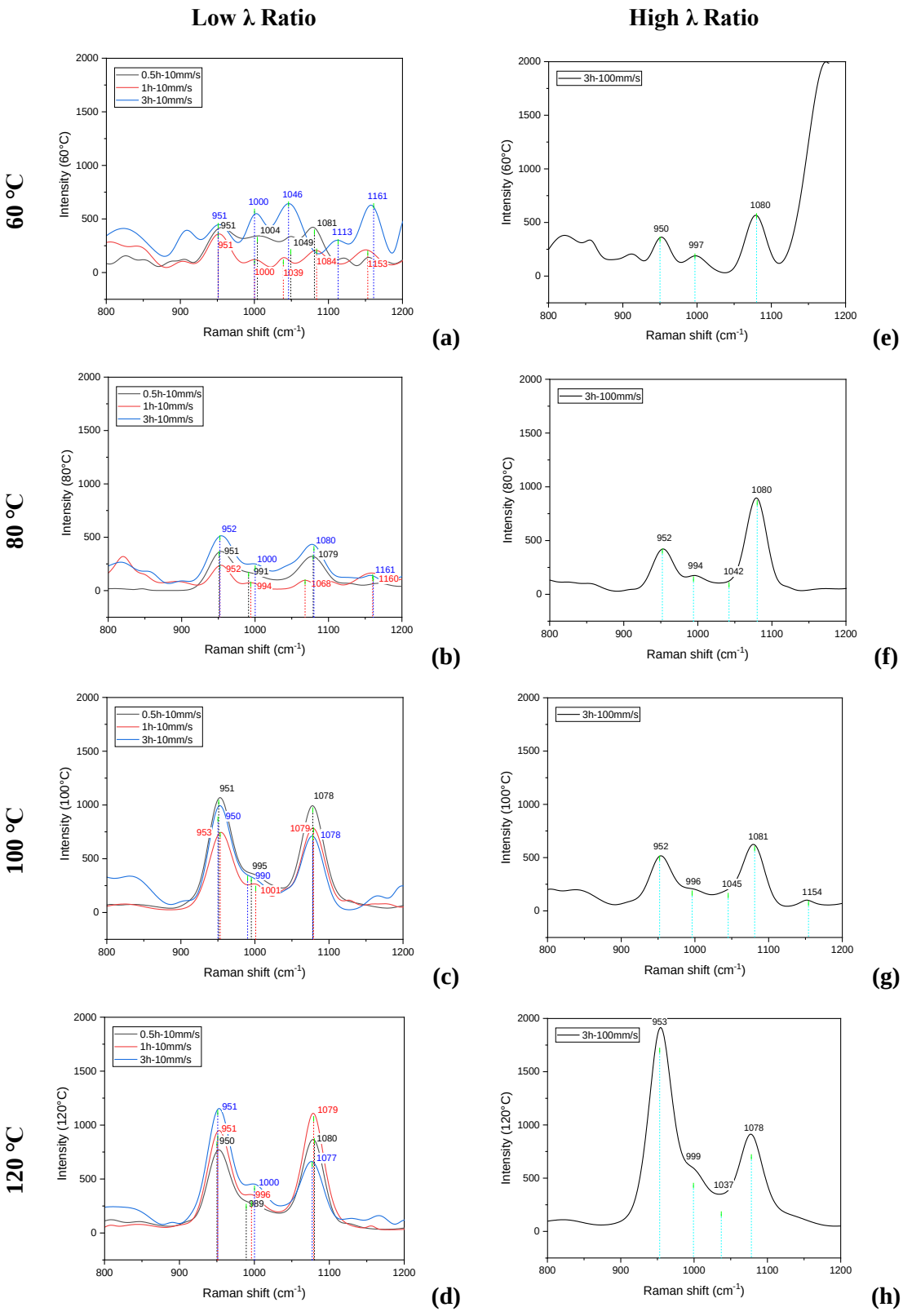

Fig. 6-9 The sections of phosphates in the Raman spectra from 800 cm^{-1} to 1200 cm^{-1} at different temperatures and λ ratios. (a-d) are the spectra of the phosphates in the tribofilm after testing for 0.5h, 1h and 3h under different temperatures at the low λ ratio. (e-h) are the results only at 3h under different temperatures at the high λ ratio.

The second peak is located at 1079±2 cm^{-1}, which can be assigned to ν_1-CO_3 with the symmetrical stretching mode or ν_3-PO_4 with the antisymmetric stretching mode [336]. The latter peak has a lower Raman shift, and its signal intensity is normally no higher than that of the peak ν_1-PO_4. Therefore, it is mainly attributed to the presence of calcium carbonate in this case. In comparison, the signal intensity of this peak at the high λ ratio is higher than that at the low λ ratio when the tribofilm thickness reaches the stable stage after 3 hours of testing. Between the two peaks, a weak peak at 998±2 cm^{-1} may be the terminator P-O stretching mode of the phosphate.

As the temperature is 60 ℃ at the low λ ratio (Fig. 6-9a), the intensities of the three peaks are weak and the disorder of the peaks of phosphates seems to increase. There is a peak around 1046 cm^{-1} appearing which can be assigned to PO_3 with the symmetrical stretching mode (see Table 6-1). Besides, the other two peaks at around 1113 cm^{-1} and 1161 cm^{-1} may be the vibration mode of PO_2 [337, 338]. Studies have shown that the increase in the disorder of phosphate may help reduce the plastic deformation caused by dislocations, resulting in surface hardening and reducing wear [335]. This may be one of the reasons why both tribofilm thickness and wear are lower at 60 ℃.

From the above Raman analysis, there are many similarities in the results at both λ ratios. When the tribofilm reaches a stable stage, the tribofilm at 60 ℃ contains more sulphides, which can be assigned to FeS_2. Phosphate is the main composition of the tribofilm, and its Raman peak intensity and crystallinity tend to increase with increasing temperature, reaching the maximum at 120 ℃. These trends of sulphides and phosphates are consistent with the XPS analysis in Fig. 5-5. The location of the PO_4 peak indicates that the cation bonded to phosphate is more likely to be calcium [336] due to the lower Raman shift, but zinc phosphate may still be present. In addition, the carbonate is present at all four temperatures and is attributed to the calcium carbonate derived from the over-based calcium sulphonate detergent in FFO, but the intensity of the peak reduces slightly when the λ ratio decreases.

The difference is that at the high λ ratio of 120 ℃, the phosphate peak has the highest intensity, which may be related to the tribofilm thickness or the amount of crystalised phosphate contained in the tribofilm. It was found by Okubo *et al.* [337] that the Raman intensities of PO_x and P-O-P peaks are consistent with the thickness of ZDDP tribofilm.

It can be speculated that when the tribofilm thickness increases or the content of phosphate increases, the signal intensity of the ν_1-PO_4 peak may be larger. On the other hand, at the high λ ratio, the peak intensity of calcium carbonate at the temperature range of 60~80 ℃ was significantly higher than that at the low λ ratio, which may indicate more detergent participation in the tribofilm formation at this time. At 120 ℃, the intensity of this peak increases, which may be attributed to the thicker tribofilm or more crystallised film.

Although Raman analysis provides a preliminary result for the type of sulphides and phosphates in the tribofilm, it is obvious that the analysis is not enough to show the peaks related to cations of zinc and calcium. Besides, Raman spectra have limitations for the information of amorphous substances. Thus, further analysis by XPS will not only verify Raman results mutually but also will explore the chemical substances that may be contained in tribofilm from different dimensions, elements and valence states, so as to supplement more information about the chemical compositions of tribofilm.

6.2.3 *Depth Profiling Analysis by XPS*

To obtain the chemical compositions of the tribofilm from the top surface to the substrate, depth profiling combined with elemental analysis (such as C, O, N, P, S, Ca and Zn) are used. The choice of the maximum etching depth depends on the tribofilm thickness and the atomic concentration of Fe. The maximum depth is about 120 nm, calculated by the etching rate of 18.175 nm/mins and the etching time. Results are shown in Fig. 6-10~Fig. 6-15. Since there is no N signal for all tested samples, N spectra are ignored.

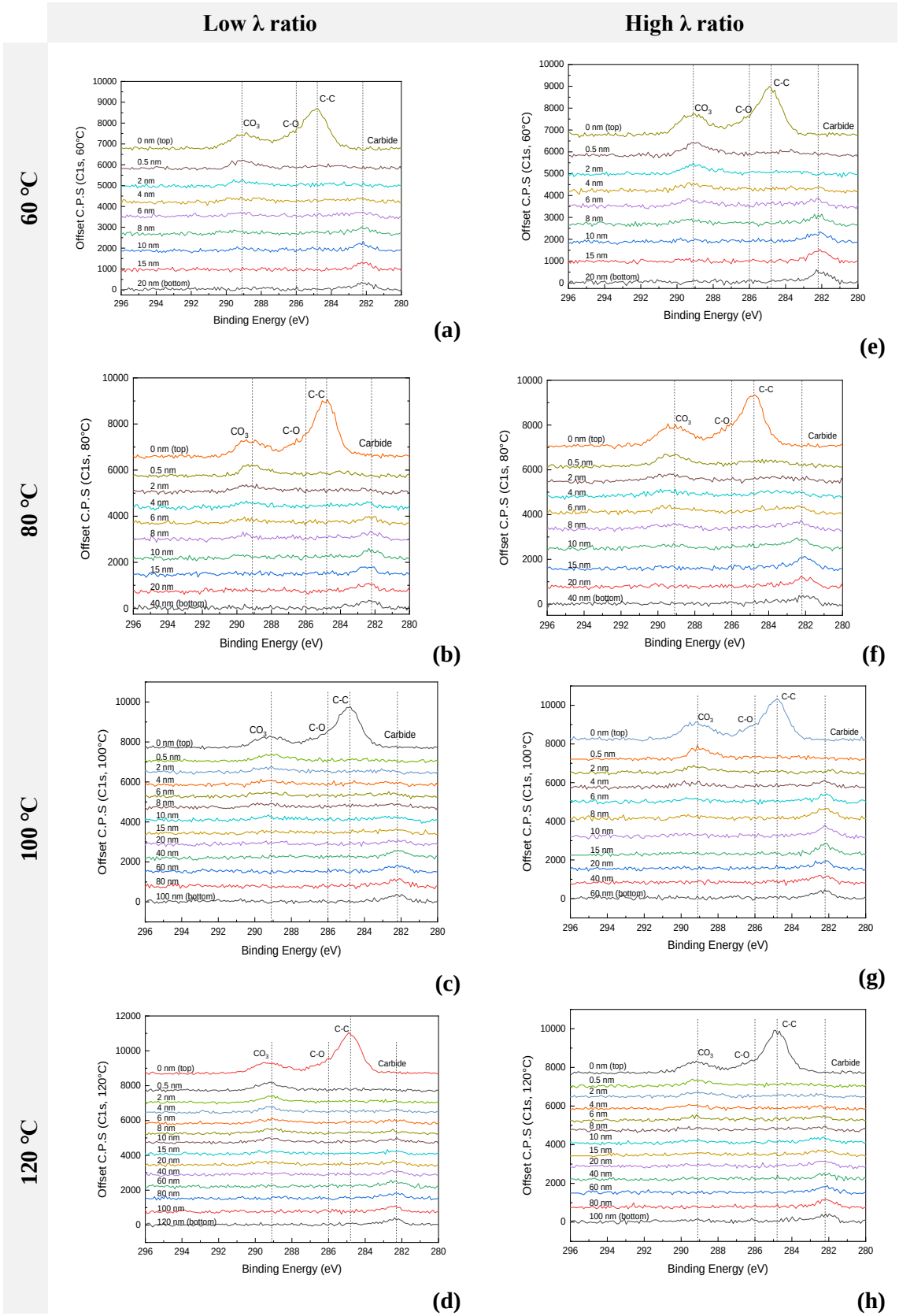

Fig. 6-10 The C1s spectra of depth profiling of tribofilm on the disc after the 3-hour test at different λ ratios and different temperatures by XPS.

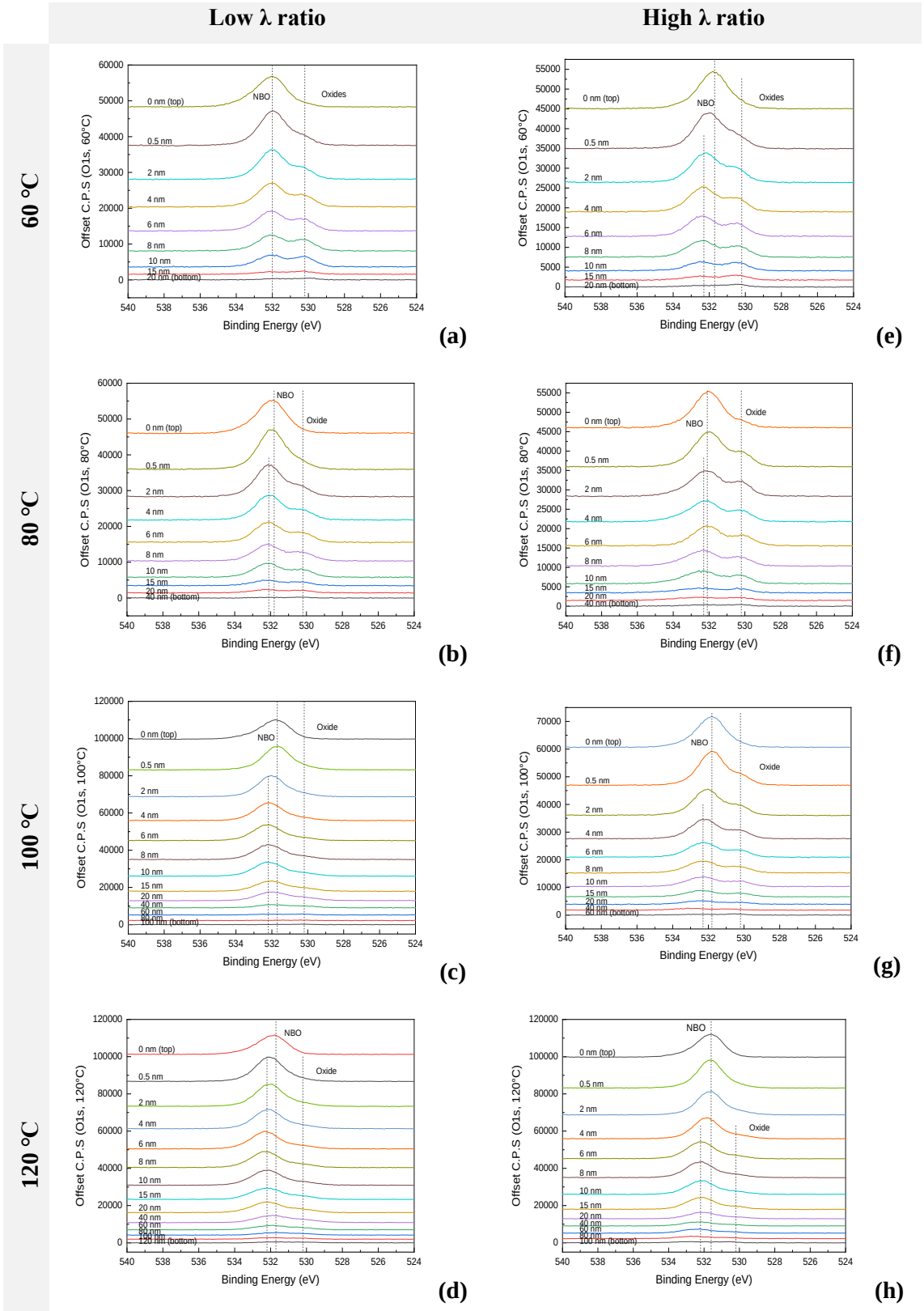

Fig. 6-11 The O1s spectra of depth profiling of tribofilm on the disc after the 3-hour test at different λ ratios and different temperatures by XPS.

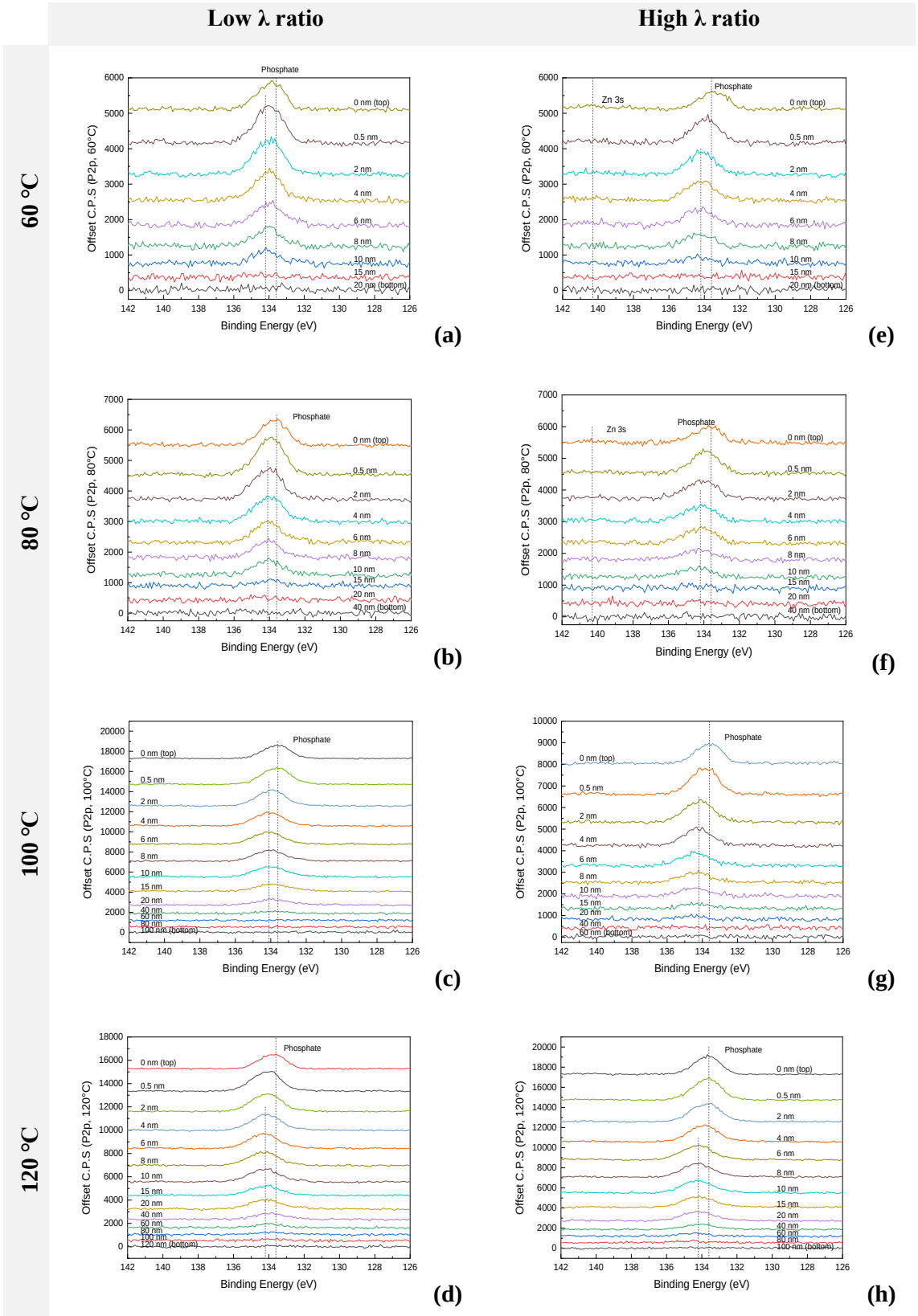

Fig. 6-12 The P2p spectra of depth profiling of tribofilm on the disc after the 3-hour test at different λ ratios and different temperatures by XPS.

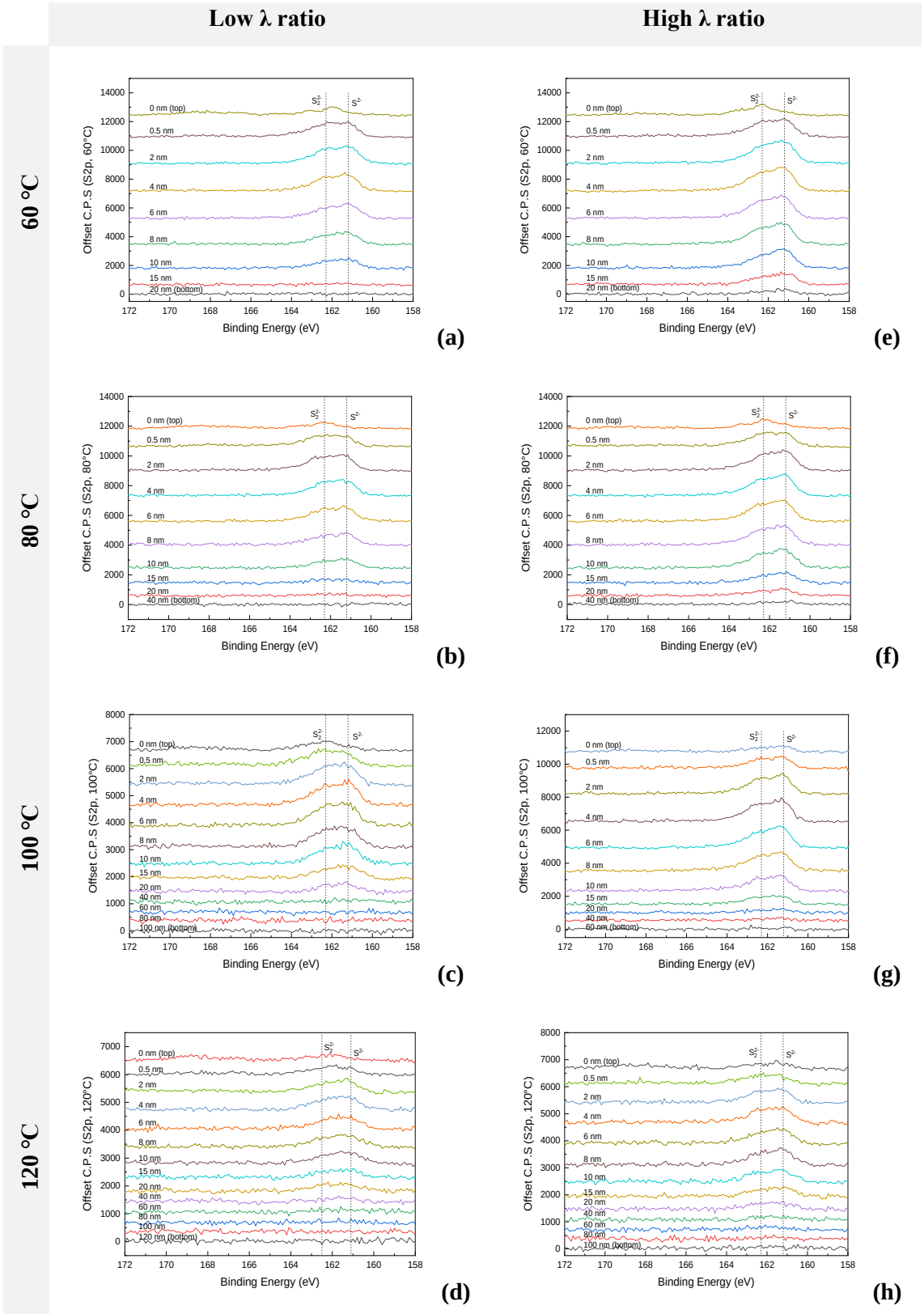

Fig. 6-13 The S2p spectra of depth profiling of tribofilm on the disc after the 3-hour test at different λ ratios and different temperatures by XPS.

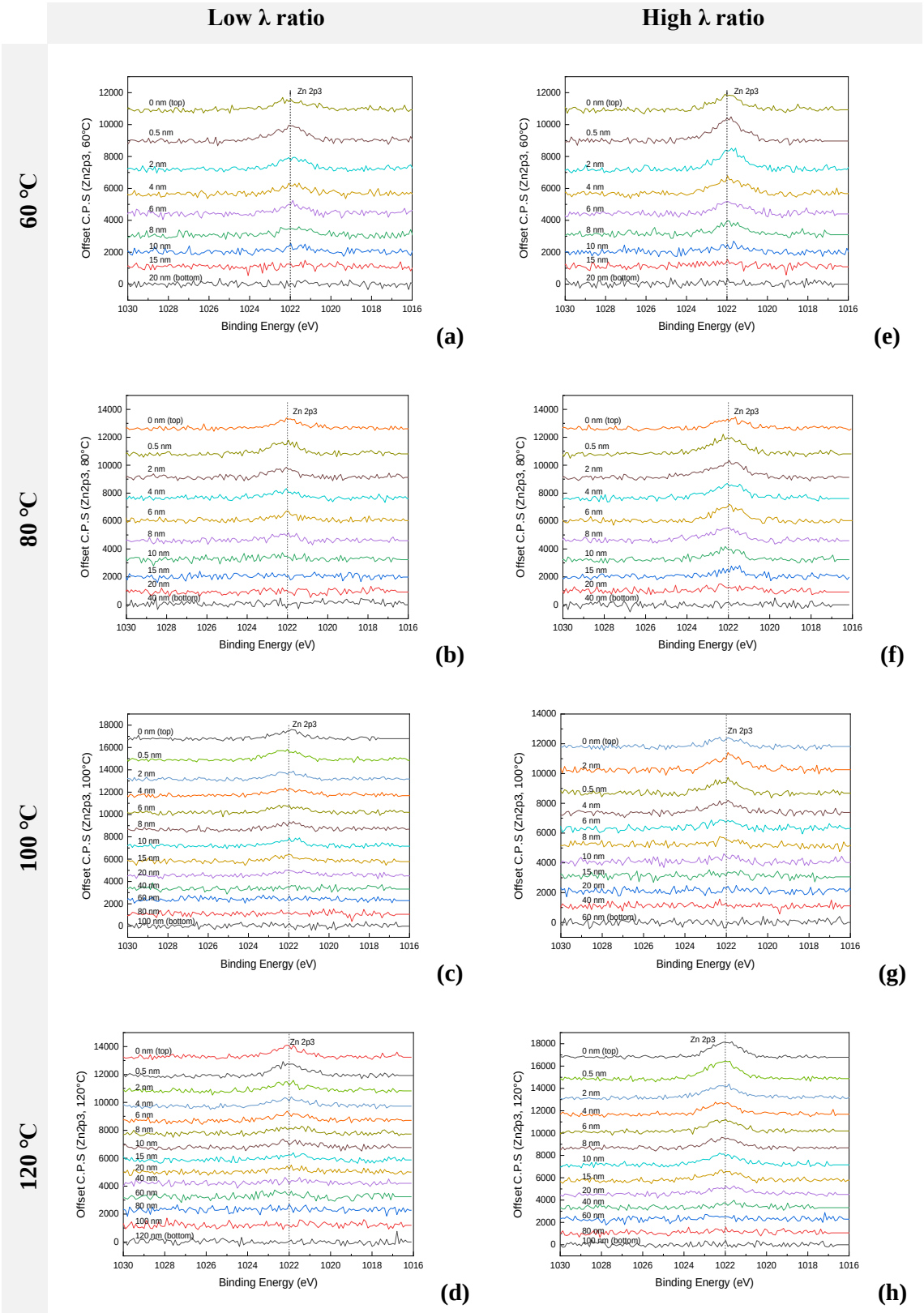

Fig. 6-14 The Zn2p3 spectra of depth profiling of tribofilm on the disc after the 3-hour test at different λ ratios and different temperatures by XPS.

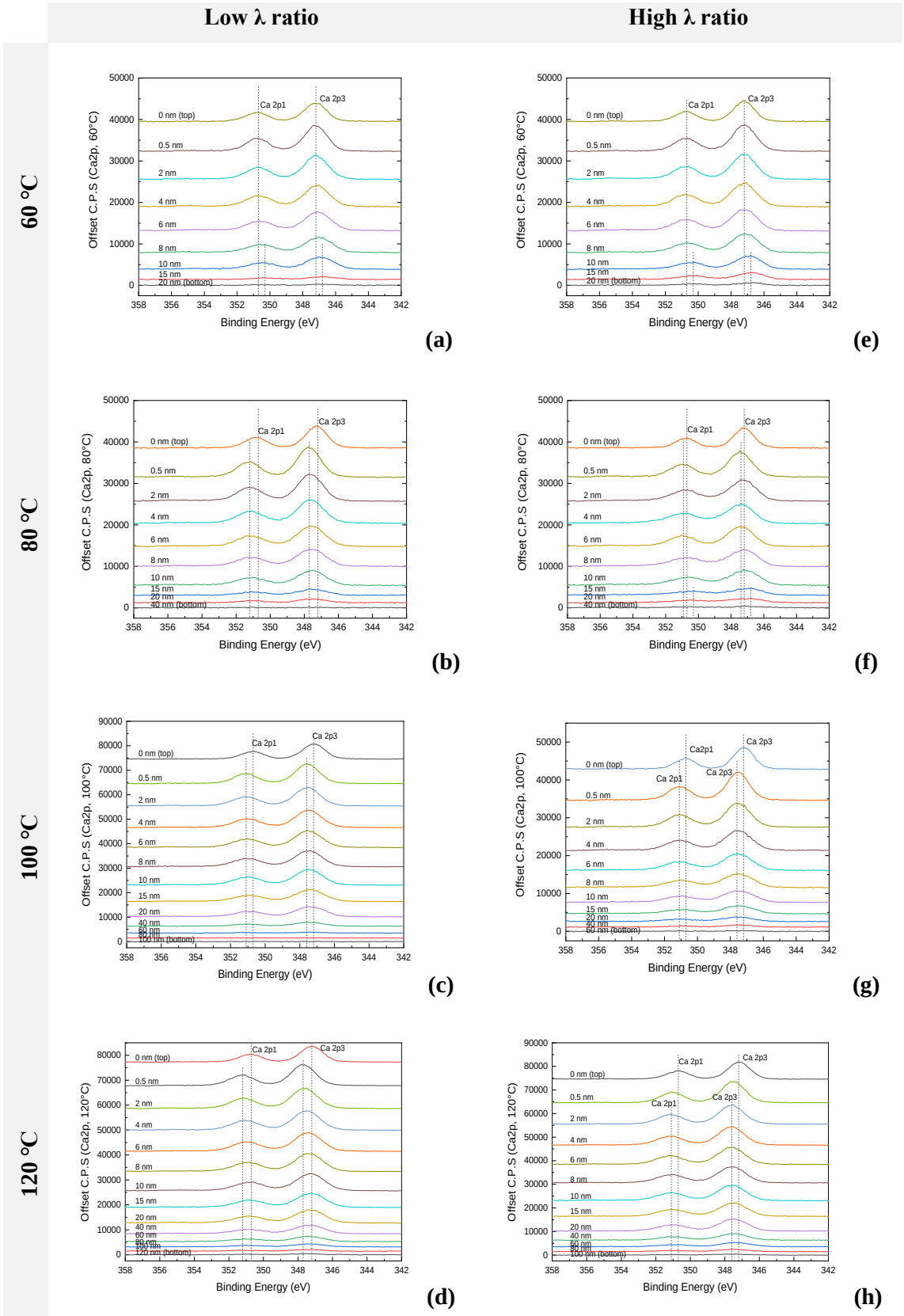

Fig. 6-15 The Ca2p spectra of depth profiling of tribofilm on the disc after the 3-hour test at different λ ratios and different temperatures by XPS.

6.2.3.1 *Carbon 1s Spectra*

Fig. 6-10 respectively shows the variation of C1s spectra with high λ ratio and low λ ratio with etching depth at four temperatures. Two separate peaks can be observed on the surface, 284.8 eV and 289.1 eV are attributed to the organic carbon bond (C-C, C-H) and the carbonate (CO_3) in calcium carbonate [22, 310, 311], respectively. Another hidden peak at 286 eV is the C-O bond in carbonate [309]. With the increase of the etching depth, the peak intensity of carbonate groups was significantly weakened, and the other two peaks disappeared. Then a peak between 282 eV and 282.5 eV appeared, which was assigned to the peak of carbide [312, 313], indicating that the depth reached the iron substrate.

According to the etching depth at which carbonate peak appears, it appears on the surface of tribofilm about 10 nm thick, which is consistent with the results of many studies on tribofilm produced by the over-based calcium sulphonate detergent [19]. The bar charts in Fig. 6-16 shows the peak area of carbonate as the function of temperatures at different λ ratios. The maximum value appears at 80 ℃ and 60 ℃ at the high and the low λ ratio, respectively, which indicates that the detergent may participate in the tribofilm formation at the lower temperature range.

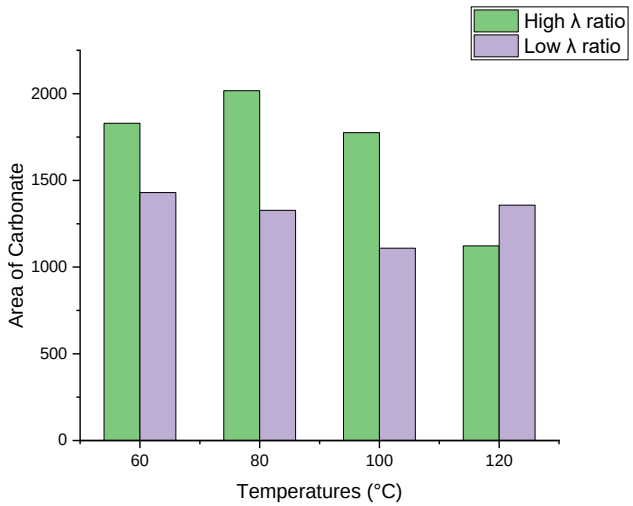

Fig. 6-16 The peak area of carbonate as the function of temperatures at different λ ratios.

6.2.3.2 *Oxygen 1s Spectra*

As shown in Fig. 6-11, there are mainly two peaks in the O1s spectra, of which the peak with lower binding energy is located at 530.2 eV and is derived from metal oxide [310]. As the temperature increases or the lambda ratio decreases, the test condition moves toward boundary lubrication, the peak intensity decreases. It may be due to the increase of contact area, so more oxides are digested during the formation of tribofilm.

On the surface of tribofilm, the peak with higher binding energy is located at 531.7 eV, which is derived from NBO (non-bridging oxygen) in phosphate, carbonate or sulphate [22, 309-311, 314]. In the middle layer of tribofilm, the peak position of NBO shifts to 532.1±0.1 eV in the direction of binding energy increase. This may be an overlap with a BO (bridging oxygen, such as P-O-P) peak, which has higher binding energy than the NBO peak [310, 315]. However, because its peak is very weak and combined with the NBO peak, it is not particularly distinguished here.

6.2.3.3 *Phosphorous 2p Spectra*

As shown in Fig. 6-12, the strongest position of the P peak is about 133.6~134.2eV. Due to the splitting of the 2p orbital, after using an area ratio of 2:1 to split the peak, the position of the P2p3 peak is approximately 133.2~133.8eV. On the surface of the tribofilm, the binding energy of the phosphate peak is lower, and as the etching depth increases, the peak shifts to the higher binding energy. The increase in the binding energy of the P2p3 (phosphate) peak may be due to the change of metal ions such as Ca, Zn and Fe (the order of binding energy: Ca≤Zn<Fe) [22, 310, 314, 316-319, 339] or the degree of phosphate polymerisation (the order of binding energy: Ortho<Pyro<Poly-phosphate) [20]. Therefore, the most likely phosphates, assigned to the P2p3 peak in Fig. 6-12, can be calcium phosphate or short-chain zinc phosphate.

The peak of Zn3s is very weak, located at about 140.3 eV (not marked in the figure, it can be obtained by splitting the peak separately), and only appears on the surface of tribofilm under high λ ratio and lower temperature conditions. It reflects the presence of zinc phosphate on the surface of tribofilm.

The peak area of P2p3 at a distance of 0.5 nm from the surface is chosen to present the phosphates in the tribofilm, which is also the position of the highest peak intensity in

tribofilm, as shown in Fig. 6-17. As the temperature increases, the area intensity of the phosphate peak increases, indicating the increase in the phosphate content in tribofilm. At the low λ ratio below 120 ℃, the peak area is larger than that at the high λ ratio, indicating that the closer to the boundary lubrication, the more phosphate is produced.

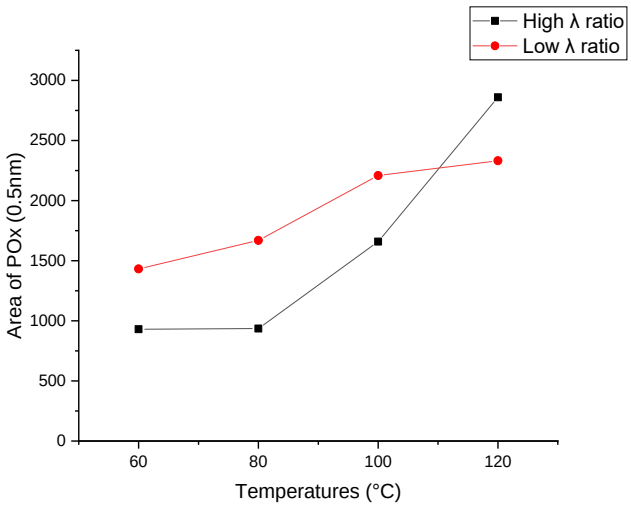

Fig. 6-17 The peak area of P2p3 at the distance of 0.5 nm from the surface as the function of temperatures at high and low λ ratios.

6.2.3.4 *Sulphur 2p Spectra*

As shown in Fig. 6-13, there are two more obvious peaks in the S2p spectra, among which the peak with lower binding energy is located at 161.7 eV and is derived from sulphides which may be one or more of CaS, ZnS and FeS. The other peak at 162.3±0.1 eV is derived from disulphide [310, 323, 324]. The Raman analysis shows that the tribofilm contains FeS_2, so it can be confirmed that there is FeS_2 in the tribofilm.

In addition, in the further peak separation of each spectrum, there is a weak peak around 168.2 eV on the top surface of the tribofilm (not shown in Fig. 6-13), which is assigned to the sulphate group with less sulphonate group [311, 321, 325] derived from over-based calcium sulphonate detergent. It indicates that calcium sulphate is present on the surface of tribofilm. Moreover, it can be seen that the signal intensity of the S peak on the surface of the tribofilm is relatively weak, and only the FeS_2 peak is more prominent, while the entire sulphide peak begins to increase at about 2 nm from the surface of the tribofilm. This shows that the sulphide-rich layer in tribofilm is covered by other substances, and because of the discontinuity of tribofilm, a small amount of FeS_2 is detected in advance

on the surface. It is agreed with previous studies on ZDDP that the sulphide layer is present between the substrate and the phosphate [5].

By comparison, there are some similarities and differences in the content of sulphides as the function of temperatures at high and low λ ratios. The peak area of sulphides at the distance of 2 nm from the surface of tribofilm is chosen to represent the content of sulphides in the tribofilm due to its highest intensity in the layered spectra of each sample, as shown in Fig. 6-18. At both λ ratios, the peak area of sulphides decreases with the increase in temperature, and the drop rate increases with temperature. However, the peak area of sulphides in the tribofilm at the high λ ratio is larger than that at the low λ ratio.

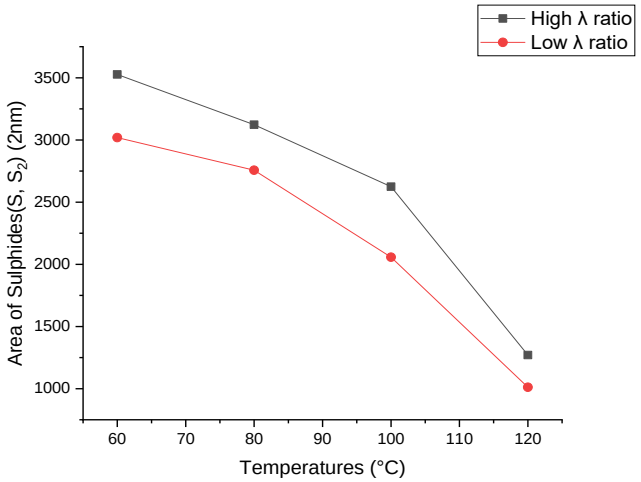

Fig. 6-18 The peak area of sulphides at the distance of 2 nm from the surface of tribofilm as the function of temperatures at high and low λ ratio.

It should be noted that this trend at the high λ ratio is different from the XPS results in Fig. 5-6b, which may be mainly due to the difference in measurement methods of XPS. The differences in the temperature at which the samples are tested could be negligible. Fig. 6-18 uses the depth profiling method to measure the spectra layer by layer, while the sulphides only at the top surface are directly measured in Fig. 5-6b. According to the former results, the sulphide layer mainly exists between phosphates and the steel substrate. Therefore, when the thickness of the phosphate layer is large, only measuring tribofilm on the top surface may cause the result that some sulphides below it cannot be detected. The depth profiling method can remove a certain thickness of phosphate layer by layer so that more sulphides can be detected, which is one of the reasons why the strongest peak intensity of sulphides appears at 2 nm from the surface. In general, for both λ ratios,

compared with the high-temperature range of 100~120 ℃, the content of sulphide at the low-temperature range of 60~80 ℃ is apparently higher and it changes little with temperature.

6.2.3.5 *Zinc 2p3 Spectra*

Zn atom is derived from ZDDP in FFO, so the product of the tribochemical reaction is most likely to be zinc phosphate or zinc sulphide. As shown in Fig. 6-14, the peak of Zn2p3 is located at 1022±0.2 eV and is present in the upper part of tribofilm, so it is attributed to zinc phosphate [310, 316]. Although in the reference spectra of zinc sulphide, the peak is located close to that of zinc phosphate, if zinc sulphide is present, it should appear in the part close to the substrate, but it is not clear.

6.2.3.6 *Calcium 2p Spectra*

The Ca-containing compounds that may be present in tribofilm may be $CaSO_4$, $CaCO_3$, $Ca(PO_4)^x$ and CaS. According to the spectra of C1s and S2p, it can be determined that there is calcium carbonate at the top layer of the tribofilm with a thickness of about 10 nm, and there are less $CaSO_4$ existing on the surface of tribofilm, which may be the product of adsorption and oxidation of a small amount of over-based calcium sulphonate [26].

The variation of the Ca2p spectra along the depth in tribofilm is shown in Fig. 6-15. Under different conditions, as the etching depth increases, that is, closer to the substrate, the Ca2p3 peak shifts to a higher or lower binding energy. Refer to the binding energy of each calcium-containing compound in Table 5-2, and it can be estimated that their binding energy ranking from low to high is $CaS<CaCO_3 \leq Ca(PO_4)_x<CaSO_4$. Therefore, the shift of binding energy may represent that there are changes in calcium-containing compounds on different layers of tribofilm.

At 60 ℃, the peak position of Ca 2p3 is mainly located at 347.2 eV, and the difference between Ca2p1 and Ca2p3 is about 3.5 eV, which is derived from calcium carbonate [309, 311]. However, this peak (including the result at 80 ℃ under high-λ condition) shifts to the lower binding energy of 346.8 eV near the bottom of the tribofilm, indicating that CaS may be present in the part of tribofilm close to the substrate. With the increase of temperature, except for the Ca2p3 peak of the surface layer located at about 347.2 eV, it

shifts to higher binding energy with the increase in depth. It can be inferred that the bulk of tribofilm contains calcium phosphate with higher binding energy.

In addition, reducing the λ ratio has no particularly large effect on the binding energy of the Ca peak, indicating that the main calcium-containing compounds are similar for both λ ratios.

XPS depth profiling analysis can be used to obtain the chemical compositions of tribofilm from the surface to near the substrate. The combined effects of temperature and λ ratio are considered. The most obvious aspects affected by these two factors are sulphides and phosphates in the tribofilms. When temperature increases or λ ratio decreases, the sulphides decrease in the tribofilm while phosphates increase (except at 120 ℃, where phosphate decreases with λ ratio decreases), which is consistent with Raman analysis.

According to the binding energy of the P2p3 peak, the main types of phosphates in tribofilm are calcium phosphate in the bulk tribofilm and short-chain zinc phosphate located on the top surface (combined with the spectra of Zn3s and Zn2p3). The peaks of S2p are respectively assigned to mono-sulphide, disulphide and sulphate/sulfonate. The disulfide is more likely to be FeS_2, according to Raman analysis, while the mono-sulfide may be FeS, ZnS or CaS. Sulphate and sulphonate are found in small amounts on the top surface of tribofilm and are derived from overbased calcium sulphonate detergent. The other component also from detergent at the top surface is calcium carbonate, which has no clear relationship with temperature and λ ratio. In addition, according to O1s spectra, the peak intensity of oxides decreases when the temperature increases or the λ ratio decreases.

According to the depth profiling analysis of XPS, there is no component directly showing the same temperature correlation with the wear result. But phosphates and sulphides in the tribofilms have an obvious tendency to change with temperature. It is suggested that the wear mechanism of FFO is influenced by the synthesis of these two substances in the formation process rather than a single component, which may be synergetic or antagonistic for wear.

6.2.4 *Atomic Analysis by XPS*

Raman analysis is a preliminary measurement of the combined effect of temperature and λ ratio on sulphides and phosphates in the tribofilm. However, because not all substances have Raman activity and it lacks the information of cations, XPS is selected for further identification of compounds in the tribofilm. Normal XPS detection mainly applies to the top layer of tribofilm, but according to the chemical compositions of ZDDP tribofilm, the chemical substances in the surface layer and near the substrate are different. Thus, The XPS depth profiling analysis with high-resolution spectra of different elements is used to identify the possible chemical compositions and their locations along with the depth of the tribofilm. Nevertheless, the information on the relative contents of those elements at each layer is not clear.

The atomic analysis by XPS can directly obtain the atomic percentage of those key elements at each layer of tribofilm and compensate the information on the relative distribution of the possible chemical compositions in tribofilm for the previous results of spectral analysis. In addition, it also provides data for subsequent modelling work, which will be explained in Chapter 7. According to the results in the previous section, the compositions analysed showed no apparent trends as the same temperature-dependent correlation as the wear trends. However, the contents of sulphides and phosphates are found to be the most temperature-dependent substances in the tribofilm, and the trend is almost not changed with the λ ratio, which is like the wear mechanisms. Therefore, in the atomic analysis, the distributions of relative P at.% and S at.% along with the depth under different temperatures and λ ratios are emphasised. Fig. 6-19 to Fig. 6-22 show the effect of λ ratios on the atomic analysis of signal C1s, O1s, P2p, S2p, Ca2p, Fe2p3 and Zn2p3 of tribofilm after 3-hour testing at different temperatures 60℃, 80℃, 100℃ and 120℃, respectively.

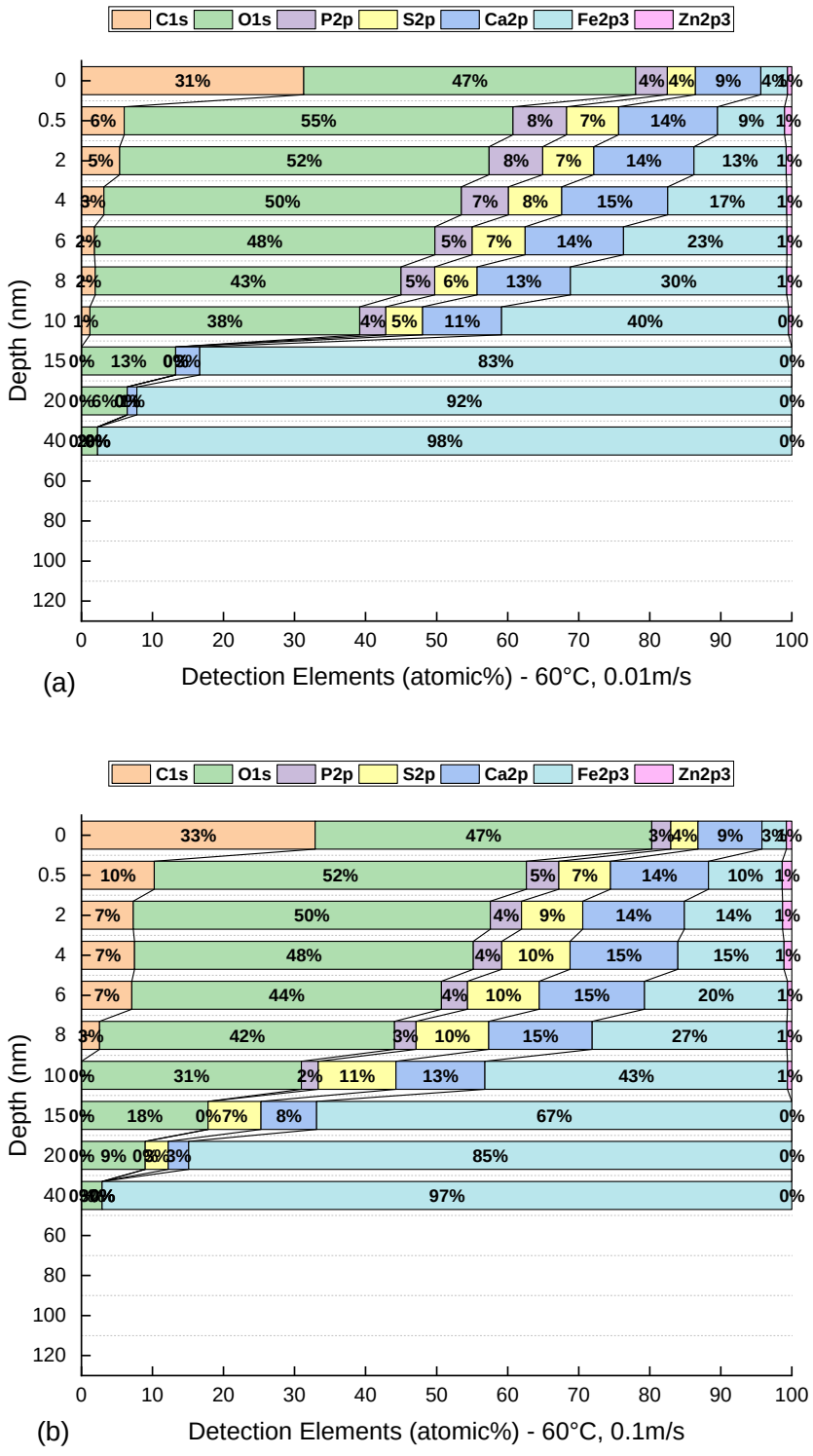

Fig. 6-19 The relative atomic percentage of the signal C1s, O1s, P2p, S2p, Ca2p, Fe2p3 and Zn2p3 at different etching depths of tribofilm after rubbing for 3 hours at <u>60 °C</u>: (a) low λ ratio and (b) high λ ratio.

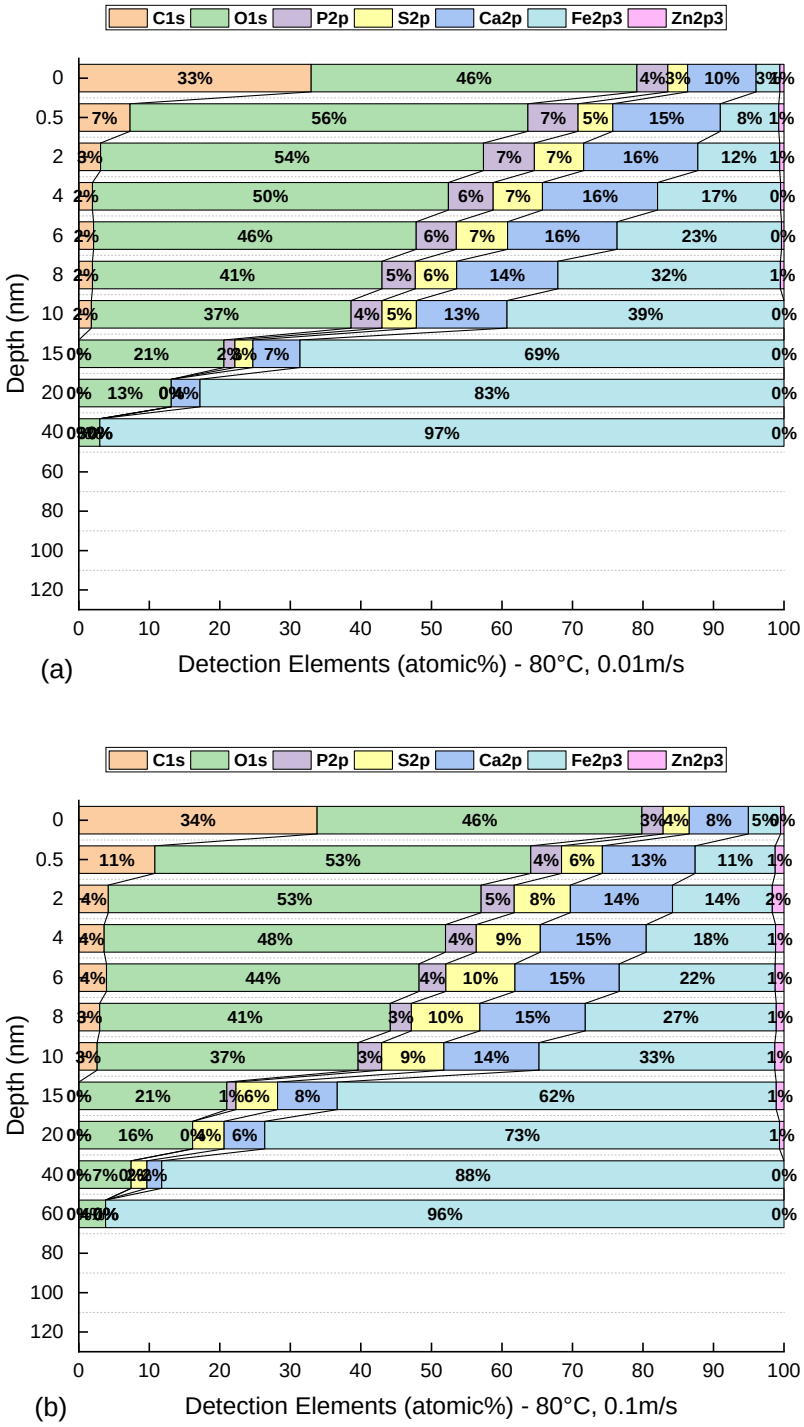

Fig. 6-20 The relative atomic percentage of the signal C1s, O1s, P2p, S2p, Ca2p, Fe2p3 and Zn2p3 at different etching depths of tribofilm after rubbing for 3 hours at 80 °C: (a) low λ ratio and (b) high λ ratio.

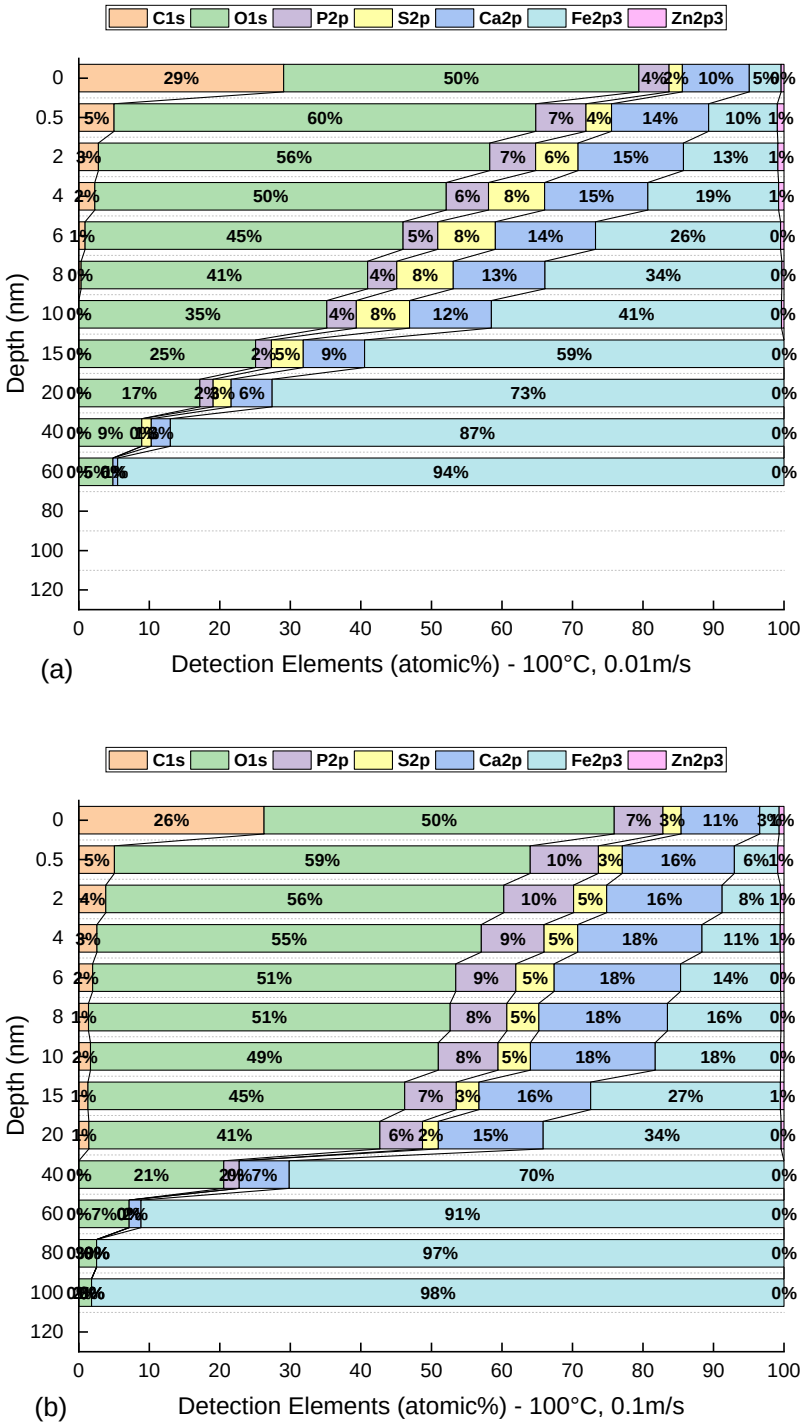

Fig. 6-21 The relative atomic percentage of the signal C1s, O1s, P2p, S2p, Ca2p, Fe2p3 and Zn2p3 at different etching depths of tribofilm after rubbing for 3 hours at 100 °C: (a) low λ ratio and (b) high λ ratio.

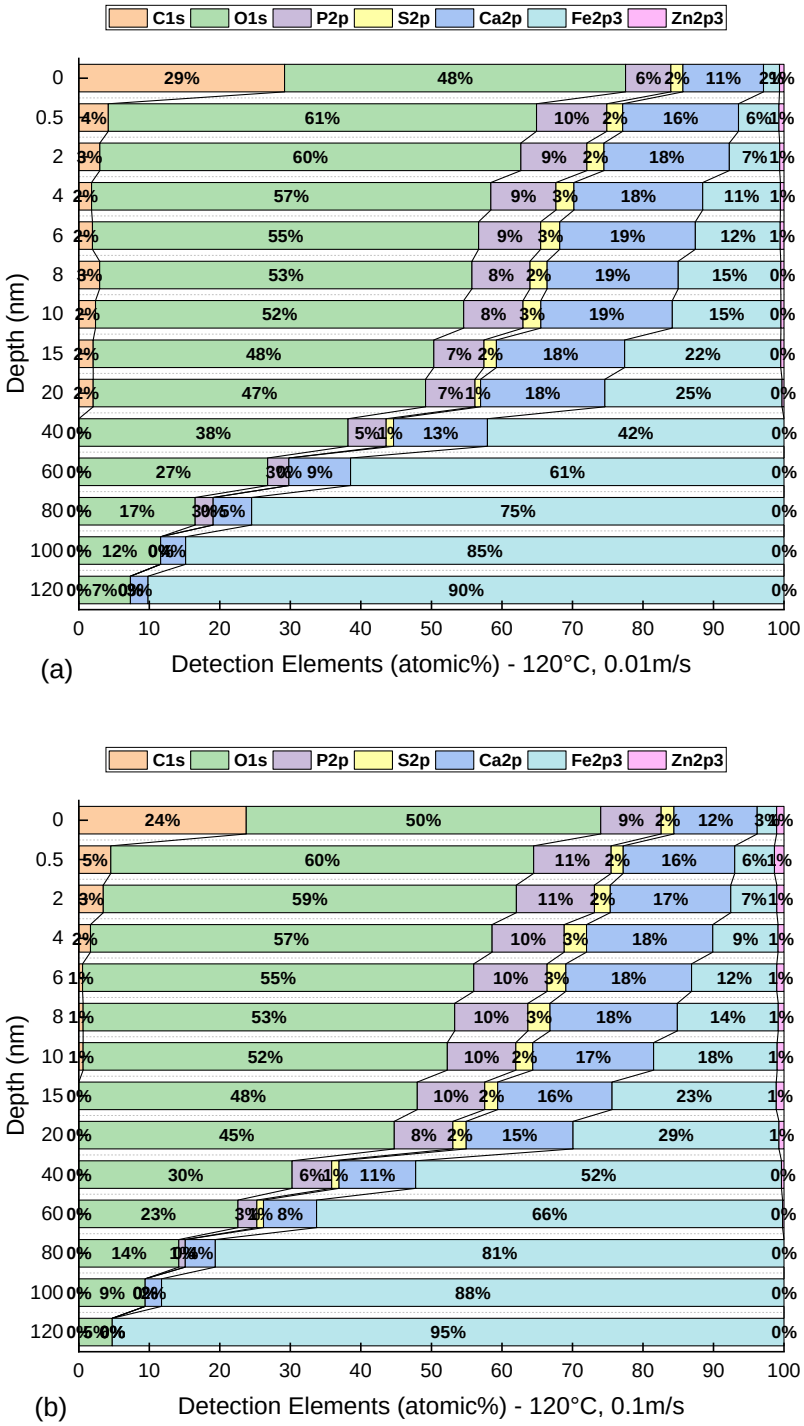

Fig. 6-22 The relative atomic percentage of the signal C1s, O1s, P2p, S2p, Ca2p, Fe2p3 and Zn2p3 at different etching depths of tribofilm after rubbing for 3 hours at 120 °C: (a) low λ ratio and (b) high λ ratio.

At 60℃, as shown in Fig. 6-19, the P% in the tribofilm is higher at low λ ratio than that at high λ ratio. On the contrary, the S% in the tribofilm is higher at the high λ ratio and there are more sulphides near the substrate. In addition, the relative percentage of C atoms at the high λ ratio is slightly higher, which can be considered as the calcium carbonate due to its distribution at the top 10 nm of the tribofilm. Besides, there are few differences between the high and the low λ ratio in the distribution and relative contents of Ca% or Zn%. In contrast, however, Ca% is higher than Zn%, which illustrates that Ca is the main cation influences the property of tribofilm to a large extent.

Fig. 6-20 and Fig. 6-21 shows the same analysis at 80 ℃ and 100 ℃, respectively. The results of P at.% and S at.% at both figures have the same trends as those at 60 ℃ on the influence of λ ratios. One of the differences is that Zn at.% at the high λ ratio is higher but Ca at.% has a slight reduction at 80℃. However, under the condition of 100 ℃, the relative contents of Zn atoms at both λ ratios decrease and the increase of the λ ratio makes the Ca at.% reduction. The other difference is that the depth distribution of C at.% in the tribofilm at 100 ℃ decreases at the high λ ratio but C at.% at 80 ℃ has a similar trend to that at 60 ℃.

The results of the atomic analysis at 120 ℃ are shown in Fig. 6-22, in which the increase of the λ ratio causes the reduction of C at.% in relative contents and depths, as the same trend as those at 100 ℃. S at.% has a significant decrease at 120 ℃ and there is almost no difference between the two λ ratios. Similarly, Ca at.% is also roughly the same at both λ ratios. Compared to the results under the temperature below 100 ℃, the biggest difference is that the main component near the substrate is phosphate at both λ ratios. Additionally, P at.% at the high λ ratio is higher than that at the low λ ratio, which is consistent with the results of spectral analysis of XPS depth profiling.

It is known from the chemical analysis in previous sections that phosphates and sulphides are the main chemical components in the tribofilm. In order to more directly compare the relative distribution and content of P or S volumetric ratios in tribofilm under different test conditions (such as temperature or λ ratio), the ratio of etching depth to the thickness $h_{balance}$ when the tribofilm reaches the stable phase is taken as the X-axis, and the volumetric ratio of P or S is taken as the Y-axis, as shown in Fig. 6-23. The $h_{balance}$ used at this time is the maximum etching depth by XPS under this condition rather than the

average thickness by MTM-SLIM, where X=0 represents the surface layer of tribofilm, and X=1 represents the interface close to the substrate. The volumetric ratio is calculated from the radius of the atom and its atomic ratio. It indicates the distributions of P vol.% or S vol.% along with depth at different temperatures when the tribofilm thickness are the same.

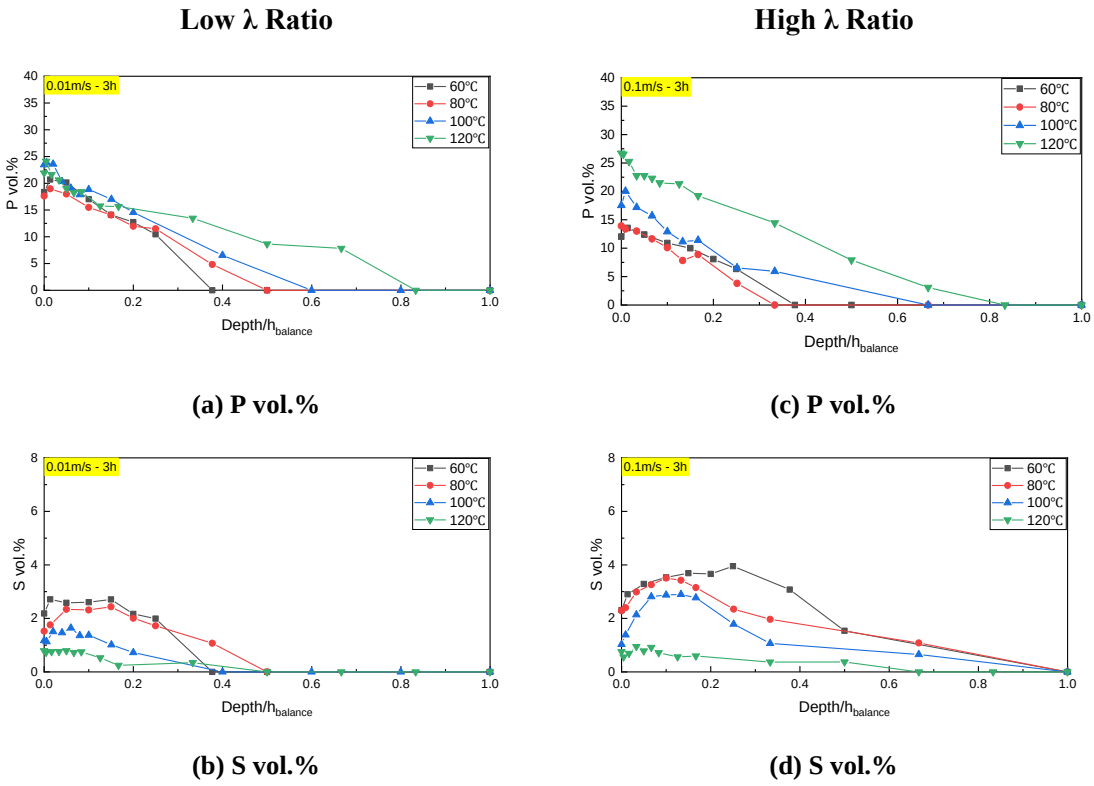

Fig. 6-23 The relative distribution and relative content of P vol.% and S vol.% along the depth direction in the tribofilm under the conditions of different λ ratios and test temperatures.

The volumetric ratio of P atoms (P vol.%) in tribofilm is more deeply distributed in the tribofilm with the increase of temperature at two λ ratios, as shown in Fig. 6-23 (a and c). P vol.% at higher temperature is larger with the increase of the λ ratio and the difference among the same temperature interval is larger than that at the low λ ratio. This, on the one hand, may be due to the difference in the tribofilm thickness when it reaches the stable phase at the high λ ratio. On the other hand, it results from the low activity of the tribochemical reaction related to the formation of phosphate under the condition of low temperature.

Fig. 6-23 (b and d) show the S vol.% as the function of unit tribofilm thickness under different temperatures at the low and the high λ ratio, respectively. The similarity for both ratios is that when the temperature rises, the value of S vol.% decreases and its distribution is shallower along with the depth. In contrast, however, when the temperature is lower than 100 ℃, S vol.% is larger at the high λ ratio under the same test temperature, and its distribution is wider along with the depth of tribofilm.

Additionally, it is worth noting that in the upper part of the tribofilm, the change of P vol.% along with the direction of depth decreases gradually, but S vol.% has a trend of first increasing and then decreasing with the depth of tribofilm. As the tribofilm is patch-like and discontinuous, with the increase of etching depth, the phosphate at the surface of tribofilm is removed and the sulphide layer near the substrate is exposed, resulting in an increase in S %. This also indicates that the tribofilm generated by FFO and ZDDP alone have a certain similarity in the structure of chemical components. Besides, In the low-temperature range, it can be speculated from the higher content and deeper positions of S % that the sulphide layer has more content and distributes wider in the tribofilm.

6.3 *Summary*

This chapter starts from the experiment of adjusting the λ ratio, but the main purposes are to eliminate the influence of oil viscosity on the wear mechanism of FFO and to confirm that the wear mechanism of FFO is consistent within a certain lubrication regime and working conditions. The main experimental results are as follows:

1) For both λ ratios, the average thickness at the stable phase increases with the increase of temperature, although the difference of thickness at the low λ ratio is small.
2) The chemical compositions of the tribofilm formed by FFO have the structure in order following: calcium carbonate/sulphate at the surface → phosphates → sulphides → substrate/iron oxides. But this does not mean that it is a layered structure, there can be a mixture of many of these substances at the same thickness/depth.
3) Detergents have a significant influence on the tribofilm, in addition to the formation of calcium carbonate/sulphate at the surface of tribofilm, the main type

of phosphate in the bulk tribofilm is calcium phosphate rather than zinc phosphate. And FeS_2 has been detected by both Raman and XPS analysis.

4) It can be obtained from the chemical analysis of Raman and XPS that when the tribofilm thickness reaches the stable stage, the content of phosphates (or P %) increases but that of sulphides (or S %) decreases with the increase of temperature. However, the values at the same test temperature interval (20 ℃) are higher at the high λ ratio. That is to say, the closer to boundary lubrication, the influence of temperature on phosphates and sulphides contained in the tribofilms decreases.
5) The wear volume has a maximum value at 80 ℃ under both λ ratios. However, at the high λ ratio, it is closer to the value of 100 ℃ while at the low λ ratio it is closer to the value of 60 ℃. In other words, the condition of 80 ℃ is in the transitional phase of the wear mechanism of FFO, but with the change of the λ ratio, the transitional temperature will be slightly moved to a higher or a lower temperature.

Nevertheless, it can be basically confirmed that the two-phase wear mechanism is valid for boundary lubrication in the test temperature range through the experiments with different λ ratios. It is suspected that the increase of wear results from the two major film-forming additives ZDDP and detergent which may have different degrees of competition or synergistic reaction at different temperatures, rather than the increase of any specific chemical components in the tribochemical reaction at that temperature.

In addition, although the tribofilm generated by the FFO has been highly influenced by the detergent, the chemical compositions of tribofilm still have a structure of distribution along with the depth, which was similar to the tribofilm generated by ZDDP only, provided a reference in the development of FFO's wear model with the effect of tribochemistry. The details of the modelling work will be explained in the next chapter.

Chapter 7 Wear Model of FFO Involving Tribochemistry Based on the Multi-layered Contact Model on Rough Surfaces

This chapter first introduces the main framework of the entire modelling work to simulate the wear model involving the tribochemistry of FFO. From the experimental results of FFO, its tribofilm has similar chemical components such as phosphates and sulphides as ZDDP-tribofilm, so the material properties of FFO-tribofilm are different from those of steel substrate. In order to calculate the influence of tribofilm on the substrate, the tribofilm is treated as a layer to change the material property of the surface and the contact state, so the 3D multilayered rough contact model is applied. Then, the wear model and tribofilm growth equation are developed based on the XPS and MTM-SLIM data, respectively and combined with the layered contact model to predict the experimental results of FFO such as tribofilm thickness and wear evolution. Finally, the extension of this model can also calculate the stress distribution and explore the relationships among the maximum stress point on the sublayer, tribofilm thickness, temperature and wear.

7.1 *Introduction of the Framework and Improvements*

As shown in Fig. 7-1, the modelling framework of the wear behaviours of FFO involving tribochemistry is designed, in which it can be mainly divided into five aspects: surface topography, layered contact algorithm, tribochemistry model, wear model and stress distribution.

Firstly, the two rough surfaces are the inputs to represent the two rubbing bodies. There are two types of methods to generate the rough surface including the numerical methods for surface reconstruction and the experimental measurements from the real surface of the sample by surface profilometers.

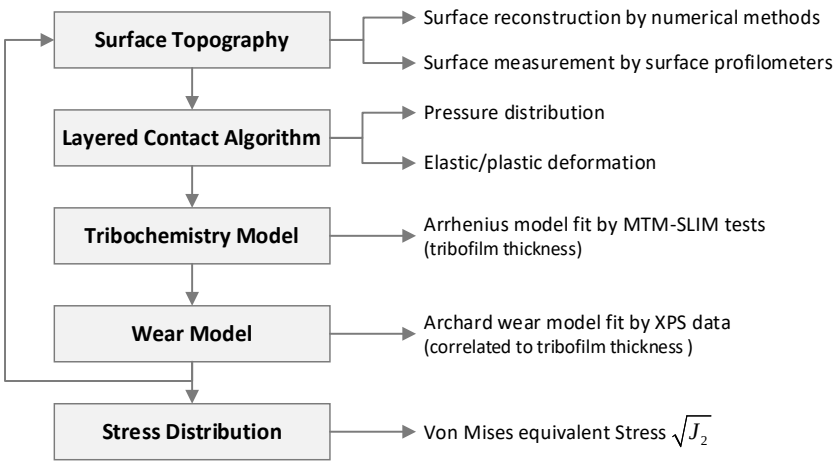

Fig. 7-1 Framework of the model to solve tribochemistry, wear behaviour and stress based on layered rough contact theory.

Then, with the inputs of working conditions and material properties, the simulation enters the contact algorithm. Since the fluid film is not continuous in the boundary lubrication so there is no need to solve the Reynolds equation and only the dry contact model is used to solve the elastic-plastic deformation and contact pressure distribution. In this model, the 3D layered contact theory is used, which can perform not only surface-related calculations based on homogeneous materials but also the layered effect of the tribofilm on the stress distribution along the depth direction.

Next, the influence of the lubricant in the model is exhibited in the tribofilm with a certain thickness and morphology, generated from the tribochemical reactions of the lubricant additives during the rubbing process. In order to simulate this process, the Arrhenius equation is applied to fit the experimental data of tribofilm thickness as the function of time at different temperatures.

In the part of the wear model, the Archard wear model is applied at each contact point to calculate the wear depth on the substrate. The wear process can be considered as two phases. As the tribofilm is not continuous, when it is not thick enough to cover the surface, the wear is regarded as the mechanical wear between the two steel surfaces. When the tribofilm grows to a thickness that is enough to be treated as a layer, then the wear coefficient is calculated from the Fe vol.% in the tribofilm fitted by XPS data, that is, the tribochemical wear is dominant.

In each computing cycle, elastic-plastic deformation, tribofilm thickness and surface wear will modify the initial surface topography and the accumulation of the tribofilm growth and wear loss as the function of time will be calculated. Besides, the stress distribution can be obtained at each time step to simulate the effect of the tribofilm on the sublayer (the substrate).

As the flowcharts of the models for calculating tribochemistry and wear are relatively similar [50, 179], it is necessary to point out the key modifications and improvements of the modelling work in this project.

1) The layered contact algorithm is used to extend the conventional 2D rough surface calculation to 3D layered rough surface calculation;
2) The tribofilm with a certain thickness is taken as a layer to more truly represent the contact state after the change of surface material properties due to the generation of tribofilm;
3) The equation of the tribochemistry model is modified based on the Arrhenius Equation and experimental results of FFO;
4) The wear model is also modified based on the experimental results of FFO, and the wear coefficient in Archard's wear equation is derived using Fe vol.% in XPS data;
5) In addition, stress distributions are simulated under different temperatures, tribofilm thickness and friction coefficients.

7.2 *Rough Surface Generation and Measurements*

Two rough surfaces are required to input the model to represent the contacting surfaces of the ball and the disc, respectively. Rough surfaces can be measured experimentally or generated numerically.

The commonly-used experimental rigs to measure the surface topography and roughness are stylus profilometry, white light interferometry and atomic force microscope, etc. The advantage of the experimental measurement is that the simulation is based on the real surface so the simulation results can be compared with the experimental results to verify the effectivity of the model and further to improve the model. A series of numerical treatments are required for the experimentally measured surfaces due to the errors of the

equipment itself and the differences in resolution. According to the ISO 25178-2-2012 standard [340], the measured surface requires removing the tilt and then being filtered before it can be used for further simulation. Numerically, a real rough surface can be regarded as a random process and can be classified as Gaussian or non-Gaussian rough surfaces according to its height distribution. The main statistical parameters and autocorrelation function used to describe it are expressed in Table 7-1 and Equ. (7-1) respectively [340]. For Gaussian rough surfaces, height standard deviation and autocorrelation length can be used to describe their characteristics, while for non-Gaussian rough surfaces, additional terms of skewness and kurtosis are needed to describe their characteristics.

According to the sampling of samples by AFM, the balls and discs used in the experiments meet the parameter requirements of the Gaussian surface ($S_{sk}=0,\ S_{ku}=3$). Therefore, the rough surfaces used in the simulation can also be generated by numerical methods, making it easier to adjust different surface parameters. Typical methods for generating rough surfaces include the moving average method [341-344], fast Fourier transformation (FFT) [345-347] and fractal method [218, 348, 349], etc.

Table 7-1 The main statistical parameters [340].

Parameters	**Formulas**
Mean value (μ)	$\mu=\frac{1}{A}\iint_A z(x,y)dxdy$
Standard deviation (σ)	$\sigma=\sqrt{\frac{1}{A}\iint_A z^2(x,y)\,dxdy}$
Skewness (S_{sk})	$S_{sk}=\frac{1}{\sigma^3}\left[\frac{1}{A}\iint_A z^3(x,y)\,dxdy\right]$
Kurtosis (S_{ku})	$S_{ku}=\frac{1}{\sigma^4}\left[\frac{1}{A}\iint_A z^4(x,y)\,dxdy\right]$

Autocorrelation Function:

$$ACF(k,l)=\frac{\iint_A z(x,y)\,z(x-k,y-l)\,dxdy}{\sigma^2} \tag{7-1}$$

where A is the surface area; $z(x,y)$ is the height of the surface z at the point (x,y) and $z(x-k,y-l)$ is the height of the same surface translated by (k, l).

In this project, the numerical rough surfaces are used in the simulation. The two Gaussian rough surfaces are generated by Hu and Tonder's method [342] to represent the ball surface and the disc surface respectively, as shown in Fig. 7-2. The computational domain and nodes will be explained further with the whole simulation procedure (Section 7.4.4).

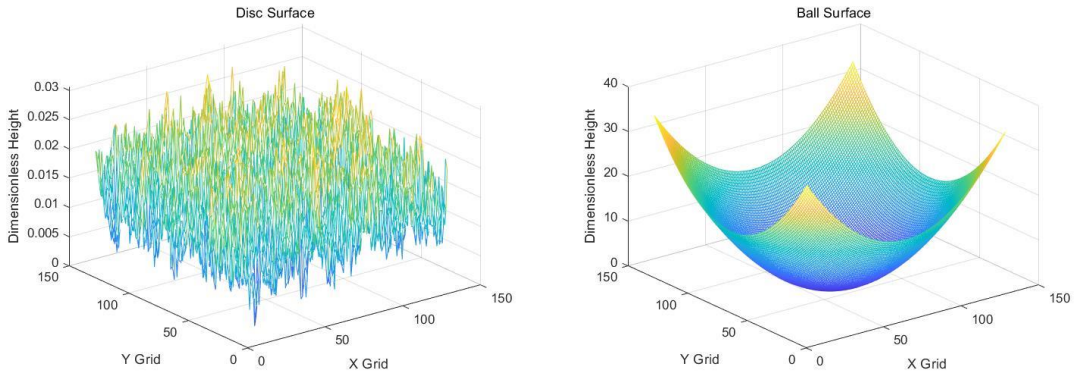

(a) steel disc **(b) steel ball**

Fig. 7-2 The generated surfaces of (a) the steel disc and (b) the steel ball by MATLAB.

(The dimensionless height is $S_z = s_z \cdot \frac{R_x}{a^2}$, see Section 7.3.2.)

7.3 *3D Multi-layered Contact Algorithm and Verifications*

7.3.1 *Theory of Elasticity Mechanics - Variational Principle*

Tian and Bhushan first used the variational inequations of minimum complementary potential energy principle to solve the contact problem for two homogeneous rough surfaces [244]. This method can calculate the contact pressure and deformation by points and is easier to be combined with optimised numerical methods. Peng and Bhushan applied this method to solve the contact problems for layered rough surfaces and stress distribution at different layers [230].

As is shown in Fig. 7-3a, for the contact between two elastic perfectly plastic solids, the minimum internal complementary potential energy V^* is

$$V^* = U_E^* - \int_\Omega p u_z^* d\Omega \tag{7-2}$$

where the complementary energy U_E^* is equal to the elastic strain energy U_E numerically for the lineal elastic material, expressed by

$$U_E = \frac{1}{2}\int_\Omega p u_z d\Omega = U_E^* \tag{7-3}$$

where $u_z = u_{z0} + u_{z1}$ is the sum of calculated deformations of two contacting solids in the z-direction.

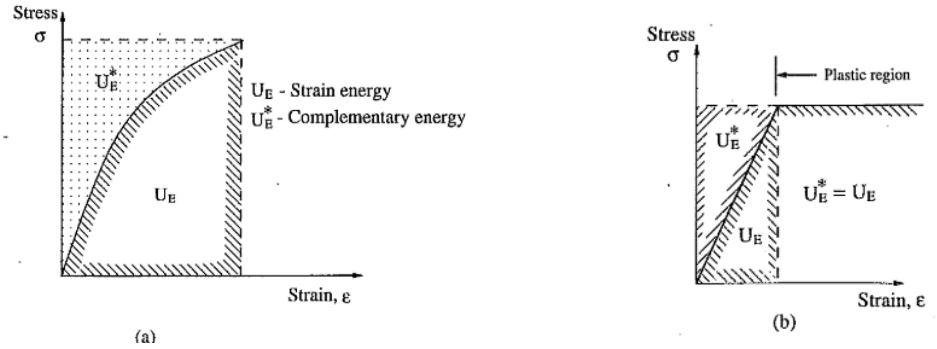

Fig. 7-3 (a) Definition of strain energy U_E and complementary energy U_E* and (b) relationship between U_E and internal U_E* for a linear elastic or elastic-perfectly plastic material [244].

By substituting Equ. (7-3) into Equ. (7-2), the latter one is modified as

$$V^* = \frac{1}{2}\int_\Omega p u_z d\Omega - \int_\Omega p u_z^* d\Omega \tag{7-4}$$

For a stable elastic system, the actual pressure minimises the total complementary potential energy and the actual deformation is used to replace the prescribed deformation, so the problem is to solve the function (7-5).

$$\min\ V^* = \min\ \left(\frac{1}{2}\int_\Omega p u_z d\Omega - \int_\Omega p u_z^* d\Omega\right) \tag{7-5}$$

If only considering the effect of normal pressure, based on the assumption of the infinite half-space of the two contact solids, the Boussinesq solutions [350] can be used to calculate the vertical deformation $u_z(x,y)$ in the contact,

$$u_z(x,y)=\frac{1}{\pi E^*}\iint_{\Omega}\frac{p(x',y')dx'dy'}{\sqrt{(x-x')^2+(y-y')^2}} \tag{7-6}$$

where E^* is the composite elastic modulus of two contacting solids, calculated from

$$\frac{1}{E^*}=\frac{1-v_1^2}{E_1}+\frac{1-v_2^2}{E_2} \tag{7-7}$$

in which E_1 and E_2 are the elastic modulus of the surface materials of two contacting solids, respectively; v_1 and v_2 are the Poisson's ratio of the surface materials of two contacting solids, respectively.

7.3.2 *Dimensionless Methods*

The dimensionless parameters used in solving the contact problem are as follows:

$$X=\frac{x}{a},\quad Y=\frac{y}{b},\quad S_{zi}=\frac{s_{zi}R_x}{a^2},\quad P=\frac{p}{p_h} \tag{7-8}$$

where a and b are the length and width of Hertzian contact area in x and y direction, respectively; $s_{zi}(i=1,2)$ is the roughness surface of two contacting solids; R_x is the surface curvature around the contact point in the x direction; p_h is the maximum Hertzian contact pressure.

For the material with a layer thickness of h, the calculation of different depth z will be included, whose dimensionless parameter is

$$Z=\frac{z}{h} \tag{7-9}$$

7.3.3 *Discretisation*

For the calculations of deformation and pressure distribution at the contact surfaces, the computation zone is $\{-2a \le x \le 2a, -2b \le y \le 2b\}$. The equidistant grids are used in the x and y direction so the spacing of each element is $\Delta x = \Delta y$. Normally, the pressure in one element can be interpolated by Lagrange's polynomial formula. When the element size is small enough, the pressure applied to each element can be considered as a constant, then Equ. (7-6) can be discretised into

$$\begin{aligned} u_z(x_i, y_j) &= \frac{1}{\pi E^*} \sum_{k=0}^{M} \sum_{j=0}^{N} C\left(x_i - x_k, y_j - y_l\right) p\left(x_k, y_l\right) \\ &= \frac{1}{\pi E^*} \sum_{k=0}^{M} \sum_{j=0}^{N} C_{ij}^{kl} \, p_{kl} \end{aligned} \tag{7-10}$$

where $u_z(x_i, y_j)$ is the deformation at each grid point; M and N are the number of points in x and y directions in the computation zone, respectively; C_{ij}^{kl} is called the influence coefficient matrix, representing the deformation of all points in the contact zone that is induced by a unit pressure $p\left(x_k, y_l\right)$ applied to point $\left(x_k, y_l\right)$. C_{ij}^{kl} depends on the material properties of contacting surfaces and the distance of the spacing of mesh points. Thus the first step to solving the elastic deformation is to get the values of C_{ij}^{kl}.

Similarly, for the calculations of deformation and stress in the contact of layered materials, assuming that a normal pressure p_{kl} is known and acting on a point $\left(x_k, y_l, 0\right)$ at the surface, the deformation and stress generated at point $A\left(x_i, y_j, z_m\right)$ in the contact zone can be expressed as:

$$\left[\begin{matrix} \sigma_A \\ u_A \end{matrix}\right]\Big|_{z=z_m} = \left[\begin{matrix} \sum_{i=1}^{M} \sum_{j=1}^{N} C_{p_{ij}}^{\sigma} \, p_{kl} \\ \sum_{i=1}^{M} \sum_{j=1}^{N} C_{p_{ij}}^{u_z} \, p_{kl} \end{matrix}\right]\Big|_{z=z_m} \tag{7-11}$$

in which M, N are the number of points in x, y directions, respectively; z_m is the depth of the layer for ICs' calculation; $C_{p_{ij}}^{\sigma}$ is the stress induced by unit pressure at depth of $z = z_m$ and $C_{p_{ij}}^{u_z}$ is the deformation induced by unit pressure at depth of $z = 0$.

If the traction force q_x induced by the normal force p is considered, in which $q_x = \mu p$ and μ is the friction coefficient, then formula (7-11) is further expressed as:

$$\left[\begin{matrix}\sigma_A \\ u_A\end{matrix}\right]\Big|_{z=z_m} = \left[\begin{matrix}\sum_{i=1}^{M}\sum_{j=1}^{N} C_{p_{ij}}^{\sigma} p_{kl} + \sum_{i=1}^{M}\sum_{j=1}^{N} C_{(q_x)_{ij}}^{\sigma} (q_x)_{kl} \\ \sum_{i=1}^{M}\sum_{j=1}^{N} C_{p_{ij}}^{u_z} p_{kl} + \sum_{i=1}^{M}\sum_{j=1}^{N} C_{(q_x)_{ij}}^{u_z} (q_x)_{kl}\end{matrix}\right]\Big|_{z=z_m} \tag{7-12}$$

where $C_{(q_x)_{ij}}^{\sigma}$ is the stress induced by unit stress q_x at depth of $z = z_m$ and $C_{(q_x)_{ij}}^{u_z}$ is the deformation induced by unit stress q_x at depth of $z = 0$.

7.3.4 *Solutions of Influence Coefficient Matrix (ICs)*

For the elastic contact problem of different material structures and numerical methods, the expressions of the influence coefficient matrix have different derivation process.

1) 2-D homogeneous materials ($z = 0$)

For homogeneous materials, Love [351] derived the approximate solution of C_{ij}^{kl} as follows.

$$C_{ij}^{kl} = \frac{1}{\pi E^*}\left\{\begin{aligned}&(x+a)\ln\left[\frac{(y+b)+\sqrt{(y+b)^2+(x+a)^2}}{(y-b)+\sqrt{(y-b)^2+(x+a)^2}}\right] \\ &+(y+b)\ln\left[\frac{(x+a)+\sqrt{(y+b)^2+(x+a)^2}}{(x-a)+\sqrt{(y+b)^2+(x-a)^2}}\right] \\ &+(x-a)\ln\left[\frac{(y-b)+\sqrt{(y-b)^2+(x-a)^2}}{(y+b)+\sqrt{(y+b)^2+(x-a)^2}}\right] \\ &+(y-b)\ln\left[\frac{(x-a)+\sqrt{(y-b)^2+(x-a)^2}}{(x-a)+\sqrt{(y-b)^2+(x+a)^2}}\right]\end{aligned}\right\} \tag{7-13}$$

Since there are a lot of repetitive calculations in subsequent convolution and iteration, the direct use of the above formula will cause a large amount of computing time. Thus, many researchers tried to use numerical methods to process the pressure distribution on the grid, so that the solution of the elastic deformation is closer to the analytical solution, and the computing time can be greatly shortened.

Liu *et al.* [352] created an 'elliptic-paraboloid surface' for pressure distribution based on the principle of 'approaching larger and using smaller' (ALUS), as shown in Fig. 7-4. Since the influence of adjacent elements and neighbouring elements is considered, the singularity problem can be avoided, which is caused by the denominator being zero when the pressure is applied to the point $\left(x_k, y_l\right)$ in Equ. (7-6).

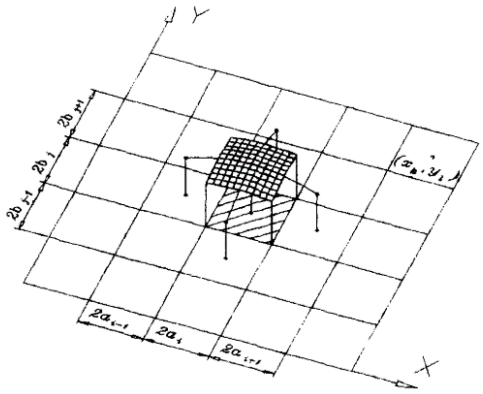

Fig. 7-4 A schematic diagram of an 'elliptical paraboloid surface' for the pressure distribution [352].

2) 3D Multi-layered Materials

For multi-layered materials, in addition to calculating the deformation caused by surface pressure, the stress distribution along the depth can also be calculated. Based on the assumptions of not large friction coefficient and no consideration of tangential displacement, the influence coefficient matrix for deformation at $z = 0$ induced by a unit normal pressure p for the 3D contact problem of layered materials are consistent with that of homogeneous materials if the homogenous material is the same as the layer material. However, the following uses another method to derive the ICs of the layered materials.

O'Sullivan and King [223] use the Papkovich-Neuber (*P-N*) elastic potentials ϕ_0 and $\vec{\phi}=(\phi_1,\phi_2,\phi_3)$ which are the *x*, *y*, *z* components of the harmonic functions for zero body forces to express the deformation and stress as follows.

$$\begin{aligned} u_i &= \frac{1}{2G}\left(\phi_{0,i} + x\cdot\phi_{1,i} + z\cdot\phi_{3,i} - (3-4\nu)\phi_i\right) \\ \sigma_{ij} &= \phi_{0,ij} + x\phi_{1,ij} + z\phi_{3,ij} - 2\nu\left(\phi_{1,1}+\phi_{3,3}\right)\delta_{ij} - (1-2\nu)\left(\phi_{i,j}+\phi_{j,i}\right) \end{aligned} \quad \textbf{(7-14)}$$

where *G* is the shear modulus; ν is the Poisson's ratio; the index of *i* and *j* are 1, 2, 3 corresponding to *x*, *y*, *z*, respectively; δ_{ij} is Kronecker delta: $\delta_{ij}=\begin{cases}1 & i=j\\ 0 & i\neq j\end{cases}$.

The functions above are automatically satisfied with the equilibrium, compatibility and Hooke's Law. For a zero force body, the number of independent functions can be reduced by arbitrarily setting one of the *P-N* potentials to zero, so ϕ_2 is removed from Equ. (7-14) due to the condition of normal load with traction force.

Since the Fourier transform decomposes the harmonic function into sinusoidal waveform at different frequencies, the superposition of these sine curves is also a harmonic function. In the frequency domain, the expressions of the transformed *P-N* potentials in the layer and the substrate are:

$$\textit{layer}:\begin{cases}\Phi_0^{(1)} = A^{(1)}e^{-\alpha z_1} + \bar{A}^{(1)}e^{\alpha z_1}\\ \Phi_1^{(1)} = B^{(1)}e^{-\alpha z_1} + \bar{B}^{(1)}e^{\alpha z_1}\\ \Phi_3^{(1)} = C^{(1)}e^{-\alpha z_1} + \bar{C}^{(1)}e^{\alpha z_1}\end{cases} \textbf{ and } \textit{Substrate}:\begin{cases}\Phi_0^{(2)} = A^{(2)}e^{-\alpha z_1}\\ \Phi_1^{(2)} = B^{(2)}e^{-\alpha z_1}\\ \Phi_3^{(2)} = C^{(2)}e^{-\alpha z_1}\end{cases} \quad \textbf{(7-15)}$$

where the line on *A*, *B* and *C* indicate their corresponding complex conjugates; $\alpha=\sqrt{m^2+n^2}$ in which *m* and *n* correspond to the frequency variables of *x* and *y* in the frequency domain after Fourier transform.

Since the assumptions of an infinite depth of the contact body, both stress and deformation are zero so $\bar{A}^{(2)}=\bar{B}^{(2)}=\bar{C}^{(2)}=0$ which has been eliminated in the Equ. (7-15). Thus, there are 9 unknown parameters $A^{(1)}$, $\bar{A}^{(1)}$, $B^{(1)}$, $\bar{B}^{(1)}$, $C^{(1)}$, $\bar{C}^{(1)}$, $A^{(2)}$, $B^{(2)}$, $C^{(2)}$ that need to be solved in Equ. (7-15).

For the contact problem of a layered material with sliding, the layer thickness can be ignored compared to the entire elastic half-space. Similarly to the homogeneous material, a rigid sphere is pressed against an elastic half-space containing a thin layer with a normal force and a traction force, as shown in Fig. 7-5.

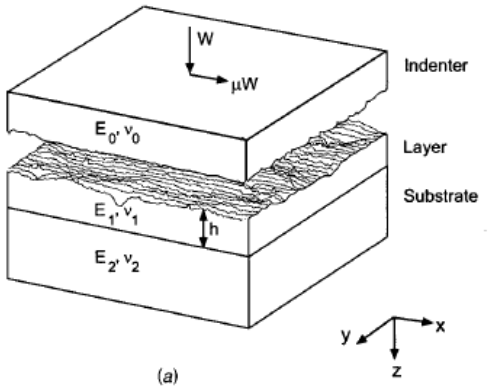

Fig. 7-5 A 3D schematic diagram of an indenter in contact with one elastic half-space with a layer [230].

The normal pressure is set to be 1 at the centre of the origin, accompanied by shear stress, that is $p(0,0,0)=1,\ q(0,0,0)=\mu$. The boundary conditions at the layer surface z_1=0 are:

$$\begin{cases} \sigma_{zz}^{(1)}(x,y,0) = -p(x,y,0) = \begin{cases} -1 & x=0, y=0 \\ 0 & x\neq 0, y\neq 0 \end{cases} \\ \sigma_{xz}^{(1)}(x,y,0) = \mu p(x,y,0) = \begin{cases} \mu & x=0, y=0 \\ 0 & x\neq 0, y\neq 0 \end{cases} \\ \sigma_{yz}^{(1)}(x,y,0) = 0 \end{cases} \tag{7-16}$$

Assuming that the layer is completely bonded to the substrate and both stress and deformation between the interface are continuous. On the interface of the layer and substrate, the boundary conditions are:

$$\begin{cases} \sigma_{xz}^{(1)}(x,y,h) = \sigma_{xz}^{(2)}(x,y,0) \\ \sigma_{yz}^{(1)}(x,y,h) = \sigma_{yz}^{(2)}(x,y,0) \\ \sigma_{zz}^{(1)}(x,y,h) = \sigma_{zz}^{(2)}(x,y,0) \end{cases} \textbf{ and } \begin{cases} u_x^{(1)}(x,y,h) = u_x^{(2)}(x,y,0) \\ u_y^{(1)}(x,y,h) = u_y^{(2)}(x,y,0) \\ u_z^{(1)}(x,y,h) = u_z^{(2)}(x,y,0) \end{cases} \tag{7-17}$$

where h is the layer thickness; (1) and (2) represent the layer and the substrate, respectively.

On the substrate, the stress and the deformation decrease to zero at a far depth from the surface.

$$\begin{cases} \sigma^{(2)}\left(x,y,\infty\right)=0 \\ u^{(2)}\left(x,y,\infty\right)=0 \end{cases} \tag{7-18}$$

Then, the 9 unknown parameters $A^{(1)}$, $\bar{A}^{(1)}$, $B^{(1)}$, $\bar{B}^{(1)}$, $C^{(1)}$, $\bar{C}^{(1)}$, $A^{(2)}$, $B^{(2)}$, $C^{(2)}$ can be solved from the 9 boundary conditions in Equ. (7-16) and Equ. (7-17), see Appendix B.

By substituting the 9 parameters into *P-N* potentials, then into Equ. (7-14), the expressions of the deformation and stress components in the frequency domain are

$$\hat{u}_x^{(j)}=\frac{1}{2G_j}\begin{Bmatrix} im\left[A^{(j)}e^{-\alpha z_j}+\bar{A}^{(j)}e^{\alpha z_j}\right]-4\left(1-\nu_j\right)\left[B^{(j)}e^{-\alpha z_j}+\bar{B}^{(j)}e^{\alpha z_j}\right] \\ +m^2\alpha^{-1}z_j\left[B^{(j)}e^{-\alpha z_j}-\bar{B}^{(j)}e^{\alpha z_j}\right]+imz_j\left[C^{(j)}e^{-\alpha z_j}+\bar{C}^{(j)}e^{\alpha z_j}\right] \\ -m\left[B_{,m}^{(j)}e^{-\alpha z_j}+\bar{B}_{,m}^{(j)}e^{\alpha z_j}\right] \end{Bmatrix}$$

$$\hat{u}_y^{(j)}=\frac{1}{2G_j}\begin{Bmatrix} in\left[A^{(j)}e^{-\alpha z_j}+\bar{A}^{(j)}e^{\alpha z_j}\right]+mn\alpha^{-1}z_j\left[B^{(j)}e^{-\alpha z_j}-\bar{B}^{(j)}e^{\alpha z_j}\right] \\ +inz_j\left[C^{(j)}e^{-\alpha z_j}+\bar{C}^{(j)}e^{\alpha z_j}\right]-n\left[B_{,m}^{(j)}e^{-\alpha z_j}+\bar{B}_{,m}^{(j)}e^{\alpha z_j}\right] \end{Bmatrix} \tag{7-19}$$

$$\hat{u}_z^{(j)}=\frac{1}{2G_j}\begin{Bmatrix} -\alpha\left[A^{(j)}e^{-\alpha z_j}-\bar{A}^{(j)}e^{\alpha z_j}\right]+imz_j\left[B^{(j)}e^{-\alpha z_j}+\bar{B}^{(j)}e^{\alpha z_j}\right] \\ -im\alpha^{-1}\left[B^{(j)}e^{-\alpha z_j}-\bar{B}^{(j)}e^{\alpha z_j}\right]-\left(3-4\nu_j\right)\left[C^{(j)}e^{-\alpha z_j}+\bar{C}^{(j)}e^{\alpha z_j}\right] \\ -\alpha z_j\left[C^{(j)}e^{-\alpha z_j}-\bar{C}^{(j)}e^{\alpha z_j}\right]-i\alpha\left[B_{,m}^{(j)}e^{-\alpha z_j}-\bar{B}_{,m}^{(j)}e^{\alpha z_j}\right] \end{Bmatrix}$$

$$\hat{\sigma}_{xx}^{(j)} = -m^2\left[A^{(j)}e^{-\alpha z_j} + \bar{A}^{(j)}e^{\alpha z_j}\right] + 2im\left(\nu_j - 2\right)\left[B^{(j)}e^{-\alpha z_j} + \bar{B}^{(j)}e^{\alpha z_j}\right]$$
$$+im^3\alpha^{-1}z_j\left[B^{(j)}e^{-\alpha z_j} - \bar{B}^{(j)}e^{\alpha z_j}\right] - m^2 z_j\left[C^{(j)}e^{-\alpha z_j} + \bar{C}^{(j)}e^{\alpha z_j}\right]$$
$$+2\alpha\nu_j\left[C^{(j)}e^{-\alpha z_j} - \bar{C}^{(j)}e^{\alpha z_j}\right] - im^2\left[B_{,m}^{(j)}e^{-\alpha z_j} + \bar{B}_{,m}^{(j)}e^{\alpha z_j}\right]$$

$$\hat{\sigma}_{yy}^{(j)} = -n^2\left[A^{(j)}e^{-\alpha z_j} + \bar{A}^{(j)}e^{\alpha z_j}\right] - 2im\nu_j\left[B^{(j)}e^{-\alpha z_j} + \bar{B}^{(j)}e^{\alpha z_j}\right]$$
$$+im^2n\alpha^{-1}z_j\left[B^{(j)}e^{-\alpha z_j} - \bar{B}^{(j)}e^{\alpha z_j}\right] - n^2 z_j\left[C^{(j)}e^{-\alpha z_j} + \bar{C}^{(j)}e^{\alpha z_j}\right]$$
$$+2\alpha\nu_j\left[C^{(j)}e^{-\alpha z_j} - \bar{C}^{(j)}e^{\alpha z_j}\right] - in^2\left[B_{,m}^{(j)}e^{-\alpha z_j} + \bar{B}_{,m}^{(j)}e^{\alpha z_j}\right]$$

$$\hat{\sigma}_{zz}^{(j)} = -\alpha^2\left[A^{(j)}e^{-\alpha z_j} + \bar{A}^{(j)}e^{\alpha z_j}\right] + 2im\left(1-\nu_j\right)\left[B^{(j)}e^{-\alpha z_j} + \bar{B}^{(j)}e^{\alpha z_j}\right]$$
$$-im\alpha z_j\left[B^{(j)}e^{-\alpha z_j} - \bar{B}^{(j)}e^{\alpha z_j}\right] - \alpha^2 z_j\left[C^{(j)}e^{-\alpha z_j} + \bar{C}^{(j)}e^{\alpha z_j}\right]$$
$$+2\alpha\left(1-\nu_j\right)\left[C^{(j)}e^{-\alpha z_j} - \bar{C}^{(j)}e^{\alpha z_j}\right] + i\alpha^2\left[B_{,m}^{(j)}e^{-\alpha z_j} + \bar{B}_{,m}^{(j)}e^{\alpha z_j}\right]$$

$$\hat{\sigma}_{xy}^{(j)} = -mn\left[A^{(j)}e^{-\alpha z_j} + \bar{A}^{(j)}e^{\alpha z_j}\right] - 2in\left(1-\nu_j\right)\left[B^{(j)}e^{-\alpha z_j} + \bar{B}^{(j)}e^{\alpha z_j}\right] \quad \textbf{(7-20)}$$
$$+im^2n\alpha^{-1}z_j\left[B^{(j)}e^{-\alpha z_j} - \bar{B}^{(j)}e^{\alpha z_j}\right] - mnz_j\left[C^{(j)}e^{-\alpha z_j} + \bar{C}^{(j)}e^{\alpha z_j}\right]$$
$$-imn\left[B_{,m}^{(j)}e^{-\alpha z_j} + \bar{B}_{,m}^{(j)}e^{\alpha z_j}\right]$$

$$\hat{\sigma}_{xz}^{(j)} = -im\alpha\left[A^{(j)}e^{-\alpha z_j} - \bar{A}^{(j)}e^{\alpha z_j}\right] - m^2 z_j\left[B^{(j)}e^{-\alpha z_j} + \bar{B}^{(j)}e^{\alpha z_j}\right]$$
$$+\left[2\alpha\left(1-\nu_j\right) + m^2\alpha^{-1}\right]\left[B^{(j)}e^{-\alpha z_j} - \bar{B}^{(j)}e^{\alpha z_j}\right]$$
$$-im\left(1-2\nu_j\right)\left[C^{(j)}e^{-\alpha z_j} + \bar{C}^{(j)}e^{\alpha z_j}\right]$$
$$-im\alpha z_j\left[C^{(j)}e^{-\alpha z_j} - \bar{C}^{(j)}e^{\alpha z_j}\right] + m\alpha\left[B_{,m}^{(j)}e^{-\alpha z_j} - \bar{B}_{,m}^{(j)}e^{\alpha z_j}\right]$$

$$\hat{\sigma}_{yz}^{(j)} = -in\alpha\left[A^{(j)}e^{-\alpha z_j} - \bar{A}^{(j)}e^{\alpha z_j}\right] - mnz_j\left[B^{(j)}e^{-\alpha z_j} + \bar{B}^{(j)}e^{\alpha z_j}\right]$$
$$+mn\alpha^{-1}\left[B^{(j)}e^{-\alpha z_j} - \bar{B}^{(j)}e^{\alpha z_j}\right] - in\left(1-2\nu_j\right)\left[C^{(j)}e^{-\alpha z_j} + \bar{C}^{(j)}e^{\alpha z_j}\right]$$
$$-in\alpha z_j\left[C^{(j)}e^{-\alpha z_j} - \bar{C}^{(j)}e^{\alpha z_j}\right] + n\alpha\left[B_{,m}^{(j)}e^{-\alpha z_j} - \bar{B}_{,m}^{(j)}e^{\alpha z_j}\right]$$

where j is 1 or 2 representing the layer or the substrate, respectively; i is the imaginary unit.

The deformation and stress components are induced by the unit pressure p with the shear stress q_x acting on the grid area of $\left\{-\frac{\Delta x}{2}<x<\frac{\Delta x}{2},-\frac{\Delta y}{2}<y<\frac{\Delta y}{2}\right\}$, so the functions Equ.(7-19) and Equ. (7-20) are the deformation and stress on the mesh point, respectively. If $C_p^{u_z(j)}$ is denoted as the influence coefficient matrix for the vertical deformation induced by the normal pressure p at the layer (j = 1) or the substrate (j = 2) , it can be calculated by

$$\begin{aligned}\hat{C}_p^{u_z(j)}=&\frac{1}{\Delta x\Delta y}\sum_{r_x=-AL}^{r_x=AL}\sum_{r_y=-AL}^{r_y=AL}\hat{u}_z\cdot\hat{Y}\\&\left(\frac{2\pi}{M_{\exp}\Delta x}i-\frac{2\pi}{\Delta x}r_x,\frac{2\pi}{M_{\exp}\Delta y}i-\frac{2\pi}{\Delta y}r_y\right)\\&\left(-M_{\exp}/2<i<M_{\exp}/2,-N_{\exp}/2<i<N_{\exp}/2\right)\end{aligned}\qquad\textbf{(7-21)}$$

where $\hat{Y}(m,n)$ is the Fourier transform of a rectangular pulse $Y(x,y)$ which is used as the shape function [253, 274]:

$$\begin{aligned}Y(x,y)&=\begin{cases}1 & |x|\le\Delta x/2 \quad and \quad |y|\le\Delta y/2\\0 & others\end{cases}\\\hat{Y}(m,n)&=\frac{4\sin(m\Delta x/2)\sin(n\Delta y/2)}{mn}\end{aligned}\qquad\textbf{(7-22)}$$

$M_{\exp}$ and $N_{\exp}$ are the refinement of the initial discrete grid points M and N; the refinement multiples $\gamma=8$ and $\gamma=4$ are respectively used for the ICs' calculation of deformation and stress; AL is used to control aliasing phenomenon but it is sufficient to set $AL=0$ in this case [253]. To avoid the singularity of the value of ICs at the origin (m=0, n=0), 64-Gaussian quadrature integration is used to estimate this value [245].

After obtaining ICs in the frequency domain, the DC-FFT method proposed by Liu *et al.* [272] is used to calculate the sum of IC matrix respectively multiplied by the Fourier transform of pressure and shear stress and then the deformation or the stress components in the time domain can be obtained by the inverse Fourier transformation (denoted as $\Im^{-1}$). The process can be expressed in Equ. (7-23) in which the symbol hat " ^ " means the corresponding Fourier transform of the matrix.

$$\begin{aligned}\mathbf{u_z} &= \mathbf{C_p^{u_z}} \otimes \mathbf{p} + \mathbf{C_{q_x}^{u_z}} \otimes \mathbf{q_x} = \Im^{-1}\left[\hat{\mathbf{C}}_\mathbf{p}^{\mathbf{u_z}} \cdot \hat{\mathbf{p}} + \hat{\mathbf{C}}_{\mathbf{q_x}}^{\mathbf{u_z}} \cdot \hat{\mathbf{q}}_\mathbf{x}\right] \\ \boldsymbol{\sigma}_{\mathbf{ij}} &= \mathbf{C_p^{\sigma_{ij}}} \otimes \mathbf{p} + \mathbf{C_{q_x}^{\sigma_{ij}}} \otimes \mathbf{q_x} = \Im^{-1}\left[\hat{\mathbf{C}}_\mathbf{p}^{\boldsymbol{\sigma}_{\mathbf{ij}}} \cdot \hat{\mathbf{p}} + \hat{\mathbf{C}}_{\mathbf{q_x}}^{\boldsymbol{\sigma}_{\mathbf{ij}}} \cdot \hat{\mathbf{q}}_\mathbf{x}\right] \quad (i \text{ and } j = x, y, z)\end{aligned} \tag{7-23}$$

In elastoplastic mechanics, von Mises stress $\sqrt{J_2}$ is usually used as equivalent stress to determine the material yielding [350], which is calculated by:

$$\sqrt{J_2} = \sqrt{\frac{1}{2}\left[\left(\sigma_{xx} - \sigma_{yy}\right)^2 + \left(\sigma_{yy} - \sigma_{zz}\right)^2 + \left(\sigma_{zz} - \sigma_{xx}\right)^2\right] + 3\left(\sigma_{xy}^2 + \sigma_{yz}^2 + \sigma_{zx}^2\right)} \tag{7-24}$$

7.3.5 *Simulation Process*

For solving the frictionless elastoplastic contact of rough surfaces, Stanley and Kato [353] proposed to use an iterative method to approximately solve the pressure *p* in the minimum complementary potential energy principle of Equ. (7-5). Almqvist *et al.* [354] improved the method to calculate the plastic deformation. Since it is assumed that there is no tangential deformation in the surface, the surface deformation of the 3D layered material with roughness is calculated by the same method. In addition, After the pressure has been obtained, the stress distribution at each layer is calculated separately.

The flowchart of the process is shown in Fig. 7-6.

The process of simulation is as follows.

1. Pre-set the initial contact pressure *p*, and update the pressure at the n^{th} iteration $p_n = p - \left(u(p) + g\right)$ according to the current rough surface geometry g and deformation $u(p)$.
2. Define the elastoplastic zone: $\left(p_n\right)_{I_0} = 0$, $\left(p_n\right)_{I_e} = p_n$ and $\left(p_n\right)_{I_p} = p_p$, and calculate the load $W_n = \left(p_n\right)_{I_e + I_p}$ in which I_e, I_p and I_0 are the index of the elastic zone, plastic zone and the rest of the contact region, respectively.

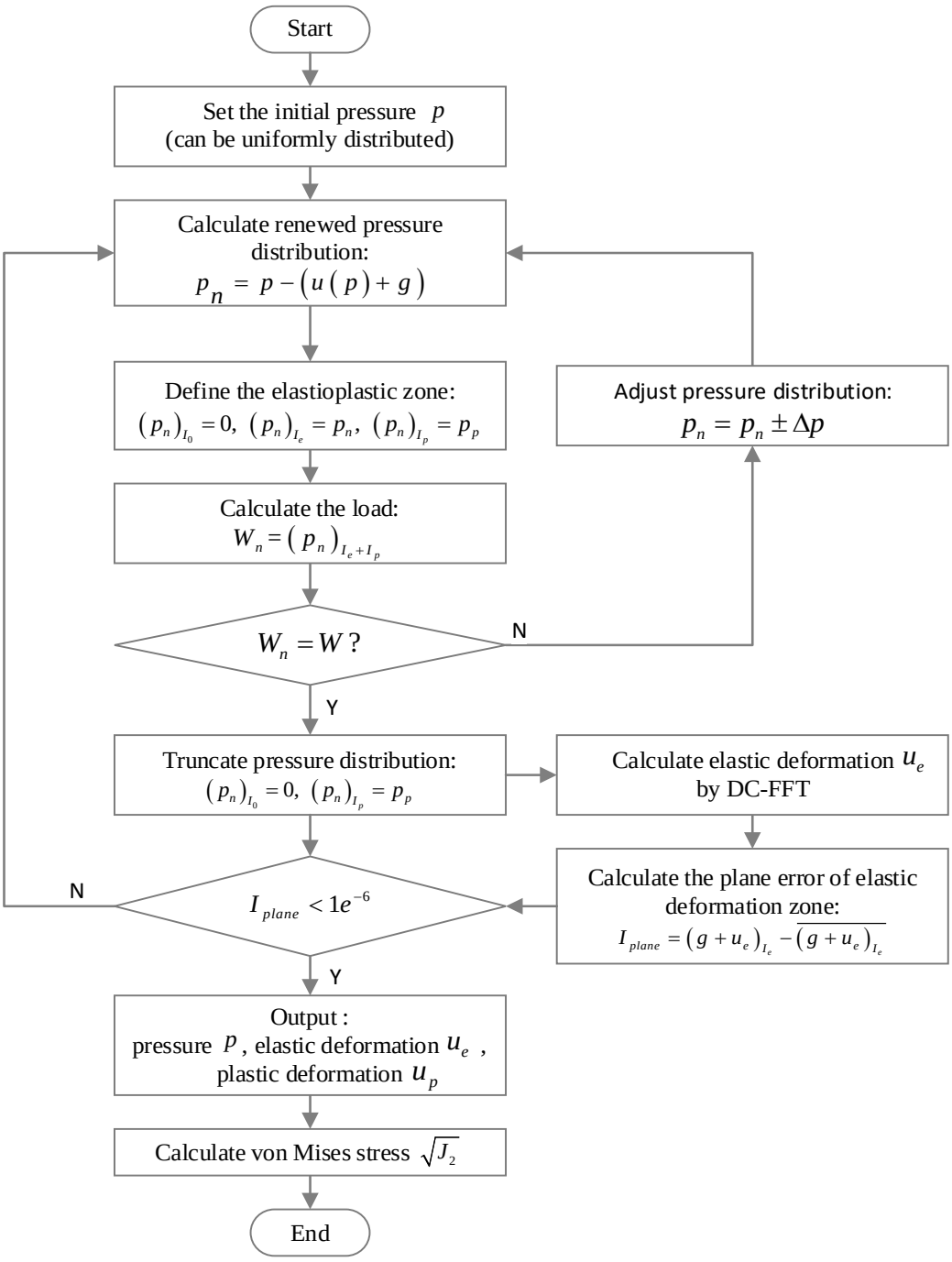

Fig. 7-6 The flowchart of the process for layered contact problem.

3. Determine if the load balance is satisfied. If not, select an appropriate constant Δp to adjust the pressure $p_n = p_n \pm \Delta p$, then repeat steps 1-3 until the convergence requirement is met. If satisfied, proceed to the next step.
4. Obtain the pressure distribution considering the plastic deformation by truncating pressure $(p_n)_{I_0} = 0$ and $(p_n)_{I_p} = p_p$, then the elastic deformation $u_e = u_z$ in Equ.(7-23) can be calculated by the FFT method.

5. Calculate the height error of the elastic deformation zone: $I_{plane} = \left(g + u_e\right)_{I_e} - \overline{\left(g + u_e\right)_{I_e}}$.
6. If the error is greater than the convergence error ε_{plane}, repeat steps 1-5. If there are no specified notifications, the convergence error of the plane ε_{plane} is 1×10^{-6}. If it is converged, proceed to the next step.
7. Output pressure distribution p_n, elastic deformation u_e and plastic deformation $u_p = \overline{\left(g + u_e\right)_{I_p}} - \left(g + u_e\right)_{I_p}$.
8. According to the pressure p_n and the pre-set depth sequence *z*, the stress distribution at each depth in Equ. (7-23) and Equ. (7-24) can be obtained by the FFT method.

The value of the initial pressure in the simulation is set to Hertzian contact pressure distribution, which also corresponds to the physical process of the boundary lubrication experiment, that is, the external load applied to the tribo-pairs first balances the contact pressure between the interfaces of the tribo-pairs, and then relative sliding occurs to appear other phenomena such as tribochemical reactions.

The adjustment of the rigid gap between the two surfaces determines the accuracy and speed of the pressure convergence, which is also the key step in adjusting the load balance. Wang *et al.* [355] proposed a Proportional-Integral-Differential controller (PID controller) to adjust the value of the rigid gap, as shown in Fig. 7-7.

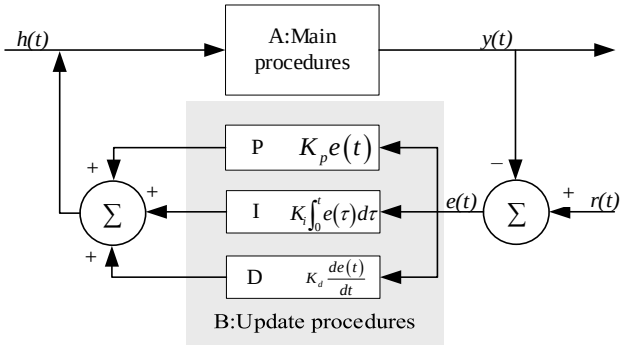

Fig. 7-7 A block diagram of the PID controller in a feedback loop [355].

In the $(n+1)^{th}$ iteration step, the discrete algorithm of the PID controller is:

$$h_{n+1} = h_n + K_p e_n + K_i \sum_{j=0}^{n} e_j + K_d \left[e_n - e_{n-1} \right] \tag{7-25}$$

where h_{n+1} is $p_n = p_n \pm \Delta p$ in step 3 of the simulation process and $e_n = W - W_n$.

One of the advantages of this method is that after choosing the appropriate values of K_p , K_i, and K_d in advance to obtain a small adjustment of the rigid gap in a single cycle to ensure the convergence, no need to adjust in subsequent cycles. The method of parameter selection is to realise that the change of the rigid gap for each adjustment is at least one order of magnitude lower than the current value of the rigid gap.

The convergence criterion of the load balance is:

$$\frac{\sum\sum |W_n - W|}{\sum\sum |W|} \le \varepsilon_W \tag{7-26}$$

If there are no special notifications, the convergence error of the load ε_W is 1×10^{-6}.

7.3.6 *Verifications*

The input parameters in this model are the same used in O'Sullivan and King's paper [223] for verification. The elastic half-space has a layer with a thickness of h on the substrate and the upper body is a rigid ball with a radius of $R = 10h$. The elastic modulus of the substrate is E_2 and the elastic modulus of the layer E_1 is proportional to E_2. The Poisson's ratio of the layer and the substrate are both 0.3. The normal load is L with the traction μL in which μ is the friction coefficient. The computation zone after dimensionless is $\left[-2 \le X \le 2,\ -2 \le Y \le 2\right]$ and the mesh size is $\Delta x = \Delta y = 0.078 a_0$.

In addition, the normalised parameters are that when the elastic modulus of the layer is the same as that of the substrate $E_1 = E_2$ and the Hertzian contact radius $a_0 = h$, the normal load $L = L_0$ and the normal pressure $p = p_{\max}$ ($p_{\max}$ is the maximum Hertzian contact pressure).

It is assumed that friction will not affect the contact pressure in the contact area. When the elastic modulus of the layer increases, the maximum contact pressure increases and the contact radius decreases, as shown in Fig. 7-8. In the case of $E_1 = 0.5E_2$, the contact radius $a = 1.219h$ and in the other case of $E_1 = 2E_2$, the contact radius $a = 0.813h$, which are very close to the results in O'Sullivan and King's work [223].

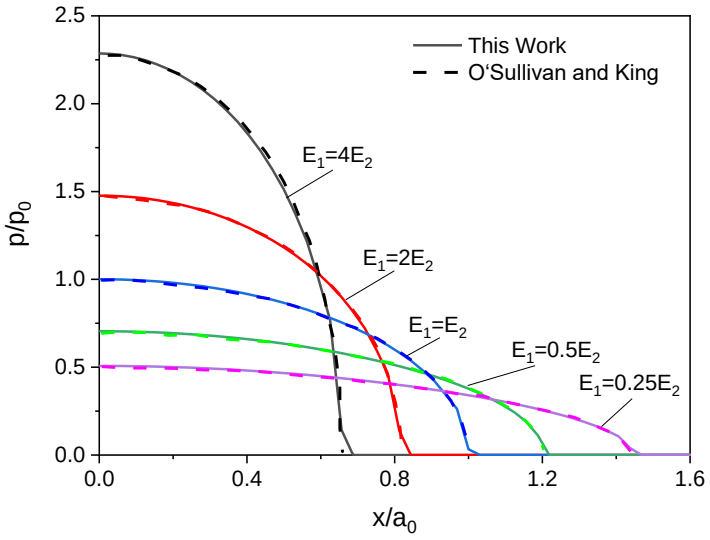

Fig. 7-8 The normal contact pressure profiles along the *x*-axis at different elastic modulus of the layer. (The solid line is the simulation results in this work and the dashed line is the results in O'Sullivan and King's work [223].)

Fig. 7-9 shows three stress components σ_{xx}, σ_{xz} and σ_{zz} at $x = y = 0$ as the function of depth z for different friction coefficients μ = 0, μ = 0.25 and μ = 0.5, where the results in the case of μ = 0.25 show a good match with O'Sullivan and King's work [223, 230]. Under different friction coefficients, both the normal stress σ_{xx} and σ_{zz} are unchanged. When the friction coefficient increases, the shear stress σ_{xz} increases.

Fig. 7-10 shows the von Mises stress $\sqrt{J_2} / p_{\max}$ at the cross-section of y=0 which represents the propensity of yielding in the layer and the substrate for different elastic modulus ratios of layer and substrate and friction coefficient, which is agreed with O'Sullivan and King's work [223, 230]. When there is no friction, the maximum stress occurs along the line of applied load, and in this case, the depth is $z / h = 0.5$. When the friction coefficient is 0.25, it can be that the point of maximum stress begins to move

toward the surface and *x*-direction. When the friction coefficient increases to 0.5, the point of maximum stress occurs on the surface $z = 0$ and the value increase as well. Under different friction coefficients, increasing the stiffness of the layer will increase the possibility of the yielding of the layer but it has a small effect on the substrate.

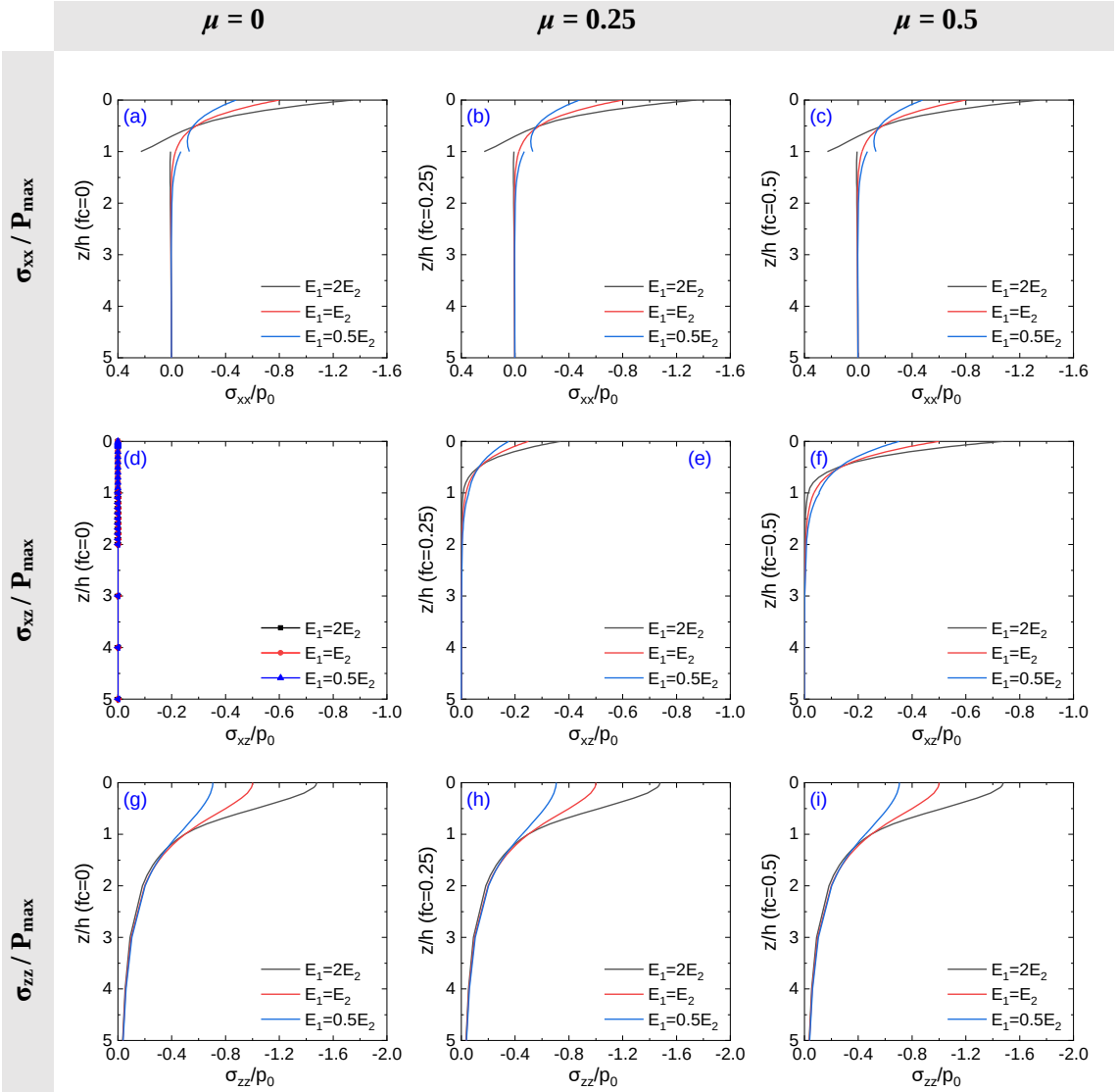

Fig. 7-9 The normalised stress components σ_{xx}, σ_{xz} and σ_{zz} at $x = y = 0$ as a function of depth z for different friction coefficients $\mu = 0$, 0.25 and 0.5.

.

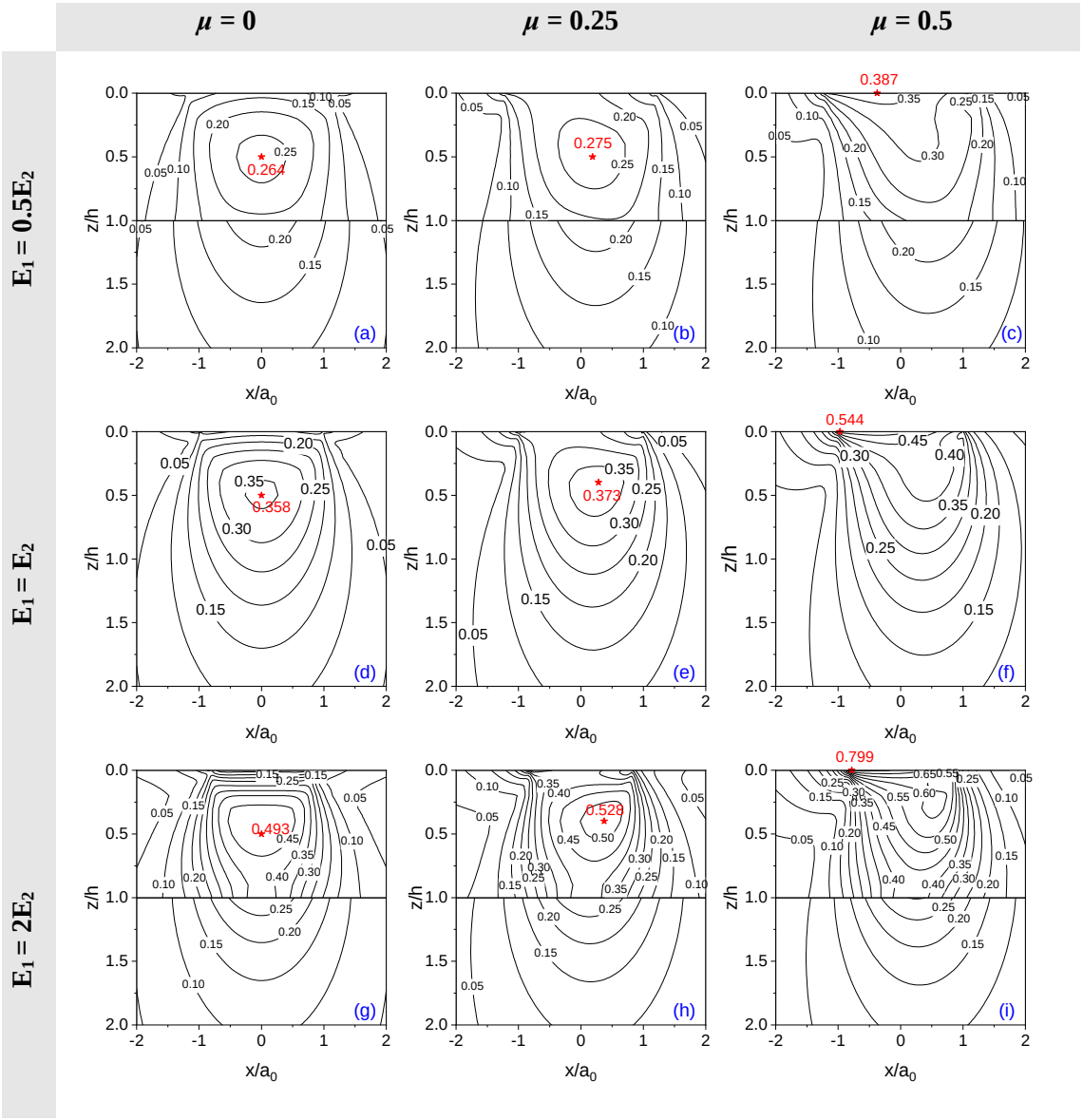

Fig. 7-10 Von Mises stress $\sqrt{J_2}$ contours at the cross-section y = 0 for different elastic modulus ratio of layer and substrate $E_1 = 0.5E_2$, $E_1 = E_2$ and $E_1 = 2E_2$.

Based on the results above, the effectiveness of the layered contact algorithm has been proved. It will be applied to the further calculation of deformation and stress with tribochemistry and wear.

7.4 *Development of the Wear Model of FFO Involving Tribochemistry*

7.4.1 *Tribofilm Growth Equation for FFO*

The tribochemical process of FFO has a certain similarity to that of ZDDP. According to the experimental results of the tribofilm growth of FFO in Chapter 5~6, the growth rate of tribofilm and the thickness at the stable phase are affected by temperatures, and the growth curve showed an exponential trend which accorded with the Arrhenius equation. In addition, although there are no microscopic experiments that can prove the effect of stress on the tribofilm growth process of FFO, it can be inferred that the tribochemical reaction process of FFO tribofilm is also related to stress because FFO contains ZDDP and the chemical structure of tribofilm is similar to that of ZDDP tribofilm.

The difference in the growth trend of FFO tribofilm is that there is a process of thickness reduction and re-growth after the tribofilm grows to a certain stage, and this phenomenon is particularly obvious at 80 ℃ and 100 ℃. There are two possible reasons for this process. First, the durability of the initial tribofilm is lower, so it is easier to be removed partly after growing to a certain thickness, and then it continues to grow a more stable tribofilm structure. The second is that both ZDDP and detergent in the FFO participate in the tribochemical reactions, so their reaction activities are different at different temperatures. Some kinds of reactions may take place preferentially, while the other temporarily reduces part of tribofilm thickness due to competition or delayed reaction, but finally has a positive effect on the increase of tribofilm thickness. No matter which hypothesis, there are at least two different tribochemical reaction rates, and there is a certain time difference between them.

Following the modelling work of Ghanbarzadeh *et al.* [179] for ZDDP tribofilm, by analogy with the expression of tribofilm thickness as the function of time and the process of fitting experimental results, the expression of tribofilm thickness of FFO is described in Equ. (7-27).

$$h = h_a(1-e^{-Ct}) + h_b(1-e^{-D(t-t_0)}) \quad \textbf{(7-27)}$$

where h_a and h_b are the maximum thickness that the two-step tribochemical reactions can reach, respectively; t_0 is the delayed time of the latter reactions; C and D are the constants relevant to the two reaction rates in brief, respectively.

First, the tribofilm growth curves under the high λ ratio at four temperatures in Fig. 5-1 are used to fit the constants in Equ. (7-27). The curve-fitting Tool in MATLAB is used to finish this process and the comparisons between the fitting results and the experimental results can be seen in Fig. 7-11. If the second growth is not considered, that is $t_0 = 0$, the results cannot capture the reduction and re-formation of the tribofilm at 80 ℃ and 100 ℃, as shown in Fig. 7-11a. In contrast, if considering a delayed time of the second step of tribofilm growth such as $t_0 = 0.5$, this phenomenon can be captured which has been highlighted by the arrows in Fig. 7-11b.

(a) t_0 = 0 **(b) t_0 = 0.5**

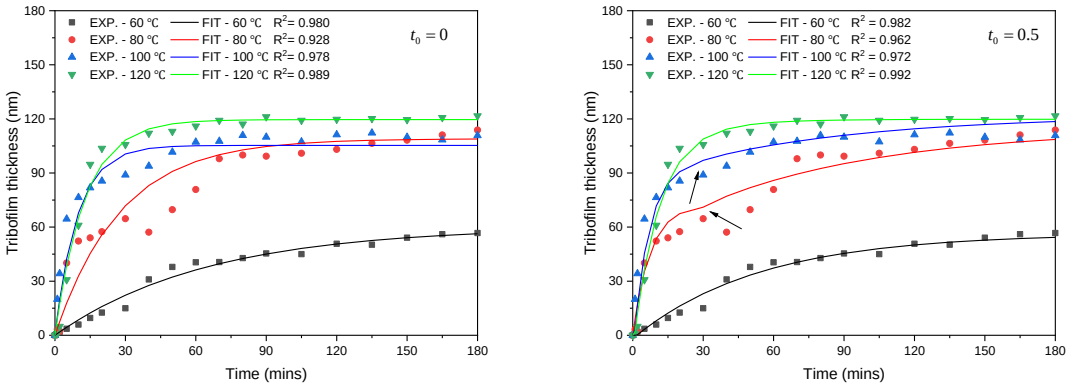

Fig. 7-11 Comparisons between fitting results and experimental results when $t_0 = 0$ and $t_0 = 0.5$ are used in the tribofilm growth equation, respectively.

Additionally, by comparing the values of R^2 (the coefficient of determination on goodness-of-fit) at different temperatures, most of the error of the curve-fitting has a reduction (that is R^2 increasing) for $t_0 = 0.5$. Thus, $t_0 = 0.5$ is applied in the simulation and the other four parameters at different temperatures are listed in Table 7-2.

It should be explained why there is no further derivation for the physical expression of the parameters C and D in Equ. (7-27). On one hand, the two-step reaction of the tribofilm

growth is only the hypothesis, which requires massive tests to prove. It has not a clear reaction process as the same as ZDDP, which can be used to discuss the physical parameters such as activation energy of the reaction and the mechanical work of stress. On the other hand, these parameters are not the most important at this stage for FFO, because the physical meaning of them even the expression of the tribofilm growth equation may be different when the recipe of the additives in FFO changes. Therefore, in the view of macro-experiments or engineering applications, the expressions in Equ. (7-27) is simple but sufficient to first develop the tribofilm growth model as it has captured the features in tribochemical reactions of FFO as much as possible.

Table 7-2 The values of four parameters in the tribofilm growth equation (7-27) obtained by fitting the experimental results of tribofilm thickness as the function of time at different temperatures.

Temperatures	**60 ℃**	**80 ℃**	**100 ℃**	**120 ℃**
h_a	53.66	72.32	97.68	115.7
C	1.122	8.1	9.94	5.655
h_b	2.691	42.45	24.18	4.116
D	1.051	0.773	0.7927	2.287

(Units: t, t_0 – hour, h_a, h_b – nm, C, D- hour^{-1})

The equation of tribofilm thickness should include two parts as growth and removal. During the growth process of tribofilm, the amount of growth is greater than the amount of removal, while in the equilibrium stage, the amount of growth and removal reach a dynamic balance. In previous modelling works, the removal rate of tribofilm thickness was assumed to be a constant [283], linearly [50] or exponentially [179] proportional to the current tribofilm thickness. However, in this case of FFO, the removal amount of tribofilm cannot be measured alone in the experiments, so the tribofilm thickness can be regarded as the result that combines the growth amount and removal amount of tribofilm.

7.4.2 *Wear Calculation for FFO*

Archard's wear equation is one of the most commonly used models in wear calculation. The wear amount or wear rate can be calculated by determining the wear coefficient K in the model when the contact pressure and working conditions are known.

According to the experimental results, the wear mechanism of FFO is related to the chemical compositions of tribofilm at different temperatures, in which the influence of sulphides is dominant in the lower temperature range while the influence of phosphates is dominant in the higher temperature range. However, both are relevant to the tribochemical reactions of tribofilm growth in essence. Thus, the wear process of FFO is divided into two phases, as shown in Fig. 7-12.

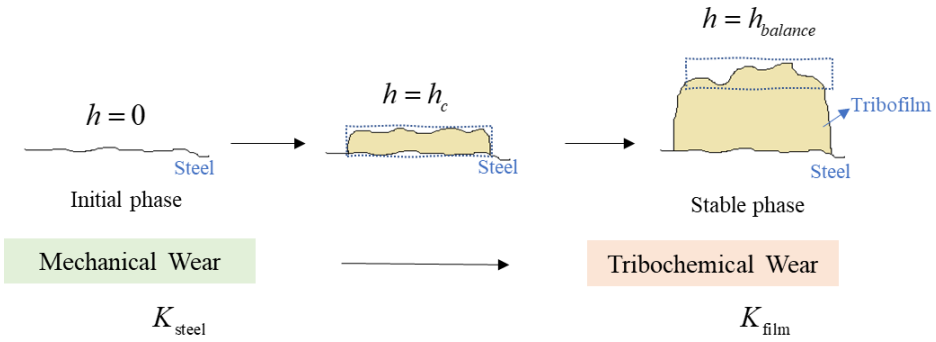

Fig. 7-12 The description of the wear process of FFO.

At the early stage of the rubbing process, tribofilm has not grown enough to cover the steel surface, so the wear is regarded to be dominated by the mechanical wear between metal surfaces. The wear coefficient K in the Archard wear equation is the wear rate of steel-steel contact, which is about 10^{-5} ~10^{-6} [356].

When the tribofilm grows to a thickness of h_c, it is assumed that there is almost no direct contact happening between the two metal surfaces. At this time, the wear results from the tribofilm generated by the tribochemical reactions, that is, the iron in the substrate entering into the tribofilm. The wear coefficient is denoted as K_{film}, which is related to the amount of iron in the tribofilm that can be calculated by the atomic percentage of iron in XPS analysis.

Bosman and Schipper [178] used the method of converting the iron atomic percentage in XPS analysis into the volumetric percentage of iron to calculate the wear loss parameter in the simulation of wear involving the tribochemistry of ZDDP. The difference from their method is that the model in this work analysed and considered the different structures and densities of Fe in the tribofilm and substrate. According to the mass conservation of iron, the loss of iron in the substrate, the tribochemical wear, is derived

from the iron mass in the tribofilm with a certain thickness. The following takes the results at 120 ℃ as an example to explain the calculation process.

The atomic percentages of iron in tribofilm at different etching depths are measured from the XPS atomic analysis, as shown in Fig. 6-19~Fig. 6-22. By referring to the atomic radius of iron, the volumetric percentage of iron Fe vol.% in tribofilm as the function of the unit depth can be estimated. Next, the third-order polynomial is applied to fit the curve, as shown in Fig. 7-13. (To simplify the description, the full fitting process and results at all temperatures in the simulation can be seen in Appendix C.)

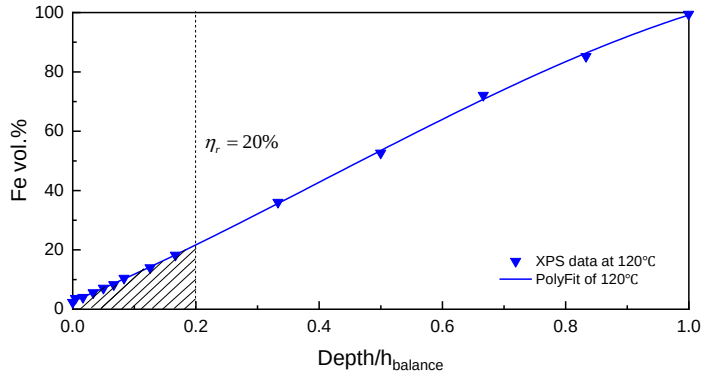

Fig. 7-13 The XPS of Fe vol.% at 120℃ and its 3rd polynomial fitting curve.

Assuming that Fe vol.% as a function of depth remains unchanged no matter what thickness tribofilm grows to, the volume of iron contained in tribofilm can be calculated if the tribofilm thickness is known.

When the tribofilm thickness reaches the stable phase, its growth rate can be considered to be equal to the removal rate, but how much tribofilm is removed in each contact process is unknown. It is assumed that the removed thickness h_r at the surface layer is proportional to the current thickness h of the tribofilm, then the ratio is denoted as η_r, that is,

$$h_r = \eta_r \cdot h \tag{7-28}$$

The removed volume of tribofilm at the surface layer is

$$V_r = h_r \cdot A_m \tag{7-29}$$

where A_m is the measurement area during the etching process.

For example, when $\eta_r = 20\%$, it means that the thickness removed is 20% of the total tribofilm thickness. As shown in Fig. 7-13, after the integration of the shaded area and the normalisation of the area, the volume fraction of iron η_{Fe-Vol} in the removed volume of tribofilm can be calculated. Then the volume of iron $V_{Fe-comp}$ contained in the removal part of tribofilm is calculated as:

$$V_{Fe-comp} = \eta_{Fe-Vol} \cdot V_r \tag{7-30}$$

According to the chemical analysis of tribofilm by Raman and XPS, Fe mainly exists in the form of iron sulphides or iron oxides in the tribofilm, so the density of iron compounds is the average value of these two, which is about $\rho_{FeO/S} = 5$ g/cm^3.

Then, the mass of iron in tribofilm can be calculated by

$$m_{Fe-comp} = \rho_{FeO/S} \cdot V_{Fe-comp} \tag{7-31}$$

When tribofilm reaches a critical thickness h_c, it is considered that the wear in the substrate is mainly dominated by the tribochemical reactions, so the mass of iron removed in the surface layer of tribofilm is equal to that lost in the substrate, that is

$$m_{Fe-wear} = m_{Fe-comp} \tag{7-32}$$

In the substrate, the density of iron is $\rho_{steel} = 7.81$ g/cm^3. Therefore, the wear volume is

$$V_{Fe-wear} = m_{Fe-wear} / \rho_{steel} \tag{7-33}$$

The average wear coefficient K_{film} at the current tribofilm thickness can be calculated by Archard's wear equation.

$$K_{film} = \frac{V_{Fe-wear} \cdot H_{film}}{P \cdot S} \quad \textbf{(7-34)}$$

where H_{film} is the hardness of the tribofilm; P is the normal load; S is the sliding distance (= sliding speed x time).

Finally, the wear depth at the contact point is calculated in Equ. (7-35).

$$h_{wear} = K_{film} \cdot P(x, y) v \Delta t / H(x, y) \quad \textbf{(7-35)}$$

in which, v is the relative sliding speed of the two contacting surfaces; Δt is the characteristic time length; $P(x, y)$ and $H(x, y)$ are the pressure and the hardness of the contact point, which can be obtained in the contact algorithm and hardness update, respectively.

7.4.3 *Mechanical Properties of Tribofilm*

7.4.3.1 *Young's Modulus and Hardness of Tribofilm*

Many studies showed that the mechanical properties of ZDDP tribofilm will be influenced by the temperatures and the chemical compositions of tribofilm. The chemical compositions of FFO tribofilm have a similar structure to those of ZDDP tribofilm in which phosphates and sulphides are the main components. Thus, the mechanical properties of FFO tribofilm can be estimated by those of ZDDP tribofilm in the literature [132-134], that is, Young's modulus and hardness of FFO tribofilm are about 40 ~ 100 GPa and 1 ~ 4.5 GPa, respectively.

Akchurin and Bosman combined an empirical variation of hardness evolution with tribofilm thickness and a compensation factor as the function of the temperature to calculate the hardness at different temperatures [50, 133, 178]. For the case of FFO, this method is also applied in the simulation to obtain the hardness of FFO tribofilm in Equ.(7-34) at four test temperatures by curve-fitting and the difference method. The results are listed in Table 7-3.

Table 7-3 The hardness of FFO tribofilm at different temperatures, estimated by the empirical curve of hardness as the function of the thickness and the compensation factor.

Temperatures	**60 ℃**	**80 ℃**	**100 ℃**	**120℃**
Thickness	60 nm	110 nm	115 nm	120 nm
Compensation factor	0.716	0.563	0.407	0.297
Hardness	2.1 GPa	1.5 GPa	1.1 GPa	0.77 GPa

In the layered contact algorithm, there is an assumption that when the average tribofilm thickness is higher than the roughness of the surface, then the tribofilm can be regarded as a continuous layer during the contact. Then, Young's modulus on the top layer will be changed from steel to tribofilm. Although it is known that the elastic modulus of ZDDP tribofilm varies with the hardness under certain conditions [132-134], the average elastic modulus of the tribofilm is set to be 85 GPa in the simulation at all temperatures to simplify the first calculation.

7.4.3.2 *Hardness Update Considering Plastic Deformation*

In the previous section, the hardness of the tribofilm in the stable phase at different temperatures is used to be the input in the simulation, while this section discusses how the hardness updates when the tribofilm grows to a different thickness and the correlation with the plastic deformation.

Andersson *et al.* [280] developed a model of tribofilm mechanics that considered the variation of plastic deformation pressure with tribofilm thickness and plastic deformation depth. The plastic deformation pressure here can be regarded as the indentation hardness of tribofilm, which is assumed to change linearly with the thickness. When tribofilm has the maximum thickness, the surface hardness of tribofilm is the minimum.

The relationship among the hardness H at the contact point (x, y), tribofilm thickness and plastic deformation of the two contacting surfaces in the computational domain is expressed in Equ. (7-36).

$$H(x,y)=\begin{cases} H_s-\dfrac{H_s-H_{film}}{h_{\max}}\left(h'-U_p\right) & \text{if } U_p<\left|h_1-h_2\right| \\ H_s-\dfrac{H_s-H_{film}}{h_{\max}}\left(h_1+h_2-U_p\right) & \text{if } \left|h_1-h_2\right|\le U_p\le h_1+h_2 \\ H_s & \text{if } h_1+h_2\le U_p \end{cases} \quad \textbf{(7-36)}$$

in which H_s and H_{film} are the hardness of the substrate and the tribofilm at the surface, respectively; $h_{\max}$ is the maximum tribofilm thickness; U_p is the plastic deformation; h_1 and h_2 are the tribofilm thickness of the two rubbing bodies at the contact point, respectively; h' is the larger thickness between h_1 and h_2.

7.4.4 *Simulation Procedure*

The flowchart to calculate tribofilm thickness, wear and stress is illustrated in Fig. 7-14. Since the objective of the simulation is to achieve the calculation of the tribofilm growth and wear based on the experimental results of FFO, the material properties and working conditions in the input parameters are determined by the experiments of FFO, as listed in Table 7-4.

Table 7-4 Input Parameters in the simulation.

Material Parameters		Working Conditions	
Ball Roughness	20 nm	**Entrainment Speed**	0.1 m/s
Disc Roughness	10 nm	**Max Hertzian Pressure**	1.15 GPa
Elastic Modulus – Steel	210 GPa	**SRR ratio**	150 %
Elastic Modulus – Tribofilm	85 GPa		
Poisson's Ratio – Steel	0.3		
Poisson's Ratio – Tribofilm	0.3		
Hardness – Steel	8 GPa		
Wear Coefficient K_{steel}	10^{-5}		

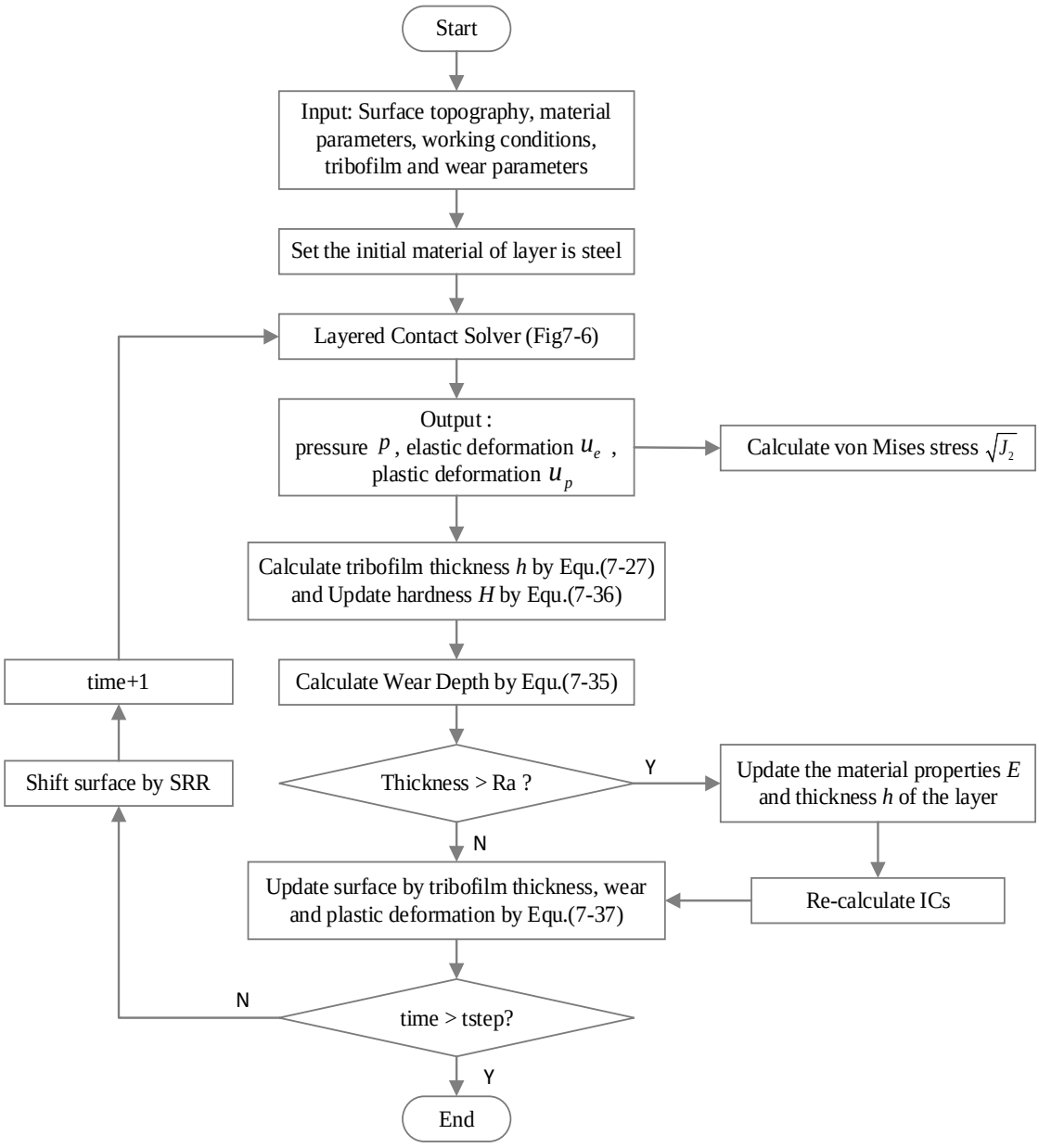

Fig. 7-14 Flowchart to calculate the tribofilm thickness, wear and stress.

The two input rough surfaces are the Gaussian rough surface generated by the numerical approach, having the roughness of 20 nm and 10 nm, representing ball surface and disc surface, respectively. The computing domain is [$-6a_0 < x < 6a_0$, $-6a_0 < y < 6a_0$] where a_0 is the Hertzian contact radius. The number of nodes is 129x129. The curve-fitting parameters of tribofilm thickness and wear at different temperatures have been listed in Sections 7.4.1~7.4.2, which will not be repeated here.

At the beginning of the simulation, both the initial material of the ball and the disc are set to be steel, that is $E_{layer} = E_{substrate} = E_{steel}$, which is the same as the simulation of homogeneous materials. The hardness update and the tribofilm growth are calculated by Equ. (7-36) and Equ. (7-27), respectively. The wear coefficient *K* in Equ. (7-35) is K_{steel} .

After calculation of several time steps, when the tribofilm thickness is greater than the surface roughness, tribofilm can be considered as a continuous layer, then the elastic modulus of the surface material is changed to that of tribofilm, that is $E_{layer} = E_{tribofilm}$. The layer thickness is the average thickness of the tribofilm at this step. Then, the influence coefficients in the layered contact model are required to be re-calculated, where the deformation and contact pressure will be updated correspondingly with the new material parameters for the contact calculation in the next time step.

In each time step, the surface topography of the ball and the disc will be changed by tribofilm thickness, wear and plastic deformation, and their relationship is expressed in Equ. (7-37).

$$\begin{cases} S_{z1}^{n+1} = S_{z1}^{n} + 0.5 \times U_p^n - h_1^n + w_1^n \\ S_{z2}^{n+1} = S_{z2}^{n} - 0.5 \times U_p^n + h_2^n - w_2^n \end{cases} \quad \textbf{(7-37)}$$

where the subscripts 1 and 2 represent the ball and the disc surface, respectively; S_z is the rough surface; *h* is the tribofilm thickness; w is the wear depth; *n* is the n^{th} time step; ± is the relative amount of increase or decrease.

For SRR shift, since the contact area is fixed at the centre of the computational domain, the rolling and sliding between the surfaces and the wear need to be realised by moving the two rough surface matrices: 1) Rolling: In each time step, both the two rough surfaces

are moved one node along the sliding direction, such as the point $(i, j)\rightarrow(i+1, j)$. 2) Sliding: When the step number n is divisible by $1/SRR$, one of the surfaces adds an additional movement of a node, such as a point $(i, j)\rightarrow(i+2, j)$. The other surface keeps one node's movement.

Finally, the 3D stress distribution of the ball and the disc can be calculated at any time step according to the current material parameters, layer parameters, contact pressure, etc.

All the simulations in this chapter have been done by MATLAB (version 2019b). The computation time to simulate a 1-hour test (equivalent to the experiment) is about 8-15 hours, mainly depending on the solution time of the contact model, whether traction is considered and the number of the depth interval set in the stress calculation.

In addition, because there are differences in time scale and length scale between the computational domain and real experiments, the experimental time represented by each iteration cannot be directly calculated. It varies by model and algorithm. The idea of adjusting the time step or the characteristic time length in this simulation is to first estimate the initial value through the minimum time required for the ball or the disc to rotate one cycle in the experiment, and then further modify the value according to the simulation results.

7.5 *Results and Discussions*

7.5.1 *Tribofilm Thickness and Wear*

The comparisons between the simulation results and experimental results of the tribofilm growth curves at different temperatures are shown in Fig. 7-15 in which the simulation results are essentially consistent with the experimental results. It also accords with the characteristics that the balanced tribofilm thickness increases with the increase of temperature. In particular, at 80 ℃ and 100 ℃, the simulation results of the growth curve of the tribofilm in the stable phase also show similar fluctuations to the experimental results, which may be caused by the increase of wear.

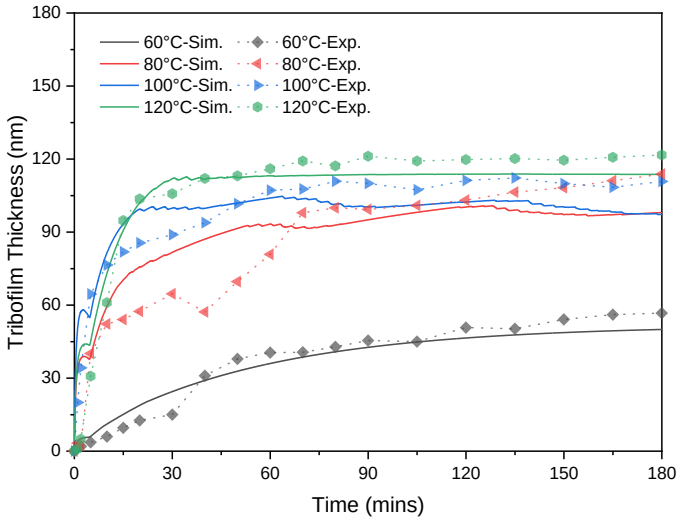

Fig. 7-15 Comparisons between the experimental results and simulation results of tribofilm thickness on the ball at different temperatures.

In the first hour of the growth stage of tribofilm, although the growth equation of tribofilm in Equ. (7-27) has taken into account the possibility of different tribochemical reaction rates of growing tribofilm, the simulation results in this part still have a relatively large error from the experiment. This indicates that there may be other factors that cause the growth rate of the tribofilm to slow down during the growth process at 80 ℃ and 100 ℃, and even the slight decrease of tribofilm, which requires further experimental and theoretical research to improve the model.

Fig. 7-16 illustrates the comparison between the simulation results and the experimental results of the average wear depth on the disc as the function of time at different temperatures. In the wear mechanism of FFO, the initial wear stage is considered to occur only the wear between steel and steel, and when the tribofilm reaches a certain thickness h_c, only the tribochemical wear is considered to occur. Therefore, it can be seen from the wear simulation results that at the four temperatures, the initial wear rate is larger and there is little difference in wear. However, when the tribofilm thickness reaches h_c, the wear rate begins to decrease and fits well with the wear slope of the experimental results at all temperatures. The thickness h_c applied in the simulation are 1.4, 2.2, 2.4 and 2.5 times the removed thickness h_r at 60, 80, 100 and 120 ℃, respectively.

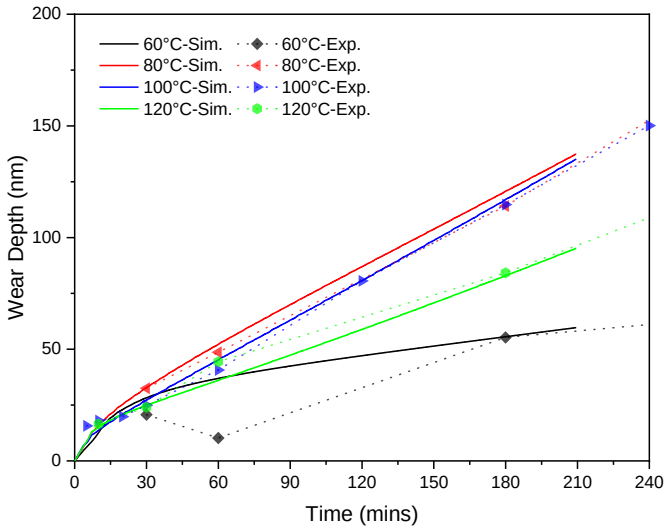

Fig. 7-16 Comparisons between the experimental results and simulation results of wear depth on the disc at different temperatures.

In general, this model achieves that the simulation results of tribofilm thickness and wear are almost consistent with the corresponding experimental results of FFO. It also satisfies the two-phase wear mechanism of FFO, that is, both the tribofilm thickness and the wear increase with the increase of temperature in the low-temperature range from 60 ℃ to 80 ℃, while in the high-temperature range from 80 ℃ to 120 ℃, the tribofilm thickness increases but the wear decreases as the temperature increases.

7.5.2 *Von Mises Stress*

The tribofilm is regarded as a surface layer covering the steel substrate, so the contact state is different after the change of material properties and thickness of the surface layer, which also affects the stress of the sublayer. In addition, considering the difference of the friction coefficients at different temperatures, the average friction coefficients when the tribofilm reaches the stable phase are calculated and used in the stress calculation, which are listed in Table 7-5.

Table 7-5 Friction coefficients in the stress calculation at different temperatures.

Temperatures	**60 ℃**	**80 ℃**	**100 ℃**	**120 ℃**
Friction Coefficient	0.108	0.122	0.124	0.132

Since the stress calculation is a three-dimensional distribution, in order to compare the calculation results more clearly, the results at the cross-section $y = 0$ are selected for

discussion. Fig. 7-17 shows von Mises stress under different temperatures at the time step equivalent to the 30 mins and 180 mins of experiments, in which the *x*-axis is dimensionless with the Hertzian contact radius a_0; the *z*-axis is the real value of depth that directly shows the tribofilm thickness (pointed out by arrow); the maximum stress position is highlighted by a five-pointed star and the dimensionless stress value is marked.

At all test temperatures, the maximum stress occurs at the interface of the tribofilm and the substrate. With the increase of test time, the maximum stress decreases slightly. This may be because the increasing contact area reduces the contact pressure or the increase of the tribofilm thickness.

At the same test time, the maximum stress values at the four temperatures have little difference, but 80 ℃ had a minimum value by comparison. Theoretically, if the surface is subjected to less stress, it will be less likely to fail. This cannot explain that not only the maximum wear appears at 80 ℃, but also the phenomenon of thickness reduction and regeneration during the growth stage of tribofilm.

There may be two reasons for these results. First, the elastic modulus of tribofilm is the constant that does not change with temperature in the simulation. However, the elastic modulus of phosphates on the surface layer should be lower than that of sulphides near the substrate, according to the studies of the mechanical properties of ZDDP tribofilm [132]. Therefore, as the temperature increases, the phosphate content in tribofilm increases and its elastic modulus may decrease. This input error affects the calculation of the stress value. Secondly, the increase of wear at 80 ℃ may be due to the poor durability of tribofilm, so it is still easy to be removed even if it suffers from lower stress. Meanwhile, more iron is consumed in the tribochemical reactions for tribofilm supplement, resulting in increased wear. This also suggests that the nature of the wear mechanism of FFO is closely related to the process and products of the tribochemical reactions of tribofilm generation.

7.5.3 *Interfacial Shear Stress*

The shear stress plays an important role in the occurrence of assisting tribochemical reactions. The distributions of interfacial shear stress at $z = 0$ of the top surface of tribofilm at different temperatures and test durations are shown in Fig. 7-18.

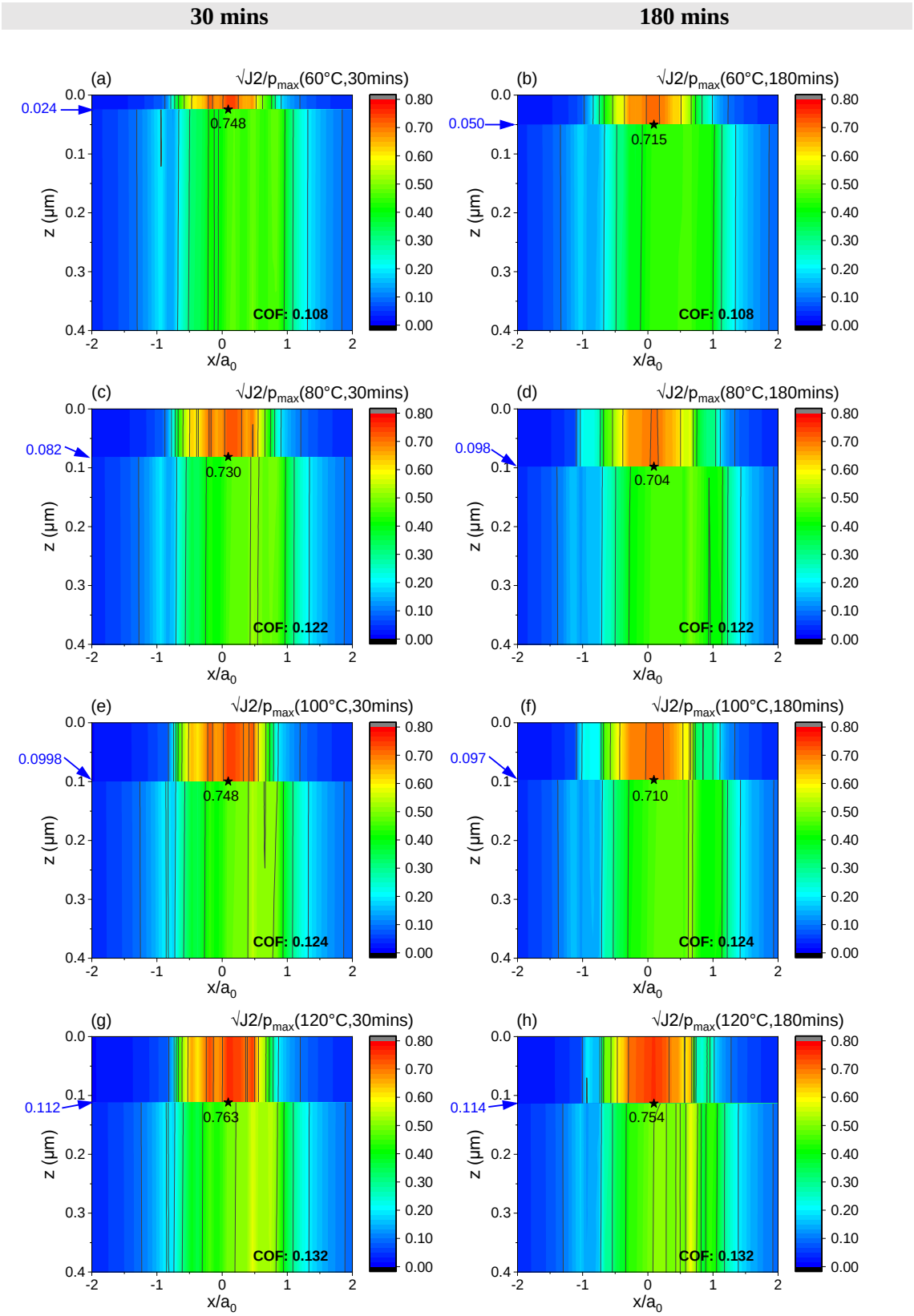

Fig. 7-17 Von Mises stress contours at the cross-section of y = 0 at different temperatures with the friction coefficient at the time steps equivalent to the 30 mins and 180 mins of experiments.

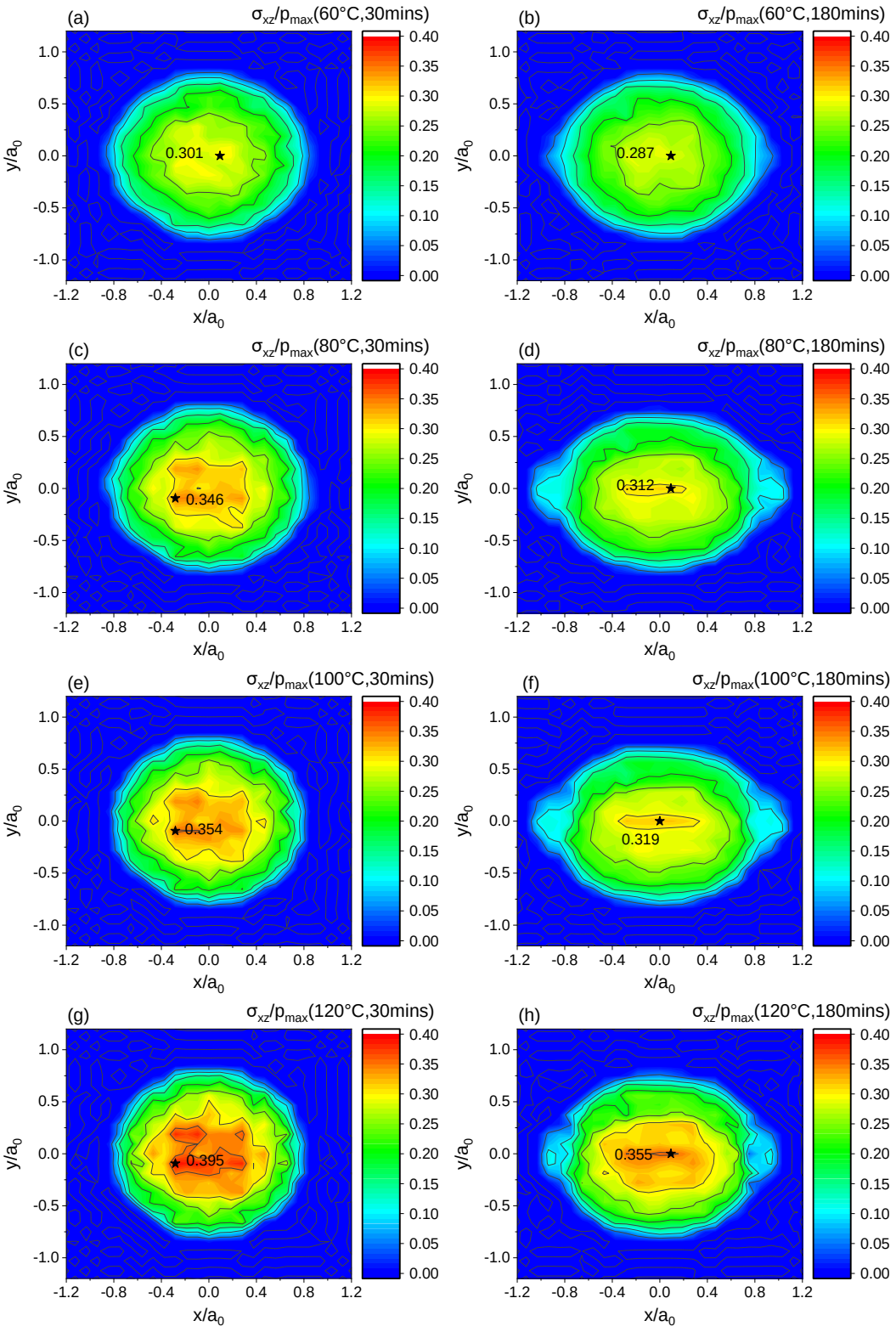

Fig. 7-18 Interfacial shear stress contours at the tribofilm surface of z = 0 at different temperatures with the friction coefficient at the time steps equivalent to the 30 mins and 180 mins of experiments.

Because of the presence of shear stress, as the test time increases, the contact area shown in the stress contour obviously deforms longer along the direction of shear force, but the maximum value of the shear stress decreases. As the temperature increases, the shear stress on the surface increases due to the increase of friction coefficient. It is also found from FFO experiments that the tribofilm thickness increases with the increase of temperature. Thus, it is consistent with the characteristic that the growth of tribofilm is promoted by both stress and temperature [52, 53, 275].

7.6 *Summary*

This chapter develops a model based on the layered contact theory for the calculation of tribofilm growth, wear and sublayer stress distribution of FFO. Based on the concept of mass conservation, a method for calculating tribochemical wear is proposed which can be applied to FFO. The main modifications and improvements of the model are as follows.

1) The tribofilm growth curves of FFO at different temperatures are used to fit the tribochemical equations. It is found that there may be two stages of different growth rates in the process of growing the tribofilm, so two different exponential growth rates are selected.

2) According to the variation of iron content with depth measured in FFO's XPS atomic analysis, the wear coefficient K in Archard's wear equation was derived and added to the wear calculation. Among the known wear models, different chemical structures of iron in tribofilm and steel substrate are firstly considered in this model. According to the mass conservation concept of iron, a more physical model is developed.

3) The tribofilm is regarded as a layer so the material properties of the surface are modified after it grows to a certain thickness, and the influence of tribofilm in the contact calculation can be considered;

4) The friction coefficients measured at different temperatures are inputted into the stress calculation, so the relationship among the shear stress on the surface of tribofilm, temperature and tribofilm thickness can be simulated.

After the experimental results of FFO were directly input or added to the simulation by means of curve fitting, the simulation results of the tribofilm growth and wear have a

good agreement with the experimental results. Then, for the results of stress calculation, the maximum stress occurs at the interface of the tribofilm and substrate at all temperatures and test times. With the increase of test time, the stress value of the sublayer decreased, which could be due to the increase of contact area or tribofilm thickness. The results of shear stress increase with the increase of temperature were successfully simulated in the distribution of shear stress at the top surface, which conforms to the characteristic that the tribochemical reaction kinetics of tribofilm is promoted by both temperature and stress.

This model framework is a successful attempt to model the tribochemical and wear characteristics of FFO with complex chemical compositions. This model expands the simulation flowcharts based on asperity-asperity contact from 2D surface to 3D layered structure, which can be also applied to the calculation of tribochemistry, wear, stress and roughness related to the coating surface in a certain field. In summary, this model provides an approach for calculating and evaluating tribochemical wear of general FFO with similar formulations and properties.

Chapter 8 Discussion

The main purpose of this research is to develop a model that can be used to predict the main tribological phenomena such as tribofilm growth, wear and stress state based on the tribochemical and wear behaviours of a commercial FFO. Therefore, in this chapter, the discussion will be carried out from the two aspects of experiments and modelling.

It has been mentioned in the literature review that fully formulated oils are usually composed of various additives such as antiwear additive, detergent, dispersant, antioxidant, etc., each of which may change the performance of lubricants. In addition, the tribological properties of fully formulated oils are usually different from single or two-component lubricant additives. In principle, from an application point of view, each FFO is unique and has certain research value. Therefore, we will first summarise FFO as a lubrication system and its trends in friction, wear and tribochemical reactions. Then, the possible interactions between single additives or additives of two components and their effects on tribofilm and wear are discussed from the perspective of the ways of iron loss in the substrate. Moreover, the effects of temperature and λ ratio on the tribofilm growth and wear mechanism are discussed. Finally, the wear phenomenon of FFO in the running-in period is discussed.

The formation of the tribofilm changes not only the surface topography but also the chemical properties of the surface material, thereby changing the contact conditions. In terms of modelling, the main innovation is to link the generation of tribofilm with the layered rough surface. While growing the tribofilm, the material properties of the surface are changed. In addition, based on the mass conservation of iron, the wear coefficient is correlated using XPS data. Besides, the influence of tribofilm on the stress distribution can be simulated. Therefore, the discussion points of modelling are also expanded from the following aspects: 1) layered contact model and the feasibility of considering tribofilm as a layer, 2) the feasibility of tribofilm formation equation, 3) wear model, and 4) stress distribution.

In the final section, the experimental deficiencies of this research and the limitations of the model are pointed out.

8.1 *Wear Mechanisms of Tribofilm Formed by the Fully Formulated Oil*

8.1.1 *Main Wear Mechanisms as a Lubricant System*

Recalling the experimental results in Sections 5.1.1 and 6.2.1, the tribofilm thickness of FFO increases with the increase of temperature, but the wear results show a two-phase wear mechanisms: phase (I) in the low-temperature range of 60~80 ℃, when the temperature increases, wear increases; and phase (II) in the high-temperature range of 100~120 ℃, when the temperature increases, wear decreases. This temperature-dependent correlation of wear mechanism is valid in the conditions of two λ ratios, that is boundary lubrication regimes. The results of FFO in the low-temperature range are different from the friction and wear test results of ZDDP alone in the same temperature range, where the thickness of ZDDP tribofilm increases with temperature, but the amount of wear decreases with the increase of thickness [179]. This also shows that the interactions of various additives in FFO has changed its tribochemical properties, and this change is not a simple synergistic or antagonistic effect.

Through Raman and XPS chemical analysis in Section 6.2.2 ~ 6.2.3, it can be obtained that the main composition of tribofilm is calcium phosphate instead of zinc phosphate, and the surface layer of tribofilm contains a thin layer of calcium carbonate. This is the same as the tribofilm generated in many experiments using both overbased calcium sulphonate detergent and ZDDP mixed in the lubricant [22, 27]. Studies have shown that overbased calcium sulphonate has an antagonistic effect on the anti-wear properties of ZDDP, and the chain length of calcium phosphate is shorter than that of zinc phosphate, then reducing the antiwear effectiveness [22-27]. However, this does not explain why the wear trends behave differently in different temperature ranges. The wear of the substrate is essentially the iron loss in the substrate, so the reason why the wear mechanism of the FFO is different from that of single or double additives can be explained by the ways of iron loss.

8.1.2 *Effects of Additives on the Iron Loss of the Substrate and Temperature Correlation*

The ways of iron loss can be considered in two types, in which it is removed mechanically, or enters the tribofilm through a tribochemical reaction. In the initial stage of the rubbing

process, without the protection of tribofilm, wear under boundary lubrication conditions occurs in direct contact between the two steel surfaces. In the comparative experiments of BO and FFO in Section 5.2.1, the wear amount and wear rate of BO are more than three times that of FFO. The specific reactions between various additives in FFO are complex. Thus, the following starts with the tribochemical reactions of single and two-component additives in the literature to discuss the possible ways of iron loss. Attempts were made to speculate on the possible causes of iron loss by various additives at different temperatures, namely the causes of wear.

8.1.2.1 *ZDDP*

There may be different opinions on the film-forming reaction process of ZDDP. From the results, Fe may be present as a small amount of iron phosphate or iron sulphide in tribofilm. The reaction of iron phosphate may originate from the acid-base neutralisation of iron oxide abrasive debris embedded in tribofilm [15], but this lacks direct experimental proof [5]. The further MD simulation shows that during the rubbing process, zinc phosphate has a digestive effect on iron oxide particles [181]. That is to say, Fe may become abrasive particles through mechanical wear and enter the tribofilm to be removed by the HASB effect. This may also be an explanation for the existence of iron phosphate.

Iron sulphide is mainly present between the phosphate tribofilm and the substrate. Shimizu and Spikes used EDX analysis to prove that in the initial stage of the rubbing process, high-S species first formed on the surface [357].

In summary, when ZDDP is used alone, there are two possible paths for iron consumption: 1) direct diffusion into tribofilm through tribochemical reaction and 2) first mechanical removal, and then diffused by chemical reaction into tribofilm.

8.1.2.2 *Overbased Calcium Sulphonate (OBCaSu) Detergent*

Overbased calcium sulphonate is another key film-forming additive in this case, but its film-forming process has been reported not to be derived from a chemical reaction with the metal surface, and there is not much iron involved in it [153]. Its anti-wear properties may come from the formation of boundary films on the metal surface by colloidal molecules and the replacement surface is worn away. Under the action of pressure and shear, the shell of the colloidal particles ruptured [153]. Because the Ca-S bond has a

weak resistance to high shear, the long-chain surface reactant is taken away, leaving the $CaCO_3$ core to crystallise on the surface [154, 155] or decompose to CaO [22, 154, 156, 157]. Therefore, if considering the consumption mechanism of Fe when overbased calcium sulphonate is used alone, the direct mechanical wear may be more than the consumption in the film formation reaction.

8.1.2.3 *Interactions between ZDDP and OBCaSu Detergent*

In the presence of ZDDP, the reaction of ZDDP or OBCaSu detergent with the substrate may have a priority problem, or the two additives may react with the substrate together. It is mainly from the perspective of phosphate formation to discuss the participation of iron in it, that is, whether iron or iron oxides will be consumed by tribochemical reactions when zinc phosphate is converted to calcium phosphate and is consumed, or when phosphate on the top surface of the tribofilm is removed during the rubbing process. Another phenomenon that more directly expresses the participation of iron in the tribofilm formation is the iron sulphide detected in tribofilm. The following first proposes three possible mechanisms based on the results at the high λ ratio.

* Mechanism (I) The reactivity of detergent is greater than that of ZDDP

Detergent preferentially reacts with the iron surface to form a boundary film of crystallised $CaCO_3$ or CaO. If the temperature is low, the reaction activity of ZDDP with the substrate is weak, or because the existing boundary film prevents it from reacting with the substrate to form phosphate, there seems to be no iron diffusion and consumption in this tribochemical path. However, it is known from the chemical analysis of FFO that when the phosphate content is insufficient, the signal of iron sulphides increases. Iron sulphides may originate from the oxidation and/or disproportionation of sulphonate [26], or they may originate from the reaction of ZDDP with the substrate [5, 316, 358]. Iron sulphides have been reported to increase the lubricity of the surface [359, 360] and can reduce abrasion to a certain extent [361-363]. In addition, the surface layer of the film still have the deposition of $CaCO_3$, and the calcite film also has a certain degree of resistance to wear [26, 158-161].

Under the condition of the high λ ratio, although there is not much tribofilm protection at 60 ℃, due to the generation of more iron sulphide which could the lubricity of the surface, and thus the friction coefficient and wear rate is lower.

* Mechanism (II) ZDDP is more reactive than detergent

When ZDDP is more active, it first reacts with the steel surface to form a film of sulphide and zinc phosphate. Then, detergent participates in the reaction. Again, in rubbing, the outer shell of the detergent colloidal particles will be broken, $CaCO_3$ is deposited and calcium sulphonate surfactant is adsorbed on the surface, which is consistent with the results of FFO's XPS analysis. This seems to be independent of whether there is ZDDP or not because the interaction between the detergent and the metal surface includes a similar deposition mechanism. Studies have shown that there is a competitive relationship between carbonate and phosphate [22], and the Ca-S bond has weak resistance to high pressure [154], so it is speculated that the Ca source that reacts with ZDDP to form calcium phosphate is more likely to be derived from the calcium sulphonate.

There is an induction time before the rapid formation of ZDDP tribofilm [49, 278, 279], and it is also reported that there is a thin but uniform film formed during this period [49]. The deposition and adsorption of $CaCO_3$ colloidal particles occur almost at the beginning of rubbing. Although it is assumed that ZDDP is highly reactive, it is unlikely that after the zinc phosphate tribofilm is completely formed, detergent on the surface layer will participate in the reaction from the top surface to the substrate. Therefore, it should be during the film formation process that zinc phosphate is produced as an intermediate product, and then it is reacted by the detergent to produce calcium phosphate. This is also consistent with the results of XPS (Section 6.2.4) that when the phosphate signal is the highest, the calcium atomic ratio of tribofilm is still higher than that of zinc, indicating that its main phosphate is still calcium phosphate, and a small amount of zinc phosphate only exists on the surface. Whether the chain length of calcium phosphate is relatively short, it still can avoid direct contact between metals after forming a certain thickness and reduce the mechanical wear on the substrate. Thus, the consumption of iron is mainly due to the tribochemical reaction that supplements the removal of the surface layer of tribofilm.

The main component of tribofilm is phosphate which has the largest content at 120 ℃. It also can be obtained from the Raman analysis that it has a relatively stable structure rather than the amorphous structure. Meanwhile, the amount of wear is relatively reduced. This is similar to the antiwear mechanism of ZDDP.

* Mechanism (III) Strong competition between detergent and ZDDP

There may be a synergistic effect of mechanisms (I) and (II) when the reactivity of one additive is not apparently stronger, or it is more likely that the advantages of mechanisms (I) and (II) in reducing wear cannot be exerted due to the increase in competition, which causes the instability of the tribofilm structure and the increase of wear.

Under the high λ condition, the results of 80 ℃ and 100 ℃ have many similarities. Both the friction coefficient and tribofilm thickness increase rapidly at the beginning. But after a certain period, the friction coefficient suddenly drops and reaches equilibrium at an intermediate value. Meanwhile, during the growth process of the tribofilm, a short thickness reduction and re-growth process occurred, where the result at 80 ℃ is more obvious than that at 100 ℃.

On one hand, it is known that the formation of ZDDP tribofilm can lead to an increase in friction coefficient, but the increase rate of the friction coefficient at the beginning is higher than that at 120 ℃ when the phosphate is dominant in the tribofilm, so there should be some unknown mixture produced in the tribofilm at 80 ℃ and 100 ℃, which cause a high friction condition.

On the other hand, due to the enhancement of the competition between the two additives, the tribofilm structure formed initially has insufficient durability. In the XPS data, the signal of phosphate in the tribofilm at 100 ℃ slightly increased, but the signal of phosphates in the Raman results is not much enhanced, which may indicate the instability of the phosphate structure to reduce the protection of the surface. At the same time, sulphide also decreases with increasing temperature in both Raman and XPS results, so the lubricity of sulphides also reduce causing wear increase. The substances after the unstable tribofilm is removed are a kind of balance between the chemical reactions of the two additives.

Therefore, the increase in wear under this mechanism has the following aspects: 1) the initial tribofilm formation rate increases, covering the iron sulphide on the surface, increasing the surface roughness and abrasion; and 2) the instability of the structure of the tribofilm formed in the initial stage also causes the phosphate to not fully exert its anti-wear performance but increases the loss of iron.

8.1.2.4 *Interactions between ZDDP and Dispersant*

Dispersants can form complexes with ZDDP molecules [28-31] and affect the contact between ZDDP and metal surfaces [38-40]. If dispersant is involved in film formation, specifically succinimide in this study, the N atom may be detected in tribofilm [168], but there is no N signal from the depth profile analysis of XPS. Therefore, the influence of the dispersant on the composition of tribofilm can be ignored. However, the dispersant is reported to increase the decomposition temperature of ZDDP [160], so this may explain why FFO has the highest content of phosphate in tribofilm at 120 ℃ and the wear reduces. The mechanism of wear reduction at this temperature is similar to the anti-wear mechanism of ZDDP, but in comparison, the mechanism operates at a higher temperature for FFO.

8.1.3 *Temperature Effect*

According to the ISO 6743-4 hydraulic fluid classification system [364], the operating temperature range of mineral oils with antiwear additive and antioxidant is about -10 ℃ ~ 90 ℃, but for some high-temperature applications, the upper temperature limit can reach 120 ℃ [97]. A large number of experiments on ZDDP (when temperature effects are not considered) were carried out at this 80 ℃ ~ 100 ℃ [48, 171, 315, 365-367], and the experimental results show that ZDDP can exert its antiwear effectiveness in the mild wear condition. The same went for detergents [25, 26, 150]. But because of this, both may be more active, leading to competition and instability of tribofilm.

In addition, after reducing the λ ratio, although the differences of tribofilm thickness at different temperatures decrease, in terms of the wear trends, the wear results of 80 ℃ and 100 ℃ are relatively higher than those of 60 ℃ and 120 ℃. From the XPS analysis, the signal intensity of iron sulphide also decreases with increasing temperature, and the signal intensity of phosphate increases with increasing temperature. This indicates that the wear

mechanism of FFO under boundary lubrication conditions is mainly related to the composition and formation process of tribofilm at different temperatures.

Compared with a single-component additive, the FFO exhibits an anti-wear mechanism like ZDDP at a higher temperature, but it can also reduce wear in the low-temperature range where tribofilm thickness is insufficient.

8.1.4 *Effects of λ Ratios*

The results of the Stribeck curve (Section 6.1) show that under the high λ ratio condition, boundary lubrication with a stable friction coefficient may not be fully realised at 60 ℃. Therefore, the lower abrasion at 60 ℃ may also be due to the reduced contact caused by the fluid sharing the pressure. Therefore, the second group of experiments purposes to reduce the λ ratio, on the one hand, in order to make the test conditions closer to boundary lubrication and eliminate the influence of viscosity on wear at lower temperatures, on the other hand, the effectiveness of the two-phase wear mechanism of FFO can also be verified under boundary lubrication conditions.

From the results of friction and wear experiments, both the tribofilm thickness and the amount of wear at the low λ ratio have relatively small differences at different temperatures. In contrast, 80 ℃ has a larger amount of wear as it does at the high λ ratio. From the results of XPS, the curve of the sulphide signal area in tribofilm with temperature is consistent with the trend of the high λ ratio, but the whole value is lower than the result at the high λ ratio. The signal of phosphate is the opposite, except that at 120 ℃, the signal area of phosphate is higher than the result of a higher lambda ratio. It indicates that under boundary lubrication conditions, the reason for temperature-dependent correlation of wear mechanism of FFO is mainly the tribochemical reactions and the chemical compositions of tribofilm, rather than the balanced thickness of the tribofilm.

8.1.5 *Running-in Wear*

It can be noticed from the FFO wear curve (Fig.5-4) that the wear rate is almost unchanged from the first 5 to 10 minutes of the test, especially at 80 ℃ and 100 ℃. This shows that the running-in period of wear is very short. Even when the tribofilm is still in the growth phase, the wear rate is almost constant. This is different from the result of

ZDDP as a single-component additive in the oil. Since the main mechanism of ZDDP resistance to wear is the formation of phosphate, which prevents direct contact between metal surfaces, although the wear rate is relatively large at the beginning, it gradually decreases with the tribofilm growth.

For FFO, the running-in process is basically completed in a very short time, and then there is an almost constant wear rate according to the reaction process of generating tribofilm. Only under the condition of 60 ℃, there is a similar phenomenon of slowing down of the wear rate, but it has already occurred in the stage where the tribofilm thickness is stable. This may be due to the low roughness of the ball and the disc, so the running-in part of the mechanical wear is finished in a short time. The subsequent wear rate is determined by the different tribochemical reaction processes or products mentioned above. Further verification needs to use samples with different roughness to conduct comparative experiments.

If the influence of roughness can be excluded, the tribofilm formation stage after the running-in stage can still maintain a constant wear rate, which is very beneficial for the use of new machines or the start-up process of the machine. Although the wear rate is relatively high in the normal operating temperature range of 80-100 ℃, a smooth wear process, especially in the running-in phase, is also required in the use of the machine.

8.2 *Numerical Work*

8.2.1 *Layered Contact Models and Tribofilm as a Layer*

It has been mentioned in the literature review that the theory and numerical methods related to the layered contact model with rough surfaces have been mature. Using the boundary element method based on the minimum total complementary energy theory is more suitable for conditions where the pressure is unknown, but only for the assumption of small deformation. The BEM method is conducive to solving complex rough surfaces, which only needs to solve the problem of the element boundary, which reduces the dimensionality of the problem.

After the rough surfaces have proceeded thousands of wear calculations, if the non-contact region is too small, it may be affected by the deformation in the wear region in the contact simulation, causing the contact model may fail to converge. Thus, the

computational domain is set to 6 times the contact diameter in the *x* and *y* direction to ensure that the deformation of the worn track will not affect the plane of the non-contact region in the contact simulation. In addition, considering that stress calculation will increase the computing time significantly, the number of nodes in the *x* and *y* direction is set to 129, which may reduce the accuracy to a certain extent. However, this study did not verify it so it can be further improved in the future if needed.

The more controversial part of this model is the use of tribofilm as a continuous layer. From experimental research, some studies have shown that ZDDP tribofilm is flowable under high pressure and shear stress [148, 149]. Therefore, it can be assumed that when the two surfaces are in contact, the tribofilm on the surface and the lubricant molecules entrained form a mixture that is a viscous and flowable layer under shear. When tribofilm reaches a certain average thickness, it is considered that it is in contact with a continuous layer covering the steel surface.

Due to the lack of experimental data, the material parameters of the FFO tribofilm are assumed to be the same as the values of the ZDDP tribofilm. According to the research of Bec *et al.* [132], the mechanical properties of tribofilm are related to its chemical structure. For example, the hardness and the elastic modulus of phosphate are 1-2 GPa and 15-40 GPa, respectively, while the hardness and the elastic modulus of the sulphide layer near the substrate are around 4.7 GPa and 90 GPa, respectively [30]. In the layered model, since only the role of tribofilm as a single layer is considered, the elastic modulus is set as a constant and does not change with temperature. But the hardness value is relevant to the calculation of plastic deformation and wear rate, so its change with temperature and tribofilm thickness has been considered in the model. In order to further improve the model, Liu *et al.*'s model for Functionally Graded Material (FGM) coated surface [197] can be used as a reference in which the model can directionally change the material properties. The elastic modulus of the surface material can be changed with depth, which is closer to the layered nature of the tribofilm.

8.2.2 *Tribofilm Formation Equation*

The growth kinetics of ZDDP tribofilm is a first-order reaction, and the growth rate can be expressed in exponential form. The stress-activated Arrhenius equation is a common choice. In comparison, the growth curve of FFO tribofilm is similar to that of ZDDP

tribofilm. Due to the interaction and competition of multiple additives, the growth curve of tribofilm may increase twice, as shown in Fig. 7-11 (80 ℃). Therefore, the equation used for the curve-fitting selects the sum of two growth equations with the exponential form in which the two has an interval time of t_0. The fluctuation of tribofilm thickness at this temperature can also be reflected in the simulation results.

Due to the complexity and uniqueness of the FFO formula, it seems unrealistic for non-lubricant manufacturers to demand the tribofilm formation equation linking to the relative concentration of additives. As a lubrication system, the equation of FFO can try to directly link to the parameters from the chemical compositions or the wear performance in the subsequent work to improve the equation instead of using the concentrations of additives. For example, from the chemical analysis of FFO, the main compositions of tribofilm are sulphides and phosphates, and the two show opposite trends with temperature changes. If there are parameters that can quantify sulphide and phosphate separately, and respectively correlate the relationship between these two parameters and wear, then a tribofilm formation equation that is more in line with the wear mechanism can be obtained. But this also requires more experiments and chemical analysis.

The removal model of tribofilm is not directly reflected in the equation of tribofilm formation. Experimentally, the formation of tribofilm should be a process of growth and removal. In the beginning, the growth rate is greater than the removal rate. As the tribofilm thickness increases, the growth rate decreases until it reaches a dynamic equilibrium, at which time it is the same as the removal rate. Some researchers measured the removal of tribofilm over time by using dispersant alone after the thickness of the tribofilm has stabilised, as an experimental basis for the removal model. However, it cannot be ruled out that the performance of the dispersant may be affected under different working conditions. Therefore, in the model, a ratio of change related to the tribofilm thickness is usually assumed to be used as the removal rate of tribofilm, which may be exponential [179], linear [50] or constant [283]. In this study, it is believed that the tribofilm growth curve used for fitting has been derived from the combined effect of tribofilm growth and removal in experiments. Therefore, there is no explicit expression in the tribofilm formation equation representing the tribofilm removal. However, it does not mean that it has not been considered. Because in the simulation of the wear model,

the removal rate of tribofilm is assumed to be proportional to the thickness at equilibrium. In this case, the ratio is assumed to be 20 %.

For FFO with a comprehensive formula, similar issues need to be considered when choosing the tribofilm formation model, to clarify what are the parameters that control friction and wear and whether the influence of additive concentration can be bypassed.

8.2.3 *Wear Model*

The Archard wear equation is used in the calculation of wear, which can be easily correlated with experimental conditions such as load, stress, and sliding distance. The wear coefficient K can also be changed according to the experimental conditions. Therefore, in tribochemical wear, K should be associated with tribochemical reactions. As is mentioned in the literature review (Section 3.6.2), the more common is the relationship between the link K and the tribofilm thickness. However, from the results of boundary lubrication experiments, it is also found that when the difference in the tribofilm thickness is small, the chemical composition in it still changes with temperature, which directly leads to the difference in the wear rate at different temperatures.

The calculation of wear is related to the iron loss in the substrate. In the previous section, the possible ways of iron loss were discussed in more detail. In general, it is summarised as the mechanical wear and the consumption in tribochemical reactions. Therefore, the wear rate is also calculated based on these two parts in this study. In the initial wear stage, when the tribofilm is insufficient to cover the surface, the wear rate of the steel-steel contact is used. In the tribochemical wear stage, iron content in tribofilm changing with tribofilm thickness was used in this study to calculate the mass of iron that needs to be supplemented in the substrate when a certain thickness is removed from the surface, as the wear rate of tribochemical reaction. When the tribofilm starts to grow, the wear rate of the surface will start to change with the tribofilm thickness. However, it can be seen from the wear test results that this running-in phase is very short, and the amount of wear in the first 10 minutes is affected by the temperature very little and can be ignored. Therefore, it can be assumed that the initial wear coefficient is the wear rate of the steel-steel contact.

8.2.4 *Stress Distributions*

Von Mises stress is the comprehensive stress commonly used in mechanics to calculate the strength of a material and is used to evaluate whether the material yields, breaks, etc. First, the von Mises stress during the growth and equilibrium stages of tribofilm is simulated, it can be seen from the stress contour of the contact area in Fig. 7-17 that the maximum stress value occurs near the contact centre on the interface between tribofilm and steel substrate. The ratio of this value to the maximum Hertzian contact pressure is about 0.7~ 0.76 for all tested temperatures, indicating that because tribofilm is relatively soft, the contact pressure to the surface of the steel substrate is reduced, which is consistent with the mechanism of tribofilms' buffering and isolating the contact. Even when the tribofilm thickness is 20 nm, the stress value is apparently reduced.

According to the stress-activated Arrhenius formula, the increase in shear stress can reduce the activation energy of the ZDDP reaction, so that ZDDP can generate tribofilm in sliding contact at moderate temperature or normal temperature. The same can also be applied to FFO containing ZDDP. The friction coefficient of FFO at different temperatures was obtained through experiments, and then the shear stress of the tribofilm interface was calculated with the model. When the temperature increases, the shear stress increases. At the same temperature, the shear stress when the tribofilm thickness reaches equilibrium decreases relative to the value of the growth stage, indicating the decrease of the tribofilm formation rate. In addition, as the test time increases, the contact area will elongate along the sliding direction, which is also predictable. This also shows the effectiveness of this method in analysing the contact pressure and shear stress under the influence of tribofilm.

8.3 *Limitations of the Study*

In the experiment, we study the growth trends and wear relationship of FFO tribofilm under the influence of temperature and λ ratio, and adequately discuss the chemical composition characteristics of FFO tribofilm, which provides sufficient data support for the numerical analysis of FFO as a lubrication system. However, there are still some limitations in the study that can be further improved.

1) A single formulation additive with the same concentration as FFO can be used for comparative experiments to study the difference of the chemical composition between FFO tribofilm and tribofilm formed by a single additive under the same working conditions, and the corresponding wear phenomenon;
2) Comparative experiments were conducted with the mixture of ZDDP and detergent as the same concentration as FFO to investigate whether the two-phase wear mechanism of FFO was dominated by the two film-forming additives and the reaction priority of the two additives;
3) Further experiments can be conducted to investigate the influence of additives that do not participate in tribofilm formation, such as dispersant, on the mechanism of FFO;

In terms of modelling, the framework of the tribofilm growth and wear model developed on the contact model of the layered rough surfaces has the following limitations or needs further improvement.

1) The principle of the minimum total complementary energy used in the model needs to be based on the principle of small displacement. Therefore, this model is not suitable for severe wear and tear, which may cause the contact calculation cycle to fail to converge.
2) When the model assumes that the tribofilm thickness is greater than its surface roughness, it can be used as a continuous layer to change the material parameters of the surface layer. Since the maximum thickness of FFO tribofilm is only about 120 nm when it reaches equilibrium, it is not suitable for the surface with a very larger roughness.
3) The parameters used in the tribofilm formation model are only valid for the tribofilm growth curve of FFO in this study, and the physical meaning of the parameters is insufficiently studied. However, for other formulations of FFO, if the physical or chemical parameters that control the growth of tribofilm are not known, it is feasible to find a formula that can contain most of the experimental phenomena from a mathematical perspective.
4) In the wear calculation, it is assumed that the wear consists only of mechanical wear and tribochemical wear at different temperatures, but there may be other mechanisms, which requires further research.

5) In the part of stress calculation, especially the shear stress, the decoupling method is used to account for the influence of friction. For the friction study of tribofilm performance, the fully coupled contact model for friction can be used.

Chapter 9 Conclusions and Future Work

9.1 *Conclusions*

The main purpose of this research is to study the tribochemical reaction and wear mechanism of a commercial fully formulated oil, and to develop a boundary lubrication model that can simulate the main phenomena such as tribofilm growth and wear of the FFO. In terms of experiments, the working conditions of FFO under the background of hydraulic piston pumps, such as Hertzian contact pressure and sliding/rolling conditions, were used to test the tribofilm growth, friction coefficient and wear evolution of FFO at different temperatures and λ ratios. The main results of the phenomena and mechanism analysis are concluded as follows.

1) The growth curve of the FFO tribofilm is similar to that of the single-component ZDDP tribofilm, both of which show a rapid increase at the beginning and then reach a dynamic equilibrium process. At the high λ ratio, the tribofilm thickness in the equilibrium phase increases significantly with the increase of temperature. At the low λ ratio, the growth rate in the initial stage decreases with increasing temperature, but the eventual tribofilm thickness in the stable phase changes little within the tested temperature range. It shows that the closer to the boundary lubrication condition, the correlation between the final tribofilm thickness and temperature decreases.
2) FFO exhibits a two-phase wear mechanism within the tested temperature range. For the high λ ratio, in the low-temperature range of 60~80 ℃, the tribofilm thickness and wear increase as the temperature increases; but in the high-temperature range of 80~120 ℃, when the temperature increases, the tribofilm thickness still increases but the wear decreases. For the low λ ratio, although the tribofilm thickness changes little with temperature, the two-phase wear mechanism is still applicable.
3) According to chemical analysis, the main composition of FFO tribofilm is calcium phosphate, and there is a calcium carbonate layer on the surface, and there may be a small amount of calcium sulphate/sulphonate or zinc phosphate. There are iron sulphides between the phosphate and the substrate.
4) As the temperature increases, the phosphate content in tribofilm increases, while the iron sulphide content decreases. In particular, the sulphide contents in tribofilm have almost the same trend with temperature under both λ ratios. However, as the λ ratio

decreases, the iron sulphide content decreases and the phosphate content increases (except for 120 ℃). This indicates that at the low λ ratio, although the tribofilm thickness varies little with temperature, the chemical compositions of tribofilm still change with temperature. It also shows that the key to controlling the FFO wear mechanism is not the tribofilm thickness, but the chemical compositions and formation process of tribofilm affected by temperature. This explains why under different λ ratio conditions, although the correlation between tribofilm thickness and temperature is different, there is a two-phase wear mechanism.

Although the growth process of FFO tribofilm is similar to that of the ZDDP tribofilm in the literature, the wear mechanism is different, which is mainly affected by the products and processes of the tribochemical reactions at different temperatures. This is also affected by the interaction between different additives, which cause different anti-wear performances at different temperatures.

Based on the boundary lubrication modelling framework, this project has developed a model that can calculate tribofilm growth, wear and stress on a three-dimensional layered rough surface. One of the characteristics of this model is that it can modify the material properties, surface topography, contact conditions and wear according to the real-time growth of the tribofilm, and simulate the sub-surface stress state under the influence of tribofilm. The main features of the model and simulation results are summarised as follows.

1) In the layered contact model, when the tribofilm thickness is greater than its surface roughness, it can be considered as a continuous layer in contact, thereby changing the material properties of the surface layer. The calculation of contact pressure and elastic/plastic deformation under the influence of tribofilm is achieved.
2) According to the exponential form of the stress-activated Arrhenius equation and the first-order reaction kinetics of ZDDP film formation, the FFO tribofilm growth model uses a mathematical formula that can describe the overall trend in the experiments, including two growth equations in the exponential form with a time interval of t_0. The simulation results can well reflect the unstable state of the tribofilm thickness during the growth phase under the conditions of 80 and 100 ℃.

3) The removal of tribofilm does not appear explicitly in the tribofilm formation equation, but it is assumed in the wear model that the removed tribofilm is proportional to the balanced thickness and does not change during the growth phase of the tribofilm.
4) Archard wear equation is used to calculate wear. Considering the possible ways of iron consumption in the substrate, the wear process is mainly divided into the mechanical wear stage and the tribochemical wear stage. In the mechanical wear stage, the wear coefficient is specified as the value of steel-to-steel contact, while in the tribochemical wear stage, the wear coefficient is related to the measured iron content in tribofilm. It is assumed that when a certain thickness or volume of tribofilm is removed, new iron in the substrate will be supplemented to the tribofilm to maintain the balanced thickness, which is the wear volume. In this model, iron exists in different compounds and densities in the tribofilm and steel substrates are considered, where in the calculation of mass converted from the volume, the forms of iron in the tribofilm are iron sulphide or iron oxide obtained by chemical analysis and there are iron atoms in the substrate. The wear results are consistent well with the experimental results.
5) This model is effective in simulating the stress calculation of subsurface influenced by the tribofilm. By calculating the von Mises stress, it can be obtained that when tribofilm is used as the surface layer, the stress at the contact centre drops to 0.7~0.76 of the maximum Hertzian contact pressure, even at a thickness of only 20 nm. The results indicate the buffering effect of tribofilm, which is consistent with the experimental trend. In addition, combined with the friction coefficient measured by experiments, the surface shear stress of tribofilm is calculated. It shows that the surface shear stress increases as the temperature increases, that is, the tribofilm thickness. This is in agreement with the stress-activated Arrhenius equation, that is, the increase in shear stress can reduce the activation energy of the tribofilm reaction, so it can promote the tribofilm formation.

This model basically realises the simulation of the key phenomena of FFO in tribofilm growth and wear, which is consistent with the experimental results. In addition, it is also effective to calculate the influence of the tribofilm and surface roughness on the subsurface stress state. Although some parameters in the tribofilm growth formula and wear model are only limited to the experimental results of FFO in this study, the model

provides a modelling framework that can add the influence of the real-time growth of tribofilm thickness on the contact state, surface topography, and subsurface stress. It can be extended to the tribofilm generated by other single-component or multi-component lubricants on a homogeneous substrate, coating materials or multi-functional surfaces by flexibly replacing the layered contact model, the tribochemical equation or the wear model, and to calculate its influence on tribofilm growth, wear or subsurface stress.

9.2 *Future Work*

Although the experimental results of the FFO in this study have certain particularities due to its special formula, the following studies are suggested to be carried out in the future for a commercial FFO with similarly complex formulation or unknown concentrations of additives.

1) Study the tribochemical reaction and wear results of the mixture containing the same concentration of ZDDP or detergent in FFO, compare the experimental results of FFO, and investigate whether there is different reactivity and competition at different temperatures.
2) Because chemical compositions or elements in FFO tribofilm have major impacts on wear such as phosphates and sulphides in this study, if there are quantifiable parameters, they could be correlated with the tribofilm formation equation or the wear model. Then, it could further explain the physical meaning of the relevant constants in the tribofilm formation equation and include the influence of tribochemical reactions in the wear model.
3) When the relationships between the FFO tribochemical reactions and the parameters related to working conditions are not clear, the black box technique could be used. For example, to establish the artificial neural network model of the parameters related to working conditions and then these results such as tribofilm thickness, friction coefficient and wear can be obtained directly.
4) In the application of the layered contact model, it can be first applied to the calculation of the contact between the coating-substrate system of lubricants containing ZDDP. Then, by selecting a more suitable layered contact model, tribofilm growth equation, wear model, and related parameters, according to the material properties and

experimental results, the effect of tribofilm on the subsurface stress can be predicted to analyse the shear stress, yield of material, etc. depending on the application.

5) In addition, by using the layered contact model of fully coupled friction, the friction calculation and stress distribution under the influence of tribofilm can also be studied.

List of References

1. Stachowiak, G. and A.W. Batchelor, *Engineering tribology*. 2013: Butterworth-Heinemann.

2. Holmberg, K. and A. Erdemir, *Influence of tribology on global energy consumption, costs and emissions.* Friction, 2017. **5**(3): p. 263-284.

3. Holmberg, K., et al., *Global energy consumption due to friction and wear in the mining industry.* Tribology International, 2017. **115**: p. 116-139.

4. Wells, H.M. and J.E. Southcombe, *The theory and practice of lubrication: the" Germ" process*. 1920: Central House.

5. Spikes, H., *The history and mechanisms of ZDDP*. Tribology letters, 2004. **17**(3): p. 469-489.

6. Asseff, P.A., *Lubricant*. 1941: US2416807A.

7. Cook, E.W. and W.D. Thomas Jr, *CRANKCASE LUBRICANT AND CHEMICAL COMPOUND THEREFOR*. 1944: US2344392.

8. FREULER, H.C., *Modified lubricating oil*. 1944: US2364283A.

9. Fang, Y. and M. Shirakashi, *Mixed Lubrication Characteristics Between the Piston and Cylinder in Hydraulic Piston Pump-Motor.* Journal of Tribology, 1995. **117**(1): p. 80-85.

10. Sakamoto, T., et al., *The reaction layer formed on steel by additives based on sulphur and phosphorus compounds under conditions of boundary lubrication.* Wear, 1982. **77**(2): p. 139-157.

11. Habeeb, J.J. and W.H. Stover, *The Role of Hydroperoxides in Engine Wear and The Effect of Zinc Dialkyldithiophosphates.* A S L E Transactions, 1986. **30**(4): p. 419-426.

12. Rounds, F., *Effects of hydroperoxides on wear as measured in four-ball wear tests.* Tribology transactions, 1993. **36**(2): p. 297-303.

13. Belin, M., J.M. Martin, and J.L. Mansot, *Role of Iron in the Amorphization Process in Friction-Induced Phosphate Glasses.* Tribology Transactions, 1989. **32**(3): p. 410-413.

14. Martin, J.M., et al., *Friction-Induced Amorphization with ZDDP—An EXAFS Study.* A S L E Transactions, 1986. **29**(4): p. 523-531.

15. Martin, J.M., *Antiwear mechanisms of zinc dithiophosphate: a chemical hardness approach.* Tribology letters, 1999. **6**(1): p. 1-8.

16. Spedding, H. and R.C. Watkins, *The antiwear mechanism of zddp's. Part I.* Tribology International, 1982. **15**(1): p. 9-12.

17. So, H. and Y.C. Lin, *The theory of antiwear for ZDDP at elevated temperature in boundary lubrication condition.* Wear, 1994. **177**(2): p. 105-115.

18. Aktary, M., M.T. McDermott, and G.A. McAlpine, *Morphology and nanomechanical properties of ZDDP antiwear films as a function of tribological contact time.* Tribology letters, 2002. **12**(3): p. 155-162.

19. Martin, J.M., et al., *The origin of anti-wear chemistry of ZDDP*. Faraday Discussions, 2012. **156**(0): p. 311-323.

20. Zhang, J. and H. Spikes, *On the mechanism of ZDDP antiwear film formation.* Tribology Letters, 2016. **63**(2): p. 24.

21. Kasrai, M., et al., *Study of the effects of Ca sulfonate on antiwear film formation by X-ray absorption spectroscopy using synchrotron radiation.* Journal of synchrotron radiation, 1999. **6**(3): p. 719-721.

22. Costello, M.T. and R.A. Urrego, *Study of Surface Films of the ZDDP and the MoDTC with Crystalline and Amorphous Overbased Calcium Sulfonates by XPS.* Tribology Transactions, 2007. **50**(2): p. 217-226.

23. Willermet, P., et al., *Formation, structure, and properties of lubricant-derived antiwear films.* Lubrication Science, 1997. **9**(4): p. 325-348.

24. Yin, Z., et al., *Application of soft X-ray absorption spectroscopy in chemical characterization of antiwear films generated by ZDDP Part II: the effect of detergents and dispersants.* Wear, 1997. **202**(2): p. 192-201.

25. Kasrai, M., et al., *X-Ray Absorption Study of the Effect of Calcium Sulfonate on Antiwear Film Formation Generated From Neutral and Basic ZDDPs: Part 1—Phosphorus Species.* Tribology Transactions, 2003. **46**(4): p. 534-542.

26. Kasrai, M., et al., *X-Ray Absorption Study of the Effect of Calcium Sulfonate on Antiwear Film Formation Generated From Neutral and Basic ZDDPs: Part 2 — Sulfur Species.* Tribology Transactions, 2003. **46**(4): p. 543-549.

27. Wan, Y., et al., *Effects of detergent on the chemistry of tribofilms from ZDDP: studied by X-ray absorption spectroscopy and XPS*, in *Tribology series*. 2002, Elsevier. p. 155-166.

28. Zhang, J., E. Yamaguchi, and H. Spikes, *The antagonism between succinimide dispersants and a secondary zinc dialkyl dithiophosphate*. Tribology Transactions, 2014. **57**(1): p. 57-65.

29. Gallopoulos, N.E. and C.K. Murphy, *Interactions between a zinc dialkylphosphorodithioate and lubricating oil dispersants.* ASLE TRANSACTIONS, 1971. **14**(1): p. 1-7.

30. Inoue, K. and H. Watanabe, *Interactions of engine oil additives.* ASLE transactions, 1983. **26**(2): p. 189-199.

31. Shiomi, M., et al., *Interaction between zinc dialkyldithiophosphate and amine.* Lubrication Science, 1989. **1**(2): p. 131-147.

32. Ramakumar, S., A.M. Rao, and S. Srivastava, *Studies on additive-additive interactions: formulation of crankcase oils towards rationalization.* Wear, 1992. **156**(1): p. 101-120.

33. Rounds, F.G., *Additive interactions and their effect on the performance of a zinc dialkyl dithiophosphate.* Asle Transactions, 1978. **21**(2): p. 91-101.

34. Harrison, P.G., P. Brown, and J. McManus, *31P NMR study of the interaction of a commercial succinimide-type lubricating oil dispersant with zinc (II) bis (O, O'-di-iso-butyldithiophosphate).* Wear, 1992. **156**(2): p. 345-349.

35. Ramakumar, S., et al., *Studies on additive‐additive interactions: effects of dispersant and antioxidant additives on the synergistic combination of overbased sulphonate and ZDDP*. Lubrication Science, 1994. **7**(1): p. 25-38.

36. Kapur, G., et al., *molecular spectroscopic studies of ZDDP—PIBS interactions.* Lubrication Science, 1998. **10**(4): p. 309-321.

37. Wilk, M.A., et al., *Method of lubricating an internal combustion engine and improving the efficiency of the emissions control system of the engine*. 2008, Google Patents.

38. Rounds, F., *Changes in friction and wear performance caused by interactions among lubricant additives.* Lubrication Science, 1989. **1**(4): p. 333-363.

39. Zhang, Z., et al., *Study of the Interaction of ZDDP and Dispersants Using X-ray Absorption Near Edge Structure Spectroscopy—Part 1: Thermal Chemical Reactions.* Tribology Letters, 2003. **15**(4): p. 377-384.

40. Plaza, S., *The Effect of Other Lubricating Oil Additives on the Adsorption of Zinc Di-Isobutyldithiophosphate on Fe and γ-Fe2O3 Powders.* ASLE transactions, 1987. **30**(2): p. 241-247.

41. Vengudusamy, B., et al., *Tribological properties of tribofilms formed from ZDDP in DLC/DLC and DLC/steel contacts.* Tribology International, 2011. **44**(2): p. 165-174.

42. Vengudusamy, B., et al., *Durability of ZDDP tribofilms formed in DLC/DLC contacts.* Tribology Letters, 2013. **51**(3): p. 469-478.

43. Haque, T., et al., *Study of the ZDDP antiwear tribofilm formed on the DLC coating using AFM and XPS techniques*, in *Automotive lubricant testing and advanced additive development*. 2008, ASTM International.

44. Shimizu, Y. and H.A. Spikes, *The influence of aluminium–silicon alloy on ZDDP tribofilm formation on the counter-surface.* Tribology letters, 2017. **65**(4): p. 1-13.

45. Burkinshaw, M., et al., *ZDDP and its interactions with an organic antiwear additive on both aluminium–silicon and model silicon surfaces.* Tribology International, 2014. **69**: p. 102-109.

46. Wan, Y., L. Cao, and Q. Xue, *Friction and wear characteristics of ZDDP in the sliding of steel against aluminum alloy.* Tribology International, 1997. **30**(10): p. 767-772.

47. Mittal, P., et al., *In situ microscopic study of tribology and growth of ZDDP antiwear tribofilms on an Al–Si alloy.* Tribology International, 2020. **151**: p. 106419.

48. Fujita, H., R. Glovnea, and H. Spikes, *Study of zinc dialkydithiophosphate antiwear film formation and removal processes, part I: experimental.* Tribology transactions, 2005. **48**(4): p. 558-566.

49. Fujita, H. and H.A. Spikes, *Study of Zinc Dialkyldithiophosphate Antiwear Film Formation and Removal Processes, Part II: Kinetic Model.* Tribology Transactions, 2005. **48**(4): p. 567-575.

50. Akchurin, A. and R. Bosman, *A Deterministic Stress-Activated Model for Tribo-Film Growth and Wear Simulation.* Tribology Letters, 2017. **65**(2): p. 59.

51. Ghanbarzadeh, A., et al., *Development of a new mechano-chemical model in boundary lubrication.* Tribology International, 2016. **93**: p. 573-582.

52. Gosvami, N., et al., *Mechanisms of antiwear tribofilm growth revealed in situ by single-asperity sliding contacts.* Science, 2015. **348**(6230): p. 102-106.

53. Dorgham, A., et al., *Single-asperity study of the reaction kinetics of P-based triboreactive films.* Tribology International, 2019. **133**: p. 288-296.

54. Ludema, K.C., *Friction, Wear, Lubrication*. 1996.

55. Bhushan, B., *Introduction to tribology*. 2013: John Wiley & Sons.

56. Amontons, G., *De la résistance causée dans les machines.* Mémoires de l'Académie Royale, 1699. **A**: p. 257-282.

57. Chowdhury, M.A., et al., *Friction Coefficient of Different Material Pairs Under Different Normal Loads and Sliding Velocities.* Tribology in Industry, 2012.

58. Wang, Q.J. and Y.W. Chung, *Encyclopedia of Tribology.* Slsevier, 2013.

59. Rabinowicz, E. and R. Tanner, *Friction and wear of materials.* Journal of Applied Mechanics, 1966. **33**(2): p. 479.

60. Buckley and DonaldH, *Surface effects in adhesion, friction, wear, and lubrication*. 1981: Surface effects in adhesion, friction, wear, and lubrication.

61. Kiejna, A. and K.F. Wojciechowski, *Adhesion between metal surfaces,* in *Metal Surface Electron Physics,* A. Kiejna and K.F. Wojciechowski, Editors. 1996, Pergamon: Oxford. p. 245-261.

62. Ferrante, J. and J.R. Smith, *A theory of adhesion at a bimetallic interface: Overlap effects.* Surface Science, 1973. **38**(1): p. 77-92.

63. Sikorski, M.E., *Correlation of the Coefficient of Adhesion With Various Physical and Mechanical Properties of Metals.* Trans. ASME. J. Basic Eng, 1963. **85**(2): p. 279-285.

64. Bowden, F.P. and G.W. Rowe, *The Adhesion of Clean Metals*. Proceedings of the Royal Society of London, 1956. **233**(1195): p. 429-442.

65. Hokkirigawa, K., K. Kato, and Z. Li, *The effect of hardness on the transition of the abrasive wear mechanism of steels.* Wear, 1988. **123**(2): p. 241-251.

66. Bhushan, B., *Tribology and mechanics of magnetic storage devices*. 2012: Springer Science & Business Media.

67. Administration, F.A., *Advisory Circular - Corrosion control for aircraft*. 2018, FAA: Washington DC.

68. Bruce, R.W., *Handbook of Lubrication and Tribology, Volume II: Theory and Design, Second Edition*. 2012, Baton Rouge: CRC Press.

69. Wen, S. and P. Huang, *Principles of tribology*. 2012: John Wiley & Sons.

70. Li, Y., et al., *Performance Margin Modeling and Reliability Analysis for Harmonic Reducer Considering Multi-Source Uncertainties and Wear*. IEEE Access, 2020. **8**: p. 171021-171033.

71. Bosman, R., J. Hol, and D.J. Schipper, *Running-in of metallic surfaces in the boundary lubrication regime.* Wear, 2011. **271**(7-8): p. 1134-1146.

72. Blau, P.J., *On the nature of running-in.* Tribology International, 2005. **38**(11-12): p. 1007-1012.

73. So, H. and R.C. Lin, *The combined effects of ZDDP, surface texture and hardness on the running-in of ferrous metals.* Tribology international, 1999. **32**(5): p. 243-253.

74. Hsu, S.M., J. Zhang, and Z. Yin, *The nature and origin of tribochemistry*. Tribology Letters, 2002. **13**(2): p. 131-139.

75. Marinescu, I.D., et al., *Tribology of abrasive machining processes*. 2004: Elsevier.

76. Heinicke, G., *Tribochemistry*. 1984: C. Hanser.

77. Fischer, T., *Tribochemistry.* Annual Review of Materials Science, 1988. **18**(1): p. 303-323.

78. Chaikin, S., *On frictional polymer.* Wear, 1967. **10**(1): p. 49-60.

79. Furey, M., *The formation of polymeric films directly on rubbing surfaces to reduce wear.* Wear, 1973. **26**(3): p. 369-392.

80. Lauer, J. and W. Jones, *Friction polymers.* Tribology and Mechanics of Magnetic Storage Systems, 1986. **3**: p. 14-23.

81. Bharat, B. and F.W. Hahn Jr, *Stains on magnetic tape heads.* Wear, 1995. **184**(2): p. 193-202.

82. Bhushan, B., *Fluid Film Lubrication*, in *Principles and Applications of Tribology*. 2013. p. 545-653.

83. Booth, J.E., *The feasibility of using electrostatic charge condition monitoring for lubricant additive screening*, in *University of Southampton*. 2008.

84. Grubin, A.N., *Investigation of the contact of machine components.* Central Scientific Research Inst. Tech. & Mech. Eng., 1949.

85. Marx, N., J. Guegan, and H.A. Spikes, *Elastohydrodynamic film thickness of soft EHL contacts using optical interferometry.* Tribology International, 2016. **99**: p. 267-277.

86. Dowson, D. and G.R. Higginson, *A Numerical Solution to the Elasto-Hydrodynamic Problem.* Journal of Mechanical Engineering Science, 1959. **1**(1): p. 6-15.

87. Dowson, D. and G.R. Higginson, *New roller-bearing lubrication formula.* Engineering Lond., 1961. **192**: p. 158.

88. Dowson, D. and G. Higginson, *Elastohydrodynamic Lubrication*. 1966, Pergamon: Press Oxford.

89. Dowson, D. and S. Toyoda. *A central film thickness formula for elastohydrodynamic line contacts*, *Elastohydrodynamics and related topics*. in *Proc. 5th Leeds-Lyon Symp., 1978*. 1978. Elsevier.

90. Hamrock, B.J. and D. Dowson, *Isothermal elastohydrodynamic lubrication of point contacts: Part I—Theoretical formulation.* 1976.

91. Hamrock, B.J. and D. Dowson, *Isothermal elastohydrodynamic lubrication of point contacts: Part II—Ellipticity parameter results.* 1976.

92. Hamrock, B.J. and D. Dowson, *Isothermal elastohydrodynamic lubrication of point contacts. Part III: Fully flooded results.* 1976.

93. Hamrock, B.J. and D. Dowson, *Isothermal elastohydrodynamic lubrication of point contacts: Part IV—starvation results.* 1977.

94. Straffelini, G., *Friction and Wear*. Methodologies for Design and Control. Switzerland: Springer International Publishing AG Switzerland, 2015.

95. Kondo, Y., T. Koyama, and S. Sasaki, *Tribological Properties of Ionic Liquids*. 2013: Tribological Properties of Ionic Liquids.

96. Stachowiak, G. and A. Batchelor, *Lubricants and their composition*, in *Engineering Tribology; Elsevier: Oxford, UK*. 2006. p. 51-101.

97. Totten, G.E. and V.J. De Negri, *Handbook of hydraulic fluid technology, second edition*. 2ed ed. CRC Press. 2011.

98. Rudnick, L.R., *Lubricant additives: chemistry and applications*. 2017: CRC Press.

99. Mang, T. and W. Dresel, *Lubricants and Lubrication, 2 Volume Set (3rd Edition)*. John Wiley & Sons. p. 117-152.

100. Canter, N., *Special Report: Trends in extreme pressure additives.* Tribology and Lubrication Technology, 2007. **63**(9): p. 10.

101. Ottewill, R.H., et al., *Small-angle neutron-scattering studies on nonaqueous dispersions Part 5: Magnesium carbonate dispersions in hydrocarbon media.* Colloid and Polymer Science, 1992. **270**(6): p. 602-608.

102. Roman, J.-P., et al., *Formation and structure of carbonate particles in reverse microemulsions.* Journal of colloid and interface science, 1991. **144**(2): p. 324-339.

103. Kandori, K., K. Kon-no, and A. Kitahara, *Formation of ionic water/oil microemulsions and their application in the preparation of CaCO3 particles.* Journal of colloid and interface science, 1988. **122**(1): p. 78-82.

104. Delfort, B., B. Daoudal, and L. Barré, *Particle size determination of (functionalized) colloidal calcium carbonate by small angle x-ray scattering—Relation with antiwear properties.* Tribology transactions, 1999. **42**(2): p. 296-302.

105. Srivastava, S.P., *Advances in lubricant additives and tribology*. 2009: Tech Books International.

106. Hamblin, P., U. Kristen, and D. Chasan, *Ashless antioxidants, copper deactivators and corrosion inhibitors: their use in lubricating oils.* Lubrication Science, 1990. **2**(4): p. 287-318.

107. Ewell, R.H. and H. Eyring, *Theory of the Viscosity of Liquids as a Function of Temperature and Pressure.* The Journal of Chemical Physics, 1937. **5**(9): p. 726-736.

108. McCoull, N. and C. Walther, *Viscosity-temperature chart.* Lubrication, June, 1921. **7**: p. 1-16.

109. International, A., *ASTM D341 Standard Practice for Viscosity-Temperature Equations and Charts for Liquid Petroleum or Hydrocarbon Products*. 2020

110. Barus, C. *Note on the dependence of viscosity on pressure and temperature*. in *Proceedings of the American Academy of Arts and Sciences*. 1891. JSTOR.

111. Fujita, H. and H. Spikes, *The formation of zinc dithiophosphate antiwear films.* Proceedings of the Institution of Mechanical Engineers, Part J: Journal of Engineering Tribology, 2004. **218**(4): p. 265-278.

112. Bidwell, J.B. and R.K. Williams, *The New Look in Lubricating Oils.* SAE Transactions, 1955. **63**: p. 349-361.

113. Chamberlin, W.B., J.C. Kelley, and M.A. Wilk, *The Impact of Passenger Car Motor Oils on Emissions Performance*. 2003, SAE International.

114. Larson, R., *THE PERFORMANCE OF ZINC DITHIOPHOSPHATES AS LUBRICATING OIL ADDITIVES.* Industrial Lubrication and Tribology, 1958. **10**(8): p. 12-19.

115. Asseff, P.A., *Discussion on pp. 87–90 to P. A. Bennett, A surface effect associated with the use of oils containing zinc dialkyl dithiophosphate.* ASLE Trans., 1959. **2**: p. 78-90.

116. Nicholls, M.A., et al., *Review of the lubrication of metallic surfaces by zinc dialkyl-dithiophosphates.* Tribology International, 2005. **38**(1): p. 15-39.

117. Taylor, L., A. Dratva, and H.A. Spikes, *Friction and Wear Behavior of Zinc Dialkyldithiophosphate Additive.* Tribology Transactions, 2000. **43**(3): p. 469-479.

118. Fuller, M.S., et al., *The use of X-ray absorption spectroscopy for monitoring the thickness of antiwear films from ZDDP*. Tribology Letters, 2000. **8**(4): p. 187-192.

119. Fuller, M., et al., *Solution decomposition of zinc dialkyl dithiophosphate and its effect on antiwear and thermal film formation studied by X-ray absorption spectroscopy.* Tribology International, 1998. **31**(10): p. 627-644.

120. Bancroft, G., et al., *Mechanisms of tribochemical film formation: stability of tribo- and thermally-generated ZDDP films.* Tribology Letters, 1997. **3**(1): p. 47-51.

121. Fuller, M., et al., *Chemical characterization of tribochemical and thermal films generated from neutral and basic ZDDPs using X-ray absorption spectroscopy.* Tribology International, 1997. **30**(4): p. 305-315.

122. Piras, F.M., A. Rossi, and N.D. Spencer, *Combined in situ (ATR FT-IR) and ex situ (XPS) study of the ZnDTP-iron surface interaction.* Tribology Letters, 2003. **15**(3): p. 181-191.

123. Sieber, I., et al., *Characterization of boundary layers formed by different metal dithiophosphates in a four-ball machine.* Wear, 1983. **85**(1): p. 43-56.

124. Masuko, M., T. Hanada, and H. Okabe, *Distinction in antiwear performance between organic sulfide and organic phosphate as EP additives for steel under rolling with sliding partial EHD conditions.* Lubrication Engineering, 1994. **50**(12): p. 972-977.

125. Masuko, M., et al., *Fundamental study of changes in friction and wear characteristics due to ZnDTP deterioration in simulating engine oil degradation during use*, in *Tribology Series*. 2003, Elsevier. p. 359-366.

126. Ueda, M., H. Spikes, and A. Kadiric, *In-situ observations of the effect of the ZDDP tribofilm growth on micropitting.* Tribology International, 2019. **138**: p. 342-352.

127. Lainé, E., A. Olver, and T. Beveridge, *Effect of lubricants on micropitting and wear.* Tribology International, 2008. **41**(11): p. 1049-1055.

128. Brizmer, V., H. Pasaribu, and G.E. Morales-Espejel, *Micropitting performance of oil additives in lubricated rolling contacts.* Tribology transactions, 2013. **56**(5): p. 739-748.

129. Cen, H., A. Morina, and A. Neville, *Effect of slide to roll ratio on the micropitting behaviour in rolling-sliding contacts lubricated with ZDDP-containing lubricants.* Tribology International, 2018. **122**: p. 210-217.

130. Soltanahmadi, S., et al., *Tribochemical study of micropitting in tribocorrosive lubricated contacts: The influence of water and relative humidity.* Tribology International, 2017. **107**: p. 184-198.

131. Soltanahmadi, S., et al., *Investigation of the effect of a diamine-based friction modifier on micropitting and the properties of tribofilms in rolling-sliding contacts.* Journal of Physics D: Applied Physics, 2016. **49**(50): p. 505302.

132. Bec, S., et al. *Relationship between mechanical properties and structures of zinc dithiophosphate anti–wear films*. in *Proceedings of the Royal Society of London A: Mathematical, Physical and Engineering Sciences*. 1999. The Royal Society.

133. Demmou, K., et al., *Temperature effects on mechanical properties of zinc dithiophosphate tribofilms.* Tribology International, 2006. **39**(12): p. 1558-1563.

134. Pereira, G., et al., *A variable temperature mechanical analysis of ZDDP-derived antiwear films formed on 52100 steel.* Wear, 2007. **262**(3): p. 461-470.

135. Taylor, L.J. and H. Spikes, *Friction-enhancing properties of ZDDP antiwear additive: part I—friction and morphology of ZDDP reaction films.* Tribology transactions, 2003. **46**(3): p. 303-309.

136. Taylor, L.J. and H.A. Spikes, *Friction-enhancing properties of ZDDP antiwear additive: part II—influence of ZDDP reaction films on EHD lubrication.* Tribology transactions, 2003. **46**(3): p. 310-314.

137. Topolovec Miklozic, K. and H.A. Spikes, *Application of Atomic Force Microscopy to the Study of Lubricant Additive Films.* Journal of Tribology, 2005. **127**(2): p. 405-415.

138. Zhang, J., et al., *Boundary Friction of ZDDP Tribofilms.* Tribology Letters, 2020. **69**(1): p. 8.

139. Bovington, C. and H. Spikes. *Prediction of the influence of lubricant formulations on fuel economy, from laboratory bench tests*. in *Proceedings of the International Tribology Conference*. 1995.

140. Taylor, R.I. and R.C. Coy, *Improved fuel efficiency by lubricant design: A review.* Proceedings of the Institution of Mechanical Engineers, Part J: Journal of Engineering Tribology, 2000. **214**(1): p. 1-15.

141. Kano, M., et al., *The effect of ZDDP in CVT fluid on increasing the traction capacity of belt-drive continuously variable transmissions.* Lubrication Science, 1999. **11**(4): p. 365-377.

142. Bell, J., K. Delargy, and A. Seeney, *Paper IX (ii) the removal of substrate material through thick zinc dithiophosphate anti-wear films,* in *Tribology series*. 1992, Elsevier. p. 387-396.

143. Pidduck, A. and G. Smith, *Scanning probe microscopy of automotive anti-wear films.* Wear, 1997. **212**(2): p. 254-264.

144. Alliston-Greiner, A.F., J.A. Greenwood, and A. Cameron, *Paper VII(i) The rheology of reaction films formed by ZDDP,* in *Tribology Series*, D. Dowson, et al., Editors. 1987, Elsevier. p. 161-167.

145. Warren, O., et al., *Nanomechanical properties of films derived from zinc dialkyldithiophosphate.* Tribology Letters, 1998. **4**(2): p. 189-198.

146. Graham, J.F., C. McCague, and P.R. Norton, *Topography and nanomechanical properties of tribochemical films derived from zinc dialkyl and diaryl dithiophosphates.* Tribology Letters, 1999. **6**(3): p. 149-157.

147. Ye, J., M. Kano, and Y. Yasuda, *Evaluation of Local Mechanical Properties in Depth in MoDTC/ZDDP and ZDDP Tribochemical Reacted Films Using Nanoindentation.* Tribology Letters, 2002. **13**(1): p. 41-47.

148. Dorgham, A.K.Y., *Reaction kinetics and rheological characteristics of ultra-thin P-based triboreactive films*. 2017, University of Leeds.

149. Dorgham, A., et al., *LOCAL OCCUPANCY OF VISCOELASTIC INTERFACES: A NEW RHEOLOGICAL PERSPECTIVE ON ANTIWEAR TRIBOFILMS.* 2017.

150. Topolovec-Miklozic, K., T.R. Forbus, and H. Spikes, *Film Forming and Friction Properties of Overbased Calcium Sulphonate Detergents.* Tribology Letters, 2008. **29**(1): p. 33-44.

151. Khan, T.A., *Swash Plate Axial-Piston Hydraulic Motors: A Study of Surface Protective Treatments for the Piston/Cylinder Interface*. 2017, University of Leeds.

152. Kubo, T., et al., *TOF-SIMS analysis of boundary films derived from calcium sulfonates.* Tribology Letters, 2006. **23**(2): p. 171-176.

153. Mansot, J., M. Hallouis, and J. Martin, *Colloidal antiwear additives 2. Tribological behaviour of colloidal additives in mild wear regime.* Colloids and Surfaces A: Physicochemical and Engineering Aspects, 1993. **75**: p. 25-31.

154. Cizaire, L., et al., *Tribochemistry of overbased calcium detergents studied by ToF-SIMS and other surface analyses.* Tribology Letters, 2004. **17**(4): p. 715-721.

155. Giasson, S., et al., *Study of boundary film formation with overbased calcium sulfonate by PM-IRRAS spectroscopy.* Thin Solid Films, 1994. **252**(2): p. 111-119.

156. Costello, M.T., R.A. Urrego, and M. Kasrai, *Study of surface films of crystalline and amorphous overbased sulfonates and sulfurized olefins by X-ray absorption near edge structure (XANES) spectroscopy.* Tribology Letters, 2007. **26**(2): p. 173-180.

157. Costello, M.T., *Study of Surface Films of Amorphous and Crystalline Overbased Calcium Sulfonate by XPS and AES.* Tribology Transactions, 2006. **49**(4): p. 592-597.

158. Morizur, M. and O. Teysset, *Antiwear actions of additives in solid dispersion.* Lubrication Science, 1992. **4**(4): p. 277-299.

159. Najman, M., et al., *Combination of ashless antiwear additives with metallic detergents: interactions with neutral and overbased calcium sulfonates.* Tribology International, 2006. **39**(4): p. 342-355.

160. Shirahama, S. and M. Hirata, *The effects of engine oil additives on valve train wear.* Lubrication Science, 1989. **1**(4): p. 365-384.

161. Minami, I., et al., *Tribochemical approach toward mechanism for synergism of lubricant additives on antiwear and friction reducing properties*, in *Tribology and Interface Engineering Series*, D. Dowson, et al., Editors. 2005, Elsevier. p. 259-268.

162. Delfort, B., M. Born, and B. Daoudal, *Functionalization of overbased calcium sulfonates-synthesis and evaluation of antiwear and extreme-pressure performances.* Lubrication Engineering, 1995: p. Medium: X; Size: pp. 981-990.

163. Kapsa, P., et al., *Antiwear mechanism of ZDDP in the presence of calcium sulfonate detergent.* 1981.

164. Martin, J.M., et al., *The two-layer structure of Zndtp tribofilms: Part I: AES, XPS and XANES analyses.* Tribology international, 2001. **34**(8): p. 523-530.

165. Willermet, P., *Some engine oil additives and their effects on antiwear film formation.* Tribology Letters, 1998. **5**(1): p. 41-47.

166. Vipper, A., et al., *Solubilizing capacity of succinimides and their mixtures with metal-containing antioxidant and detergent additives.* Chemistry and Technology of Fuels and Oils, 1975. **11**(4): p. 302-305.

167. Forbes, E., A. Groszek, and E. Neustadter, *Adsorption studies on lubricating oil additives.* Journal of Colloid and Interface Science, 1970. **33**(4): p. 629.

168. Yamaguchi, E.S., et al., *Study of the Interaction of ZDDP and Dispersants Using X-ray Absorption Near Edge Structure Spectroscopy—Part 2: Tribochemical Reactions.* Tribology Letters, 2003. **15**(4): p. 385-394.

169. Barcroft, F. and D. Park, *Interactions on heated metal surfaces between zinc dialkyldithiophosphates and other lubricating oil additives.* Wear, 1986. **108**(3): p. 213-234.

170. Martin, J., et al., *Role of nitrogen in tribochemical interaction between Zndtp and succinimide in boundary lubrication.* Tribology International, 2000. **33**(7): p. 453-459.

171. Pereira, G., et al., *Chemical and mechanical analysis of tribofilms from fully formulated oils Part 1 – Films on 52100 steel.* Tribology - Materials, Surfaces & Interfaces, 2013. **1**(1): p. 48-61.

172. Vakis, A.I., et al., *Modeling and simulation in tribology across scales: An overview.* Tribology International, 2018.

173. Ghanbarzadeh, A., *Mechano-chemical modelling of boundary lubrication*. 2016, University of Leeds.

174. Buyukkaya, E. and M. Cerit, *Thermal analysis of a ceramic coating diesel engine piston using 3-D finite element method.* Surface and Coatings Technology, 2007. **202**(2): p. 398-402.

175. Tang, H., Y. Ren, and J. Xiang, *Fully-coupled thermomechanical analysis for sliding contact between textured slipper and swashplate in axial piston pump.* International Journal of Heat and Mass Transfer, 2020. **163**: p. 120521.

176. Bhushan, B., *Contact Mechanics of Rough Surfaces in Tribology: Single Asperity Contact.* Applied Mechanics Reviews, 1996. **49**(5): p. 275-298.

177. Bhushan, B., *Contact mechanics of rough surfaces in tribology: multiple asperity contact.* Tribology letters, 1998. **4**(1): p. 1-35.

178. Bosman, R. and D.J. Schipper, *Mild wear prediction of boundary-lubricated contacts.* Tribology letters, 2011. **42**(2): p. 169-178.

179. Ghanbarzadeh, A., et al., *A semi-deterministic wear model considering the effect of zinc dialkyl dithiophosphate tribofilm.* Tribology Letters, 2016. **61**(1): p. 12.

180. Minfray, C., et al., *Experimental and molecular dynamics simulations of tribochemical reactions with ZDDP: zinc phosphate–iron oxide reaction.* Tribology Transactions, 2008. **51**(5): p. 589-601.

181. Martin, J.M., et al., *Anti-wear Chemistry of ZDDP and Calcium Borate Nano-additive. Coupling Experiments, Chemical Hardness Predictions, and MD Calculations.* Tribology Letters, 2013. **50**(1): p. 95-104.

182. Onodera, T., et al., *Antiwear Chemistry of ZDDP: Coupling Classical MD and Tight-Binding Quantum Chemical MD Methods (TB-QCMD).* Tribology Letters, 2013. **50**(1): p. 31-39.

183. Verma, P., et al., *Tetrahydropyrazolopyridines as antifriction and antiwear agents: experimental and DFT calculations.* RSC Advances, 2020. **10**(17): p. 10188-10196.

184. Harrison, J., et al., *Neutral zinc (II) O, O-di-alkyldithiopho-sphates—variable temperature 31P NMR and quantum chemical study of the ZDDP monomer–dimer equilibrium.* Magnetic Resonance in Chemistry, 2008. **46**(2): p. 115-124.

185. Mosey, N.J. and T.K. Woo, *Finite Temperature Structure and Dynamics of Zinc Dialkyldithiophosphate Wear Inhibitors: A Density Functional Theory and ab Initio Molecular Dynamics Study.* The Journal of Physical Chemistry A, 2003. **107**(25): p. 5058-5070.

186. Onodera, T., et al., *Influence of nanometer scale film structure of ZDDP tribofilm on Its mechanical properties: A computational chemistry study.* Applied Surface Science, 2009. **256**(4): p. 976-979.

187. Pereira, K., T. Yue, and M.A. Wahab, *Multiscale analysis of the effect of roughness on fretting wear.* Tribology International, 2017. **110**: p. 222-231.

188. Nehme, G., R. Mourhatch, and P.B. Aswath, *Effect of contact load and lubricant volume on the properties of tribofilms formed under boundary lubrication in a fully formulated oil under extreme load conditions.* Wear, 2010. **268**(9-10): p. 1129-1147.

189. Anciaux, G. and J.F. Molinari, *Contact mechanics at the nanoscale, a 3D multiscale approach.* International journal for numerical methods in engineering, 2009. **79**(9): p. 1041-1067.

190. Hertz, H., *Uber die beruhrung fester elastische korper und uber die harte (On the contact of rigid elastic solids and on hardness).* Verhandlungen des Vereins zur Beforderung des Gewerbefleisses, Leipzig, 1882.

191. Constantinescu, A., et al., *Symbolic and numerical solution of the axisymmetric indentation problem for a multilayered elastic coating.* International Journal of Solids and Structures, 2013. **50**(18): p. 2798-2807.

192. Komvopoulos, K. and Z.-Q. Gong, *Stress analysis of a layered elastic solid in contact with a rough surface exhibiting fractal behavior.* International Journal of Solids and Structures, 2007. **44**(7-8): p. 2109-2129.

193. Chen, W.W., et al., *Modeling elasto-plastic indentation on layered materials using the equivalent inclusion method.* International Journal of Solids and Structures, 2010. **47**(20): p. 2841-2854.

194. Kot, M., et al., *Analysis of spherical indentations of coating-substrate systems: experiments and finite element modeling.* Materials & Design, 2013. **43**: p. 99-111.

195. Bagault, C., et al., *Contact analyses for anisotropic half-space coated with an anisotropic layer: Effect of the anisotropy on the pressure distribution and contact area.* International Journal of Solids and Structures, 2013. **50**(5): p. 743-754.

196. Birman, V. and L.W. Byrd, *Modeling and analysis of functionally graded materials and structures.* 2007.

197. Liu, T.-J., et al., *Axisymmetric adhesive contact problem for functionally graded materials coating based on the linear multi-layered model.* Mechanics Based Design of Structures and Machines, 2019: p. 1-18.

198. Chidlow, S. and M. Teodorescu, *Sliding contact problems involving inhomogeneous materials comprising a coating-transition layer-substrate and a rigid punch.* International journal of Solids and Structures, 2014. **51**(10): p. 1931-1945.

199. Putignano, C., G. Carbone, and D. Dini, *Mechanics of rough contacts in elastic and viscoelastic thin layers.* International Journal of Solids and Structures, 2015. **69-70**: p. 507-517.

200. Zhang, M., et al., *Elasto-plastic contact of materials containing double-layered inhomogeneities.* International Journal of Solids and Structures, 2017. **126-127**: p. 208-224.

201. Peng, W. and B. Bhushan, *A Numerical Three-Dimensional Model for the Contact of Layered Elastic/Plastic Solids With Rough Surfaces by a Variational Principle.* Journal of Tribology, 2001. **123**(2): p. 330.

202. Yu, C., Z. Wang, and Q.J. Wang, *Analytical frequency response functions for contact of multilayered materials.* Mechanics of Materials, 2014. **76**: p. 102-120.

203. Ciavarella, M., *The generalized Cattaneo partial slip plane contact problem. I—Theory.* International Journal of solids and structures, 1998. **35**(18): p. 2349-2362.

204. Dini, D. and D. Hills, *A method based on asymptotics for the refined solution of almost complete partial slip contact problems.* European Journal of Mechanics-A/Solids, 2003. **22**(6): p. 851-859.

205. Sackfield, A., D. Hills, and H. Qiu, *Side-contact of sharp indenters, including the effects of friction.* International journal of mechanical sciences, 2007. **49**(5): p. 567-576.

206. Flicek, R., D. Hills, and D. Dini, *Sharp edged contacts subject to fretting: A description of corner behaviour.* International Journal of Fatigue, 2015. **71**: p. 26-34.

207. Sundaram, N. and T. Farris, *Mechanics of advancing pin-loaded contacts with friction.* Journal of the Mechanics and Physics of Solids, 2010. **58**(11): p. 1819-1833.

208. Archard, J.F., *Elastic Deformation and the Laws of Friction.* Proceedings of the Royal Society of London. Series A, Mathematical and Physical Sciences, 1957. **243**(1233): p. 190-205.

209. Bowden, F.P. and D. Tabor, *The friction and lubrication of solids*. Vol. 1. 2001: Oxford university press.

210. Greenwood, J.A. and J.P. Williamson, *Contact of nominally flat surfaces.* Proceedings of the royal society of London. Series A. Mathematical and physical sciences, 1966. **295**(1442): p. 300-319.

211. Nayak, P.R., *Random process model of rough surfaces in plastic contact.* Wear, 1973. **26**(3): p. 305-333.

212. Longuet-Higgins, M.S., *Statistical properties of an isotropic random surface.* Philosophical Transactions of the Royal Society of London. Series A, Mathematical and Physical Sciences, 1957. **250**(975): p. 157-174.

213. Bush, A., R. Gibson, and T. Thomas, *The elastic contact of a rough surface.* Wear, 1975. **35**(1): p. 87-111.

214. Greenwood, J., *A simplified elliptic model of rough surface contact.* Wear, 2006. **261**(2): p. 191-200.

215. Majumdar, A. and B. Bhushan., *Fractal Model of Elastic-Plastic Contact Between Rough Surfaces.* 1991.

216. Panda, S., et al., *Spectral approach on multiscale roughness characterization of nominally rough surfaces.* Journal of Tribology, 2017. **139**(3).

217. Yuan, W., et al., *Statistical contact model of rough surfaces: The role of surface tension.* International Journal of Solids and Structures, 2018. **138**: p. 217-223.

218. Majumdar, A. and C.L. Tien, *Fractal characterization and simulation of rough surfaces.* Wear, 1990. **136**(2): p. 313-327.

219. Mandelbrot, B., *How long is the coast of Britain? Statistical self-similarity and fractional dimension.* science, 1967. **156**(3775): p. 636-638.

220. Wang, S. and K. Komvopoulos, *A fractal theory of the interfacial temperature distribution in the slow sliding regime: Part II—multiple domains, elastoplastic contacts and applications.* 1994.

221. Yan, W. and K. Komvopoulos, *Contact analysis of elastic-plastic fractal surfaces.* Journal of applied physics, 1998. **84**(7): p. 3617-3624.

222. Bhushan, B. and W. Peng, *Contact mechanics of multilayered rough surfaces.* Applied Mechanics Reviews, 2002. **55**(5): p. 435-480.

223. O'Sullivan, T.C. and R.B. King, *Sliding Contact Stress Field Due to a Spherical Indenter on a Layered Elastic Half-Space.* Journal of Tribology, 1988. **110**(2): p. 235-240.

224. Bhushan, B. and S. Cai, *Dry and Wet Contact Modeling of Multilayered Rough Solid Surfaces.* Applied Mechanics Reviews, 2008. **61**(5).

225. Burmister, D.M., *The General Theory of Stresses and Displacements in Layered Systems. I.* Journal of Applied Physics, 1945. **16**(2): p. 89-94.

226. Burmister, D.M., *The General Theory of Stresses and Displacements in Layered Soil Systems. II.* Journal of Applied Physics, 1945. **16**(3): p. 126-127.

227. Burmister, D.M., *The General Theory of Stresses and Displacements in Layered Soil Systems. III.* Journal of Applied Physics, 1945. **16**(5): p. 296-302.

228. Chen, W., *Computation of stresses and displacements in a layered elastic medium.* International Journal of Engineering Science, 1971. **9**(9): p. 775-800.

229. Chen, W. and P. Engel, *Impact and contact stress analysis in multilayer media.* International Journal of Solids and Structures, 1972. **8**(11): p. 1257-1281.

230. Peng , W. and B. Bhushan, *Sliding Contact Analysis of Layered Elastic/Plastic Solids With Rough Surfaces.* Journal of Tribology, 2001. **124**(1): p. 46-61.

231. GUPTA, P.K. and J.A. WALOWIT, *Contact Stresses Between m Elastic Cylinder and a Layered Elastic Solid.* ASME, 1974. **96**: p. 250-257.

232. Cole, S.J. and R.S. Sayles, *A Numerical Model for the Contact of Layered Elastic Bodies With Real Rough Surfaces.* Journal of Tribology, 1992. **114**(2): p. 334-340.

233. Komvopoulos, K., *Finite element analysis of a layered elastic solid in normal contact with a rigid surface.* 1988.

234. Komvopoulos, K., *Elastic-plastic finite element analysis of indented layered media.* 1989.

235. Diao, D., K. Kato, and K. Hayashi, *The maximum tensile stres on a hard coating under sliding friction.* Tribology International, 1994. **27**(4): p. 267-272.

236. Kral, E., K. Komvopoulos, and D. Bogy, *Elastic-plastic finite element analysis of repeated indentation of a half-space by a rigid sphere.* 1993.

237. Kral, E., K. Komvopoulos, and D. Bogy, *Finite element analysis of repeated indentation of an elastic-plastic layered medium by a rigid sphere, Part II: Subsurface results.* 1995.

238. Stephens, L., Y. Liu, and E. Meletis, *Finite element analysis of the initial yielding behavior of a hard coating/substrate system with functionally graded interface under indentation and friction.* J. Trib., 2000. **122**(2): p. 381-387.

239. Kral, E. and K. Komvopoulos, *Three-dimensional finite element analysis of surface deformation and stresses in an elastic-plastic layered medium subjected to indentation and sliding contact loading.* 1996.

240. Komvopoulos, K. and D.-H. Choi, *Elastic finite element analysis of multi-asperity contacts.* 1992.

241. Oden, J. and J. Martins, *Models and computational methods for dynamic friction phenomena.* Computer methods in applied mechanics and engineering, 1985. **52**(1-3): p. 527-634.

242. Martins, J., J. Oden, and F. Simoes, *A study of static and kinetic friction.* International Journal of Engineering Science, 1990. **28**(1): p. 29-92.

243. Mao, K., T. Bell, and Y. Sun, *Effect of sliding friction on contact stresses for multi-layered elastic bodies with rough surfaces.* 1997.

244. Tian, X. and B. Bhushan, *A numerical three-dimensional model for the contact of rough surfaces by variational principle.* Journal of tribology, 1996. **118**(1): p. 33-42.

245. Nogi, T. and T. Kato, *Influence of a Hard Surface Layer on the Limit of Elastic Contact—Part I: Analysis Using a Real Surface Model.* Journal of Tribology, 1997. **119**(3): p. 493-500.

246. Polonsky, I. and L.M. Keer, *A fast and accurate method for numerical analysis of elastic layered contacts.* J. Trib., 2000. **122**(1): p. 30-35.

247. Polonsky, I. and L. Keer, *A numerical method for solving rough contact problems based on the multi-level multi-summation and conjugate gradient techniques.* Wear, 1999. **231**(2): p. 206-219.

248. Richards, T.H. and T.J. Lardner, *Energy Methods in Stress Analysis With an Introduction to Finite-Element Techniques.* Journal of Applied Mechanics, 1979.

249. Cai, S. and B. Bhushan, *A numerical three-dimensional contact model for rough, multilayered elastic/plastic solid surfaces.* Wear, 2005. **259**(7): p. 1408-1423.

250. Peng, W. and B. Bhushan, *Transient analysis of sliding contact of layered elastic/plastic solids with rough surfaces.* Microsystem Technologies, 2003. **9**(5): p. 340-345.

251. Wang, Z., H. Yu, and Q. Wang, *Layer-substrate system with an imperfectly bonded interface: Spring-like condition.* International Journal of Mechanical Sciences, 2017. **134**: p. 315-335.

252. Yu, C., et al., *Maximum von Mises Stress and Its Location in Trilayer Materials in Contact.* Journal of Tribology, 2016. **138**(4).

253. Wang, Z., H. Yu, and Q. Wang, *Layer-substrate system with an imperfectly bonded interface: Coupled dislocation-like and force-like conditions.* International Journal of Solids and Structures, 2017. **122-123**: p. 91-109.

254. Guell, D. and J. Dundurs, *Further results on center of dilatation and residual stresses in joined elastic half-spaces*, in *Developments in theoretical and applied mechanics*. 1967, Elsevier. p. 105-115.

255. Wang, Z., H. Yu, and Q. Wang, *Analytical solutions for elastic fields caused by eigenstrains in two joined and perfectly bonded half-spaces and related problems.* International Journal of Plasticity, 2016. **76**: p. 1-28.

256. Jones, J. and J. Whittier, *Waves at a flexibly bonded interface.* 1967.

257. Lene, F. and D. Leguillon, *Homogenized constitutive law for a partially cohesive composite material.* International Journal of Solids and Structures, 1982. **18**(5): p. 443-458.

258. Achenbach, J.D. and H. Zhu, *Effect of interfacial zone on mechanical behavior and failure of fiber-reinforced composites.* Journal of the Mechanics and Physics of Solids, 1989. **37**(3): p. 381-393.

259. Hashin, Z., *Thermoelastic properties of fiber composites with imperfect interface.* Mechanics of Materials, 1990. **8**(4): p. 333-348.

260. Hashin, Z., *The spherical inclusion with imperfect interface.* 1991.

261. Qu, J., *The effect of slightly weakened interfaces on the overall elastic properties of composite materials.* Mechanics of Materials, 1993. **14**(4): p. 269-281.

262. Yu, H.Y., *A new dislocation-like model for imperfect interfaces and their effect on load transfer.* Composites Part A: Applied Science and Manufacturing, 1998. **29**(9): p. 1057-1062.

263. Yu, H., Y. Wei, and F. Chiang, *Load transfer at imperfect interfaces—dislocation-like model.* International journal of engineering science, 2002. **40**(14): p. 1647-1662.

264. Pan, E., *Three-dimensional Green's functions in anisotropic elastic bimaterials with imperfect interfaces.* J. Appl. Mech., 2003. **70**(2): p. 180-190.

265. Benveniste, Y. and T. Chen, *On the Saint-Venant torsion of composite bars with imperfect interfaces.* Proceedings of the Royal Society of London. Series A: Mathematical, Physical and Engineering Sciences, 2001. **457**(2005): p. 231-255.

266. Yu, H. and S. Sanday, *Elastic fields in joined half-spaces due to nuclei of strain.* Proceedings of the Royal Society of London. Series A: Mathematical and Physical Sciences, 1991. **434**(1892): p. 503-519.

267. Dundurs, J. and M. Hete´ nyi, *Transmission of force between two semi-infinite solids.* 1965.

268. Yu, H., Z. Wang, and Q. Wang, *Analytical solutions for the elastic fields caused by eigenstrains in two frictionlessly joined half-spaces.* International Journal of Solids and Structures, 2016. **100-101**: p. 74-94.

269. Li, D., et al., *Elastic fields caused by eigenstrains in two joined half-spaces with an interface of coupled imperfections: Dislocation-like and force-like conditions.* International Journal of Engineering Science, 2018. **126**: p. 22-52.

270. Ju, Y. and T. Farris, *Spectral analysis of two-dimensional contact problems.* Journal of tribology, 1996. **118**(2): p. 320-328.

271. Polonsky, I. and L.M. Keer, *Fast methods for solving rough contact problems: a comparative study.* J. Trib., 2000. **122**(1): p. 36-41.

272. Liu, S., Q. Wang, and G. Liu, *A versatile method of discrete convolution and FFT (DC-FFT) for contact analyses.* Wear, 2000. **243**(1-2): p. 101-111.

273. Press, W.H., et al., *Numerical recipes in Fortran 77: volume 1, volume 1 of Fortran numerical recipes: the art of scientific computing*. 1992: Cambridge university press.

274. Liu, S. and Q. Wang, *Studying Contact Stress Fields Caused by Surface Tractions With a Discrete Convolution and Fast Fourier Transform Algorithm.* Journal of Tribology, 2002. **124**(1): p. 36-45.

275. Bulgarevich, S.B., et al., *Kinetics of mechanoactivation of tribochemical processes.* Journal of Friction and Wear, 2012. **33**(5): p. 345-353.

276. Shimizu, Y. and H.A. Spikes, *The influence of slide–roll ratio on ZDDP tribofilm formation.* Tribology Letters, 2016. **64**(2): p. 19.

277. Crank, J., *The mathematics of diffusion*. 1979: Oxford university press.

278. Luther Von, H. and S. Sinha, *On Reaction Kinetics and Thermal Decomposition of Zinc Dialkyldithiophosphate.* Erdol u Kohle-Erd.-Petr., 1964. **17**: p. 91-97.

279. Yamaguchi, E., et al., *Boundary film formation by ZnDTPs and detergents using ECR.* Tribology transactions, 1998. **41**(2): p. 262-272.

280. Andersson, J., et al., *Semi-deterministic chemo-mechanical model of boundary lubrication.* Faraday discussions, 2012. **156**(1): p. 343-360.

281. Felts, J.R., et al., *Direct mechanochemical cleavage of functional groups from graphene.* Nature Communications, 2015. **6**(1): p. 6467.

282. Jacobs, T.D. and R.W. Carpick, *Nanoscale wear as a stress-assisted chemical reaction.* Nat Nanotechnol, 2013. **8**(2): p. 108-12.

283. Domínguez-García, S., et al., *Mass balance of the tribofilm in lubricated systems.* Tribology International, 2021. **155**.

284. Domínguez-García, S., et al., *Delumping Strategy to Infer Lubrication Reaction Pathways in Internal Combustion Engines.* International Journal of Chemical Reactor Engineering, 2020. **18**(1).

285. Constales, D., G.S. Yablonsky, and G.B. Marin, *Predicting kinetic dependences and closing the balance: Wei and Prater revisited.* Chemical Engineering Science, 2015. **123**: p. 328-333.

286. Aris, R., *Prolegomena to the rational analysis of systems of chemical reactions.* Archive for rational mechanics and analysis, 1965. **19**(2): p. 81-99.

287. Wei, J., *Structure of complex chemical reaction systems.* Industrial & Engineering Chemistry Fundamentals, 1965. **4**(2): p. 161-167.

288. Meng, H.-C., *Wear Modeling Evaluation and Categorization of Wear Models*. 1994, The University of Michigan.

289. Barwell, F., *Wear of metals.* Wear, 1958. **1**(4): p. 317-332.

290. Rhee, S., *Wear equation for polymers sliding against metal surfaces.* Wear, 1970. **16**(6): p. 431-445.

291. Archard, J., *Contact and rubbing of flat surfaces.* Journal of applied physics, 1953. **24**(8): p. 981-988.

292. Suh, N.P., *The delamination theory of wear.* Wear, 1973. **25**(1): p. 111-124.

293. Hornbogen, E., *The role of fracture toughness in the wear of metals.* Wear, 1975. **33**(2): p. 251-259.

294. Challen, J. and P. Oxley, *An explanation of the different regimes of friction and wear using asperity deformation models.* Wear, 1979. **53**(2): p. 229-243.

295. Evans, A., *Fundamentals of friction and wear of materials.* ASM, 1980. **439**.

296. Holm, R., *Electric Contacts, Hugo Gebers.* Förlag (Stockholm, Sweden), 1946.

297. Bosman, R. and D.J. Schipper, *On the transition from mild to severe wear of lubricated, concentrated contacts: The IRG (OECD) transition diagram.* Wear, 2010. **269**(7): p. 581-589.

298. Bryant, M.D., M.M. Khonsari, and F.F. Ling, *On the thermodynamics of degradation.* Proceedings of the Royal Society A: Mathematical, Physical and Engineering Sciences, 2008. **464**(2096): p. 2001-2014.

299. Doelling, K.L., et al., *An experimental study of the correlation between wear and entropy flow in machinery components.* Journal of Applied Physics, 2000. **88**(5): p. 2999-3003.

300. RABINOWICZ, E., *Wear coefficients-metals.* Wear control handbook, 1980.

301. Topolovec-Miklozic, K., T.R. Forbus, and H.A. Spikes, *Film thickness and roughness of ZDDP antiwear films.* Tribology Letters, 2007. **26**(2): p. 161-171.

302. Cann, P.M., H.A. Spikes, and J. Hutchinson, *The Development of a Spacer Layer Imaging Method (SLIM) for Mapping Elastohydrodynamic Contacts.* Tribology Transactions, 1996. **39**(4): p. 915-921.

303. Benedet, J., et al., *Spurious mild wear measurement using white light interference microscopy in the presence of antiwear films.* Tribology Transactions, 2009. **52**(6): p. 841-846.

304. Pavliček, P. and O. Hýbl, *White-light interferometry on rough surfaces--measurement uncertainty caused by surface roughness.* Applied optics, 2008. **47**(16): p. 2941-2949.

305. Swapp, S. *Scanning Electron Microscopy (SEM).* 2009 [cited 2018 01 July].

306. Atoms, E. *The Scanning Electron Microscope (SEM).* 2015 [cited 2018 01 July].

307. Yue, Y., et al., *Monitoring the cementitious materials subjected to sulfate attack with optical fiber excitation Raman spectroscopy.* Optical Engineering, 2013. **52**(10): p. 104107.

308. VD Heide, P., *X-Ray Photoelectron Spectroscopy: An Introduction to Principles and Practices*. 2012: X-Ray Photoelectron Spectroscopy: An Introduction to Principles and Practices.

309. Biesinger, M., *X-ray Photoelectron Spectroscopy (XPS) reference pages.* Surface Science Western, University of Western Ontario, Ontario, 2015.

310. Heubergera, R. and A.R.a.N.D.S. , *XPS study of the influence of temperature on ZnDTP tribofilm composition.* 2007.

311. Cizaire, L., et al., *Chemical analysis of overbased calcium sulfonate detergents by coupling XPS, ToF-SIMS, XANES, and EFTEM.* Colloids and Surfaces A: Physicochemical and Engineering Aspects, 2004. **238**(1-3): p. 151-158.

312. Li, Y., et al., *Atomically Defined Iron Carbide Surface for Fischer–Tropsch Synthesis Catalysis.* ACS Catalysis, 2019. **9**(2): p. 1264-1273.

313. Furlan, A., et al., *Structure and bonding in amorphous iron carbide thin films.* Journal of Physics: Condensed Matter, 2015. **27**(4): p. 045002.

314. Chusuei, C.C., et al., *Calcium phosphate phase identification using XPS and time-of-flight cluster SIMS.* Analytical chemistry, 1999. **71**(1): p. 149-153.

315. Ueda, M., A. Kadiric, and H. Spikes, *On the Crystallinity and Durability of ZDDP Tribofilm.* Tribology Letters, 2019. **67**(4).

316. Minfray, C., et al., *A multi-technique approach of tribofilm characterisation.* Thin Solid Films, 2004. **447**: p. 272-277.

317. Wang, Y. and P.M. Sherwood, *Iron (III) phosphate (FePO4) by XPS.* Surface Science Spectra, 2002. **9**(1): p. 99-105.

318. Wang, Y., D.J. Asunskis, and P.M.A. Sherwood, *Iron (II) Phosphate (Fe3(PO4)2 by XPS.* Surface Science Spectra, 2002. **9**(1): p. 91-98.

319. Liu, Y., et al., *Synthesis of different structured FePO4 for the enhanced conversion of methyl cellulose to 5-hydroxymethylfurfural.* RSC Advances, 2017. **7**(81): p. 51281-51289.

320. Barreca, D., et al., *Analysis of nanocrystalline ZnS thin films by XPS.* Surface Science Spectra, 2002. **9**(1): p. 54-61.

321. Bahadur, S., D. Gong, and J. Anderegg, *Investigation of the influence of CaS, CaO and CaF2 fillers on the transfer and wear of nylon by microscopy and XPS analysis.* Wear, 1996. **197**(1-2): p. 271-279.

322. Nyenge, R.L., H.C. Swart, and O.M. Ntwaeaborwa, *Luminescent properties, intensity degradation and X-ray photoelectron spectroscopy analysis of CaS:Eu2+ powder.* Optical Materials, 2015. **40**: p. 68-75.

323. Chaturvedi, S., et al., *XPS and LEED study of a single-crystal surface of pyrite.* American Mineralogist, 1996. **81**(1-2): p. 261-264.

324. Mattila, S., J. Leiro, and K. Laajalehto, *Surface XPS core-level shifts of FeS2.* Applied surface science, 2003. **212**: p. 97-100.

325. Luque, A., et al., *Analysis of the surface of different marbles by X-ray photoelectron spectroscopy (XPS) to evaluate decay by SO 2 attack.* Environmental earth sciences, 2013. **68**(3): p. 833-845.

326. Wan, S., et al., *Tribochemistry of adaptive integrated interfaces at boundary lubricated contacts.* Sci Rep, 2017. **7**(1): p. 9935.

327. Booser, E.R., *CRC Handbook of lubrication : theory and practice of tribology.* CRC Press, 1984.

328. Lafuente, B., et al., *1. The power of databases: The RRUFF project*, in *Highlights in mineralogical crystallography*. 2015, De Gruyter (O). p. 1-30.

329. Song, C., et al., *Hydrothermal synthesis of iron pyrite (FeS2) as efficient counter electrodes for dye-sensitized solar cells.* Solar Energy, 2016. **133**: p. 429-436.

330. Liu, T., et al., *Enhanced Raman intensity in ZnS planar and channel waveguide structures via carbon ion implantation.* Optical Materials, 2021. **112**: p. 110733.

331. Kim, J.H., et al., *Raman spectroscopy of ZnS nanostructures.* Journal of Raman Spectroscopy, 2012.

332. Avril, C., et al., *Raman spectroscopic properties and Raman identification of CaS-MgS-MnS-FeS-Cr2FeS4 sulfides in meteorites and reduced sulfur-rich systems.* Meteoritics & Planetary Science, 2013. **48**(8): p. 1415-1426.

333. Gachot, C., et al., *Microstructural and Chemical Characterization of the Tribolayer Formation in Highly Loaded Cylindrical Roller Thrust Bearings.* Lubricants, 2016. **4**(2): p. 19.

334. Faruck, A.A.M., et al., *How lubricant formulations and properties influence the performance of rotorcraft transmissions under loss of lubrication conditions.* Tribology International, 2020. **151**: p. 106390.

335. Brow, R.K., et al., *The short-range structure of zinc polyphosphate glass.* Journal of Non-Crystalline Solids, 1995. **191**(1-2): p. 45-55.

336. Kazanci, M., et al., *Complementary information on in vitro conversion of amorphous (precursor) calcium phosphate to hydroxyapatite from Raman microspectroscopy and wide-angle X-ray scattering.* Calcified tissue international, 2006. **79**(5): p. 354-359.

337. Okubo, H., C. Tadokoro, and S. Sasaki, *In Situ Raman-SLIM Monitoring for the Formation Processes of MoDTC and ZDDP Tribofilms at Steel/Steel Contacts under Boundary Lubrication.* Tribology Online, 2020. **15**(3): p. 105-116.

338. Pemberton, J.E., et al., *Raman spectroscopy of calcium phosphate glasses with varying calcium oxide modifier concentrations.* Chemistry of Materials, 1991. **3**(1): p. 195-200.

339. Crobu, M., et al., *Tribochemistry of bulk zinc metaphosphate glasses.* Tribology letters, 2010. **39**(2): p. 121-134.

340. ISO, *ISO 25178-2-2012 Geometrical product specifications (GPS) -- Surface texture: Areal -- Part 2: Terms, definitions and surface texture parameters*. 2012: Switzerland.

341. Patir, N., *A numerical procedure for random generation of rough surfaces.* Wear, 1978. **47**(2): p. 263-277.

342. Hu, Y.Z. and K. Tonder, *Simulation of 3-D Random Rough-Surface by 2-D Digital-Filter and Fourier-Analysis.* International Journal of Machine Tools & Manufacture, 1992. **32**(1-2): p. 83-90.

343. Bakolas, V., *Numerical generation of arbitrarily oriented non-Gaussian three-dimensional rough surfaces.* Wear, 2003. **254**(5-6): p. 546-554.

344. Minet, C., et al., *Analysis and Modeling of the Topography of Mechanical Seal Faces.* Tribology Transactions, 2010. **53**(6): p. 799-815.

345. Wu, J.-J., *Simulation of rough surfaces with FFT.* Tribology International, 2000. **33**(1): p. 47-58.

346. Wu, J.-J., *Simulation of non-Gaussian surfaces with FFT.* Tribology International, 2004. **37**(4): p. 339-346.

347. Wang, Y., et al., *A Simulation Method for Non-Gaussian Rough Surfaces Using Fast Fourier Transform and Translation Process Theory.* Journal of Tribology, 2017. **140**(2): p. 021403.

348. Zahouani, H., R. Vargiolu, and J.L. Loubet, *Fractal models of surface topography and contact mechanics.* Mathematical & Computer Modelling, 1998. **28**(4-8): p. 517-534.

349. Thomas, T.R., B. Rosén, and N. Amini, *Fractal characterisation of the anisotropy of rough surfaces.* Wear, 1999. **232**(1): p. 41-50.

350. Johnson, K.L., *Contact Mechanics*. 1987: Cambridge university press.

351. Love, A.E.H., *IX. The stress produced in a semi-infinite solid by pressure on part of the boundary*. Philosophical Transactions of the Royal Society of London. Series A, Containing Papers of a Mathematical or Physical Character, 1929. **228**(659-669): p. 377-420.

352. Liu, S., M.J. Ju, and C.X. Yang, *Elliptic-paraboloid method for calculating surface elastic deformation in EHL.* Tribology international, 1993. **26**(6): p. 443-448.

353. Stanley, H. and T. Kato, *An FFT-based method for rough surface contact.* Journal of tribology, 1997. **119**(3): p. 481-485.

354. Almqvist, A., et al., *On the dry elasto-plastic contact of nominally flat surfaces.* Tribology international, 2007. **40**(4): p. 574-579.

355. Wang, Y., Y. Liu, and Y. Wang. *A method for improving the capability of convergence of numerical lubrication simulation by using the PID controller*. in *IFToMM World Congress on Mechanism and Machine Science*. 2019. Springer.

356. Kato, K., *3 - Friction and wear of passive metals and coatings*, in *Tribocorrosion of Passive Metals and Coatings*, D. Landolt and S. Mischler, Editors. 2011, Woodhead Publishing. p. 65-99.

357. Shimizu, Y. and H.A. Spikes, *The Tribofilm Formation of ZDDP Under Reciprocating Pure Sliding Conditions.* Tribology Letters, 2016. **64**(3): p. 46.

358. Dorgham, A., et al., *In situ synchrotron XAS study of the decomposition kinetics of ZDDP triboreactive interfaces.* RSC Advances, 2018. **8**(59): p. 34168-34181.

359. Peng, T., et al., *Solid FeS lubricant: a possible alternative to MoS2 for Cu–Fe-based friction materials.* International Journal of Minerals, Metallurgy, and Materials, 2017. **24**(11): p. 1278-1283.

360. Peng, T., et al., *Low-cost solid FeS lubricant as a possible alternative to MoS2 for producing Fe-based friction materials.* International Journal of Minerals, Metallurgy, and Materials, 2017. **24**(1): p. 115-121.

361. Wang, H.-D., et al., *Characterization and tribological properties of plasma sprayed FeS solid lubrication coatings.* Materials characterization, 2005. **55**(1): p. 43-49.

362. Wang, H.-d., et al., *Investigation on friction and wear behaviors of FeS films on L6 steel surface.* Applied Surface Science, 2005. **252**(4): p. 1084-1091.

363. Lee, I. and I. Park, *Solid lubrication coating of FeS layer on the surface of SKD 61 steel produced by plasma sulfnitriding.* Surface and Coatings Technology, 2006. **200**(11): p. 3540-3543.

364. ISO, *6743-4:2015 Lubricants, industrial oils and related products (class L) — Classification — Part 4: Family H (Hydraulic systems)*. 2015, British Standars Insititution.

365. Aota, H., et al., *Tribological Properties of Nitrided Steels Lubricated with Fully Formulated Oils in Boundary Lubrication Condition.* Tribology Online, 2018. **13**(3): p. 166-171.

366. Brizmer, V., et al., *The Influence of Tribolayer Formation on Tribological Performance of Rolling/Sliding Contacts.* Tribology Letters, 2017. **65**(2): p. 57.

367. Ji, H., et al., *Zinc-dialkyl-dithiophosphate antiwear films: dependence on contact pressure and sliding speed.* Wear, 2005. **258**(5-6): p. 789-799.

Appendix A Raw Raman Spectra

1. Sulphides

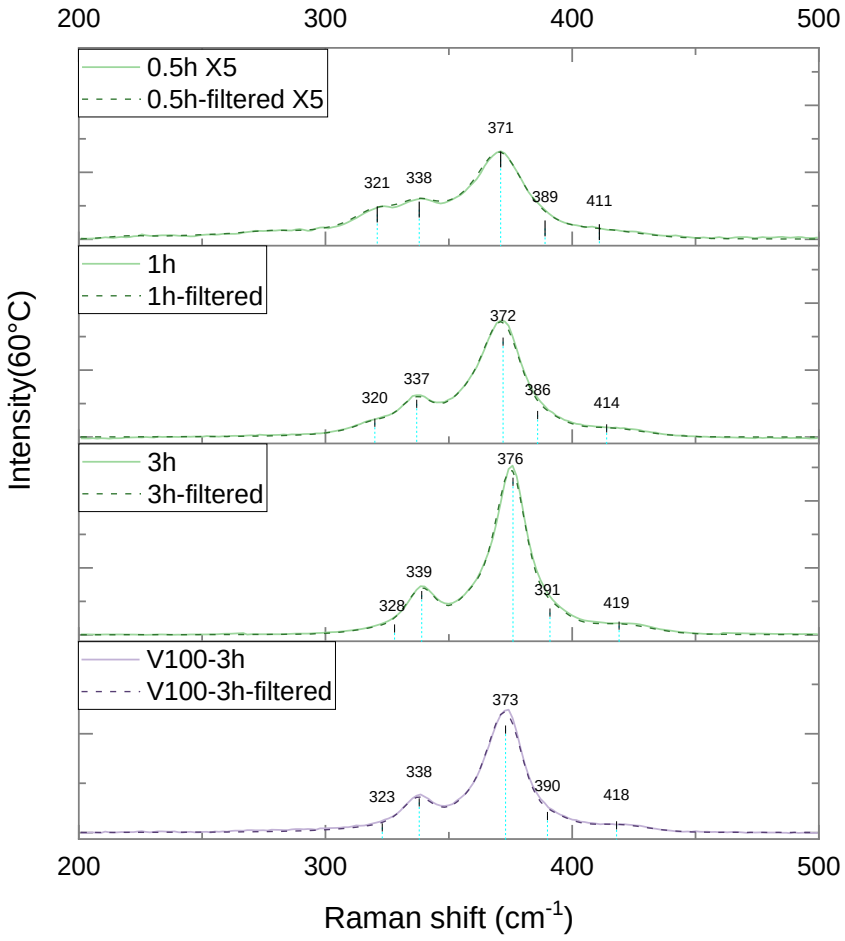

Fig. A-1 Raw and filtered Raman spectra of sulphide section at 60 ℃.

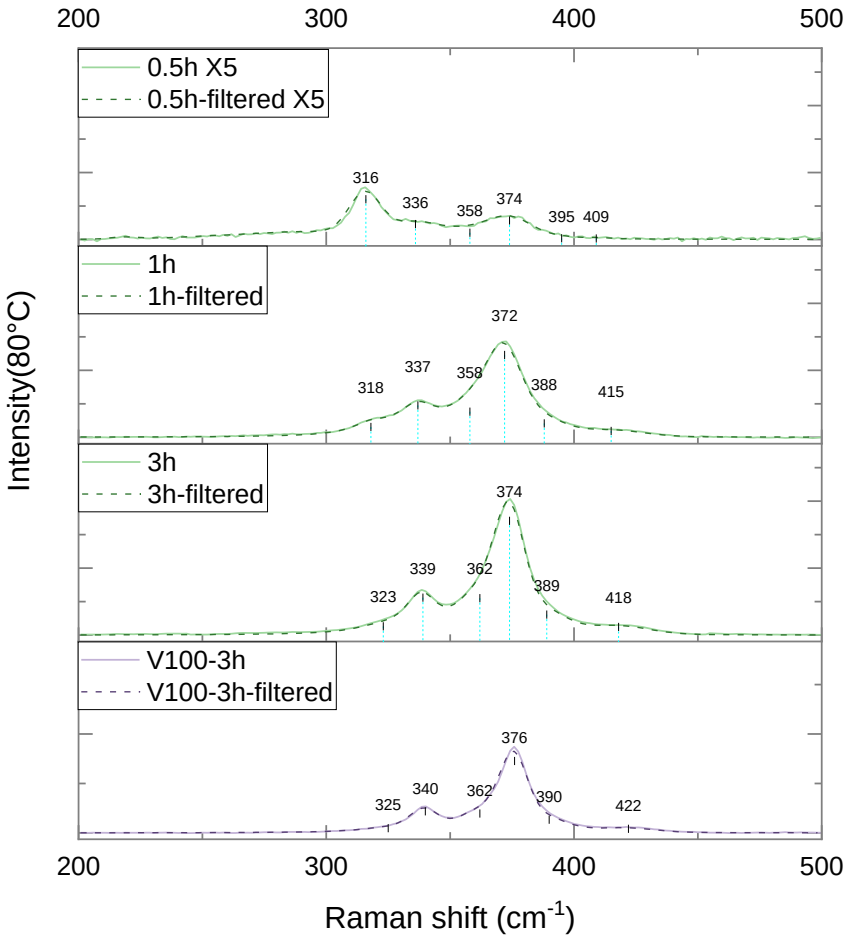

Fig. A-2 Raw and filtered Raman spectra of sulphide section at 80 °C.

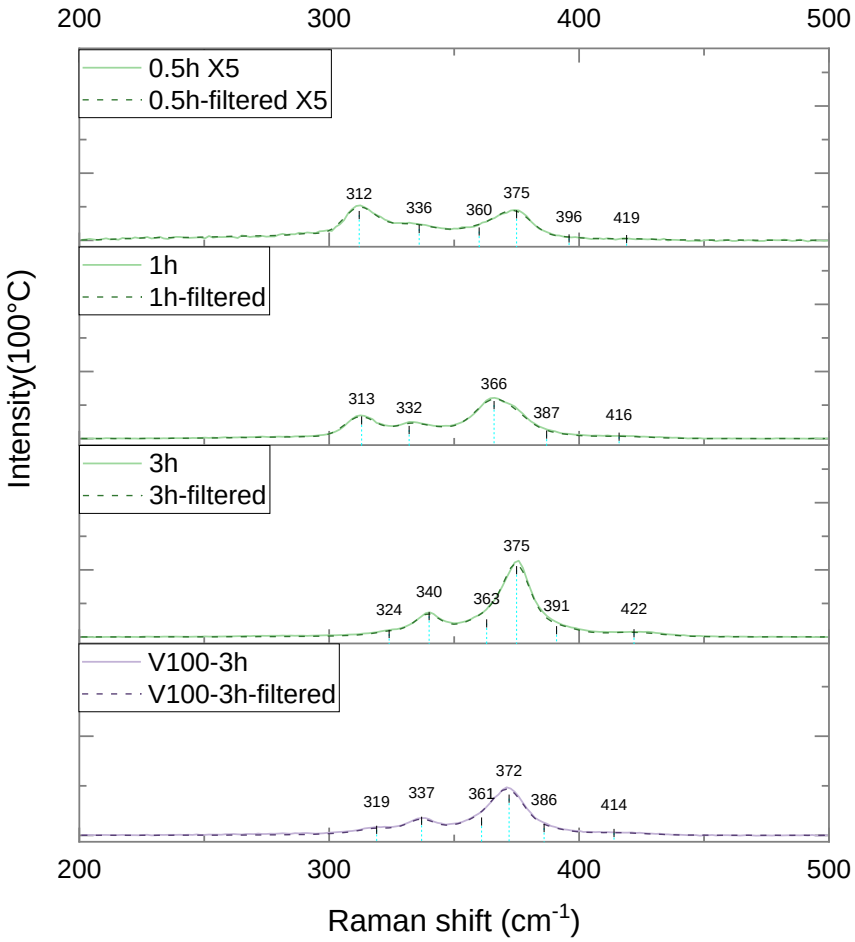

Fig. A-3 Raw and filtered Raman spectra of sulphide section at 100 °C.

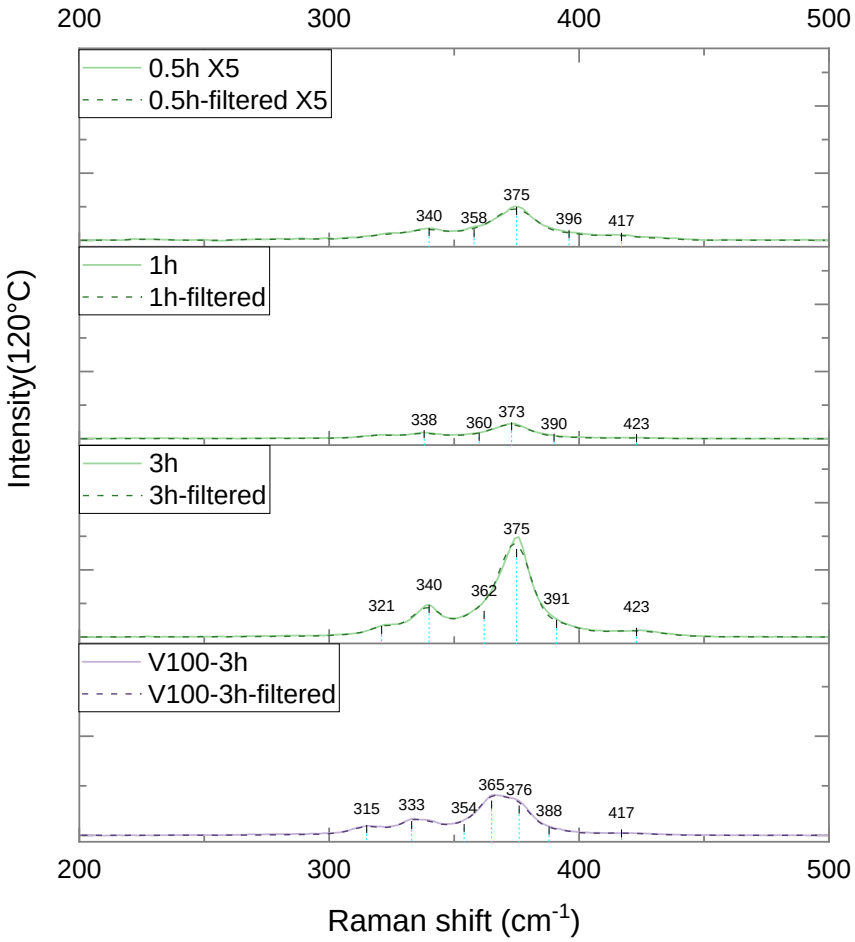

Fig. A-4 Raw and filtered Raman spectra of sulphide section at 120 °C.

2. Phosphates

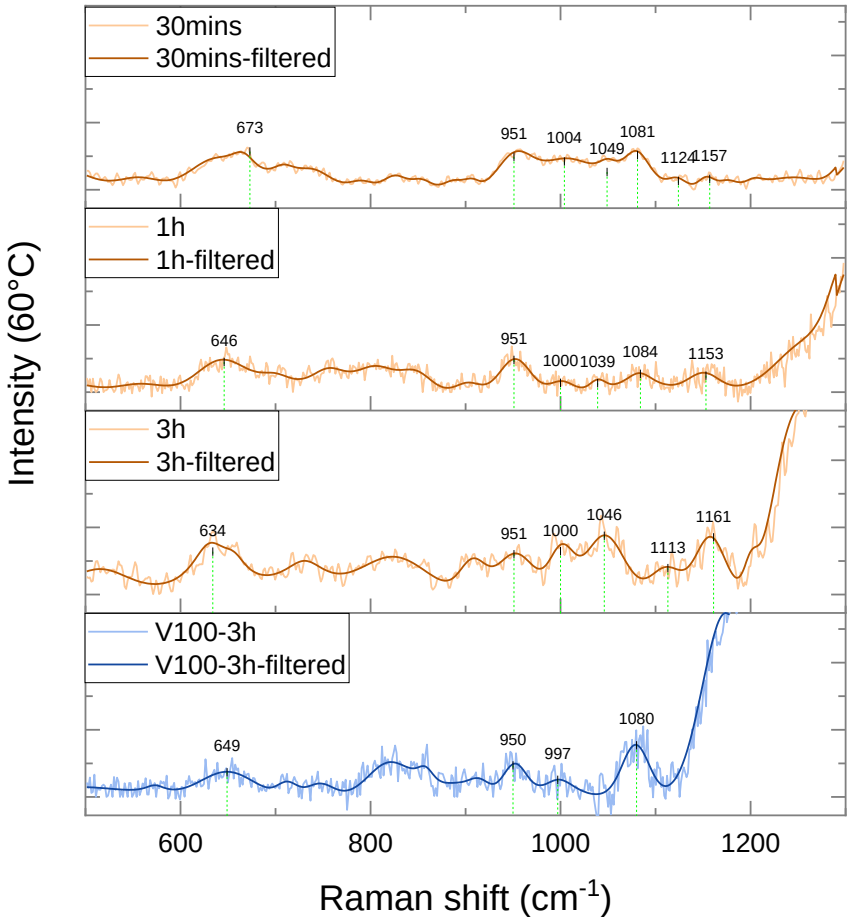

Fig. A-5 Raw and filtered Raman spectra of phosphate section at 60 ℃.

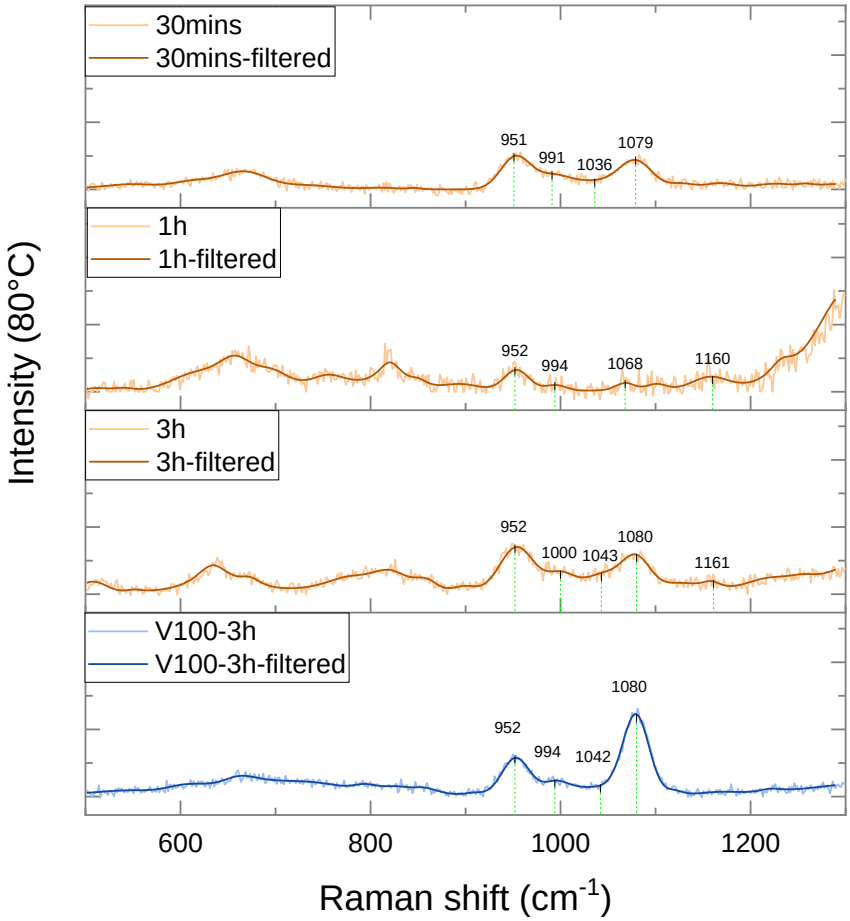

Fig. A-6 Raw and filtered Raman spectra of phosphate section at 80 ℃.

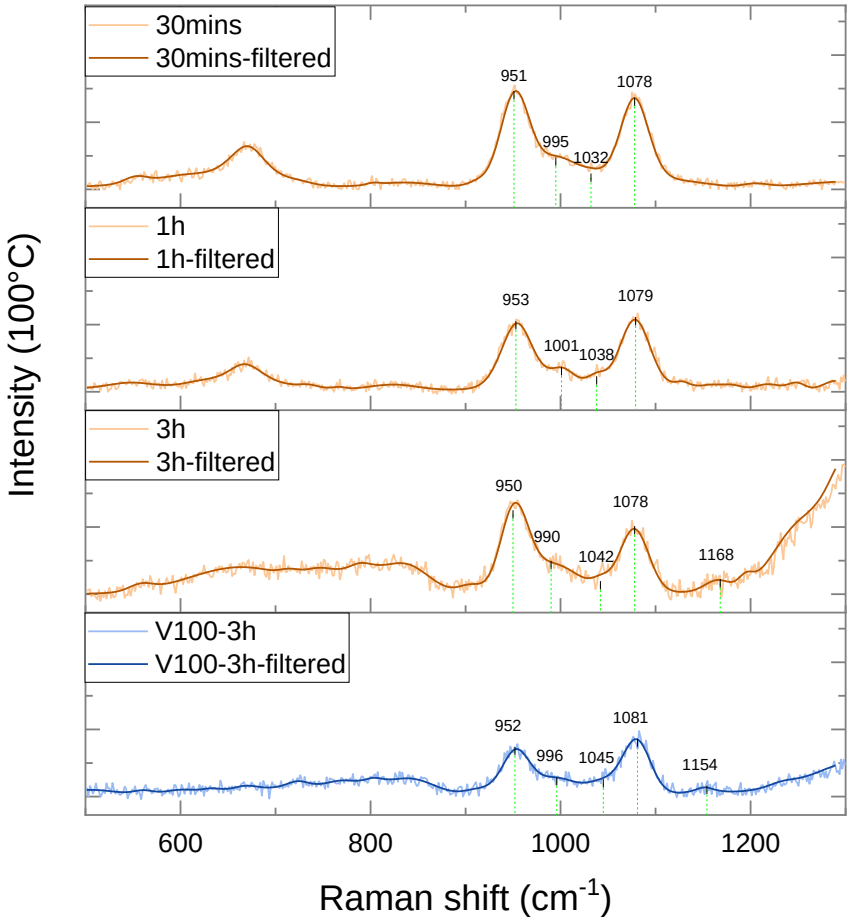

Fig. A-7 Raw and filtered Raman spectra of phosphate section at <u>100 °C</u>.

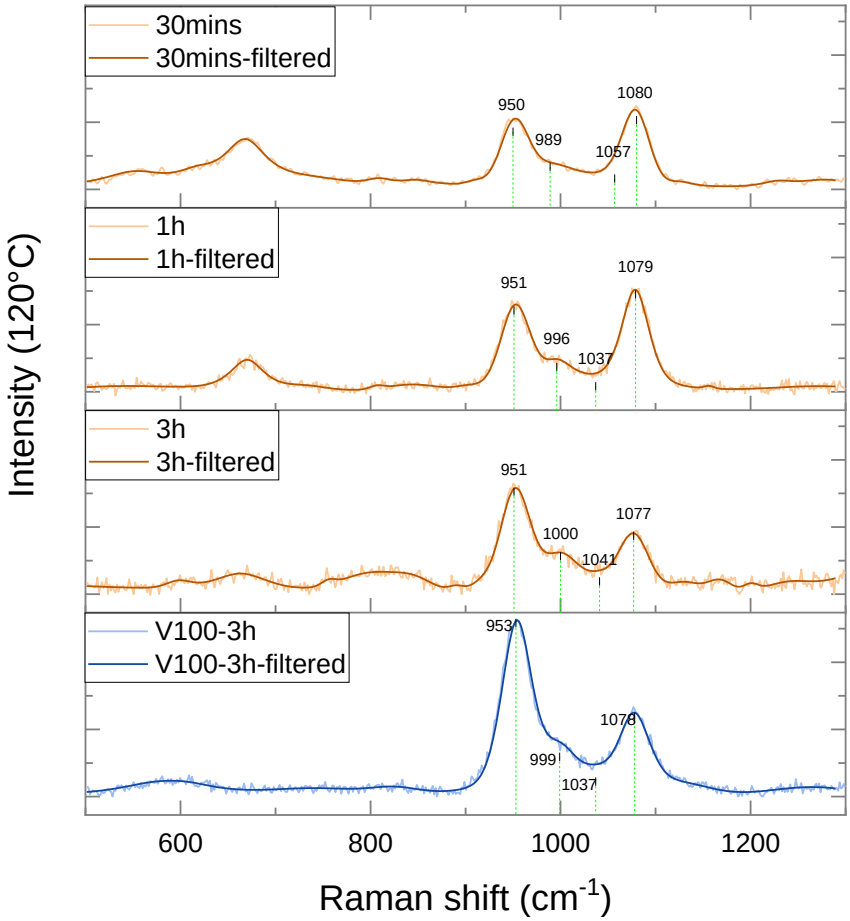

Fig. A-8 Raw and filtered Raman spectra of phosphate section at 120 °C.

Appendix B Solutions of the Parameters $A^{(1)}$, $\bar{A}^{(1)}$, $B^{(1)}$, $\bar{B}^{(1)}$, $C^{(1)}$, $\bar{C}^{(1)}$, $A^{(2)}$, $B^{(2)}$ and $C^{(2)}$

Due to the 3 parameters $B^{(1)}$, $\bar{B}^{(1)}$, and $B^{(2)}$ only related to tangential force, so they can be calculated separately at first.

$$\begin{aligned}
\bar{B}^{(1)} &= -\left[\frac{(G-1)e^{-2\alpha h}}{(1+G)+(1-G)e^{-2\alpha h}}\right]\frac{\bar{q}(m,n,0)}{2\alpha(1-\nu_1)} \\
B^{(1)} &= \bar{B}^{(1)} - \frac{\bar{q}(m,n)}{2\alpha(1-\nu_1)} \\
B^{(2)} &= -2\left(\frac{1-\nu_1}{1-\nu_2}\right)\left[\frac{e^{-2\alpha h}}{(1+\mu)+(1-\mu)e^{-2\alpha h}}\right]\frac{\bar{q}(m,n,0)}{2\alpha(1-\nu_1)}
\end{aligned} \qquad \textbf{(B-1)}$$

Where $G = G_1 / G_2$, $G_1 = \dfrac{E_1}{2(1+\nu_1)}$ and $G_2 = \dfrac{E_2}{2(1+\nu_2)}$ are the shear modulus of layer and substrate, respectively; $\bar{q}(m,n,0) = \mu\bar{p}(m,n,0)$ and μ is friction coefficient; $\bar{p}(m,n,0)$ is the Fourier transform of pressure $p(x,y,0)$ and equals to 1 everywhere.

The expressions for the remaining 6 parameters related to terms *A* and *C* are shown in the equation set (B-2).

$$\begin{aligned}
\left\langle \alpha^2 R_1 \right\rangle &= \alpha^2\left(A^{(1)} - \bar{A}^{(1)}\right) + \alpha(1-2\nu_1)\left(C^{(1)} + \bar{C}^{(1)}\right) \\
\left\langle \alpha^2 R_2 \right\rangle &= \alpha^2\left(A^{(1)} + \bar{A}^{(1)}\right) - 2\alpha(1-\nu_1)\left(\bar{C}^{(1)} - C^{(1)}\right) \\
\left\langle \alpha^2 R_3 \right\rangle &= \alpha\begin{bmatrix} \alpha A^{(1)} - \alpha\bar{A}^{(1)}e^{2\alpha h} + \left((1-2\nu_1)+\alpha h\right)C^{(1)} + \left((1-2\nu_1)-\alpha h\right)e^{2\alpha h}\bar{C}^{(1)} \\ -\alpha e^{\alpha h}A^{(2)} - (1-2\nu_2)e^{\alpha h}C^{(2)} \end{bmatrix} \\
\left\langle \alpha^2 R_4 \right\rangle &= \alpha\begin{bmatrix} \alpha A^{(1)} + \alpha e^{2\alpha h}\bar{A}^{(1)} - \alpha e^{\alpha h}A^{(2)} + \left(\alpha h + 2(1-\nu_1)\right)C^{(1)} \\ +\left(\alpha h - 2(1-\nu_1)\right)e^{2\alpha h}\bar{C}^{(1)} - 2(1-\nu_2)e^{\alpha h}C^{(2)} \end{bmatrix} \\
\left\langle \alpha^2 R_5 \right\rangle &= \alpha\left[\alpha A^{(1)} + \alpha e^{2\alpha h}\bar{A}^{(1)} + \alpha h C^{(1)} + \alpha h e^{2\alpha h}\bar{C}^{(1)} - G\alpha e^{\alpha h}A^{(2)}\right] \\
\left\langle \alpha^2 R_6 \right\rangle &= \alpha\begin{bmatrix} \alpha A^{(1)} - \alpha e^{2\alpha h}\bar{A}^{(1)} + \left(\alpha h + (3-4\nu_1)\right)C^{(1)} - \left(\alpha h - (3-4\nu_1)\right)e^{2\alpha h}\bar{C}^{(1)} \\ -\alpha G e^{\alpha h}A^{(2)} - (3-4\nu_2)Ge^{\alpha h}C^{(2)} \end{bmatrix}
\end{aligned} \qquad \textbf{(B-2)}$$

The terms λ, k, θ and S_0 are set to satisfy:

$$\lambda = 1 - \frac{4(1-\nu_1)}{1+\mu(3-4\nu_2)},\ k = \frac{\mu-1}{\mu+(3-4\nu_1)},\ \theta = e^{2\alpha h}$$
$$S_0 = \left[\mu+(3-4\nu_1)\right]\left[1-ke^{-2\alpha h}\right] = \left[\mu+(3-4\nu_1)\right]\left[1-\frac{k}{\theta}\right] \quad \textbf{(B-3)}$$

Then, the solutions of the 6 unknown parameters in the equation set (B-2) are:

$$C^{(1)} = \frac{(1-\lambda)kS_0R_c}{4(1-\nu_1)(\mu-1)\left[(\lambda/\theta-1)(k/\theta-1)-4\alpha^2h^2k/\theta\right]}$$
$$\bar{C}^{(1)} = \frac{2\alpha h(1/\theta)C^{(1)}+(1/\theta)R_a}{S_0}$$
$$A^{(1)} = \frac{1}{2\alpha}\left[-(3-4\nu_1)C^{(1)}+\bar{C}^{(1)}+\alpha(R_1+R_2)\right]$$
$$\bar{A}^{(1)} = \frac{1}{2\alpha}\left(-C^{(1)}+(3-4\nu_1)\bar{C}^{(1)}-\alpha(R_1-R_2)\right) \quad \textbf{(B-4)}$$
$$C^{(2)} = \frac{(1-\lambda)\alpha/\sqrt{\theta}}{4(1-\nu_1)}(R_3-R_4+R_5-R_6)+(1-\lambda)C^{(1)}/\sqrt{\theta}$$
$$A^{(2)} = -\frac{h\theta(1-k)}{\sqrt{\theta}(k-\theta)}C^{(1)}-\frac{(3-4\nu_2)}{2\alpha}C^{(2)}+\frac{\left[R_1+R_2-(R_3+R_4)\right]}{2\sqrt{\theta}}+\frac{(1/\theta)R_a}{2S_0}\left(\frac{1-\theta}{\alpha\sqrt{\theta}}\right)$$

where

$$R_a = \alpha\left[(\mu-1)(R_1+R_2)-\mu(R_3+R_4)+(R_5+R_6)\right]$$
$$R_b = \alpha\left[(R_2-R_1)+(R_3-R_4)/\theta-\frac{(1-\lambda)}{4\theta(1-\nu_1)}\left[(R_3-R_4)+(R_5-R_6)\right]\right]$$
$$R_c = \frac{4(1-\nu_1)}{1-\lambda}\left(\frac{2\alpha hR_a/\theta}{S_0}+R_b\right)$$

Appendix C Polynomial Fitting of the Fe vol.% in XPS Analysis

In order to calculate the wear coefficient *K* in the phase of tribochemical wear, the curve of Fe vol.% in XPS analysis with unit depth should be fitted. The polynomial equation is chosen according to the characteristic of the curve. In order to select the appropriate order of the polynomial equation, Fig. C-1 compares the fitting results of the 3rd and 4th order of the polynomial equations.

It can be seen that the 3rd-order polynomial equation is more in line with the trend that the Fe vol.% in tribofilm increases with the increase of the depth, although the fitting error of the 4th-order polynomial equation is smaller. Therefore, the 3rd-order polynomial equation is selected for wear calculation, and their constant values at different temperatures are listed in Table C-1.

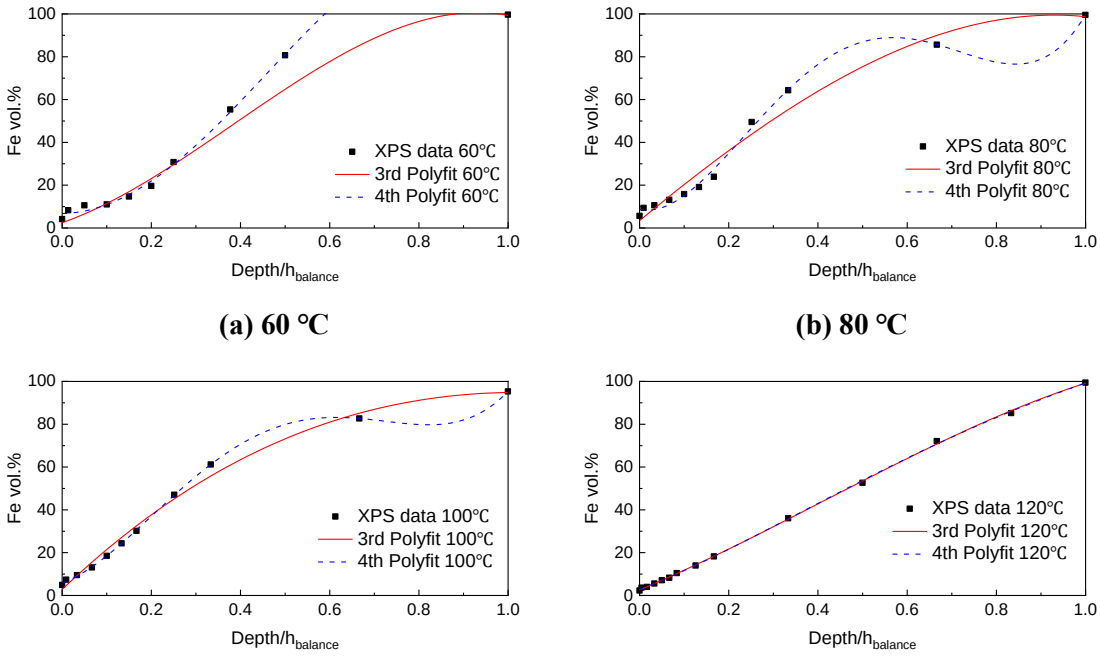

(a) 60 ℃ **(b) 80 ℃**

(c) 100 ℃ **(d) 120 ℃**

Fig. C-1 The comparisons of using the 3rd and the 4th order polynomial equations to fit the Fe vol.% as the function of unit depth at the temperatures of (a) 60 ℃, (b) 80 ℃, (c) 100 ℃ and (d) 120 ℃ are shown separately.

Table C-1 The parameters in the 3rd polynomial fitting of the Fe vol.% as the function of the unit depth at different temperatures.

Temperature	**60℃**	**80℃**	**100℃**	**120℃**
Function	$y = p_1x^3 + p_2x^2 + p_3x + p_4$			
p_1	-159.4	-39.23	17.67	-39.47
p_2	183.6	-38.18	-123.8	48.85
p_3	72.63	172.7	198.1	87.17
p_4	2.503	3.424	2.87	2.635

(*y* – *Fe vol.%*; *x* – *Depth*/ $h_{balance}$)